DISSERTATION

MILLIMETER AND SUB-MILLIMETER WAVE RADIOMETERS FOR ATMOSPHERIC REMOTE SENSING FROM CUBESAT PLATFORMS

Submitted by

Mehmet Ogut

Department of Electrical and Computer Engineering

In partial fulfillment of the requirements

For the Degree of Doctor of Philosophy

Colorado State University

Fort Collins, Colorado

Fall 2018

Doctoral Committee:

Advisor: Steven C. Reising

V. Chandrasekar
Christian Kummerow
Jothiram Vivekanandan

ABSTRACT

MILLIMETER AND SUB-MILLIMETER WAVE RADIOMETERS FOR ATMOSPHERIC REMOTE SENSING FROM CUBESAT PLATFORMS

Knowledge of the distribution of water vapor and its dynamics is essential to improve understanding of atmospheric events that have impacts on human activity including the formation of clouds and precipitation. In addition, water vapor is a major greenhouse gas that directly affects the global climate. Furthermore, water vapor as a medium of heat exchange plays a major role in the Earth's energy balance. Therefore, an improved knowledge of atmospheric water vapor will improve studies in meteorology, climatology and hydrology.

Microwave and millimeter-wave passive remote sensing of the atmosphere has been performed using ground-based, airborne and satellite instruments. The accuracy and reliability of these measurements are important for the quality of the retrieved atmospheric variables, including water vapor, cloud ice and liquid water. CubeSats, as an emerging type of small satellite, have advantages over traditional larger satellites in terms of cost to design, launch and operate. Hence, they enable testing and implementing new technologies and concepts for atmospheric remote sensing to improve the quality of the retrieved data products.

The Tropospheric Water and Cloud Ice radiometer instrument for deployment on 6U CubeSats is currently being developed to enable global observations of upper

tropospheric and lower stratospheric cloud ice and water vapor using high frequency millimeter and sub-millimeter-wave radiometric channels at 15 frequencies from 118 to 670 GHz. The instrument is designed to meet the stringent size, weight and power requirements of CubeSats, in addition to radiometric specifications to obtain highly accurate and reliable radiometric measurements.

A low-noise, highly-reliable command and data handling subsystem is designed to control the synchronized simultaneous acquisition of the analog radiometric measurements. The control and data handling subsystem also operates the interface among the subsystems of the TWICE instrument. In addition, the FPGA on the command and data handling board controls the 670 GHz receiver LNA switching signal and its synchronization with the radiometric acquisition, sends radiometric data and system information to an on-board computer. The FPGA also performs voltage monitoring and current sensing of various sub-circuits of the instrument for system health monitoring.

A low-noise, high-efficiency power regulation system is designed to provide regulated voltages at the required current ratings to all active devices in the front-end receivers and the command and data handling system. Analog switches on the power regulation boards controlled by the FPGA in the command and data handling subsystem enables turning on and off each TWICE radiometer subsystem without affecting the operation of other radiometer subsystems. The current sensing and voltage monitoring devices continuously monitor system health information.

The on-orbit reliability of the command and data handling and power regulation boards has been studied. Heavy-ion testing of the electronic devices has been conducted at the Texas A&M Cyclotron Facility. The reliability of the electronic systems of the Tropospheric Water and Cloud Ice radiometer has been analyzed based on the radiation testing results for the electronics under low Earth orbit-like radiation conditions. A system-level radiation effects mitigation strategy has been studied. The designed command and data handling and power regulation boards are expected to be resistant to radiation related effects during on-orbit operation.

The command and data handling and power regulation boards have been integrated with the 240 GHz, 310 GHz and 670 GHz front-end receivers for end-to-end integrated radiometer testing. The functionality of the integrated system has been successfully verified. Y-factor testing has been conducted using an ambient blackbody target at room temperature and another blackbody target submerged in liquid nitrogen at 77 K. The stability and noise performance of the receivers have been characterized. A 1/f noise mitigation technique for the 670 GHz receiver has been successfully implemented. Test results have shown that the integrated system meets the radiometric design requirements, in addition to the size, mass and power requirements of 6U class satellites.

A noise wave model analysis has been performed on an artificially generated Dicke-switching radiometer instrument. The effect of each subsystem in the radiometer architecture on the noise performance of the system has been investigated. An artificial neural network-based deep learning calibration technique has been

developed for microwave, millimeter-wave and sub-millimeter-wave radiometer calibration. This new deep learning technique has been successfully applied to calibrate the artificially generated Dicke-switching radiometer. The deep learning calibrator estimates the antenna temperature at high accuracy for several cases tested, including non-linearity and gain variations in the radiometer output voltage. This deep learning calibrator has been successfully implemented to estimate antenna temperatures from voltage measurements by the High-Frequency Airborne Microwave and Millimeter-Wave Radiometer instrument during the West-Coast Flight Campaign conducted in 2014. The estimated antenna temperatures are in agreement with those obtained from conventional calibration techniques. This, in turn, indicates that the deep learning calibrator can be applied for radiometric calibration.

A multi-channel, multi-angle wet-path delay retrieval algorithm has been developed using radiometric measurements at millimeter-wave window channels. This algorithm has been demonstrated using radiometer measurements during the West-Coast Flight Campaign conducted in 2014. The results show that the wet-pet delay retrievals at millimeter-wave channels are in good agreement with the retrievals at the microwave channels. As a result, the proposed retrieval algorithm can be applied to improve the spatial resolution of wet-path delay retrievals by using millimeter-wave window channels.

ACKNOWLEDGMENTS

I would first like to thank my advisor, Prof. Steven C. Reising, for his guidance of my research and Ph.D. dissertation. I would also like to thank Prof. V. Chandrasekar, Prof. Christian Kummerow and Dr. Jothiram Vivekanandan for their input to my dissertation and for serving on my committee.

I would like to thank Dr. Xavier Bosch-Lluis and Dr. Yuriy V. Goncharenko for their support and guidance. I would also like to thank all other members of the Microwave Systems Laboratory at Colorado State University, specially Braxton Kilmer and Jared McKneely.

I would like to thank all the members of the NASA TWICE IIP-13 project team at the NASA/Caltech Jet Propulsion Laboratory (JPL) and the Northrop Grumman Corporation (NGC). In addition, I would like to thank Dr. Pekka Kangaslahti, Dr. Alan Tanner, Dr. Robert Jarnot, Dr. Erich Schlecht, Dr. Isaac Ramos-Perez, Dr. Sharmila Padmanabhan and Dr. Xavier Bosch-Lluis for their valuable contributions as part of the NASA TWICE IIP-13 project as well as serving as JPL reviewers. Also, I would like to acknowledge Dr. William Deal and Dr. Alex Zamora of NGC for their valuable assistance.

Finally, I owe my deepest gratitude to my family for their continuous and unparalleled love, help and moral support. I also would like to thank my friends for their support and patience.

DEDICATION

To my family for their support

TABLE OF CONTENTS

LIST OF TABLES

LIST OF FIGURES

Chapter I Introduction

The distribution of atmospheric water vapor and its dynamics are essential to a comprehensive understanding of meteorological and climatological processes. Acting as a primary medium of heat exchange, water vapor significantly affects the energy balance of the Earth. In addition, since water vapor is a major greenhouse gas, it plays a dominant role in the global climate. Moreover, many atmospheric processes, including cloud formation and evolution, as well as precipitation and evaporation, depend on atmospheric water vapor. Therefore, knowledge of atmospheric water vapor and its spatio-temporal variation is critical for weather prediction and climatological studies [1].

More generally, improved knowledge of three phases of the atmospheric water, i.e., vapor, liquid and ice, is expected to lead to better understanding of the formation and evolution of clouds, as well as precipitation and the global water cycle. Furthermore, such knowledge will contribute to improve the accuracy of weather and climate models. This, in turn, will improve the reliability of atmospheric predictions, including those of rain, snow, sleet, hail and more generally of severe weather [2].

Measurements of atmospheric water vapor have been conducted using in-situ techniques such as weather balloons since the 1960s. Wet-path delay (WPD) retrievals have been performed using remotely sensed measurements from ground-based [3], airborne [4], [5], [6] and satellite platforms [7], [8] since the 1970s. These

measurements are useful for weather prediction, climatological studies and to provide the necessary WPD corrections for radar altimeters [6].

Improving the accuracy and the spatial resolution of WPD retrievals may advance understanding of the microphysics and the global distribution of atmospheric water vapor [10]. This may help weather models for the prediction of convective events [11], [12]. However, the footprint size of currently-used satellite microwave radiometers limits the accuracy and the resolution of the retrievals, especially in the vicinity of land-ocean boundaries, as illustrated in Figure 1. Since the maximum size of reflector antennas of space-borne radiometers is limited, one can instead increase the operating frequency, which in turn decreases the wavelength with a

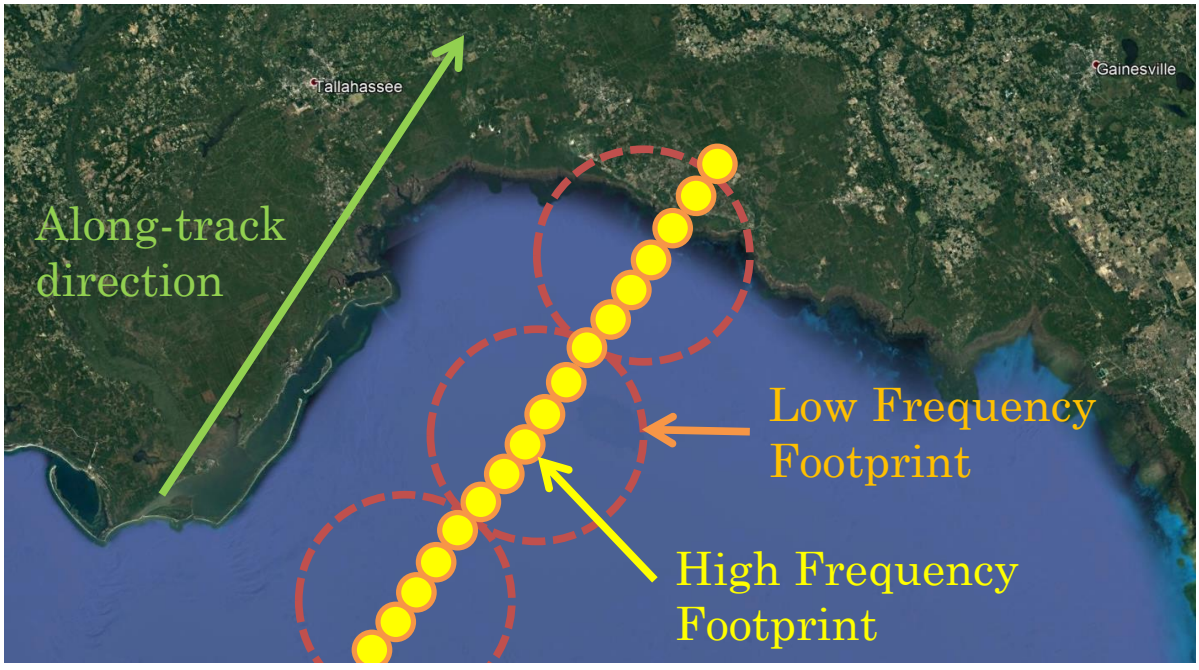

Figure 1: High frequency millimeter wave channels (up to 300 GHz) can provide smaller footprint size than microwave channels allowing enhanced resolution for altimetry studies.

fixed antenna size, consequently decreasing the radiometer spot size on the surface, as shown in Figure 1 [13].

Water in the form of ice clouds modulates Earth's climate and affects precipitation, atmospheric structure and cloud dynamics [9]. Global observations of ice clouds are performed using satellite instruments such as radars [10] and infrared radiometers [11]. However, these instruments are less sensitive to ice cloud particle sizes between 100 µm and l mm [9]. This is because the interaction of ice particles with electromagnetic radiation strongly depends on the ratio between the ice particle size and the observation wavelength. For this reason, radiometers operating in the sub-millimeter-wave frequency range are well suited to observe ice cloud particles in the size range of 100 µm to l mm to fill the gap between radar and infrared radiometers, as first introduced by Evans and Stephens in 1995 [12]. Due to recent developments in sub-millimeter-wave receiver technology, there has been an increasing interest in using millimeter and sub-millimeter-wave radiometry for cloud ice observations [9], [13], [14].

1.1. CubeSats Overview

A small satellite (SmallSat) is defined as any satellite that weighs less than 300 kg. A CubeSat is a type of SmallSat that is based on a standard CubeSat Unit (1U) with the volume of a 10 cm cube and a mass of up to 1.33 kg [15]. Depending on the specifications of design and launch, the size of CubeSats varies from 1U to at least 12U, with recent standards allowing 50% greater mass density for 6U than for 3U or smaller CubeSats [16]. A 1U and 3U CubeSat standard models are shown in

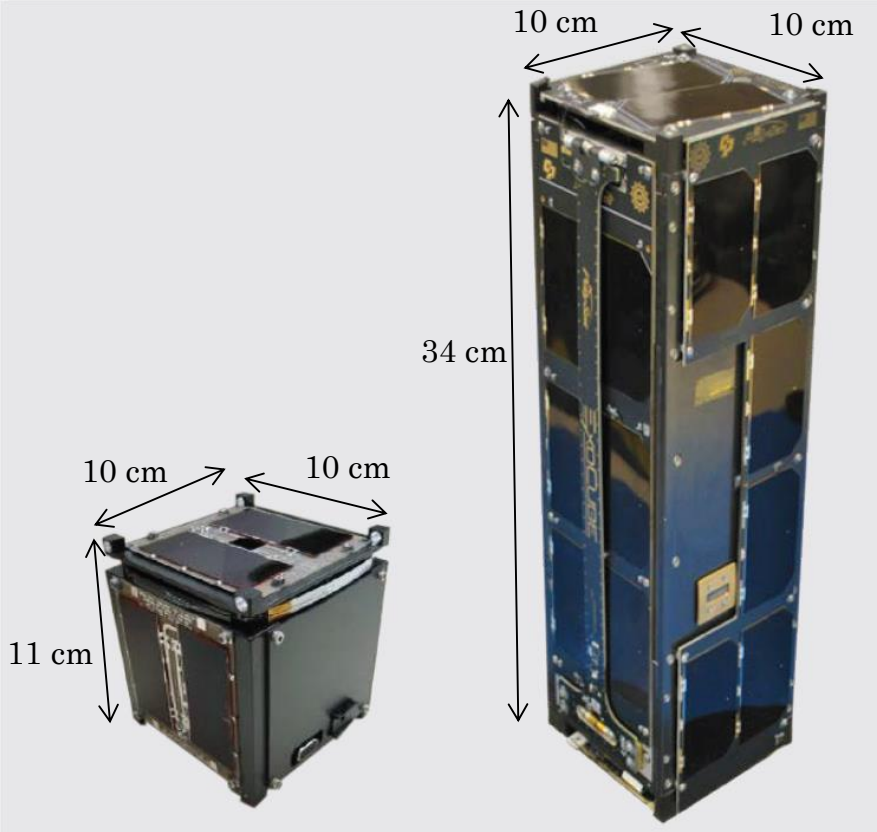

Figure 2: The standard 1U CubeSat model (left) and the standard 3U CubeSat model (right) are given with unit dimensions [17].

Figure 2 to provide a visual comparison for the miniaturized size of the instrument [17].

1.1.1 Historical Development of CubeSats

SmallSats have large cost to build, design and launch since each has its own specific challenges. Therefore, it is not usually affordable for the academic scientific community to build a SmallSat. Hence, the CubeSats which are a standardized form of SmallSats, have been first introduced in 1999 by Prof. Puig-Suari of California Polytechnic State University and Prof. Twiggs of Space Systems

Development Laboratory at Stanford University to allow universities an affordable access to the space [17].

CubeSats have recently emerged as important to the aerospace industry, universities and national governments. This increased interest is largely due to advances in attitude determination and control systems (ADCS), computing, navigation and communications technology, leading to substantial reduction of satellite mass and volume into a small form factor [18]. In addition, SmallSats and CubeSats are much less expensive to develop, launch, and operate than traditional larger satellites. They also have more rapid development cycles and the potential to be deployed in on-orbit "string of pearls" constellations for much lower cost than that of traditional larger satellites. Due to the increased availability and decreased cost of launch opportunities based on the use of excess launch vehicle space unused by the primary payload, the number of CubeSat launches has dramatically increased in recent years, currently substantially exceeding 100 per year [19], [20].

1.1.2 Deploying CubeSats into the Orbit

CubeSats can be put into orbit either using rockets that put them straight in the final orbit or going through the International Space Station (ISS). The ones that are sent to the ISS are finally released into their orbit by the ISS astronauts using a dispenser unit. The CubeSats that do not stop at the ISS are released to their orbit using a dispenser unit attached to the CubeSat as an interface between the CubeSat and the launch vehicle. The dispenser unit also provides protection to the CubeSat during the launch [17].

National Aeronautics and Space Administration (NASA) CubeSat Launch Initiative (CSLI) provides launch opportunity to the universities in U.S. for launching their own CubeSat either using the excess capacity of future launches or through the deployment from the ISS. Depending on the availability of the rockets, various types of rockets are used by CSLI for launching CubeSats into the space as shown in Figure 3.

1.1.3 CubeSats in Space

CubeSats serve to the science and technology community in various different ways:

1.1.3.1 Educational

The CubeSats are used to educate engineers and students because of their various advantages over larger satellites to design, build and launch at low-cost in a short lead time. The educational CubeSats usually have a simple payload such as a camera, a sensor and a communication module. The development time and budget to build such a system is affordable for universities.

1.1.3.1 Technology Demonstration

CubeSats are an important platform for testing future technologies and new concepts since they have short development times and low budgets compared to larger traditional satellites. NASA and some universities have been using CubeSats to increase technology readiness level (TRL) on new instruments and concepts. The devices and systems with increased TRL levels will be available for the new system designs as a part of the large mission if they meet the requirements. For instance,

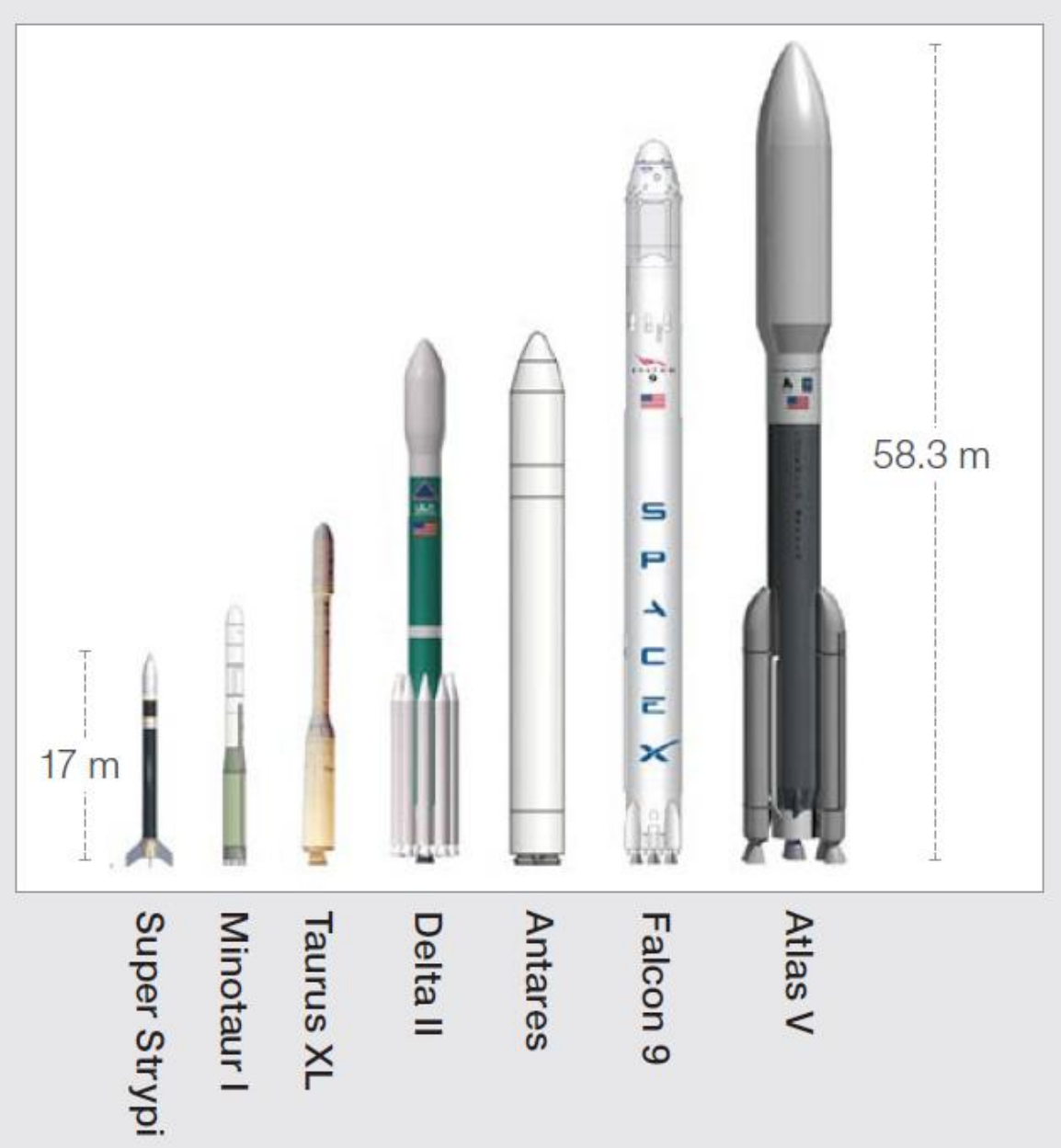

Figure 3: Various rockets used for launching CubeSats into the space [17].

the Temporal Experiment for Storms and Tropical Storms Demonstrator (TEMPEST-D) is a CubeSat mission led by Colorado State University (CSU) in partnership with NASA Jet Propulsion Laboratory and Blue Canyon Technologies has been launched in May 2018 [21]. The TEMPEST-D is a technology

demonstration mission sponsored by NASA for testing future technologies for increasing the TRL of the systems for future technologies.

1.1.3.2 Science Mission

CubeSats can be also used as a science mission in addition to their usage for education or technology demonstration purposes. Their low cost to design and launch in addition to short development times make them suitable for scientific mission in comparison to traditional larger satellites with longer development times at high cost to build and launch. For instance, the Time Resolved Observations of Precipitation structure and storm Intensity with a Constellation of SmallSats (TROPICS) led by Massachusetts Institute of Technology (MIT) Lincoln Laboratory is a 3U CubeSat planned to provide microwave measurements of tropical hurricanes and typhoons. As science objectives, TROPICS aims to relate precipitation structure evolution, including diurnal cycle, to the evolution of the upper-level warm core and associated intensity changes, the occurrence of intense precipitation cores (convective bursts) to storm intensity evolution and the retrieved environmental moisture measurements to coincident measures of storm structure (including size) and intensity [22].

1.1.4 CubeSat Radiometers

CubeSats have much lower costs of design, launch and operation than traditional larger satellites. Recent developments in computing and communication technology, very-large scale integration (VLSI) and micro-electromechanical systems (MEMS)

design have substantially reduced the mass, volume and power of microwave radiometers, making CubeSat deployment feasible. As a result, the number of CubeSat missions with on-board microwave and millimeter-wave radiometers has substantially increased in the past few years [19].

The stringent size, weight and power (SWaP) requirements of CubeSats present new challenges for the microwave and millimeter radiometry. The small volume of CubeSats enforces the designers for miniaturizing all the parts of the radiometers in a way that the instrument fits into small form factor of the CubeSat. The limited power from the instrument solar panels and the maximum weight restrictions also imposes further restriction on the design and operational techniques of the CubeSat radiometers. Furthermore, the on-orbit reliability of the radiometer should allow obtaining radiometric data to be used for scientific and technology demonstration purposes.

Figure 4 shows TEMPEST-D [23], Micro-sized Microwave Atmospheric Satellite (MicroMAS) [24], the CubeSat Radiometer Radio Frequency Interference Technology Validation (CubeRRT) [25] and the Tropospheric Water and Cloud Ice (TWICE) [26] radiometer CubeSat instruments. MicroMAS is a 3U CubeSat technology demonstration mission led by MIT in collaboration with the University of Massachusetts Amherts. MicroMAS has nine radiometric channels operating near the 118.75 GHz oxygen absorption line [24]. CubeRRT is a 6U CubeSat technology demonstration mission led by Ohio State University in collaboration with NASA Goddard Space Flight Center (GSFC), NASA JPL and Blue Canyon

Technology. CubeRRT has nine tunable frequency bands from 6 to 40 GHz frequency ranges at single polarization [25]. TWICE is a 6U CubeSat mission led by Colorado State University in collaboration with NASA JPL and Northrop Grumman Corporation. TWICE has 16 radiometric channels from 118 GHz to 670 GHz frequencies for upper tropospheric water vapor and lower stratospheric cloud ice monitoring [26].

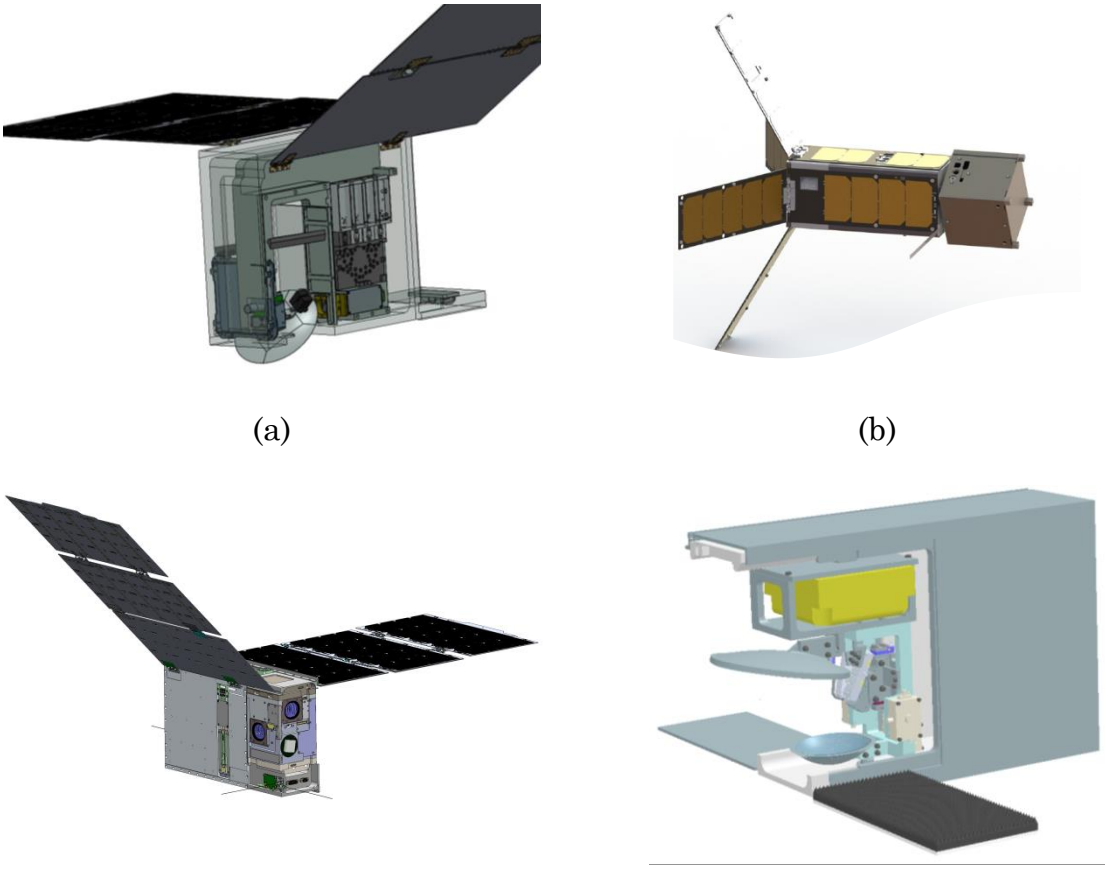

(a) (b)

(c) (d)

Figure 4: CubeSat radiometers: (a) TEMPEST-D, (b) MicroMAS, (c) CubeRRT, (d) TWICE

1.2. Organization of the Dissertation

The chapters of the dissertation are organized as the following:

- The fundamental radiometric principles are given including thermal radiation, Planck's Blackbody Radiation Law and radiative transfer theory in Chapter II. In addition, various radiometer architectures used in atmospheric remote sensing are presented and discussed.
- Chapter III describes the TWICE instrument. It explains the various subsystems of the instrument including the front-end receivers.
- Chapter IV discusses the design, testing and analysis of the C&DH and power regulation boards of the TWICE instrument.
- Chapter V focuses on the reliability of the TWICE electronics. The radiation analysis, testing and mitigation techniques are presented.
- Chapter VI presents end-to-end radiometric testing using the integrated TWICE receivers, the C&DH and power regulation boards. A radiometer characterization is performed to analyze the noise performance and stability of the integrated system.
- Chapter VII presents the radiometer noise-wave model which is used to characterize and analyze the noise sources in a radiometer. The noise characteristic of an artificially generated Dicke-switching radiometer is studied.
- Chapter VIII discusses an artificial neural network based deep learning calibrator algorithm. The new technique is demonstrated on an artificially

generated Dicke-switching radiometer and the HAMMR WCFC radiometric measurements.

- Chapter IX presents a new technique for WPD retrieval using millimeter-wave window channel radiometric measurements. The developed technique is validated using the HAMMR WCFC radiometric measurements.

Chapter II Radiometry Overview

This chapter discusses the fundamentals of passive remote sensing of the atmospheric constituents including water vapor, cloud ice and temperature at microwave, millimeter-wave and sub-millimeter-wave frequencies. Atmospheric radiation, the radiative transfer theory and radiometer topologies are analyzed. Furthermore, the millimeter and sub-millimeter-wave radiometry for atmospheric remote sensing is discussed.

2.1. Thermal Radiation and Kirchoff's Law

Any substance above absolute temperature radiates electromagnetic radiation due to oscillations of molecules over a continuous range of frequencies. An ideal blackbody object is a perfect absorber that all radiation incident upon its surface is absorbed at all frequencies. At the same time, a blackbody object is a perfect emitter. The amount of absorption and emission for a blackbody is always larger than any non-blackbody object [27].

For any object, amount of radiation absorbed equals to the amount of radiation emitted at the state of equilibrium. The equilibrium condition for a material is defined by Kirchoff's Law as:

$$E_\lambda(T) = \varepsilon_\lambda B_\lambda(T) \tag{II.1}$$

where $B_\lambda(T)$ is the radiation of an ideal blackbody object, $E_\lambda(T)$ is the emitted radiation and ε_λ is the emissivity of the object. A blackbody object has emissivity of "1" since it is a perfect emitter. On the other hand, a gray body object is defined as a

non-perfect emitter. In other words, radiation incident on a gray body object is partially reflected, transmitted or absorb. For any gray body, the emissivity is lower than "1" and it is assumed to be constant and independent of the wavelength [27].

2.2. Planck's Blackbody Radiation

Classical mechanics derived to explain material physics is inadequate to explain the wavelength distribution of a cavity radiation takes and its dependency on the temperature of the cavity walls. When the wavelength approaches to zero for a cavity, the number of states should be infinite according to classical mechanics. However, Planck approached this problem by providing an explanation based on quantum mechanics stating that the emitted radiation can only have discrete sets of energy levels. These energy levels are defined by Bohr's equation for a quantum number n [28]:

$$E = nhv \tag{II.2}$$

where v is the frequency of oscillations in the walls of the cavity and h is the Planck's constant [=6.626x10^{-34} joules]. The quantum theory model for a blackbody describes the emitted radiation emitted from the cavity as discrete packets of energy quanta. The radiation emitted from a blackbody is uniform in all direction defined by Planck's radiation law as:

$$B_f = \frac{2hf^3}{c^2}\left[1/\left(e^{\frac{hf}{kT}} - 1\right)\right] \tag{II.3}$$

where B_f is the blackbody spectral brightness [W m^{-2} sr^{-1} Hz^{-1}], c is the speed of light [m/s], T is absolute temperature in Kelvin, f is the frequency in Hertz and k is Boltzmann's constant [1.381x10^{-23} joule/K] [27].

The Planck's blackbody radiation curves are plotted using Equation (II.3) in Figure 5 at three different temperatures for the frequency range of 1 GHz to 1000 THz. The spectral brightness of the curves given in Figure 5 is increased with the temperature. The frequency at the maximum spectral radiance occurs is temperature dependent and increases with the temperature. As it is illustrated in Figure 5, the curve for 500 K absolute temperature has the highest spectral radiance at the highest frequency within the curves plotted.

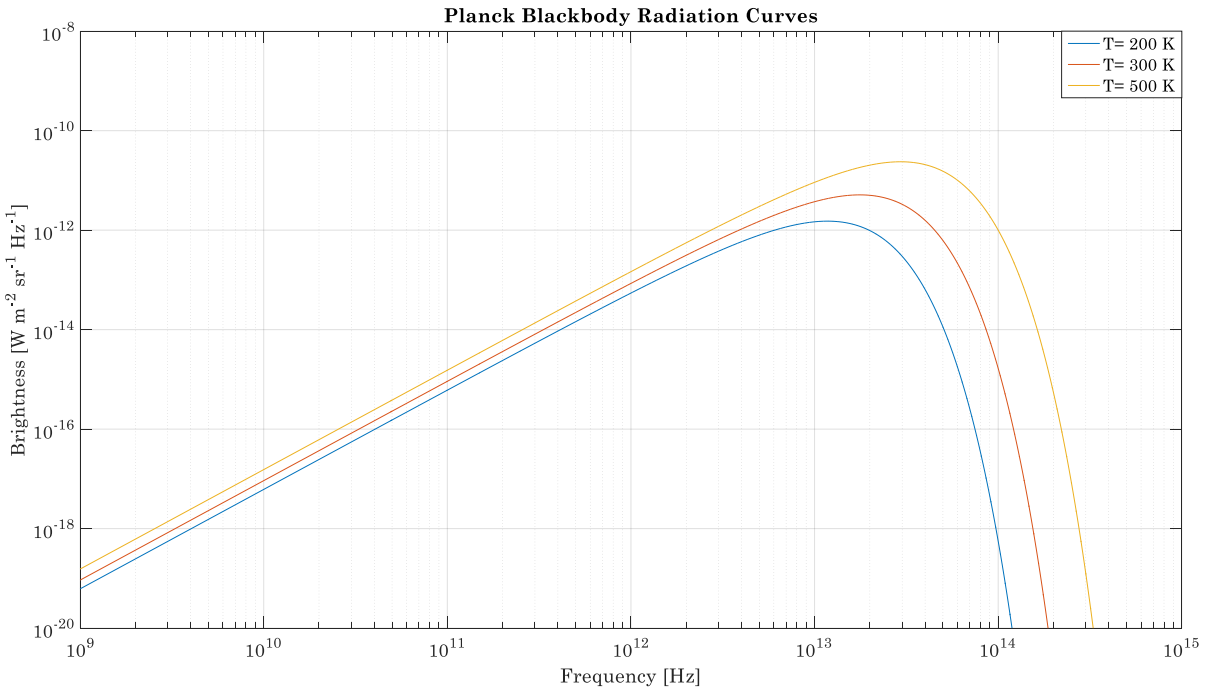

Figure 5: Planck spectral brightness radiation curves at three different absolute temperatures with varying frequency are given with respect to frequency for the range of 1 GHz to 1000 THz.

The relationship between the wavelength (λ_{max}) of the maximum emission for a given Planck radiation curve at a given temperature is explained with the Wien's displacement law by taking the partial derivative of the spectral brightness with respect to the wavelength [27]:

$$\frac{\partial B_\lambda}{\partial \lambda} = 0 \tag{II.4}$$

which results in:

$$T\lambda_{max} = 2898 \ \ [\mu m\ K] \tag{II.5}$$

The spectral intensity provided in Equation (II.3) is simplified depending on the wavelength of the radiation. For shorter wavelengths, where λ approaches zero, Wien's distribution is used to approximate the Planck's blackbody radiation. In this case:

$$hf \gg kT \tag{II.6}$$

Then, Equation (II.3) is defined as:

$$B_\lambda = \frac{2hc^2}{\lambda^5} e^{-hc/k\lambda T} \tag{II.7}$$

For longer wavelengths, where λ gets larger, Rayleigh-Jeans distribution is used to approximate Planck's function. For Rayleigh-Jeans limit:

$$hf \ll kT \tag{II.8}$$

Then, Equation (II.3) is written by applying the first order Taylor approximation to the exponential term:

$$B_\lambda = 2kT\frac{1}{\lambda^2} \tag{II.9}$$

For passive microwave and millimeter-wave remote sensing, the long-wave Rayleigh-Jeans approximation is applied where the emission received is directly proportional to temperature as given in Equation (II.9) [29], [30].

The total brightness for a band-limited emission (Δf) is described using the Equation (II.9) as:

$$B_{bb} = B_f \Delta f = \frac{2kT}{\lambda^2}\Delta f \tag{II.10}$$

The gray body expression for the brightness given in the equation above is used to obtain a generalized expression since the objects exist in nature has emissivity lower than "1":

$$B(\theta,\phi) = \frac{2kT_B(\theta,\phi)}{\lambda^2}\Delta f \tag{II.11}$$

where $T_B(\theta,\phi)$ is used to express brightness temperature in the direction of given elevation (θ) and azimuth angles (ϕ). Thus, the emissivity relates the brightness temperature to a blackbody temperature and the brightness for a gray body to those for a blackbody as [27]:

$$\varepsilon = \frac{B(\theta,\phi)}{B_{bb}} = \frac{T_B}{T} \tag{II.12}$$

The equation above is useful to express the physical temperature of an object in terms of the brightness temperature. This linear relationship simplifies the

calculations for the power received by a radiometer antenna for atmospheric remote sensing that will be explained in detail in the following sections.

2.3. Blackbody Power Received by an Antenna

The differential radiated power over a differential solid angle ($d\Omega$) for a blackbody source detected by a lossless antenna is expressed as:

$$dP_{bb} = A_r B(\theta,\phi) F_n(\theta,\phi) d\Omega \tag{II.13}$$

where A_r is the effective aperture of the antenna and $F_n(\theta,\phi)$ is the antenna normalized radiation pattern in the direction of given elevation (θ) and azimuth angles (ϕ). The Rayleigh-Jeans distribution for Planck's blackbody radiation discussed in the previous section is used in Equation (II.13) to calculate the total received power over all elevation and azimuth angles for a lossless antenna [31]:

$$P_{bb} = kT\Delta f \frac{A_r}{\lambda^2} \iint_{4\pi} F_n(\theta,\phi) d\Omega \tag{II.14}$$

The integration of the antenna normalized radiation pattern per solid angle is defined for all the azimuth and elevation angles as the antenna pattern solid angle:

$$\Omega_p = \iint_{4\pi} F_n(\theta,\phi) d\Omega = \frac{\lambda^2}{A_r} \tag{II.15}$$

The simplified power-temperature linear relationship is obtained using the definition of pattern solid angle in Equation (II.14) as:

$$P_{bb} = kT\Delta f \tag{II.16}$$

The expression above directly relates the brightness temperature to the radiated power received that provides a simplified expression for the power received by a radiometer for atmospheric remote sensing explained in the next section.

2.4. Radiative Transfer Theory

Lambert's law of extinction defines the change in radiated intensity passing through a differential length (ds) illustrated in Figure 6 as [32]:

$$dI_v = -\sigma_{ext} I_v ds \tag{II.17}$$

where σ_{ext} is the extinction coefficient and I_v is the intensity. This emitted radiation can be absorbed or scattered by particles in the atmosphere. The extinction occurs as a result of absorption and scattering as:

$$\sigma_{ext} = \sigma_{sca} + \sigma_{abs} \tag{II.18}$$

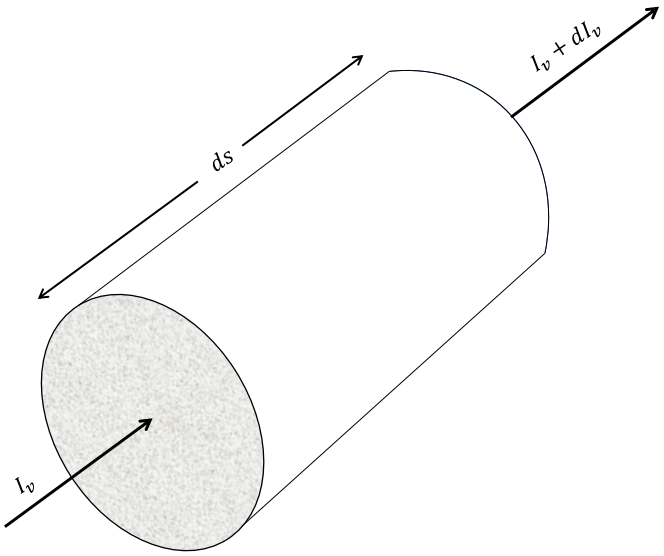

Figure 6: Extinction of radiation passing through a differential length.

The optical path over an infinitesimal length of ds is defined as:

$$d\tau = \sigma_{ext} ds \tag{II.19}$$

The optical depth is the optical depth for a vertical path. The optical thickness of the medium that radiation is passing through is calculated as:

$$\tau_v = \int_{s\prime}^{s"} \sigma_{ext,v}(s) ds \tag{II.20}$$

Then, the intensity at the point s" of the path in terms of point s′ of the path is expressed using the definition of the optical thickness according to Beer's law:

$$I_v(s") = I_v(s')e^{-\tau_v} \tag{II.21}$$

The equation above defines radiative transfer along a path ds for the contribution of extinction. The net change also depends on the emission due to sources as:

$$dI_v = dI_v(emission) + dI_v(extinction) \tag{II.22}$$

Then, the change of specific intensity along the path ds can be written as:

$$\frac{dI_v}{ds} = -\sigma_{ext,v}(I_v - J_v) \tag{II.23}$$

where J_v is the source function of the emission. For a scatter-free medium, the extinction coefficient defined in Equation (II.18) is defined with only absorption coefficient. Then, re-writing Equation (II.23) using the absorption coefficient:

$$-\frac{dI_v}{\sigma_{abs,v} ds} = I_v - B_v \tag{II.24}$$

where B_v is used to represent the thermodynamic equilibrium sources in the lower atmosphere where emission equals to absorption. Then, using Equation (II.19) in Equation (II.24):

$$-\frac{dI_v(s)}{d\tau(s',s)} = I_v(s) - B_v(T(s)) \tag{II.25}$$

where $T(s)$ is the temperature of layer s. Multiplying both sides with the exponential of the optical thickness as the following:

$$\frac{dI_v(s)e^{-\tau(s',s)}}{d\tau(s',s)} = -I_v(s)e^{-\tau(s',s)} + B_v(T(s))e^{-\tau(s',s)} \tag{II.26}$$

Then, organizing the terms:

$$\frac{dI_v(s)e^{-\tau(s',s)}}{d\tau(s',s)} + I_v(s)e^{-\tau(s',s)} = B_v(T(s))e^{-\tau(s',s)} \tag{II.27}$$

Modifying the left side of the equation above as a differentiable function with respect to optical thickness:

$$\frac{d(I_v(s)e^{-\tau(s',s)})}{d\tau(s',s)} = -B_v(T(s))e^{-\tau(s',s)} \tag{II.28}$$

Then, the above equation is written as:

$$-d(I_v(s)e^{-\tau(s',s)}) = B_v(T(s))e^{-\tau(s',s)}d\tau(s',s) \tag{II.29}$$

Integrating both sides yields:

$$I_v(s') = I_v(0)e^{-\tau(s',s)} - \int_0^{s'} B_v(T(s))e^{-\tau(s',s)}d\tau(s',s) \tag{II.30}$$

Using the definition of optical thickness given in Equation (II.20) in the above equation results in:

$$I_v(s') = I_v(0)e^{-\int_0^{s'}\sigma_{ext,v}(s")ds"} + \int_0^{s'} B_v(T(s))e^{-\int_s^{s'}\sigma_{ext,v}(s")ds"}\sigma_{ext,v}(s)ds \quad \text{(II.31)}$$

The radiative transfer theory is defined in Equation (II.31) shows the spectral intensity received at s'. The first term at the right of the equation above represents the background radiation transmitted through the whole atmosphere whereas the second term on the right shows the thermal emission transmitted to the atmosphere from layer s.

The Rayleigh-Jeans approximation given in Equation (II.11) is used for the radiative transfer theory in terms of brightness temperatures that provides easiness to radiometry for the calculations [33]:

$$T_B(s') = T_B(0)e^{-\int_0^{s'}\sigma_{ext,v}(s")ds"} + \int_0^{s'} T(s)e^{-\int_s^{s'}\sigma_{ext,v}(s")ds"}\sigma_{ext,v}(s)ds \quad \text{(II.32)}$$

2.5. Radiometric Remote Sensing of the Atmosphere

Passive remote sensing of the atmosphere using a downward looking radiometer antenna is illustrated in Figure 7. In this representation, T_{DN} is used to represent the downward radiation reaching to the surface of the Earth and scattered back to the atmosphere as T_{SCAT}. Then, T_{UP} is the upwelling radiation emitted in the atmosphere. The surface with emissivity ε and surface temperature T_s emits radiation to the atmosphere defined by T_{SURF}.

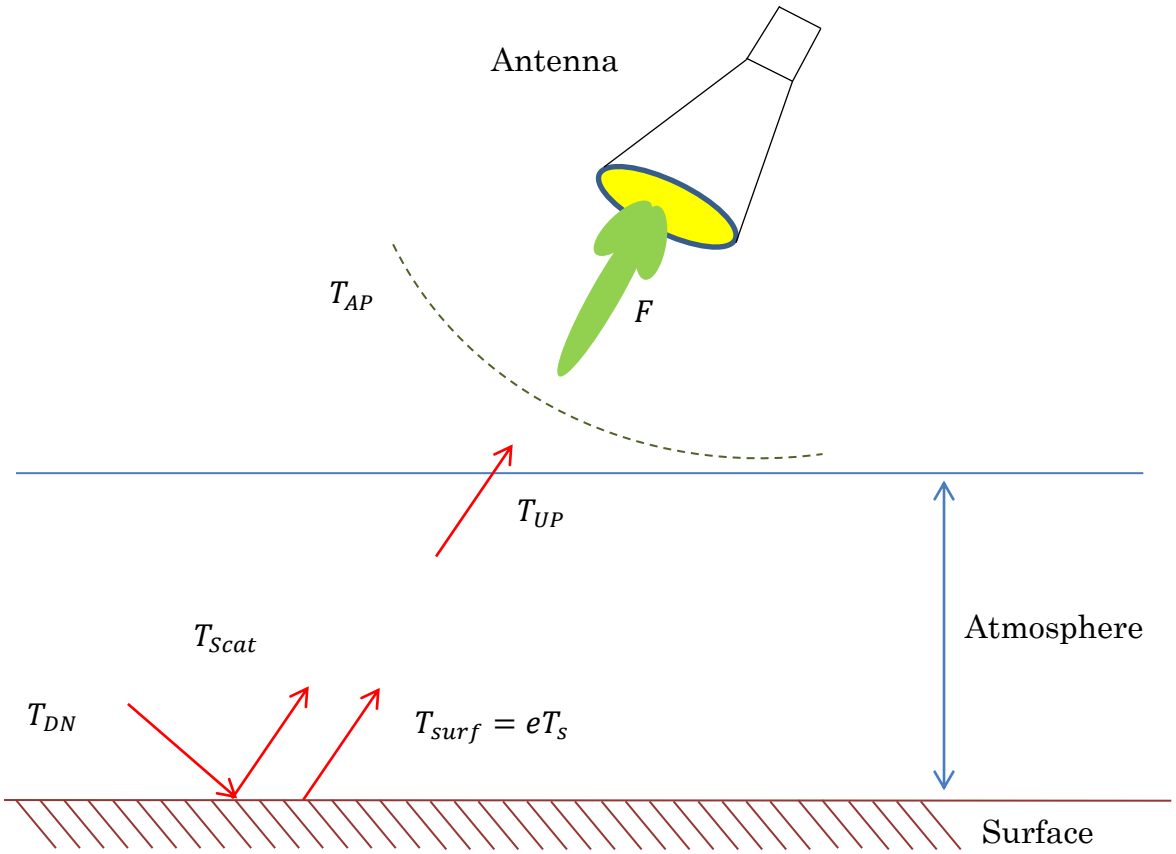

Figure 7: Passive remote sensing of the atmosphere with a downward looking radiometer antenna.

The brightness temperature due to the radiation collected at the aperture of the antenna is called as the apparent temperature defined by T_{AP}. Using the radiative transfer theory developed in the previous section with the downwelling, upwelling and surface radiation components provided, the apparent temperature can be written as [27]:

$$T_{AP} = T_{atm\_up}(1 - \Upsilon_{ui}) + \Upsilon_{ui} e T_s + (T_{atm\_down}(1 - \Upsilon_{di}) + T_{cb}\Upsilon_{di}))(1 - e)\Upsilon_{ui} \qquad \text{(II.33)}$$

where T_{cb} is the cosmic background radiation temperature, Υ_{ui} is the upwelling transmissivity and Υ_{di} is the downwelling transmissivity at frequency i. The upwelling transmissivity is expressed in terms of the zenith optical depth using the definition given in Equation (II.20) as the following:

$$\Upsilon_{ui} = e^{-\frac{\tau_i}{cos\theta}} \tag{II.34}$$

where θ is the incidence angle.

The apparent temperature is measured as antenna temperature by a radiometric antenna having a radiation pattern F as depicted in Figure 7. The antenna temperature T_A is defined in terms of the apparent temperature for a lossless antenna as:

$$T_A = \frac{\iint_{4\pi} T_{AP}(\theta,\varphi) F_n(\theta,\varphi) d\Omega}{\iint_{4\pi} F_n(\theta,\varphi) d\Omega} \tag{II.35}$$

where $F_n(\theta,\varphi)$ is the normalized antenna radiation pattern in θ elevation and φ azimuth directions [27].

2.6. Radiometer Architectures Overview

Several radiometer architecture design strategies have been developed in microwave, millimeter-wave and sub-millimeter-wave radiometry. The need for various different design strategies depend on operating frequencies, expected effective noise temperature, operating characteristic such as sampling time or scanning strategy and mounting platform including ground based, airborne or space-borne platforms. The different design strategies tries to optimize the

performance of a radiometer for an improved sensitivity, stability and accuracy based on the size, weight and power requirements of the system [34], [35].

Each radiometer type presented in the next subsections can be either direct detection or super-heterodyne receiver architecture. In direct detection scheme, there is no down conversion of radio frequency (RF) into an intermediate frequency (IF). Super-heterodyne receivers employ a mixer block where a local oscillator is used to down-convert RF signal into an IF signal. The IF signal can be amplified further before detection.

2.6.1 Total Power Radiometer

A block diagram of a total power radiometer is shown in Figure 8. The radiated power is received by the antenna and transmitted through a waveguide. Then, low-noise amplifiers (LNAs) amplify the signal. Band-pass filters (BPFs) in the front-end receivers select the band for the operation frequency. The power of the measured signal is obtained using a square-law voltage diode. The voltage at the output of the voltage detector is linearly proportional to the detected power by the detector. Further amplification is applied at post-detection video amplifiers before the signal is integrated for digital acquisition system [34].

Total power radiometers do not include any internal calibrator. The system temperature of the total power radiometer defined by T_{sys} is the sum of the antenna temperature (T_A) and the receiver noise temperature (T_{rec}) as:

$$T_{sys} = T_A + T_{rec} \tag{II.36}$$

The voltage measured at the output of the square-law detected is expressed as:

$$V_{out,TPR} = k\Delta BG\beta T_{sys} \tag{II.37}$$

where G is the total pre-detection gain of the receiver, ΔB is the receiver bandwidth and β is the detector sensitivity given in V/W.

The radiometric resolution (NEΔT) of an ideal total power radiometer ignoring the gain fluctuation is given as:

$$NE\Delta T = \frac{T_{sys}}{\sqrt{\Delta B \tau_{int}}} \tag{II.38}$$

where τ_{int} is the integration time of the receiver. However, the output of a total power radiometer fluctuates due to 1/f noise of the receiver especially due to detector diode and LNAs [36]. Taking into consideration of the effect of gain fluctuations, the output voltage given in Equation (II.37) is modified into:

$$V_{out,TPR} = k\Delta B(G + \Delta G)\beta T_{sys} \tag{II.39}$$

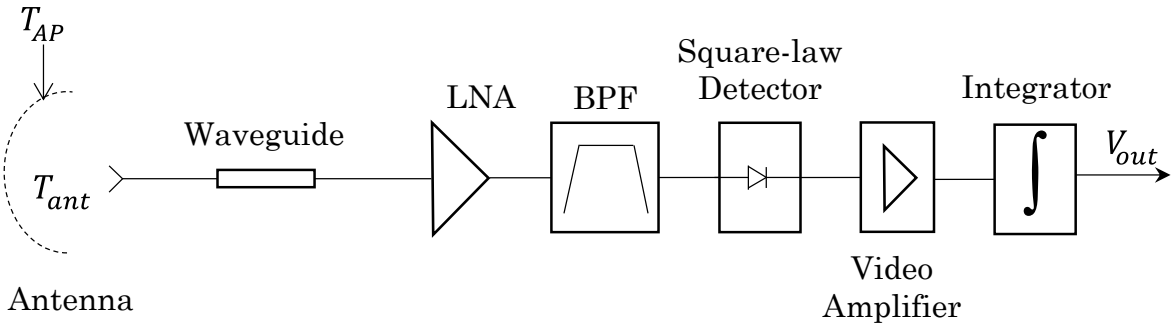

Figure 8: Block diagram of a total power radiometer.

where ΔG represents the amount of gain variation in the receiver. The amount of uncertainty in terms of temperature due to gain variation is given by:

$$\Delta T_G = T_{sys}\left(\frac{\Delta G}{G}\right) \tag{II.40}$$

Thus the NEΔT of a total power radiometer including the gain fluctuations is the combination of the one for the ideal radiometer and the uncertainty due to gain fluctuations:

$$NE\Delta T = \sqrt{(NE\Delta T_{ideal})^2 + (\Delta T_G)^2} \tag{II.41}$$

Thus, the above equation can be re-written using the definition of NEΔT for an ideal radiometer given in Equation (II.41) as:

$$NE\Delta T = T_{sys}\sqrt{\frac{1}{\Delta B \tau_{int}} + \left(\frac{\Delta G}{G}\right)^2} \tag{II.42}$$

The gain variations due to 1/f noise within a total power radiometer degrade the NEΔT performance of the radiometer. Internal calibration strategies are used to improve the stability, accuracy and radiometric resolution of a radiometer. The next sections describe the architecture of those radiometer types.

2.6.2 Dicke-Switching Radiometer

A block diagram of a Dicke-switching radiometer is shown in Figure 9. The major difference in the block diagram of a Dicke-switching radiometer than those for a total power radiometer is a matched reference load attached to the hardware with a switch connected between the waveguide and the LNA. This single-pole double-

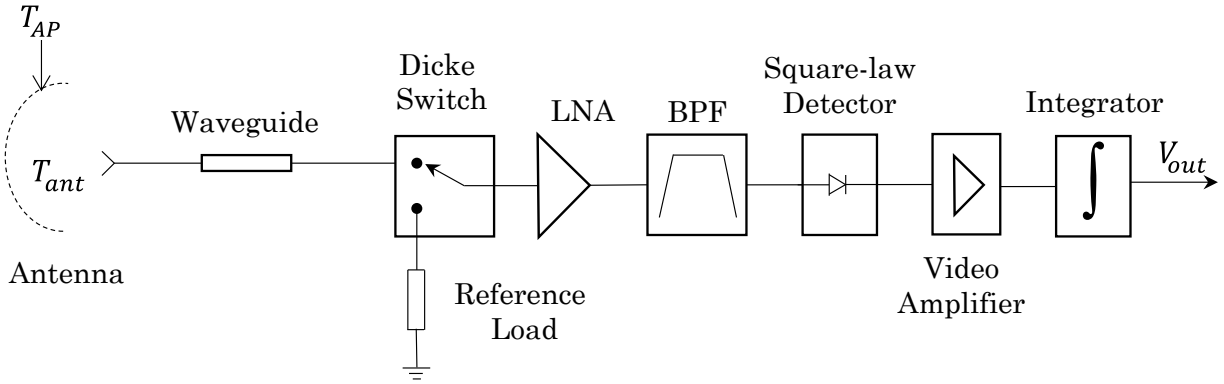

Figure 9: Block diagram of a Dicke-switching radiometer.

throw (SPDT) switch named as Dicke-switch used to improve the performance of the receiver for 1/f noise elimination. The Dicke switch is controlled from control and data handling (C&DH) system of the receiver synchronized with the radiometric acquisition [34], [35], [37].

The input of the first LNA block after the Dicke switch is changed between the antenna and the matched reference load. The frequency of the Dicke-switch should be higher than 1/f noise frequency to track the gain variations due to 1/f noise within the receiver. In this case, the gain variations are cancelled out by the fact that they are constant during a switching cycle.

When the Dicke-switch is at the antenna position, the receiver measures the antenna temperature defined by T_A. Otherwise, the receiver measures the equivalent noise temperature given by T_{ref} of the matched reference load. The operation of a Dicke-switching radiometer is similar to a total power radiometer after the Dicke-switch until the power detection. The BPF limits the power bandwidth of the amplified signal by LNAs. Then, square law detector detects the

band-limited, amplified power. After the square law detector, another switch is used to switch to a positive unity gain amplifier for the antenna temperature measurements, and to a negative unity gain amplifier for the matched reference load measurements. The switching is synchronized with the Dicke-switch and the radiometric acquisition.

During the positive unity gain amplification stage, the antenna temperature is measured at the output as:

$$V_1 = mT_{sys} = m(T_A + T_{rec}) \tag{II.43}$$

where m is used to represent receiver temperature to voltage gain constant. Similarly, the output voltage for the negative unity gain amplification cycle for the matched reference load measurements can be written as:

$$V_2 = m(T_{ref} + T_{rec}) \tag{II.44}$$

The output of a Dicke-switching radiometer is represented by using the output voltage definitions in Equations (II.43) and (II.44) as:

$$V_{out,Dicke} = m\left(T_A - T_{ref}\right) \tag{II.45}$$

As shown in the equation above, the receiver noise temperature is cancelled from the output voltage measurements for a Dicke-switching radiometer. The NEΔT of a Dicke-switching radiometer when the Dicke-switch is at the antenna is calculated as:

$$NE\Delta T_1 = \frac{T_A + T_{rec}}{\sqrt{\Delta B(\tau_{int}/2)}} \tag{II.46}$$

Similarly, the NEΔT for the matched reference load measurements is expressed as:

$$NE\Delta T_2 = \frac{T_{ref} + T_{rec}}{\sqrt{\Delta B(^{\tau_{int}}/_2)}} \tag{II.47}$$

The uncertainty given in Equations (II.46) and (II.47) are statistically independent. Thus, the expected NEΔT for an ideal Dicke-switch radiometer is given as:

$$NE\Delta T_{ideal} = \sqrt{(NE\Delta T_1)^2 + (NE\Delta T_2)^2} \tag{II.48}$$

Employing the definitions for $NE\Delta T_1$ and $NE\Delta T_2$ in the above equation:

$$NE\Delta T_{ideal} = \frac{\sqrt{2(T_A + T_{rec})^2 + \left(T_{ref} + T_{rec}\right)^2}}{\sqrt{\Delta B \tau_{int}}} \tag{II.49}$$

For Dicke-switching radiometers, the equivalent noise temperature of the matched reference load is usually close to the antenna temperature. In other words:

$$T_A \cong T_{ref} \tag{II.50}$$

Employing the assumption given in Equation (II.50) into Equation (II.49) yields:

$$NE\Delta T_{ideal} = 2\frac{T_A + T_{rec}}{\sqrt{\Delta B \tau_{int}}} = 2\frac{T_{sys}}{\sqrt{\Delta B \tau_{int}}} \tag{II.51}$$

Thus, the equation given above formulating radiometric resolution for an ideal Dicke-switching radiometer is factor 2 times the one for an ideal total power radiometer given in Equation (II.38). This, in turn, shows that the cost of adding a

Dicke switch to the radiometer architecture is the degradation of the radiometric resolution.

The generalized expression for the radiometric resolution of a Dicke-switching radiometer is obtained by including the uncertainty due to gain fluctuations as the following [34]:

$$NE\Delta T = \left[\frac{2(T_A + T_{rec})^2 + 2\left(T_{ref} + T_{rec}\right)^2}{\Delta B \tau_{int}} + \left(\frac{\Delta G}{G}\right)^2 \left(T_A - T_{ref}\right)^2\right]^{1/2} \quad \text{(II.52)}$$

The uncertainty due to gain fluctuations for a Dicke-switching radiometer is expressed with the last term on the equation above. The difference between the antenna temperature and the equivalent noise temperature of the matched reference load are close to each other minimizing the term due to gain fluctuations for a Dicke-switching radiometer.

2.6.3 Noise Injection Radiometer

The Dicke-switching radiometers discussed in the previous section are effective on eliminating 1/f noise from the radiometric measurement. However, if the antenna temperature is almost the same with the noise equivalent temperature of the matched reference load, the output voltage of a Dicke-switching radiometer given in Equation (II.45) becomes almost zero. The noise injection from a known noise source is employed to prevent such a case for maintaining the operational stability of the radiometer for all radiometric measurement range [34], [35].

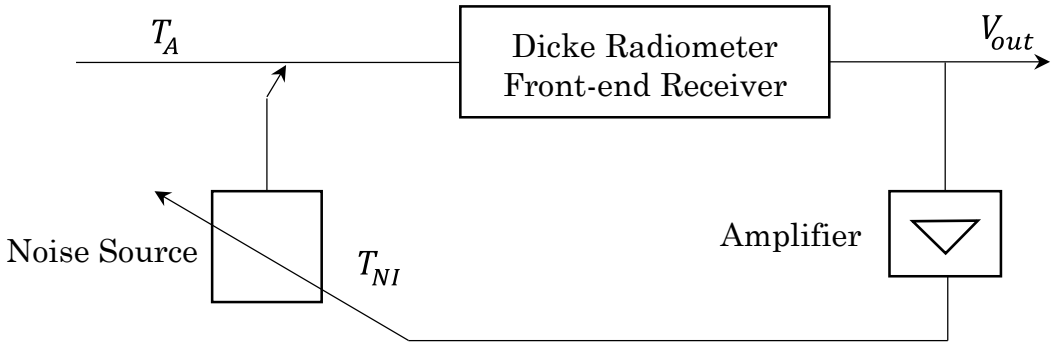

Figure 10: Operational block diagram of a noise injection radiometer.

An operational block diagram of a noise injection radiometer is given in Figure 10. A known controlled noise source is added to the antenna temperature measurements before the Dicke switch of a Dicke-switching radiometer. A closed loop control is used with an amplifier having a controlled loop gain to maintain zero output voltage by setting the noise temperature to the temperature difference between the reference load noise temperature and the antenna temperature.

For a noise injected radiometer, we define another variable (T_A') to represent the temperature at the input of the Dicke switch as:

$$T_A' \triangleq T_A + T_{NI} \tag{II.53}$$

where T_{NI} is the noise injection temperature. Thus the output voltage of a noise injection radiometer is given as:

$$V_{out,NIR} = m\left(T_A' - T_{ref}\right)G = 0 \tag{II.54}$$

Then, using the definitions given in Equations (II.53) and (II.54), the antenna temperature is found in terms of the noise injection temperature and reference load temperature as:

$$T_A = T_{ref} - T_{NI} \tag{II.55}$$

The antenna temperature is estimate in a noise injection radiometer by employing an accurate noise source as provided with the equation above. The radiometric resolution of a noise injection radiometer is similar to one for a Dicke-switching radiometer given in Equation (II.51):

$$NE\Delta T = 2\frac{T_A{}' + T_{rec}}{\sqrt{\Delta B\tau_{int}}} \tag{II.56}$$

The radiometric resolution given above can be further simplified into:

$$NE\Delta T = 2\frac{T_{ref} + T_{rec}}{\sqrt{\Delta B\tau_{int}}} \tag{II.57}$$

Since it has been implied in Equation (II.54):

$$T_A' = T_{ref} \tag{II.58}$$

2.7. System Noise Figure

The noise figure of a component is defined as the amount of degradation of the signal to noise ratio at the output when compared to its input. For any network, the noise figure is not smaller than one and expressed as [38]:

$$F = \frac{S_i/N_i}{S_o/N_o} \geq 1 \tag{II.59}$$

where S_i and N_i are the input signal and noise power respectively whereas S_o and N_o are the ones for output. For a noisy network with bandwidth B and gain G, the noise figure is written as:

$$F = \frac{S_i}{kT_oB}\frac{k(T_o + T_e)GB}{GS_i} = \frac{T_o + T_e}{T_o} = 1 + \frac{T_e}{T_o} \tag{II.60}$$

where T_o is room temperature at 290 K and T_e is the equivalent noise temperature of the network.

Solving the equation above for the equivalent noise temperature yields:

$$T_e = (F - 1)T_o \tag{II.61}$$

The calculation of the noise figure and noise temperature for a cascaded system follows a similar procedure outlined for a single network. A two-step cascaded network is illustrated in Figure 11. The noise power at the output of first stage is written as:

$$N_1 = G_1kB(T_o + T_{e1}) \tag{II.62}$$

and the noise power at the output of the second stage is found as:

$$N_o = G_2(N_1 + kBT_{e2}) \tag{II.63}$$

Using the definition given in Equation (II.62) in the above equation:

$$N_o = G_2(G_1kB(T_o + T_{e1}) + kBT_{e2}) \tag{II.64}$$

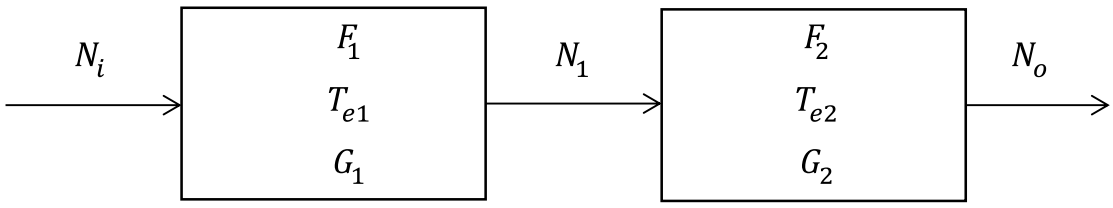

Figure 11: The noise figure, noise temperature and gain of two networks are provided for the calculation of cascaded noise figure and temperature analysis.

The noise power definition given in the above equation can be written by organizing the terms:

$$N_o = G_1 G_2 kB(T_o + T_{e1} + \frac{T_{e2}}{G_1}) \tag{II.65}$$

Comparing the equation above with the Equation (II.62), one can rewrite it as:

$$N_o = G_{cas} kB(T_o + T_{cas}) \tag{II.66}$$

where the cascaded noise temperature defined as:

$$T_{cas} = T_{e1} + \frac{T_{e2}}{G_1} \tag{II.67}$$

and the cascaded gain is given as:

$$G_{cas} = G_1 G_2 \tag{II.68}$$

The cascaded noise figure is found applying the definition of the equivalent noise temperature in terms of the noise figure given in Equation (II.61) into the cascaded noise temperature definition given in Equation (II.67) as:

$$F_{cas} = F_1 + \frac{F_2 - 1}{G_1} \tag{II.69}$$

For a lossy line in thermal equilibrium at temperature T, the equivalent noise temperature is found as [38]:

$$T_e = (L - 1)T \tag{II.70}$$

where L is the loss factor of the line. The noise figure given in Equation (II.60) is rewritten for a lossy line as:

$$F = 1 + (L - 1)\frac{T}{T_o} \tag{II.71}$$

The formulations for noise figure and noise temperature provided in this section are useful to estimate the noise temperature of the receiver theoretically at the design step by measuring the noise figure of each component individually at laboratory conditions.

2.8. Conclusions

Planck's Law can be used to explain the thermal radiation spectrum of any substance as a result of molecular oscillations over a frequency range above absolute temperature. The power received by an antenna due to thermal radiation is explained. The Radiative Transfer Theory is used to analyze the apparent temperature received by an antenna in atmospheric remote sensing through passive instruments. The sensitivity of the observing instrument to the atmospheric parameters including water vapor and oxygen affects the measured antenna temperature by the Radiative Transfer Theory allowing the retrievals of these parameters from radiometric measurements. In addition, the radiometer design architectures and operating principles are discussed and analyzed. Noise figure analysis is used to determine the performance of the cascaded front-end receivers of a radiometer instrument.

Chapter III Tropospheric Water and Cloud Ice (TWICE) Millimeter- and Sub-Millimeter-wave Radiometer for a 6U Class Satellite

This chapter presents the Tropospheric Water and Cloud Ice (TWICE) millimeter- and sub-millimeter-wave radiometer instrument. The main specifications of the radiometer instrument are described. Then, orbital calculations and design considerations are presented. The front-end receivers are explained. The command and data handling (C&DH) system, power regulation system, radiation reliability and receiver characterization are discussed in the following chapters.

3.1. The Tropospheric Water and Cloud Ice (TWICE) Millimeter- and Sub-Millimeter-wave Radiometer Overview

The TWICE instrument is under development to observe ice water content, ice particle size distribution as well as upper tropospheric water vapor and temperature profiles using wide-band millimeter- and sub-millimeter wave radiometer measurements at 15 frequencies from 118 GHz to 670 GHz in three frequency bands, as shown in Figure 12 [26], [39].

TWICE is managed by the NASA Earth Science Technology Office (ESTO) under the 2013 Instrument Incubator Program (IIP). TWICE is a collaborative effort led by Colorado State University (CSU) in partnership with the NASA Jet Propulsion Laboratory (JPL) and Northrop Grumman Corporation (NGC). The TWICE radiometers are based on 25-nm and 35-nm InP High Electron Mobility Transistor (HEMT) designs to realize millimeter and sub-millimeter-wave low-noise amplifiers (LNAs) [40]. Low-noise and low-power receivers have been designed based on InP

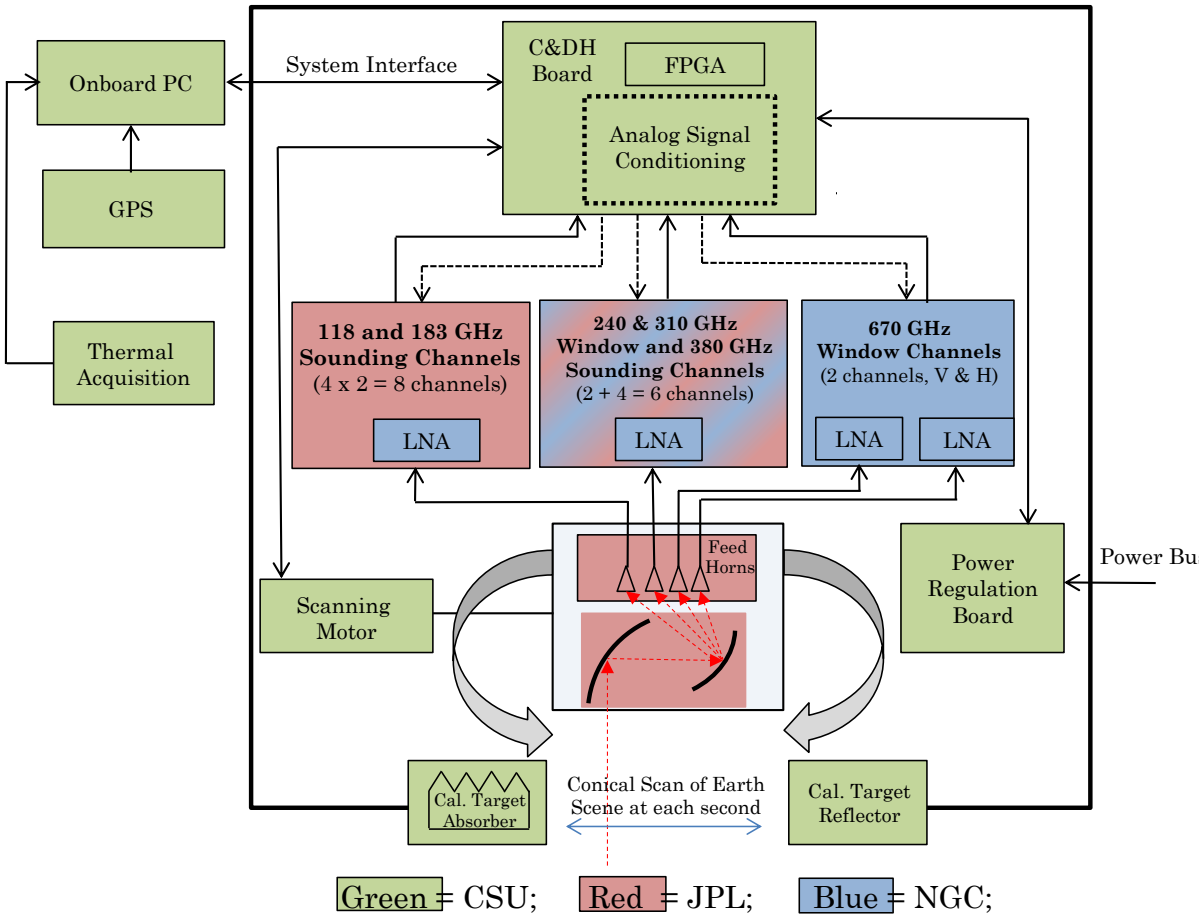

Figure 12: TWICE functional block diagram, showing areas of responsibility among CSU (green), JPL (red) and NGC (blue).

HEMT LNAs packaged in integrated receiver front-ends in small form factors at millimeter- and sub-millimeter-wave frequencies [41]. These include direct-detection receivers at 240 GHz, 310 GHz and 670 GHz, with dual-polarization capability at the highest of these three frequencies. TWICE also measures four frequencies near each of three absorption lines for atmospheric profiling. These receivers measure temperature profiling channels near the oxygen line at 118.75 GHz, as well as water vapor profiling channels near absorption lines at 183.31 GHz and 380.20 GHz [14].

TWICE is under development for space-borne deployment in a 6U-Class satellite (6U CubeSat) platform with exterior dimensions of approximately 36 x 23 x 10 cm and mass of up to 12 kg [16]. A CAD model of the instrument in a 6U CubeSat is shown in Fig. 2.2. The TWICE instrument is designed for deployment from the International Space Station (ISS) via NanoRacks into a low-Earth orbit (LEO) with ~400 km altitude at 51.6° inclination for a 1-2 year mission lifetime [26].

As illustrated in Figure 13, the radiation from the scene is reflected from the primary reflector onto the secondary reflector and then focused onto three feed horns covering three frequency bands using a single quasi-optical system. The TWICE quasi-optical assembly scans conically, observing the Earth scene over a

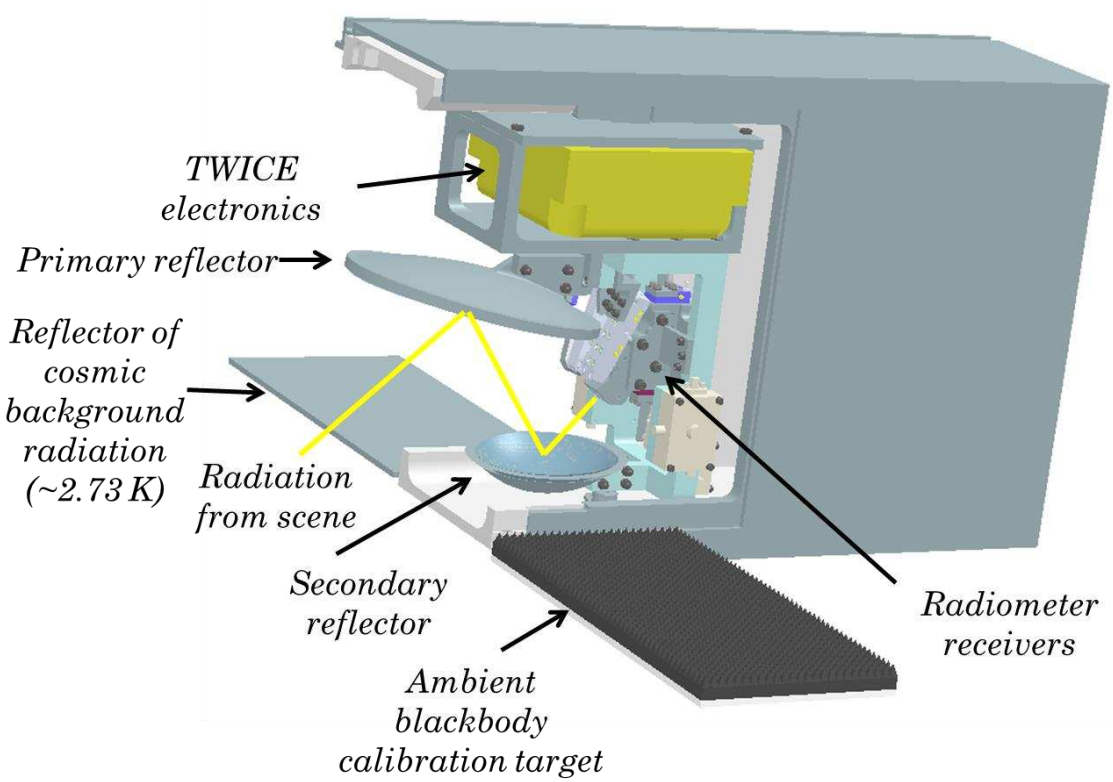

Figure 13: TWICE 6U-class satellite CAD model.

130˚ arc every 1 second with 749 km swath width at 400 km altitude with 45˚ look-angle at the satellite. Since the entire conical scan extends over 200º, TWICE radiometers can also measure an ambient calibration target and the reflected cosmic microwave background (at 2.73 K). In this way, TWICE performs two-point end-to-end calibration during every one-second conical scan cycle.

3.2. TWICE Orbital Parameters

The calculation of each TWICE orbital parameter is explained in the following subsections.

3.2.1 TWICE Orbital Speed and Period

The TWICE 6U CubeSat instrument is under design for a possible deployment from the ISS for orbital operation at around 400 km altitude. The TWICE satellite speed at TWICE orbital altitude is calculated as [42]:

$$v_{sat} = \sqrt{\frac{G * M_{Earth}}{R_{sat}}} = 7.68\, x\, 10^{3}\ [\mathrm{m/s}] \tag{III.1}$$

where v_{sat} is the speed of the TWICE instrument in [m/s], G is the gravitational constant in [N m^2 kg^{-2}], M_{Earth} is the mass of the Earth in kg and R_{sat} is the satellite orbital radius in m. These variables are given as:

- Gravitational Constant:

$$G = 6.67\, x\, 10^{-11}\ [\mathrm{N\ m^2\ kg^{-2}}] \tag{III.2}$$

- Earth's mass:

$$M_{Earth} = 5.98\, x\, 10^{24}\ [\mathrm{kg}] \tag{III.3}$$

- Satellite orbital radius:

$$R_{sat} = R_{Earth} + h_{TWICE} = 6.37\ x\ 10^6 + 0.4\ x\ 10^6 = 6.77\ x\ 10^6\ [\text{m}] \quad \text{(III.4)}$$

where R_{Earth} is the radius of the Earth assuming a spherical structure and h_{TWICE} is the expected TWICE orbital altitude.

The orbital period of the TWICE instrument is defined as the time required to complete one complete revolution around the Earth. The TWICE orbital period is calculated using the Newton's law of gravitation and the centripetal force equation as [42]:

$$T_{sat} = \sqrt{\frac{4 * \pi^2 * {R_{sat}}^3}{G * M_{Earth}}} = 92.3\ [\text{min}] \quad \text{(III.5)}$$

The orbital period is used to calculate the angular radial speed of the TWICE instrument which is the degree that TWICE instrument takes in the orbit per second which is found by:

$$V_{sat,ang} = \frac{360°}{T_{sat}} = 0.065°\ [\text{s}^{-1}] \quad \text{(III.6)}$$

The ground speed of the TWICE instrument is defined as the speed of the TWICE instrument with respect to a point on the Earth surface. The ground speed is calculated using the angular speed found above as:

$$V_{ground} = 2 * \pi * R_{Earth} * \frac{V_{sat,ang}}{360°} = 7.22\ [\text{km}] \quad \text{(III.7)}$$

The TWICE ground speed found in the equation above is an important parameter for footprint coverage calculations as well as the instrument scanning speed calculations.

3.2.2 TWICE Incidence Angle and Swath Width

The TWICE instrument performs conical scanning of Earth view at 45° constant looking angle. The illustration of the TWICE orbital operation is illustrated in Figure 14 assuming a spherical Earth surface and 6371 km Earth radius. The unknown parameter d needs to be found in order to calculate the incidence angle. One can apply the Pythagorean Theorem to the bottom triangle in Figure 14 as the following:

$$R_{Earth}{}^2 = (R_{Earth} - d)^2 + (H + d)^2 \tag{III.8}$$

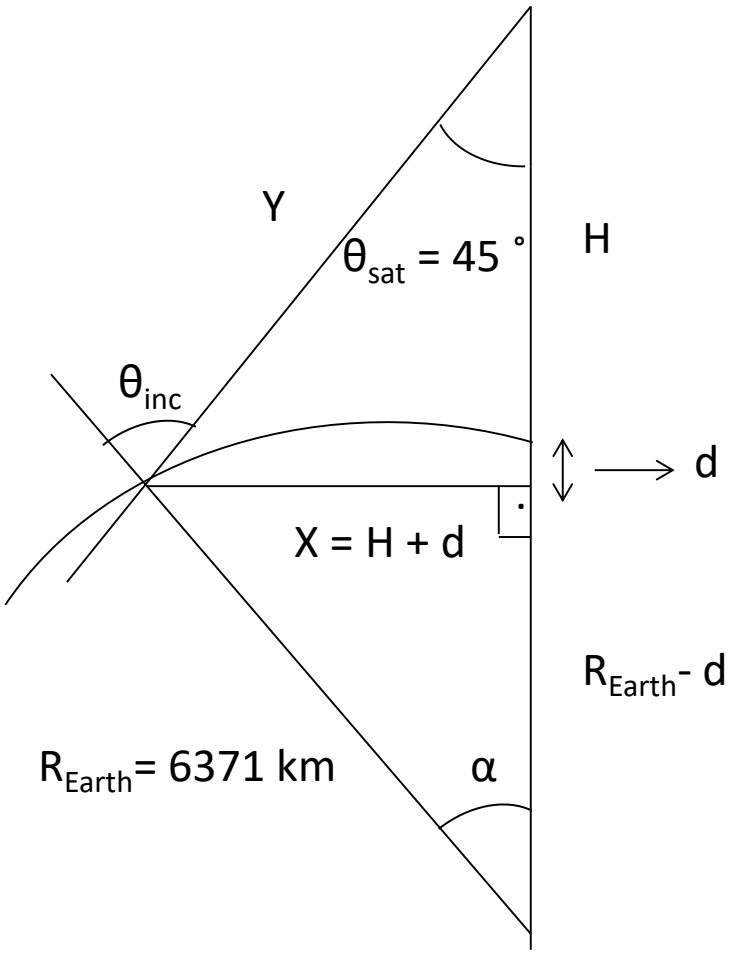

Figure 14: Illustration of TWICE orbital view.

Organizing the terms in the equation above yields:

$$R_{Earth}{}^2 = R_{Earth}{}^2 - 2 * R_{Earth} * d + d^2 + H^2 + 2 * H * d + d^2 \quad \text{(III.9)}$$

The equation above is further simplified into:

$$2 * d^2 + 2 * d * (H - R_{Earth}) + H^2 = 0 \quad \text{(III.10)}$$

The positive root of the equation above gives the distance d after plugging other parameters and solving for d.

As shown in Figure 14, the projected distance from the satellite to the observation point on the ground is simply the sum of satellite altitude and distance d for 45° satellite looking angle:

$$X = H + d \quad \text{(III.11)}$$

After calculating the parameter d and X, the distance from the satellite to the observation point on the ground can be calculated for a 45° satellite looking angle using the equation:

$$Y = \frac{H + d}{cos\theta_{sat}} = \frac{X}{cos\theta_{sat}} \quad \text{(III.12)}$$

The angle α at the bottom triangle needs to be calculated to find the incidence angle. Applying the trigonometric identity for the bottom triangle results in:

$$\alpha = \cos(\frac{R_{Earth} - d}{R_{Earth}})^{-1} \quad \text{(III.13)}$$

The sum of all the angles at the half circle should add up to 180°:

$$180° = \theta_{inc} + (90° - \theta_{sat}) + (90° - \alpha) \quad \text{(III.14)}$$

For a 45° satellite looking angle:

$$\theta_{inc} = 180° - 45° - (90° - \alpha) = 45° + \alpha \quad \text{(III.15)}$$

The incidence angle calculated in the equation above is used to project footprints of the TWICE instrument.

The swath width of a radiometer instrument is defined as the maximum width on the ground surface that the instrument can scan. The contour of the radiometric observations is defined as the total arc length over the swath width of the instrument. This has been illustrated in Figure 15 when TWICE views the Earth while scanning over a 120° arc with a radius X which is found by Equation (III.11). The contour C is found by [34]:

$$C = 2 * \pi * X * \frac{\theta_{scan}}{360°} \quad \text{(III.16)}$$

where θ_{scan} is 120° for the TWICE instrument. The swath width of the instrument is calculated as:

$$S = 2 * X * \sin(\frac{\theta_{scan}}{2}) \quad \text{(III.17)}$$

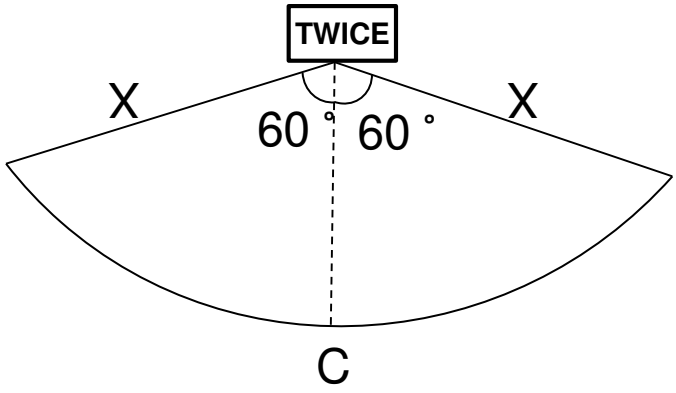

Figure 15: TWICE views the Earth while scanning over a 120° arc with a radius X (top view).

The incidence angle, the swath width and other orbital parameters are calculated for different orbital altitudes. The results are summarized in Table 1.

Table 1: The TWICE orbital parameters are calculated for different expected altitudes

H [km]	D [km]	X [km]	Y [km]	θinc [deg]	S [km]
350	10.19	360.19	509.39	48.241	623.87
400	13.43	413.43	584.68	48.721	716.08
450	17.15	467.15	660.65	49.205	809.13

3.3. TWICE Front-end Receivers

The TWICE instrument has 4 sets of frequency channels as outlined in the block diagram shown in Figure 12.

3.3.1 TWICE Low Frequency Sounding Channels

The TWICE instrument has 4 radiometric channels near 118 GHz oxygen absorption line and 4 radiometric channels near 183 GHz water vapor absorption line. These sounding channels are used for temperature and water vapor vertical profiling of the atmosphere [39].

118 and 183 GHz TWICE receivers are super-heterodyne radiometers down-converting the detected signal into IF before the detection. The dielectric resonator oscillators (DROs) mounted externally on the scanning part of the instrument on the sides provide local oscillator (LO) signals for the multipliers for the receiver modules. 118 and 183 GHz horn is the largest horn of the instrument mounted to

prevent blockage of other horns for the other receiver blocks. The LNAs at 118 and 183 GHz receivers are designed by the NGC. The design and manufacturing of other parts are carried out by the JPL.

3.3.2 TWICE 240/310 GHz Radiometer and 380 GHz Sounding Channels

The high frequency sounding channels at 4 different frequencies near 380 GHz water vapor absorption line are used for water vapor profiling. The sounding channels at near 380 GHz frequency are super-heterodyne receivers as the other sounding channels at near 118 and 183 GHz frequency.

The radiometric channels centered at 240 and 310 GHz frequencies are used with 670 GHz channel for ice particle size detection. As shown in Figure 16, the interaction of ice particles with the radiation strongly depends on the ratio of ice particle size to the observation wavelength. The observation frequencies of TWICE radiometers at 240, 310 and 670 GHz are expected to provide ice particle information with various particle sizes at lower stratosphere [9], [14].

The TWICE radiometers at 240 and 310 GHz frequencies are direct detection total power radiometers. The received radiometric signal is amplified with LNAs and band limited by the BPFs before detected by the voltage detector diode.

3.3.3 TWICE 670 GHz Receivers

The TWICE instrument has dual polarized 670 GHz radiometers for detection of ice particles larger than 100 μm but smaller than 0.5 mm as shown in Figure 16. The TWICE 670 GHz receivers are direct detection total power radiometers. The

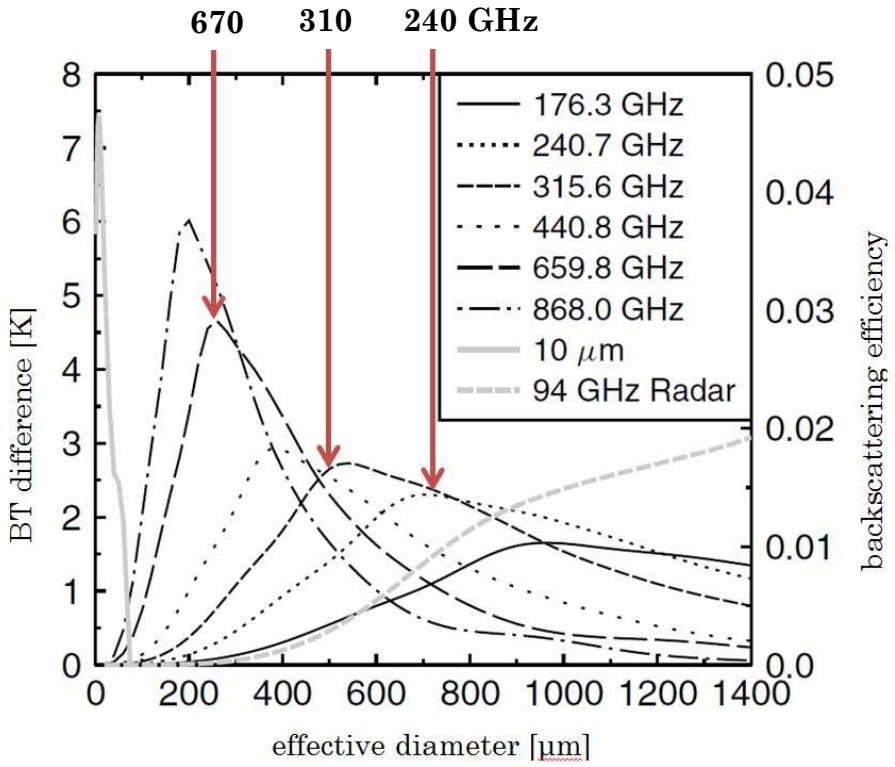

Figure 16: Ice particle scattering for varying particle size [9].

receiver has 3 LNA blocks and 2 BPF blocks before the power is detected by the detector diode as shown in Figure 17. InP HEMT technology has been used by NGC to manufacture low-power, low-noise LNAs for 670 GHz receiver [40]. The expected receiver noise temperature of 670 GHz receiver is calculated from the 10.6 dB noise figure measurements using the Equation (II.61) as the following:

$$T_{rec} = 290 * (\mathrm{F} - 1) = 290 * (11.48 - 1) \cong 3000\ [\mathrm{K}] \qquad \text{(III.18)}$$

The improvements have been made on the 670 GHz receiver to minimize the effect of 1/f noise from the radiometric measurements. The new technique which is

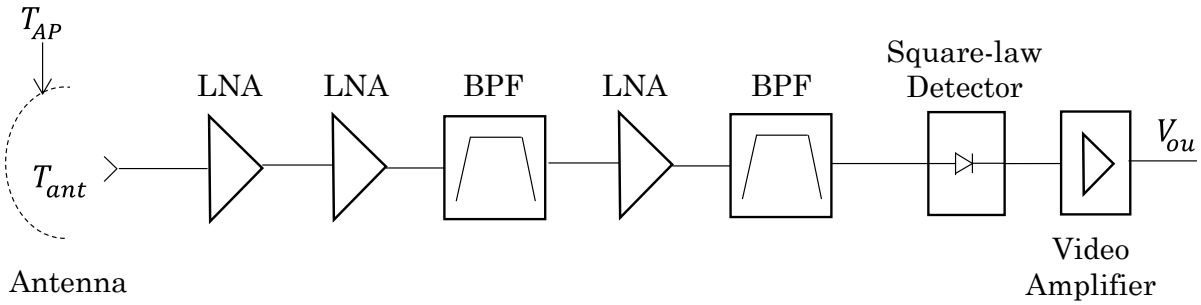

Figure 17: TWICE 670 GHz direct-detection total-power 670 GHz radiometer block diagram.

different than the conventional total power radiometer operation is explained in detail with the measured results in Chapter VI Radiometer Characterization and Testing.

3.3.4 Summary

TWICE front-end receiver channels and their main specifications are summarized in Table 2. As described in this section, TWICE operates at 15 different frequency channels from 118 GHz to 670 GHz frequencies.

3.4. TWICE Scanning Strategy

TWICE radiometer performs conical scanning of the Earth view at 30 revolution-per-minute (RPM) moving in a back-and-forth motion through 200 scanning degree as illustrated in Figure 18. During one scan cycle, the instrument scans ambient calibration target and cold sky reflector for the utilization of end-to-end calibration of the instrument. The Earth view is measured during 120° motor scan angle. The

Table 2: The TWICE front-end receivers channel specifications

Channel [GHz]	Type	Number of Channels	BW [GHz]
118	Sounder	4	1
183	Sounder	4	1
240	Radiometer	1	10
310	Radiometer	1	10
380	Sounder	4	1
670	Radiometer	2 (H and V)	20

instrument has 45° constant looking angle when it performs conical scanning for radiometric measurements.

3.5. TWICE Housekeeping Systems

The on-board computer (OBC) of the TWICE instrument stores all the radiometric data sent from the Field Programmable Gate Array (FPGA) on the C&DH board for transmitting them to the ground station. The OBC receives the configuration files from the ground station and sends them to the C&DH board.

The TWICE instrument uses an Ellipse-D Global Positioning System (GPS) module from SBG Systems for ground and airborne demonstrations of the instrument. The GPS modules is expected to provide high accuracy needed for raw, pitch and yaw in addition to provide precise longitude, longitude and altitude information needed for geolocation of the radiometric footprints from an airborne demonstration campaign.

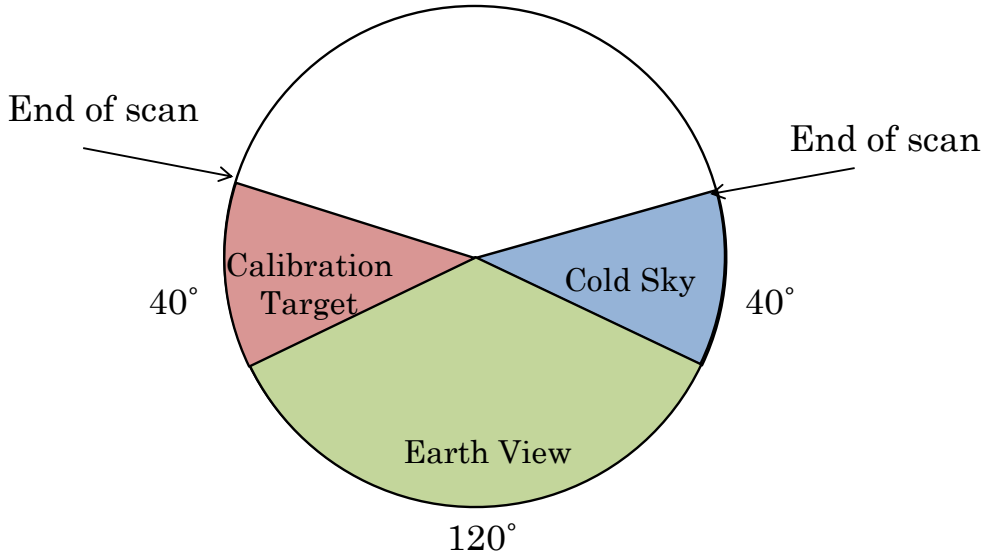

Figure 18: TWICE motor scan diagram for one complete scan cycle.

For the space flight, a space qualified GPS module will be used which is suitable for high accuracy space applications.

The thermal monitoring of the TWICE receivers and other subsystems are accomplished through negative temperature coefficient (NTC) thermistors mounted on the devices. A thermal acquisition board placed on the stationary part of the instrument performs the digital acquisition of the analog thermistor data.

3.6. Conclusions

The TWICE instrument is being designed to monitor upper-tropospheric lower stratospheric cloud ice and water vapor as a collaborative effort between CSU, NASA/JPL and NGC. The TWICE orbital parameters are calculated to determine the functional and environmental design parameters of the instrument. The TWICE

instrument has three sets of frequency channels. The sounders near 118 GHz are used for temperature profiling and the ones near 183 GHz and 380 GHz are used for water vapor profiling. The radiometric channels at 240 GHz, 310 GHz and 670 GHz frequencies are used for water vapor and cloud-ice monitoring. The TWICE scanning strategy is determined to obtain a contiguous sampling of the Earth's atmosphere. The temperature monitoring of various subsystems are performed for checking the system health during on-orbit operation.

Chapter IV Radiometric Data Acquisition System

The goal of this chapter is to explain the design and testing radiometric data acquisition system of TWICE. It presents the design requirements and how they are determined to achieve high performance from the radiometric measurements of the TWICE instrument. The C&DH and power regulation system design will be explained in detail. The test results for each subsystem and integrated system will be analyzed both for the TWICE functional requirements from an electronic design and radiometer operation point of view.

4.1. Introduction

The C&DH board of the TWICE instrument is a mixed analog-digital circuit board. On the analog side, analog signal conditioning circuit consisting of analog-to-digital converters (ADCs) performs synchronous digital acquisition of analog signals from the 16 radiometric channels of the TWICE instrument, each corresponding to antenna temperatures. The digitized radiometric data are sent to the OBC using the FPGA. Furthermore, current sensing and voltage monitoring device on C&DH board continuously checks the current and voltage values of different on-board circuits of the C&DH system. As shown in Figure 19, the FPGA on the digital part of the C&DH acts like a central processing unit of the instrument sending the command signals to other TWICE subsystems in addition to controlling the synchronous acquisition of the radiometric signals. The FPGA is also responsible for the synchronization of the 670 GHz receiver LNA switch digital control signal from

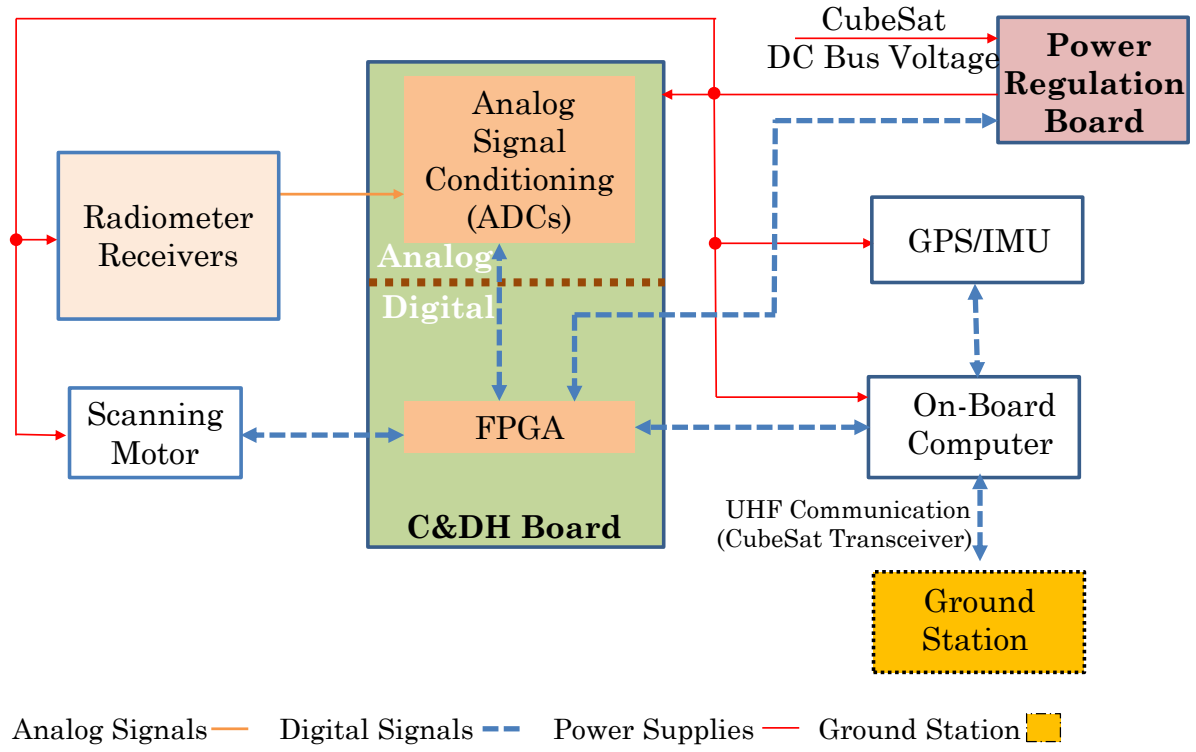

Figure 19: TWICE electronics system integration block diagram showing how each system interfaces with each other.

FPGA with the digital acquisition of the analog radiometric signals. The OBC is used for the storage of the scanning motor information, GPS/IMU data and digitized radiometric and thermal information for ground station data transmission. Finally, the CubeSat DC bus voltage input to the power regulation board. The regulated voltages at required current rating are distributed to all subsystems by the power regulation board [26].

4.2. TWICE C&DH System Design Procedure

The design process of TWICE radiometric data acquisition system is defined at four-steps as shown in Figure 20. At the initial stage of the design, radiometric receivers

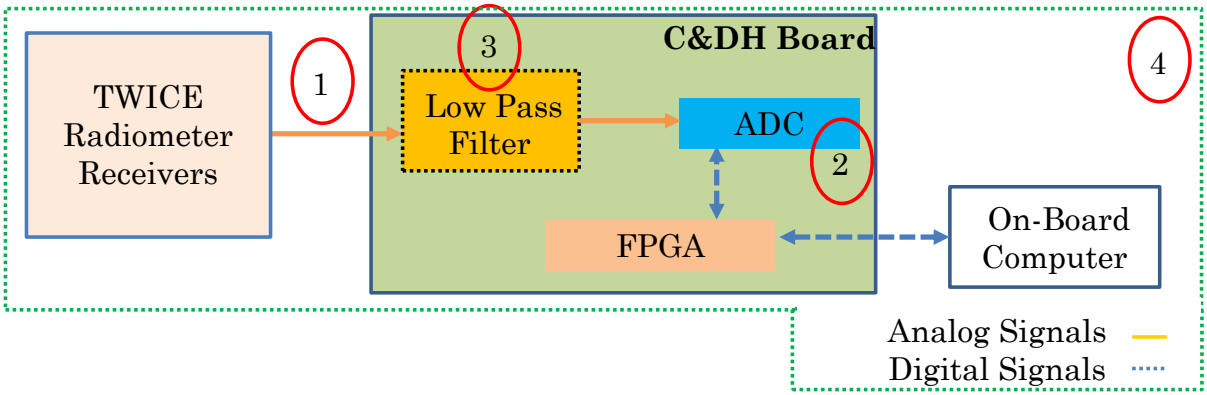

Figure 20: TWICE radiometric data acquisition system design process.

and system radiometric design parameters are defined. The expected noise-equivalent delta-temperature (NEΔT) of the receivers is used to calculate the number of quantization steps required at data acquisition. Therefore, the digitizer will have enough resolution to sense the antenna temperature measurements better than the receiver NEΔT. The required number of bits for TWICE ADCs are calculated as at least 16 bits per channel. The expected antenna footprint size and scan speed are used to determine the sampling time required to have contiguous sampling of the radiometers. The ADC data throughput rate is calculated based on the ADC integration time for contiguous sampling. Other parameters for ADC are determined to design a low-noise, low-power and size efficient system for synchronous acquisition of 16 radiometric channels [43].

4.3. TWICE C&DH Design Parameters

The determination of the parameters for the C&DH design imposed by the front-end receivers has critical importance to achieve high quality and reliable radiometric data from the TWICE instrument.

4.3.1 Number of Analog Channels

The number of analog input channels at the radiometric acquisition system directly affects the design complexity and system performance. The TWICE instrument has 3 sets of frequency channels as shown in the TWICE instrument block diagram in Figure 12. TWICE instrument has 4 sounding channels at each of near 118 GHz oxygen line for temperature profiling and near 183 GHz and near 380 GHz water vapor line for water vapor profiling. In addition to 12 sounding channels, TWICE instrument has radiometric channels at 240 GHz, 310 GHz and 670 GHz (dual-polarized) frequencies for water-vapor and cloud-ice monitoring. Thus, the acquisition system of the TWICE instrument should acquire 16 radiometric channels of the instrument.

The acquisition of the radiometric channels should be performed simultaneously in synchronization with each other to obtain the radiometric information of the same footprint through different frequency channels. This, in turn, will be used to estimate water vapor and ice particle information from the radiometric measurements with the help of the data collected through different radiometric channels containing different information over the same footprint area.

As a result, the designed acquisition system should have the ability to perform synchronous simultaneous acquisition of the 16 radiometric channels. The analog-to-digital conversion should have 16 independent channels in order to fulfill this requirement.

4.3.2 Footprint and Sampling Time Analysis

The footprint and sampling time analysis is conducted to achieve a contiguous coverage of the Earth scene. The main considerations are the coverage in the cross-track direction and the coverage in the along-track direction.

4.3.2.1 Along-track Coverage

The along-track direction is defined as the direction in the motion of the TWICE CubeSat instrument as illustrated in Figure 21. The contiguous coverage in the along-track direction is independent from the analog-to-digital converter (ADC) sampling time and depends on the TWICE instrument ground speed, the footprint size in the along-track dimension and the scanning rate of the instrument. The ground speed of the instrument is calculated in the TWICE orbital analysis section as 7.2 km/s at TWICE orbital altitude. The along-track dimension of the footprints

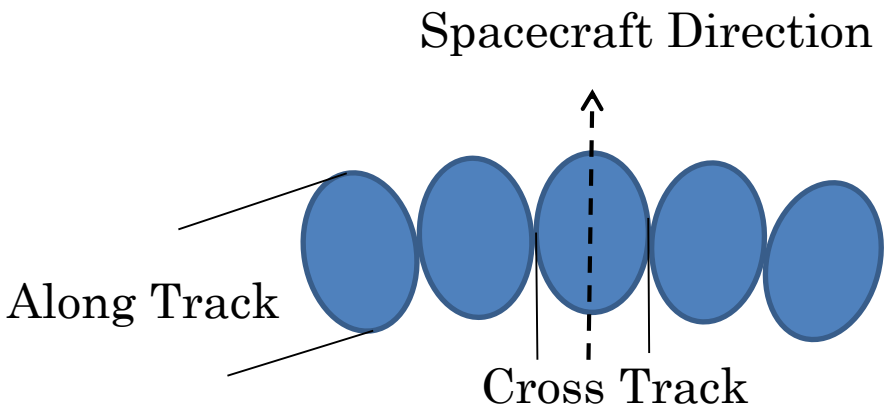

Figure 21: The graphical illustration of along-track and cross-track footprint directions for a radiometer instrument.

is calculated by projecting the beam on the footprint for each frequency channel using -3 dB beamwidth information. The motor scan speed is set to have 1 second scan revisit time as explained in the TWICE scan strategy.

The along-track footprints of the TWICE instrument are illustrated for four channels at 670 GHz H-Pol and V-Pol, 310 GHz and 118 GHz in Figure 22. The coverage analysis performed shows that all the channels accept high frequency 670

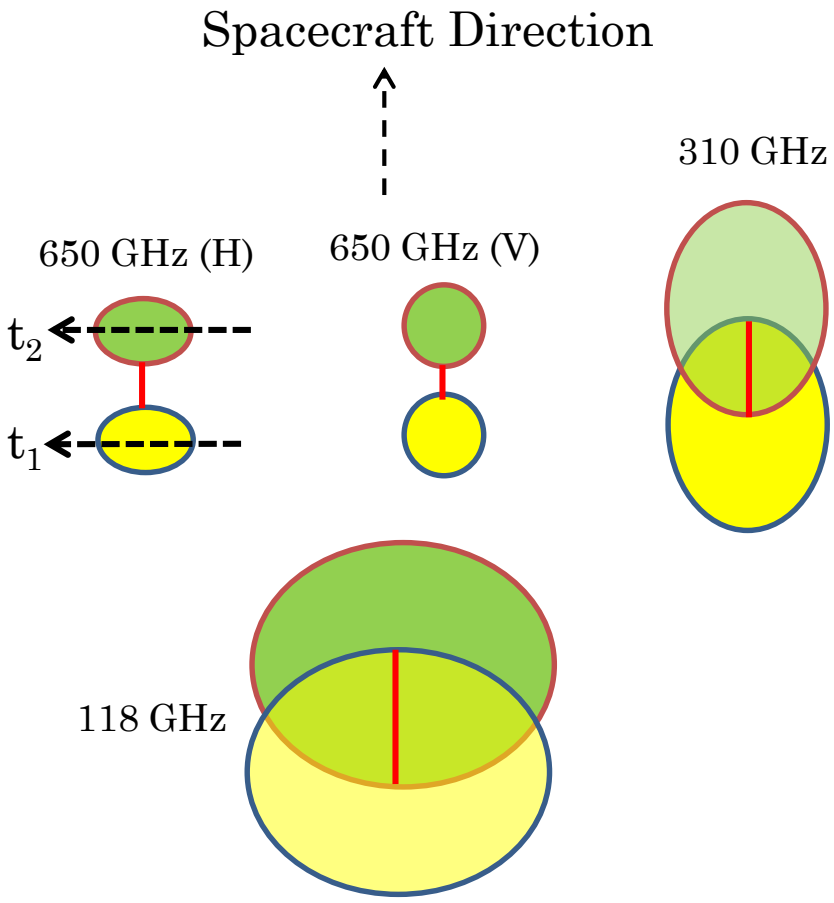

Figure 22: TWICE along-track direction coverage for 118 GHz, 310 GHz and 670 GHz radiometric channels.

GHz channels have complete coverage of the Earth scene in the along-track direction. The gap between high frequency channel footprints in the along-track direction is negligible compared to size of the clouds. The complete coverage can be provided for these channels by increasing the scanning speed of the motor at the cost of increased torques and motor size but it is not required as a science objective of the TWICE considering the size of the clouds. The analysis in the along-track direction is summarized in Table 3.

Table 3: The TWICE along-track coverage analysis for various radiometric channels

Frequency Channel	Along-Track [km]	Footprint Overlap [km]
118 GHz	15	+7.8
310 GHz	13	+5.8
670 GHz (H)	4	-3.2
670 GHz (V)	5	-2.2

4.3.2.2 Cross-track coverage

The coverage of the instrument in cross-track direction can be achieved by setting up the footprint sampling time accordingly. As illustrated in Figure 15, the antenna scans the contour C during one scan cycle. It takes 0.47 second for the motor to scan the Earth scene portion of the scan cycle given in Figure 18. The number of footprints during one scan cycle (N_{FP}) for the TWICE radiometers is calculated by [34]:

$$N_{FP} = \frac{C}{FPS} \tag{IV.1}$$

where FPS is the cross-track footprint size of the radiometers calculated using the projection of the 3 dB beam on the observation area. The required maximum radiometer footprint time for each receiver to achieve full coverage (τ_{max}) is calculated by taking the ratio of the scanning time (t_{scan}) to the number of footprints as:

$$\tau_{max} = \frac{t_{scan}}{N_{FP}} \tag{IV.2}$$

Using the orbital parameters of the TWICE instrument that calculated in the previous section of this thesis, and the Equations (IV.1) and (IV.2), the maximum footprint sampling time for each receiver has been calculated. Table 4 summarizes the maximum footprint sampling time calculation for each receiver channel in addition to presenting the radiometer cross-track footprint size and number of footprints per scan.

The radiometer footprint time given in Table 4 is the actual footprint time of the radiometer instrument directly calculated from the -3 dB beamwidth of the frequency channel as defined in Equation (IV.2). The footprint sampling is determined to obtain a common sampling time among different channels of the instrument for the measurements of the same footprint area synchronized and simultaneous with the other instrument channels. The footprint sampling time has to be set to the same number for the channels being simultaneously acquired with

Table 4: The TWICE radiometric acquisition maximum footprint sampling time requirement for contiguous coverage

Frequency [GHz]	Cross-Track Footprint [km]	Number of Footprint per Scan [N_{FP}]	Sampling Time [ms]		
			Radiometer Footprint Time [ms]	Footprint Sampling Time [ms]	ADC Sampling Time [ms]
118	19	46	10.31	8.00	4.00
183	12	72	6.51	8.00	4.00
240	13	67	7.06	4.00	2.00
310	10	87	5.43	4.00	2.00
380	8	108	4.34	4.00	2.00
670	5	173	2.71	4.00	2.00

the same ADC chip since the ADC channels in general cannot be set to a different sampling time. One can use one ADC chip per channel and synchronize the acquisition with the system clock. However, this is not recommended for a CubeSat design considering the miniaturized structure of the instrument. The ADC maximum sampling time is determined to obtain the Nyquist sampling time. However, one can sample faster than the required sampling time and implement a digital averaging inside the FPGA or at OBC as a digital post-processing.

The ADC chip used in the TWICE design should be able to have minimum 500 samples-per-second (SPS) sampling rate per radiometric channel in order to achieve the required performance needed based on the footprint sampling time analysis.

The expected radiometric resolution of the TWICE frequency channels can be calculated using the footprint sampling time, the bandwidth of the receivers and the system noise temperature as explained in the next section for determining the number of bits needed in the ADC chip for radiometric acquisition.

4.3.3 Number of Discrete Quantization Levels

The number of discrete quantization level of the radiometric data is critical in determining the performance of a radiometer since it directly affects how well the instrument can resolve the radiometric measurements. The radiometric resolution performance of the front-end receivers and antenna for the radiometric brightness temperature measurements can be significantly degraded, if the resolution of the digital acquisition is poor.

The radiometric resolutions of each TWICE radiometer can be calculated using the definition of the NEΔT for a total power radiometer ignoring the gain fluctuation in Equation (II.38). The required resolution in the radiometric acquisition should be better than the radiometric resolution. The discrete quantization levels for an ADC chip is given as:

$$V_{bit} = \frac{V_{FS}}{2^n} \tag{IV.3}$$

where V_{bit} is the bit resolution of the ADC in V per bit, V_{FS} is the full-scale analog input voltage range of the ADC in V, n is the number of bits of the ADC chip and 2^n is the number of quantization levels of the ADC chip. A first order of magnitude

estimate can be provided by comparing the bit resolution with the radiometric resolution as:

$$V_{bit} \ll NE\Delta T \tag{IV.4}$$

or this can be expressed using the definition of NEΔT given in Equation (II.38) and the definition of V_{bit} in Equation (IV.3) as:

$$\frac{V_{FS}}{2^n} \ll \frac{T_{sys}}{\sqrt{\Delta B \tau_{int}}} \tag{IV.5}$$

With the assumption of the system temperature (T_{sys}) to span the complete full-scale range of the ADC (V_{FS}), this equation simplified into:

$$\frac{1}{2^n} \ll \frac{1}{\sqrt{\Delta B \tau_{int}}} \tag{IV.6}$$

The comparison of the bit resolution with respect to radiometric resolution is performed for all radiometric channels of the TWICE instrument. The analysis for 670 GHz frequency channel is shown in Figure 23.

The bit analysis plot shows that the minimum number of noise-free bit resolution required at the radiometric acquisition is between 13 and 14. An ADC having 14 noise-free bit resolution will be enough to maintain the NEΔT performance of the front-end receivers and the antenna. However, adding extra bits to the ADC bit requirements is a necessity considering the noise and the voltage range of the radiometric signal. Thus, based on the analysis made on the number of bits

required in the ADC chip, a minimum 16-bit requirement has been decided on the radiometric acquisition system design.

4.3.4 Radiometer Output Voltage Range and Polarity

The radiometric power detected by the square-law detector diode is amplified by using the video amplifiers before the radiometric data is transmitted to the C&DH board for the radiometric acquisition. The post-detection amplification at the front-end receivers minimizes the effect of the noise coupling into the radiometric signal in transmission from the receivers to the radiometric acquisition board. The output voltage range of the radiometers is set to be no more than 5.0 V for the on-orbit

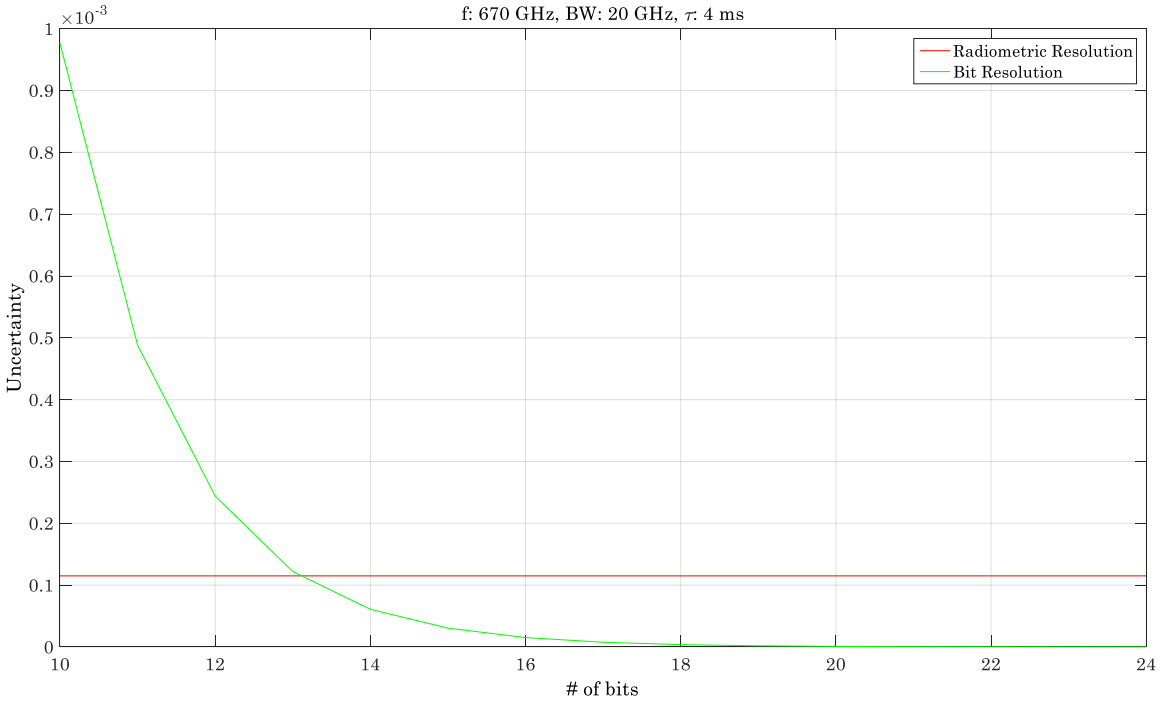

Figure 23: TWICE bit calculation analysis for 670 GHz receiver.

operation of the instruments. The output voltage has only positive voltage polarity. Therefore, the ADC chip used on the C&DH board should be able to accept the analog radiometric signals up to 5 V at positive polarity.

4.3.5 Summary of the Specifications

The design specifications found in this section are summarized in Table 5. As a summary, the design requires analog to digital conversion at minimum 16 bits per channel at 500 SPS for an analog input voltage between 0 to 5 V voltage range. In addition to specifications summarized, the designed system should be performing simultaneous, low-noise synchronized 16 channel radiometric acquisition. The radiometric acquisition system design will be made based on the parameters given in this chart.

Table 5: The TWICE radiometer acquisition design specifications based on the front-end receiver parameters

Specification	Value
Minimum Number of Bits	16
Number of Channels	16
Analog Input Voltage Range	0 – 5.0 V
Signal Polarity	Positive
Minimum Data Throughut Rate	500 SPS

4.4. Data Converter Selection

The ADC chip should be selected according to the design specifications defined in the previous section. In addition, there are several considerations for the ADC chip selection [44].

4.4.1 ADC Architecture

There are three different mainly used data converter architectures in the market which are sigma-delta (Σ-Δ) ADC, successive approximation register (SAR) ADC and pipeline ADC. The comparison of these different type of ADC structures is important for the selection of the most suitable for the TWICE instrument [45], [46]. Pipeline architecture is mainly used for high-speed application where the sampling speed is greater than 5 MSPS. The acquisition is performed in a queue as similar to a production band in a factory. The number of quantization levels is limited. Therefore, the high resolution cannot be obtained for this architecture. Furthermore, they are not power efficient since they are designed for high speed applications [45], [47]. As a conclusion, the pipeline ADC architecture is not considered as an option in the TWICE radiometer acquisition system design due to their low-resolution and high power consumption in comparison to Σ-Δ and SAR ADC architecture types.

SAR ADCs employ a capacitive array structure for radiometric acquisition. Each capacitor represents a fraction of the analog full-scale voltage range. The input capacitor is compared with the capacitors one by one using the analog switches inside the ADC. The resulting register value is read as the acquired value and

stored in the output registers of the chip. The SAR ADCs have low latency when compared to pipeline and Σ-Δ ADCs [45].

Finally, a Σ-Δ converter employs a ΔΣ modulator and a digital/decimation filter. The ΔΣ modulator usually has higher order of integrators for the integration of the analog input signal. The sampling rate at the modulator is much faster than the output data sampling rate. Then, the modulated signal at higher sampling rate is filter at digital and decimation filter to a lower desired sampling rate. Oversampling of the analog signals inside the ΔΣ modulator shifts the quantization noise to higher frequency. As a result, the noise shaping property of the Σ-Δ converters provide good noise performance for the analog to digital conversion [47], [48], [49], [50].

The comparison of the pipeline, SAR and Σ-Δ ADCs are given in Figure 24 [45]. The pipeline architecture has the highest sampling rate while the lowest resolution among the ADCs presented. The Σ-Δ ADCs have the highest resolution but their sampling rate is low compared to other ADC architectures. The current state of the art Σ-Δ ADCs can quantize analog input data up to 32-bit resolution [50].

The SAR and Σ-Δ ADCs are considered for the prototype design based on the resolution, sampling rate and power consumption considerations.

4.4.2 ADC Polarity

There are three different types of ADC architectures based on the signal polarity that are commonly applied [51].

4.4.2.1 Single-Ended

Only a single wire connection is made from the analog input source to the data converter analog input pin for radiometric conversion for a single-ended ADC. This kind of architecture cannot detect common mode noise and not preferable for the designs maybe susceptible to noise.

If the input signal can only take positive values, then it is called as unipolar single-ended ADC. As an example, AD7091R data converter can only accept unipolar single-ended inputs [52]. The bipolar single-ended ADCs can have negative and

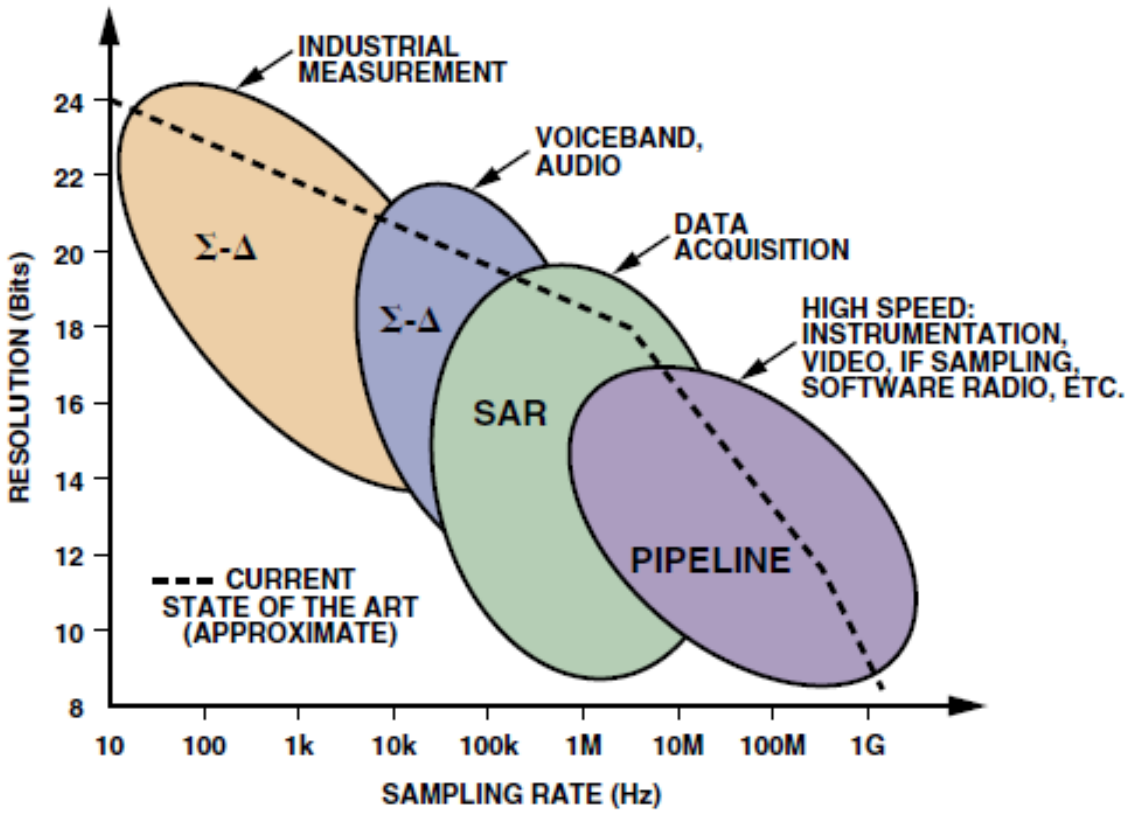

Figure 24: Comparison of different ADC architectures for their performance [45].

positive analog input voltage at their single wire input. AD7656A is a bipolar single-ended ADC chip performing 16-bit data conversion [53].

4.4.2.2 Pseudo-Differential

Pseudo-differential ADCs are similar to single-ended ADCs accepting one-wire analog radiometer signals. However, different than single-ended ADCs, pseudo-differential ADCs has the ground sensing capability of the analog input voltage. However, ground-sense pin has usually low input voltage range. As an example to a pseudo-differential ADC, AD7606 can perform 8-channel simultaneous 16-bit radiometric acquisition [54].

4.4.2.3 Differential

Differential ADCs can accept two-wire analog signals for analog to digital data conversion. These ADCs compare the positive analog input terminal with the negative input terminal. The conversion is performed relative to differential pair analog input pins of the ADC. These types of ADCs have better immunity to common mode noise on the signals. As an example, ADS1178 is a differential 8-channel, 16-bit, simultaneous sampling ADC [55]. AD7609 is also a differential 8-channel ADC but with 18-bit resolution [56].

4.4.2.4 Considerations for the TWICE radiometer

The TWICE front-end receivers have single-ended radiometric output signals. However, the ground pin of the receivers needs to be sensed to achieve low-noise performance needed for radiometric acquisition. Therefore, true single-ended data

converters are not considered for TWICE radiometer data acquisition system design. Pseudo-differential SAR 16-bit ADC AD7606 is used in the prototype system design with ground-sensing option [54]. Differential 16-bit Σ-Δ ADC ADS1178 and 18-bit SAR ADC AD7609 are used with the negative input pin as the ground-sensing pin on the prototype system design [55], [56].

4.5. TWICE C&DH System Design Requirements and Strategy

The TWICE C&DH design consists of two stages. At the first stage, which is named as prototype design, the primary goal is to design a circuit board that will lead to an optimum design for the final circuit board design. At prototype design phase, the functionality of selected components and the entire board is analyzed and different design architectures are tested. The performance of the designed prototype system is evaluated when it is integrated with the 670 GHz prototype front-end receiver. End-to-end test performance of the prototype design is analyzed.

The environmental tests are conducted to estimate the on-orbit system behavior of the TWICE electronics at low-Earth orbit (LEO) altitude include the thermal cycling and radiation testing.

The final C&DH system design is performed based on the results of functionality tests of the prototype boards, radiation testing of ICs and the prototype 670-GHz receiver end-to-end radiometer testing. The design strategy followed for the TWICE C&DH system is summarized in Table 6.

The TWICE C&DH design requirements are determined based on the system level functional analysis considering the science requirements of the TWICE 6U CubeSat

Table 6: The TWICE C&DH board design strategy

Design	Goals
Prototype Design	• Test functionality of selected components and entire board • Verify that design meets specifications • Test for single-event effect (SEE) tolerance at the Texas A&M cyclotron • Test for LEO orbit-like thermal cycling • Test with 670 GHz radiometer prototype integrated receiver
Final Design	• Update based on results of functionality, SEE and thermal tests • Correct any design errors in the prototype

radiometer instrument. The design requirements are summarized in Table 7. The stringent size, weight and power (SWaP) requirements of 6U-class CubeSat instruments imposes less than 2 W power consumption and less than 1U dimension width on the design of the C&DH board. Environmental radiation and thermal considerations are critical for achieving a reliable on-orbit operation. The number of channels and the resolution per channel are determined to achieve the required functional capability for radiometric brightness temperature measurements as explained in the previous sections.

4.6. C&DH Prototype Boards Design

The prototype C&DH board block diagram given in Figure 25 presents the main ICs used in the system design as well as how the system interfaces with the other

Table 7: The TWICE C&DH board design requirements

Parameter	Value
Allocated DC Power Budget	~ 2 W
Board Dimensions	• ~ 9.5 x 9 cm (Prototype) • 7.0 x 14.5 cm (Final)
On-orbit at 350-450 km altitude and 30° to 91° inclination	• Tolerant of Thermal Cycling • Resistant to Single Event Effects
Number of analog input channels	16 - simultaneous
Resolution of analog-to-digital converter	At least 16 bits per channel

subsystems of the TWICE 6U CubeSat instrument. The C&DH prototype board mainly consists of an FPGA, 3 different types of ADCs, the current sensing and voltage monitoring IC and connectors used for the interface.

The FPGA used on the board is a military grade (MIL-grade) PROASIC3EL type MicroSemi low-power FPGA with 484 BGA package [57]. The FPGA has flash type architecture and extended and low-power version of other PROASIC family FPGAs.

There are one 16-bit 8-channel Σ-Δ ADC (ADS1178) [55], one 16-bit 8-channel SAR ADC (AD7606) [54] and one 18-bit 8-channel SAR ADC (AD7609) [56] on the prototype design. The ADS1178 and the AD7606 are used for the radiometric acquisition while the AD7609 acquires the analog thermistor data. The ADC selection is done based on the analysis performed for determining the radiometric acquisition system design parameters given in the previous sections. The low-power consumption, low-noise and noise-shaping future of ADS1178 make it more suitable

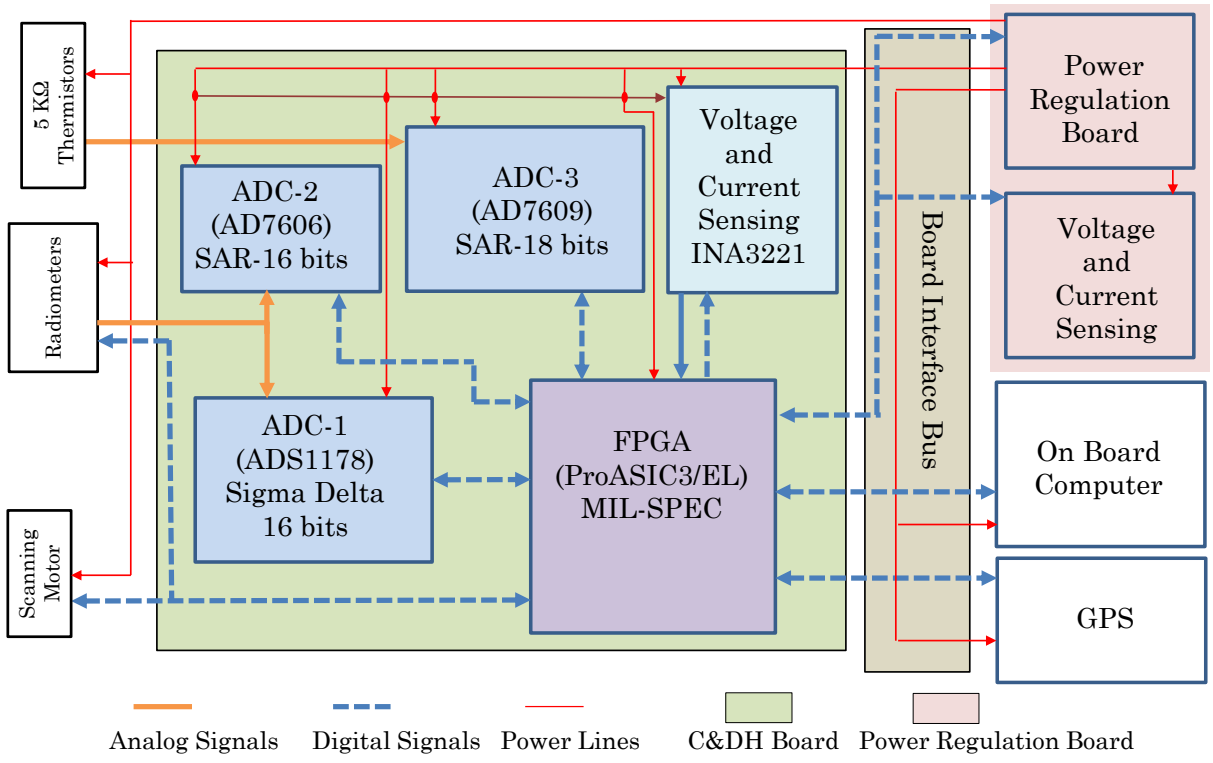

Figure 25: The prototype C&DH board overview showing the main ICs used in the design and how the system interfaces with the other subsystems of the TWICE instrument.

for low-noise, low-power radiometric acquisition system. However, ADS1178 cannot be operated at high sampling rates due to its high latency. On the other hand, the AD7606 has slightly higher power consumption in comparison to ADS1178 but still it is at the acceptable level when the design requirements are considered. Finally, the radiation characteristics of both of the ADCs are not known. Therefore, the radiation testing needs to be performed for both ICs. The radiation evaluation of these ADCs and other components in the TWICE electronics design will be explained in Chapter V on-orbit instrument reliability.

The comparison of the main characteristics and the expected performance for ADS1178 and AD7606 is given in Table 8. The AD7609 has similar operational

Table 8: The comparison of the ADCs used in the C&DH prototype board

Property	ADS1178	AD7606
ADC Structure	Σ-Δ	SAR
Power Consumption	50 mW to 245 mW	100 mW (Operational Mode)
Max. Sampling Rate	52 kSPS	200 kSPS
Channels/resolution	8 (simultaneous), 16 bits	8 (simultaneous), 16 bits
Input type	Differential	Pseudo Differential
SNR	97 dB	86 dB
THD	-105 dB	-107 dB
Package	64 HTQFP	64 LQFP
Operating Temp.	-40°C to +85°C	-40°C to +85°C
Pros and Cons in the Design	• Low noise device (6th order modulator eliminates the low frequency noise). • One sample per footprint will reduce the power consumption. • Low power consumption at low sampling rate. • Radiation testing needs to be performed.	• An embedded 2nd order filter with cut-off frequency of 23 kHz at the input of the chip. • Radiometric data can be sampled faster and averaged inside the FPGA. • Radiation testing needs to be performed.

performance with other SAR ADC. However, the AD7609 has 18-bit resolution which is higher than the AD7606. Also, AD7609 can accept differential inputs whereas AD7606 is only used for pseudo-differential analog inputs.

Finally, the current sensing and voltage monitoring IC (INA3221) is used continuously monitor the current and voltage values of the ADC main supply power,

digital I/O supply power and FPGA core power lines. The INA3221 IC continuously measures the shunt and bus voltage of the power lines being monitored. The shunt voltage is converted into current value using the current sensing resistor value connected where the shunt voltage is measured between its terminals. The current sensing and voltage monitoring of different sub-circuits of the C&DH prototype system is used to maintain the system health in addition to obtaining the power consumption values for debugging purposes. This, in turn, enables for evaluation of the system performance and system functionality.

The TWICE C&DH prototype board employs three different connectors for analog radiometric signals. The Micro-D connector is smaller in size with multiple pins in single connector housing [58]. This makes it suitable for CubeSat applications considering the size restriction. Furthermore, the Micro-D is available in space-grade, military-grade and industrial-grade version. Hence, the reliability of these connectors is ensured in space operating conditions. The second type connector is MSSS which is a product of Micro-Mode Products Inc. and is used on 670 GHz receivers by NGC [59]. This connector provides coaxial cable output but not volume efficient especially for CubeSats. Lastly, SSMB and SSMC type connectors are similar to SMA type connector that is mainly used in RF applications [60]. SSMB/C type connectors provide coaxial cable output. They are smaller than SMA type connectors but still they are not as space efficient as Micro-D connectors.

The digital interface of the C&DH prototype board is provided with a PC/104 type connector [61]. The PC/104 connectors occupy less space on the board and they are

easy to mount and dis-mount the cables. They also provide easiness to stack multiple boards and are commonly used in CubeSats. Finally, the regulated voltages at required current ratings to the C&DH prototype board are transmitted through Micro-D connectors from power regulation prototype board. The graphical representation of the connectors used on the C&DH prototype board is given in Figure 26.

The front-side of the fabricated prototype C&DH board is given in Figure 27. The board is powered from power regulation board through Micro-D 25 connectors. The

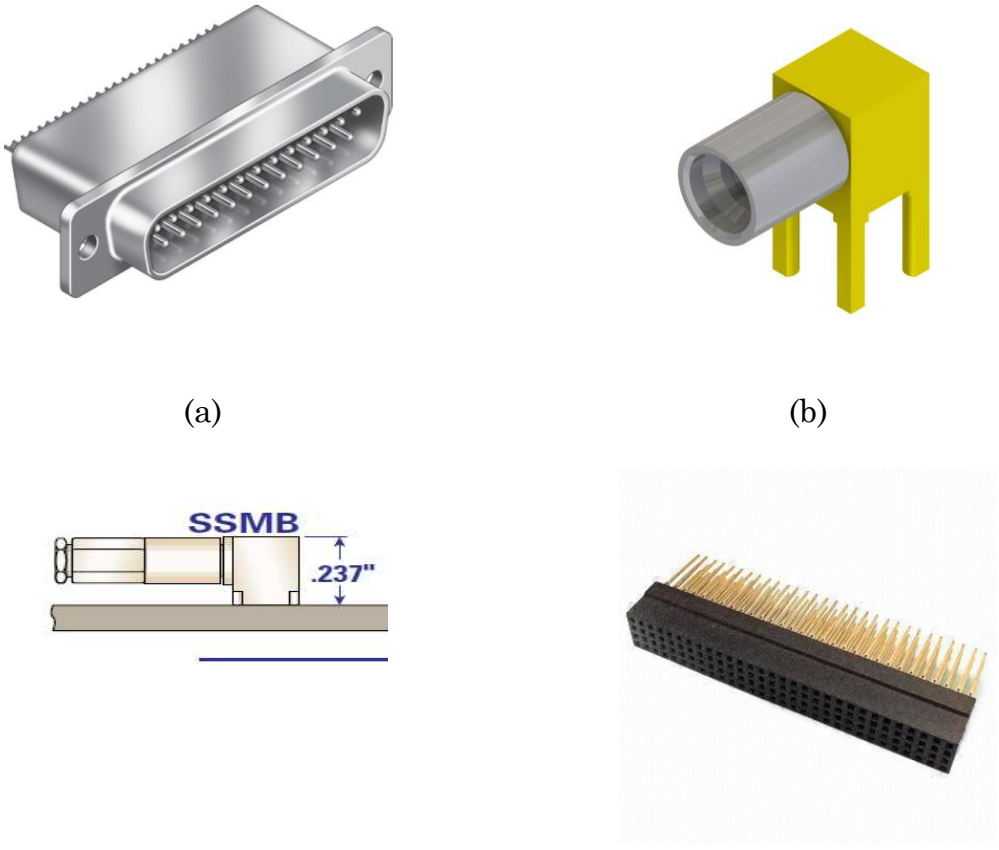

(a) (b)

(c) (d)

Figure 26: The connectors used on the prototype C&DH board: a) Micro-D [58], b) MSSS [59], c) SSMB [60] and d) PC/104 [61]

synchronized acquisition of analog radiometric signals received by three different type of connectors is controlled with the FPGA. The Serial Peripheral Interface (SPI)-to-Universal Serial Bus (USB) device is used for debugging purposes. It transmits the acquired radiometric signals, thermistor information as well as the data obtained from current sensing and voltage monitoring IC to an external laptop computer.

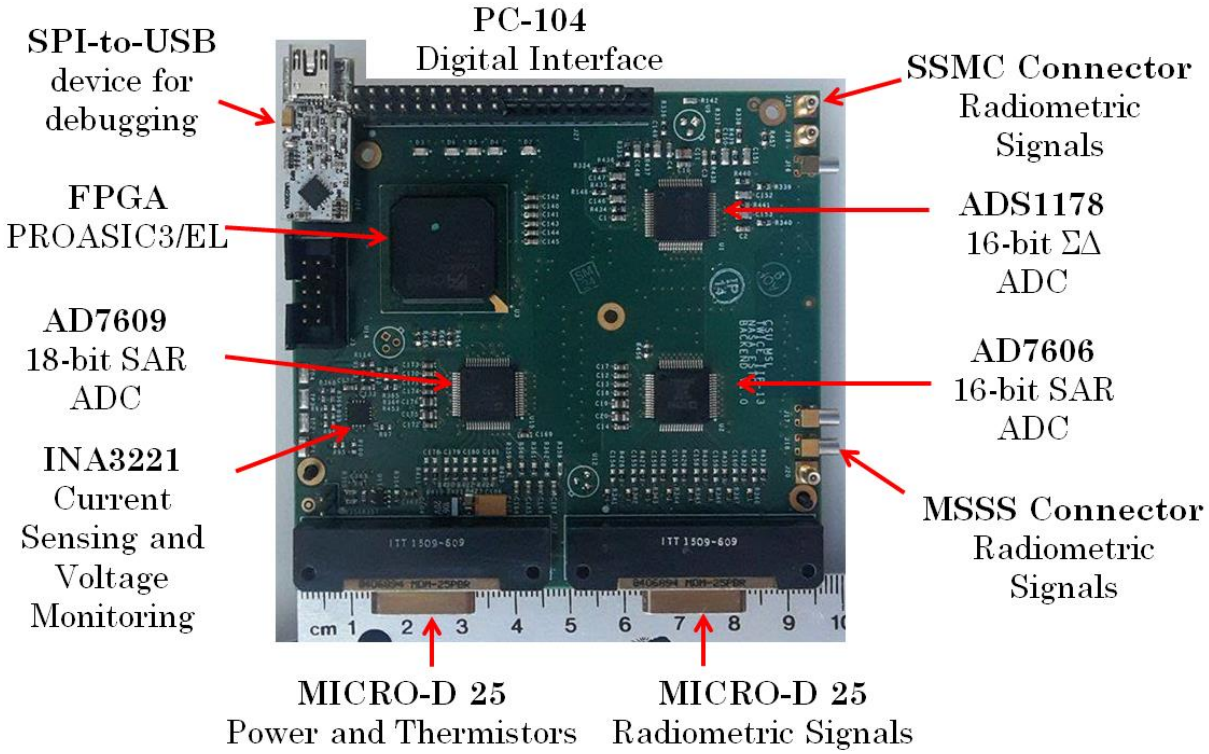

Figure 27: The prototype C&DH board. The top layer is shown with the main ICs and connectors for the interfaces.

4.7. Power Regulation Boards Prototype Design

The TWICE power regulation board is responsible system for the regulation of the main CubeSat DC power supply into the required voltage and current ratings of

different subsystems in the TWICE instrument and the transmitting the power to those systems.

The TWICE power regulation system design employs a centralized power distribution strategy where all the power regulation is performed on the power regulation board. There are some exception to this design rule for some sensitive parts in the TWICE instrument such as DROs and FPGA where they have their voltage regulator at their end.

The power regulation board design strategy consists of two steps as similar to the C&DH system design defined in Table 6. At prototype design, the goal is to test different voltage regulators ICs and different voltage regulation strategies to optimize the final board design in terms of power efficiency, reliability and size.

The TWICE power regulation board design constraints for final and prototype designs are summarized in Table 9. One of the primary design goals is to improve the efficiency of the system by reducing the power loss during voltage regulation on the power regulation board. Thus, an energy efficient power regulation board makes more power available for the other subsystems out of limited total CubeSat power. A hybrid power regulation scheme is considered for the power regulation board. It means that a 2-stage power regulation topology is designed for the most of the devices. The first stage voltage regulation is accomplished with switching power supplies (SPSs). The SPSs have much higher power efficiency up to 95% for some parts in comparison to linear regulator. However, they are considered to generate more noisy output voltage compared to linear regulators. Thus, the first stage is

Table 9: The TWICE power regulation board design requirements

Parameter	Value
Power Efficiency	High to reduce power loss (~ 75%)
Board Dimensions	• ~ 9.5 x 9 cm (Prototype) • 7.0 x 12.7 cm (Final)
On-orbit at 350-450 km altitude and 30° to 91° inclination	• Tolerant of Thermal Cycling • Resistant to Single Event Effects
Other Specifications	• Reliable • Low output voltage swing • Provide the necessary voltages with required current ratings to all subsystems in TWICE • Include switches to turn on or off each radiometer channel • Monitoring current and voltage of selected regulators

built to improve the efficiency while the second stage is employed to improve the noise performance. The hybrid power regulation design strategy block diagram is given for the front-end power regulation in Figure 28.

The board dimensions for prototype and final boards are determined to fit the system into a 1U dimension of the CubeSat. The radiation and thermal requirements also apply to power regulation board as the C&DH board. The designed power regulation system should reliably power the subsystems of the TWICE instrument at required current and voltage rating, and low output voltage swing.

The current sensing and voltage monitoring ICs have been placed on the power regulation board to continuously monitor the voltage and current values of different

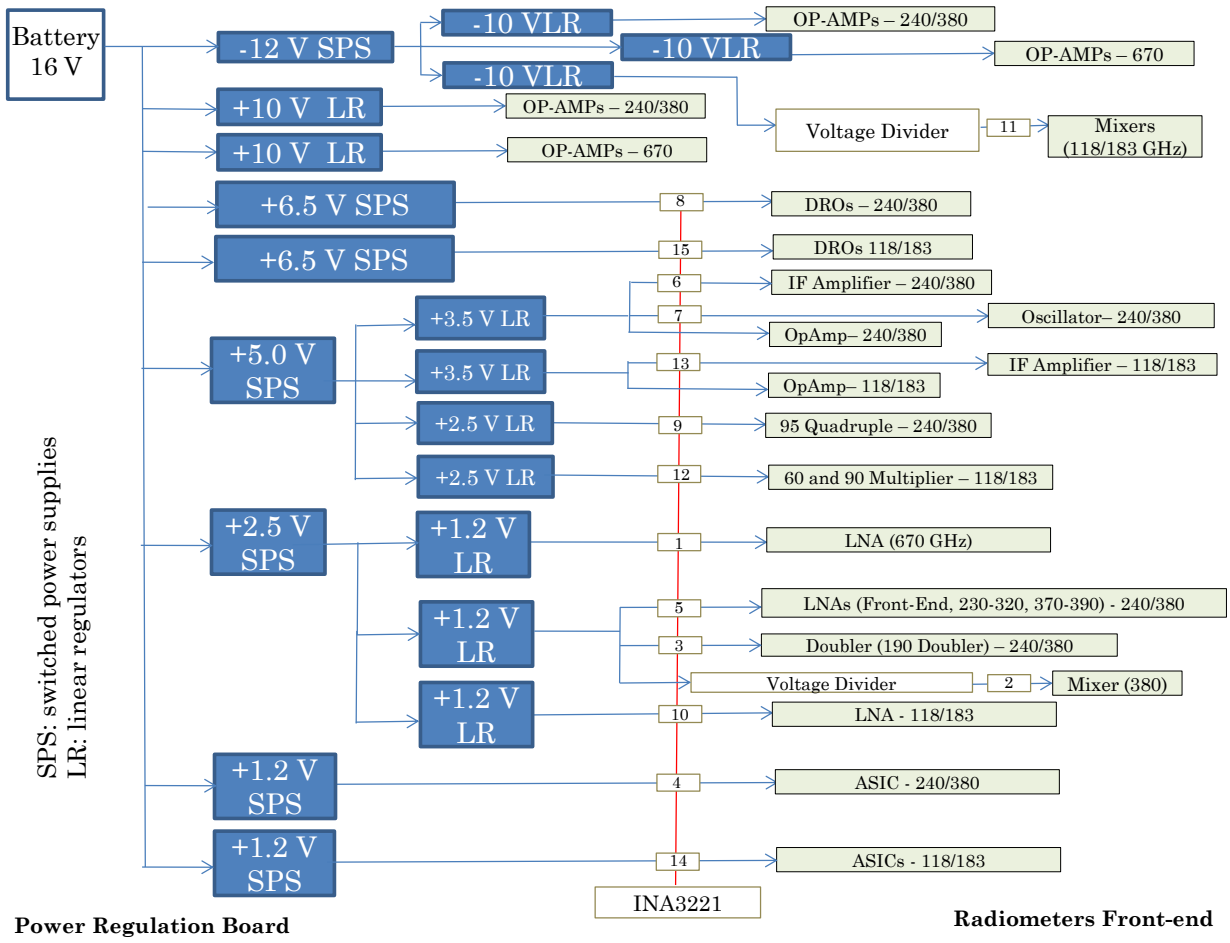

Figure 28: Power regulation board front-end systems power regulation and distribution block diagram

sub-circuits in the TWICE instrument that power regulation board supplies power. There are 20 sub-circuits being monitored in the prototype board which are given in Table 10. These current and sensing and voltage monitoring ICs mainly serves two critical functionalities for the TWICE 6U-class satellite instrument. The first one is to obtain the current and voltage information of different devices within the system for debugging purposes. The second one is to detect devices failing during on-orbit operation. Therefore, the system shuts down the complete subsystem where the

Table 10: The TWICE prototype power regulation board current sensing and voltage monitoring nodes

Sub-system	Monitored Part	Sub-system	Monitored Part
240/380 GHz Radiometers and Sounders	• 380 Mixer • Doublers • ASIC • LNAs • IF Amplifier • Oscillator • DRO • Quadruple	118/183 GHz Sounders	• LNA 190 • Mixers • Multipliers • IF Amplifiers • ASICs • DROs
670 GHz	• LNAs	Scanning Motor	• Motor
Front-end	• All front-end	GPS&OBC	• GPS&OBC
C&DH	• All C&DH	Space part	• All space

failing device is included through analog switches on the power regulation board controlled from the FPGA on the C&DH board. Thus, the healthy parts of the instrument will be able to function without any problem. This will also protect the CubeSat battery from drained due to excessive power consumption of the failing parts. Furthermore, if one able to detect the malfunctioning parts during on-orbit operation, the future technologies can try to mitigate the problem for other planned missions.

The part selection for the power regulation board has been made to improve the efficiency and reliability of the power regulation system as well as with the considerations of the other design specifications given in Table 9. In addition, the prototype design has been performed to accomplish testing various power supply

design techniques. The expected efficiency of the overall system is calculated based on the individual operating characteristics and performance of each circuit element. The overall expected power efficiency for the prototype board has been summarized in Table 11. The estimate given in this chart is based on the preliminary calculations of the power consumptions for each subsystem in the TWICE instrument.

The manufactured prototype power regulation boards are shown in Figure 29. The digital interface of this board with the prototype C&DH board is provided through PC/104 type connector. In addition to transmitting the sensed current and voltage information via inter-integrated circuit (I2C) communication, the digital interface

Table 11: Expected power efficiency of the prototype power regulation board

Subsystem	Max. Power Delivered* [mW]	Dissipated Power [mW]	Total Power [mW]	Power Efficiency η [%]
Radiometer Frontends	7,860	3,530	11,390	69
C&DH Board	2,530	672	3,202	79
OBC	440	77	517	85‡
GPS	880	155	1,035	85‡
Spinning Motor	1,100	194	1,294	85‡
Total	12,810	4,628	17,438	73.5

*Note: 20% contingency ‡Best Current Estimate (November, 2015)

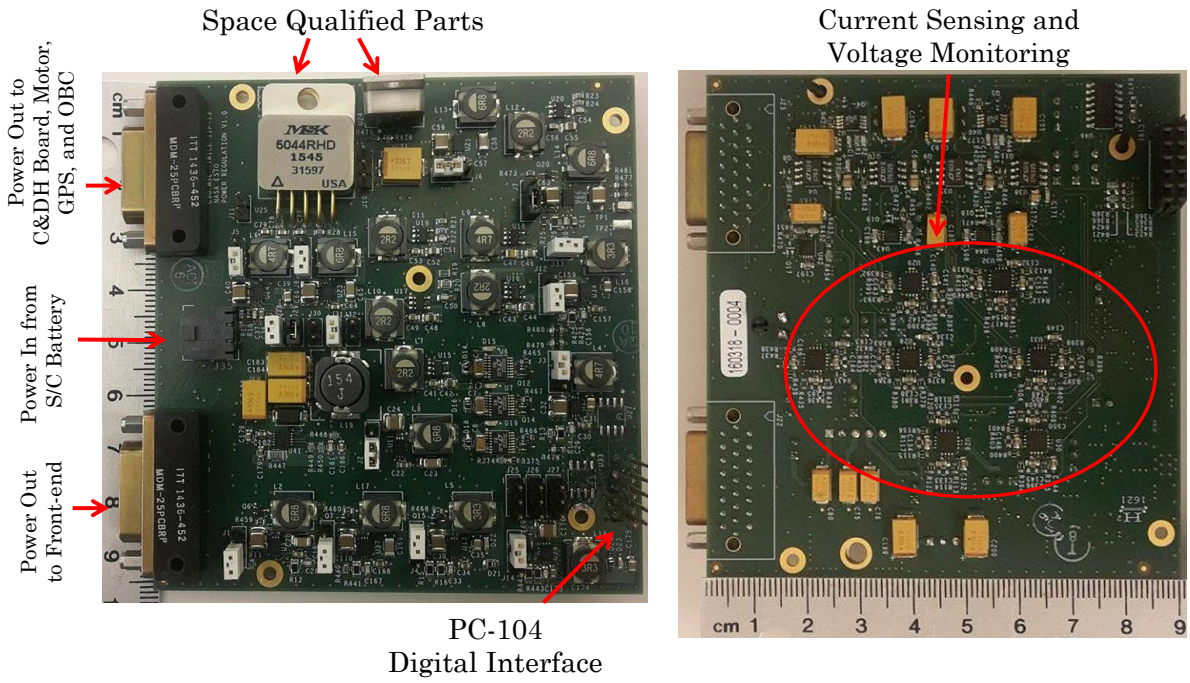

(a) (b)

Figure 29: The prototype power regulation board. a) Front side of the board showing the interfaces. b) Back side of the board showing the current sensing and voltage monitoring ICs in addition to other components.

also transmits digital shut-down signals from the FPGA on the C&DH board. The regulated power is distributed to other subsystems of the TWICE instrument via Micro-D connectors.

4.8. Testing Prototype C&DH and Power Regulation Boards

The tests to determine the functionality and analyze the performance of the prototype C&DH and power regulation boards have been carried out on each individual system separately and when two systems are integrated.

4.8.1 The C&DH Prototype Testing

The tests applied on the C&DH prototype system are grouped according to the purpose of the test.

4.8.1.1 Basic Functionality Tests

The basic functionality of the tests includes the operational ability of the FPGA. The acquisition system and current sensing system will be tested based on the success of these tests.

The first test applied to prototype C&DH board is to check if there is any short circuit on the main power supply lines. The short circuit test is performed without powering the system. Even though it is considered that this has been tested by the company which assembled the boards, validation is important not only to test but also to get familiar with the printed circuit board (PCB) before starting the actual testing with the power on.

After the system is powered on, the FPGA functionality is the first test should be applied to the board before programming the FPGA. For this test, the joint test action group (JTAG) FPGA response is checked using the Libero SoC software developed by Microsemi. The very high speed integrated circuit (VHSIC) hardware description language (VHDL) programming of the FPGA is done after the FPGA is scanned and response is detected.

A simple light emitting diode (LED) blinking VHDL code has been written in VHDL and loaded to the FPGA. The goal is to check the functionality of the board one by

one starting from the basics. The LEDs are set to blink at some frequency on the code. The blinking LED is tested successfully.

Next, the debugging pins of the C&DH board have been used for testing our ability to generate proper clock signal from the FPGA using the phased-locked loop (PLL) circuit of the FPGA. Different clocking signals at various different frequencies have been generated and they have been validated using an oscilloscope.

Following validation of the clock generation using the FPGA PLL, the communication of the C&DH board with an external laptop computer using an on-board SPI-to-USB communication board has been tested. The VHDL programming of the FPGA has been performed to generate some predefined data stream to be transmitted to the external laptop computer at some certain communication frequency. The received data on the computer has been verified in addition to the data rate. For this test, a basic communication and acquisition code has been written in the programming language Python to enable data transfer from the FPGA into the laptop computer and parse the received data stream into a meaningful data format.

The next section explains the data acquisition system testing of the prototype boards.

4.8.1.2 Data Acquisition Tests

The FPGA is programmed in VHDL to control the analog-to-digital conversion through analog input channels of the ADCs. The primary concern while doing these tests is to confirm the operational status of the ADCs one by one under controlled

laboratory environment. The testing diagram is given in Figure 30. The parts have been covered so far are tick-marked in green on the block diagram.

During the test, each ADC has been tested separately using a signal generator as a source of the analog input signals. Power supplies are used to power the C&DH prototype board. A parsing code has been written on Python on an external laptop computer to process the acquisition from all different ADCs into a meaningful data format.

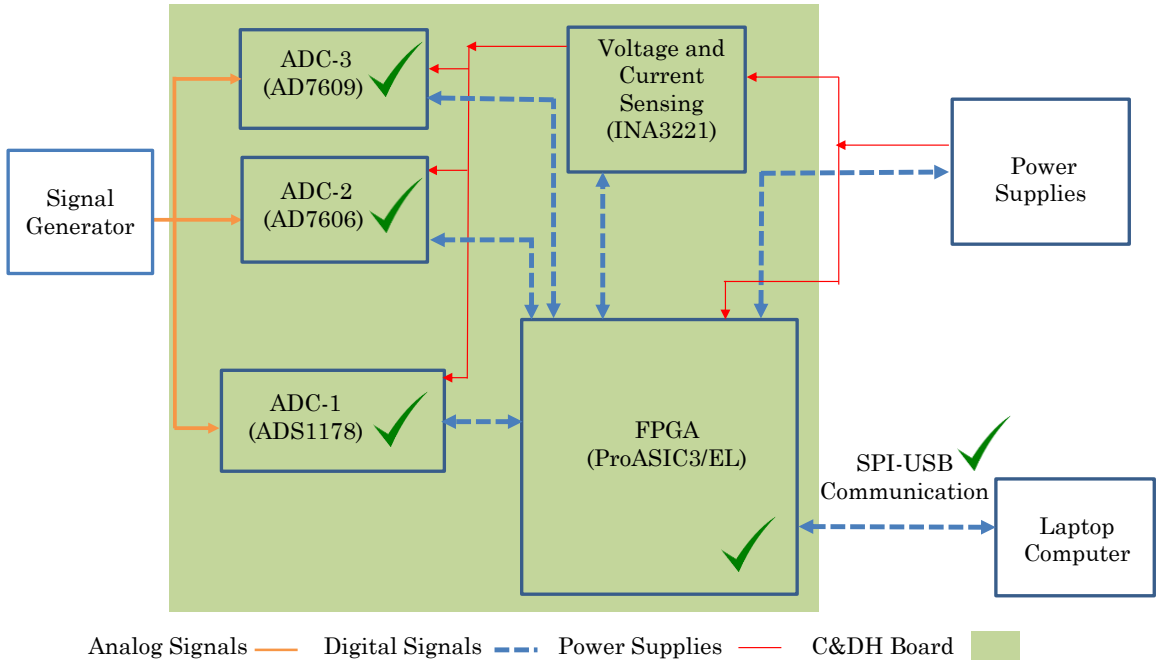

Figure 30: Prototype C&DH boards testing setup block diagram.

4.8.1.3 Current Sensing and Voltage Monitoring on C&DH

The current sensing and voltage monitoring IC INA3221 is controlled by the FPGA through I2C communication [62]. The VHDL code is written to control the current

and voltage acquisition of the INA3221 device. An acquired current and voltage waveform is given in Figure 31. The on-board current sensing and voltage monitoring for C&DH is done for the FPGA and ADC power supply lines, and the I/O power supply for the FPGA and ADCs.

The multimeter and power supply readings are noted for 5.0 V ADC supply voltage line, 2.5 V digital I/O supply voltage line and 1.5 V FPGA core voltage supply line for a comparison with the INA3221 readings. The results of the multimeter and power supply reading are given in Table 12. The multimeter and power supply

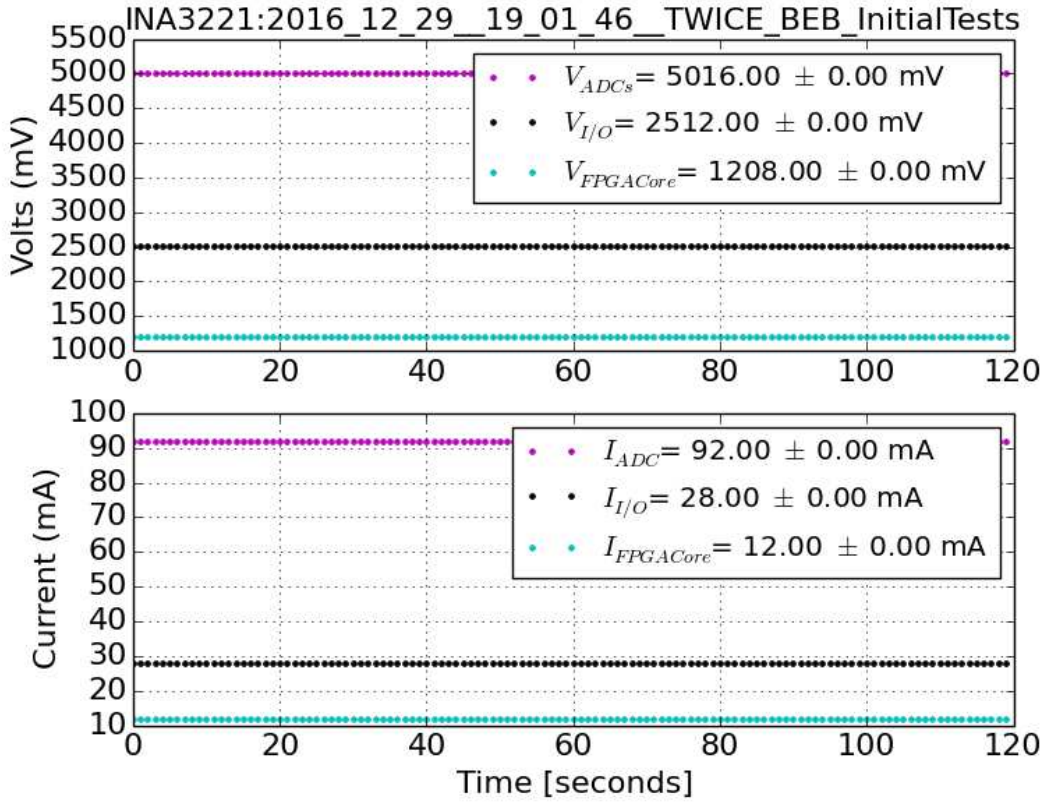

Figure 31: Current and voltage acquisition of different sub-circuits on C&DH prototype boards via INA3221. Top plot shows voltage acquisition in mV and the bottom plot shows current acquisition in mA.

Table 12: The analysis of INA3221 performance for the C&DH current sensing and voltage monitoring

a) Voltage Monitoring

Device	Voltage Acquisition [mV]		
	Multimeter Reading	INA3221 Reading	Difference in Readings
All 3 ADCs	10.31	8.00	4.00
All I/Os + LEDs	6.51	8.00	4.00
FPGA Core	7.06	4.00	2.00

a) Current Sensing

Device	Current Acquisition [mA]			
	Power Supply Reading	INA3221 Reading	Difference in Readings	Power Supply Resolution
All 3 ADCs	100	104	4.00	10
All I/Os + LEDs	30	28	2	10
FPGA Core	14	13	1	1

readings are consistent with the INA3221 reading as summarized in the result based on 8 mV and 4 mA the resolution of the INA3221 for voltage and current measurements respectively. Thus, the results indicate that INA3221 reliably measures the voltage and current on the C&DH board.

4.8.2 The Prototype Power Regulation Boards Testing

The manufactured prototype power regulation boards have been tested to verify their functional capability before the integration with the prototype C&DH boards. The functionality testing setup block diagram is shown in Figure 32. The output of each voltage regulator has been tested under several operating conditions. Light-load, nominal-load and heavy-load resistive network is connected at the output of each regulator. Power efficiency, output voltage fluctuations and load regulation are analyzed.

The output voltage waveform of voltage regulators is continuously monitored with an oscilloscope connected at the regulated power line. Among the voltage regulators on the power regulation board, the switching power supplies need special attention since their output is considered to be noisier than the linear regulators.

The LTC3621 switching power supply output waveforms recorded by an oscilloscope are shown in Figure 33 [63]. This switching power supply has two modes of

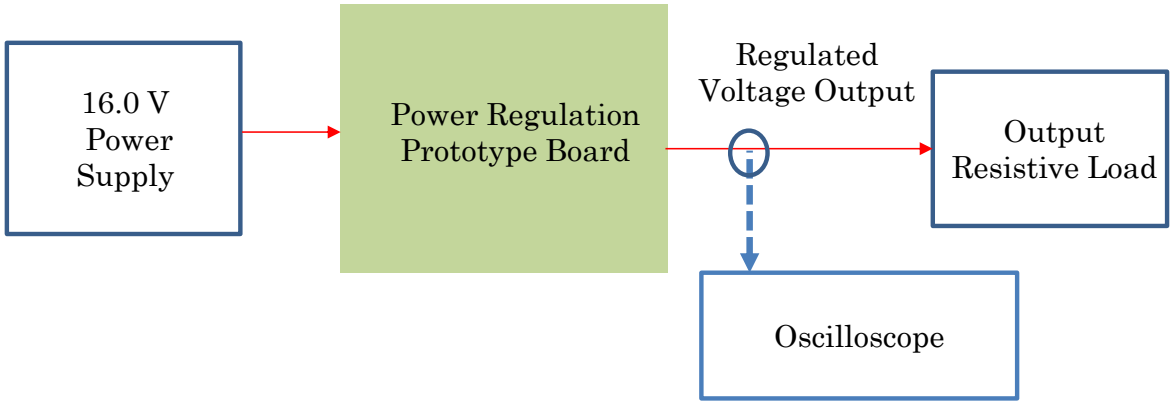

Figure 32: Prototype power regulation board functionality testing setup block diagram.

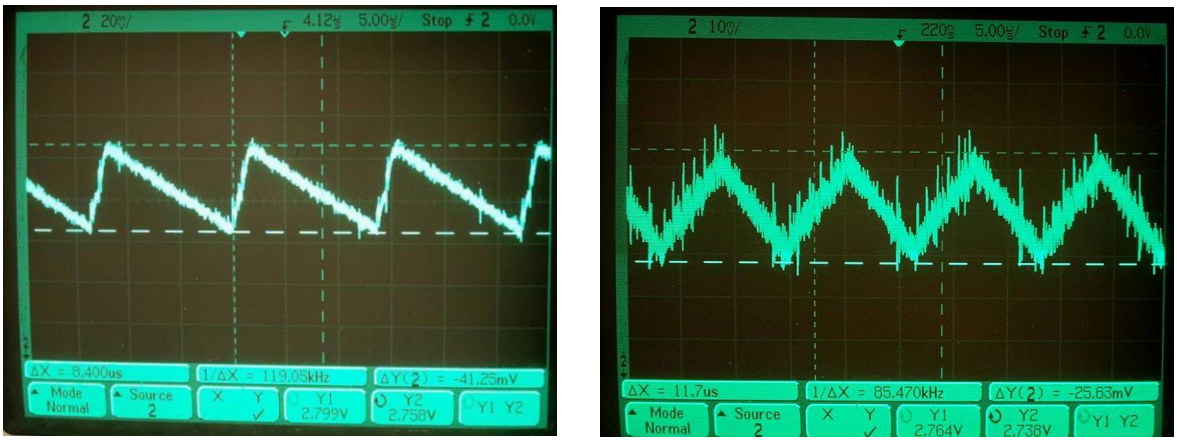

a) b)

Figure 33: LTC3621 functionality tests oscilloscope measurements. a) Device is operating in burst mode. b) Pulse-skipping mode measurements.

operation. The LTC3621 uses a current limiter circuit to switch-on and off for output voltage regulation when it is operated at burst mode. The burst mode can be also referred as pulse frequency modulation (PFM) mode of a switching power supply. This mode of operation uses a lower frequency for output voltage regulation compared to other modes of operation. On the other hand, the LTC3621 internal transistors are turned-on and off continuously at constant frequency at each clock cycle of operation at pulse-skipping mode. This mode can be referred as pulse-width modulation (PWM) mode for a switching power supply.

The output voltage waveforms given in Figure 33 are obtained for the 2.7 V FPGA voltage regulation line when 28 mA of current is being drawn over a 100.3 Ω resistive load at the output considering the case in which the power supply is supplying power to the FPGA on the C&DH board. At the output of the regulator,

40 mV and 25 mV peak-to-peak output voltage ripple is measured at burst mode and pulse skipping mode respectively. The frequency for the burst mode is 70 kHz, which is lower than the one for pulse skipping mode at 85 kHz as expected. The measurements also show that the burst mode has 80 % efficiency for voltage regulation which is significantly higher than the pulse skipping mode at 59 %.

The tests have been repeated for several different conditions including light-load and heavy-load cases. As a conclusion for this specific voltage supply, the burst mode provides higher efficiency than the pulse skipping mode when the output current is lower than 100 mA. At heavy load, both modes have similar efficiency. For all cases, pulse skipping mode provides lower output voltage ripple than the burst mode. However, the output voltage ripple can further be reduced by changing the parameters of the LC filter at the output of the regulator.

The testing of current sensing and voltage monitoring ICs on the prototype power regulation board requires the integration of the power board with the C&DH board since INA3221s on the power board are controlled by the FPGA on the C&DH board. These tests will be explained in the next section on the integration testing of two systems.

4.8.3 The Integration Testing of the Prototype C&DH and Power Boards

The prototype C&DH and power regulation boards are stacked through PC/104 connector and the mounting hole as shown in Figure 34.The back sides of tow boards face each other while the top side of the C&DH board is looking outside which makes it easy to access from the outside. The prototype C&DH board is

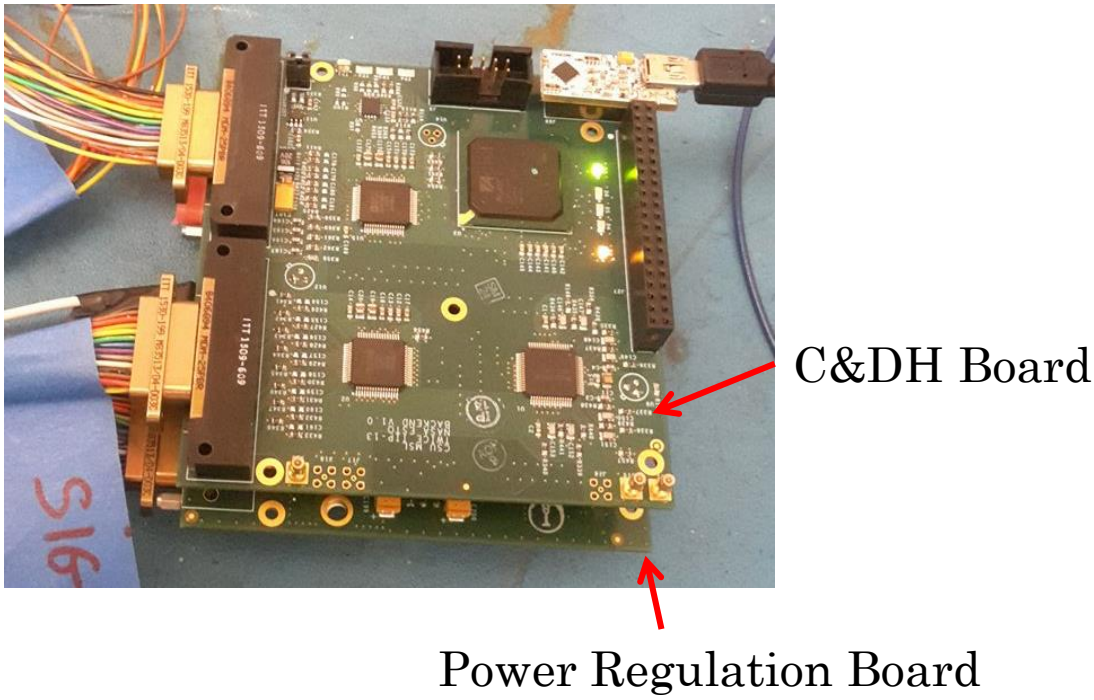

Figure 34: The prototype C&DH and power regulation boards are stacked thorugh PC/104 connector and mounting holes.

powered with the prototype power regulation board for the integrated system testing.

4.8.3.1 Functionality Tests

The functionality tests on the integrated system have been applied as shown in Figure 35. During the tests, a saw-tooth pattern waveform is supplied to the analog input channels of all the ADCs from the signal generator. The ADCs controlled from the FPGA have performed the synchronized and simultaneous acquisition of the same analog input signal. The digitized signal has been sent to the FPGA from all 3 ADCs to be transferred to an external laptop computer through the SPI-to-USB communication module. The acquisition software program coded in Python and

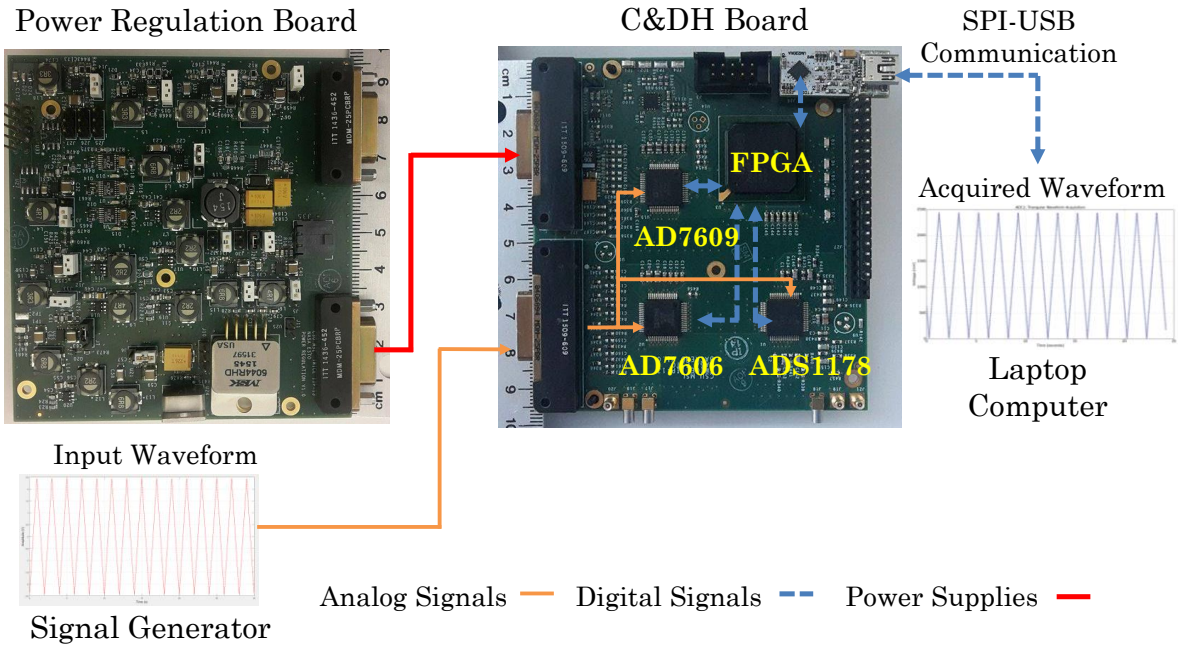

Figure 35: Testing the functionality of the integrated prototype C&DH and power regulation boards.

running on the external laptop computer has processed the received signal from the C&DH board. The comparison of the received signal on the external laptop computer with the generated signal on the signal generator indicating that the C&DH board performs simultaneous acquisition through all the ADCs.

The goal of integrated system testing is not only verify the performance of the hardware design, but also the VHDL programming of the FPGA and Python coding of the acquisition software running on the external laptop computer.

4.8.3.2 The Current Sensing and Voltage Monitoring on Power Board

There are 7 current sensing and voltage monitoring ICs on the prototype power regulation board for tracking the system health of 21 different sub-circuits or subsystems in the TWICE instrument. There are 2 independent I2C lines

connecting INA3221s on the power board to the FPGA on the prototype C&DH board. One I2C line controls 4 INA3221s while the other governs remaining 3 INA3221s. The chip selection is made by the FPGA through the address bit selection on the I2C line. The INA3221 allows setting 4 different address configurations with a single bit address pin as shown in Table 13. The address bit is sent to all the INA3221 devices on the same I2C line from the FPGA but the device with the hardware address wiring matching with the address bit responds to the FPGA.

Table 13: The address bit configuration of the INA3221 for multiple chip operation on the same I2C line

INA3221 Address Bit	Chip Select
Logic Low (Ground)	Chip 0
Logic High (3.0 V)	Chip 1
SDA (Serial Data Line)	Chip 2
SCL (Serial Clock Line)	Chip 3

Current and voltage values are acquired by all 7 INA3221 devices on the prototype power regulation board controlled by the FPGA on the prototype C&DH board. The current and voltage measurements of INA3221 on 16 V power supply line for C&DH and front-end power regulation are given in Figure 36. The results indicate that 16.0 V main supply voltage is successfully used by the regulators for front-end and back-end regulators. It is also important to note that 46 mA of total current is being drawn from 16 V main supply line for the C&DH voltage regulation and operation.

In other words, the total power consumption for the C&DH subsystem including the power lost in the C&DH voltage regulation on the power regulation board is found as:

$$16\,V * 46\,mA = 736\ [\text{mW}] \tag{IV.7}$$

The total power consumption found above is much below than 2 W of allocated power budget of the C&DH board given in Table 7 even though it includes the lost at the power regulation. The operating conditions for the power analysis are:

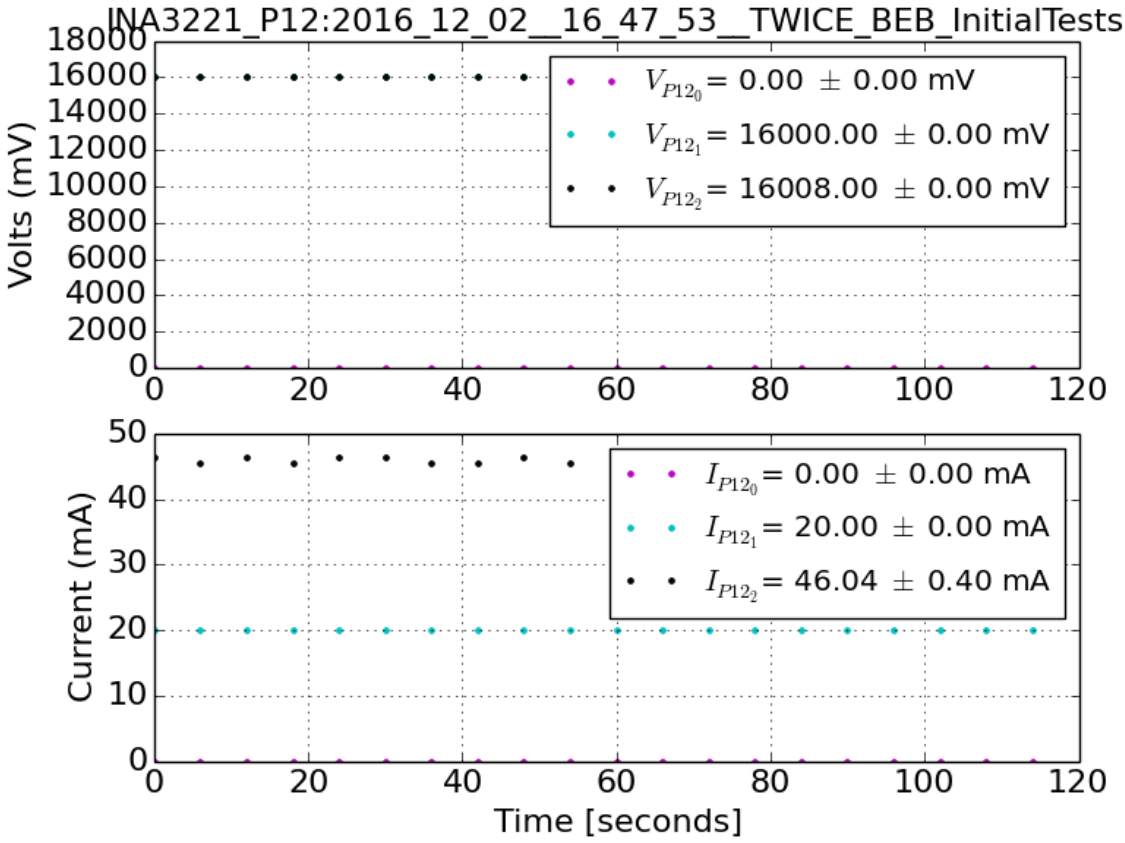

Figure 36: Current and voltage acquisition on the prototype power regulation boards via INA3221 controlled by the FPGA on the prototype C&DH board. Top plot shows voltage acquisition in mV and the bottom plot shows current acquisition in mA.

- All 3 ADCs are in acquisition mode.
- The FPGA is operational at 15 MHz clock frequency
- SPI-to-USB communication is active.
- All devices on the C&DH board are powered on.
- 2 LEDs are ON as power indicators.
- The power board is stacked to the C&DH board and two independent I2C lines are active for 7 operational current sensing and voltage monitoring devices.
- 3 thermistors are connected to the C&DH prototype board for a thermal acquisition.

The power consumption of the prototype C&DH board is our concern for estimating the efficiency of the power regulation board for the C&DH voltage regulation and compare it with the design specifications given in Table 9. The voltage and current values measured from the prototype C&DH board are given in Table 14. The total power consumption of the C&DH board is measured as 588 mW, which is significantly lower than the 2 W allocated power budget for the C&DH operations. Using the overall power consumption analysis made in Equation (IV.7), the efficiency of the power regulation board is calculated as:

$$\eta = \frac{588}{736} = 80\% \tag{IV.8}$$

Table 14: The measured power consumption on the prototype C&DH board provided for different devices on the board in addition to total power consumption.

Device	Voltage [V]	Current [mA]	Power [mW]
3 ADCs (incl. 2 SAR ADCs)	4.98	92	458
Sigma-Delta ADC	1.8	10	18
All I/Os + LEDs	2.51	28	70
FPGA - Core	2.75	12	33
FPGA - JTAG	1.81	5	9
Total			**588**
Total (including power lost in back-end voltage regulation)	16.0	46.0	**736.0**

The efficiency analysis on the power regulation board for the prototype C&DH voltage regulation shows that the estimated efficiency is higher than the design requirement defined in Table 9.

The next consideration is the total power efficiency of the power regulation board when all the regulators are operational supplying regulated power at the required current to each subsystem. For this study, a resistive load has been connected at the output of the systems to mimic the current consumption of the subsystems except the C&DH board since the actual prototype C&DH boards are connected to the power regulation output. The measured efficiency on the power regulation board is given in Table 15 with the expected efficiency as preciously calculated in detail in

Table 15: The measured efficiency of the prototype C&DH board provided for different subsystems with the expected efficiency calculated at pre-design stage

Subsystem	Expected Efficiency(1) (%)	Measured Efficiency (%)
Radiometer Front-ends	69	71
C&DH Board	79	80
On-Board Computer and GPS	85	88
Scanning Motor	85	87
Total	**73**	**75**

(1) Pre-design estimate.

Table 11 for comparison. The measured efficiency for the power regulation of all the subsystems is slightly better than the expected efficiency. In addition, the total power efficiency of the power regulation board is found as 75% matching the design requirement summarized in Table 9.

The next consideration on the integrated prototype design testing is check the noise performance of the system that is critical especially for the overall brightness temperature measurements of the TWICE radiometers.

4.8.3.3 Noise Performance Analysis of the Radiometric Acquisition System

The radiometric signals needs to be acquired using a low-noise system (compared to NEΔT) to avoid adding noise that limits the performance of the front-end and the

antenna for brightness temperature measurements. For a physically built radiometric acquisition system, the noise is inherent in the process of analog-to-digital conversion due to non-idealities in the system.

The input-referred noise, quantization noise and distortion are the main categories for the noise sources that exit in a non-ideal data conversion system. An analog-to-digital data converter matches analog input signals to some digital code at the output based on their digitization levels and input voltage range in comparison to the input signal. An ideal converter would be one that matching every analog signal to unique digital code. However, it is not physically feasible to build such an ideal ADC. The physical ADCs that assumed to be perfect (e.g. ignoring all the noise except the quantization error) matches some certain analog input voltage range to the same digital code. As a result the conversion error occurs from the actual signal. The resulting error is called as quantization error and it is illustrated in Figure 37. The quantization noise limits the signal-to-noise ratio (SNR) of an ADC. For a perfect ADC (e.g.: only the quantization noise is considered), the SNR value is calculated as [64]:

$$SNR = 6.02 * N + 1.76 \text{ [dB]} \tag{IV.9}$$

where N is the number of bits in a perfect ADC. The value given above is not physically achievable due to the distortion in the acquisition. However, one can compare the measured SNR value from an ADC and compare it with the one for a perfect ADC to have a comparable analysis for the distortion over the dynamic range of the ADC.

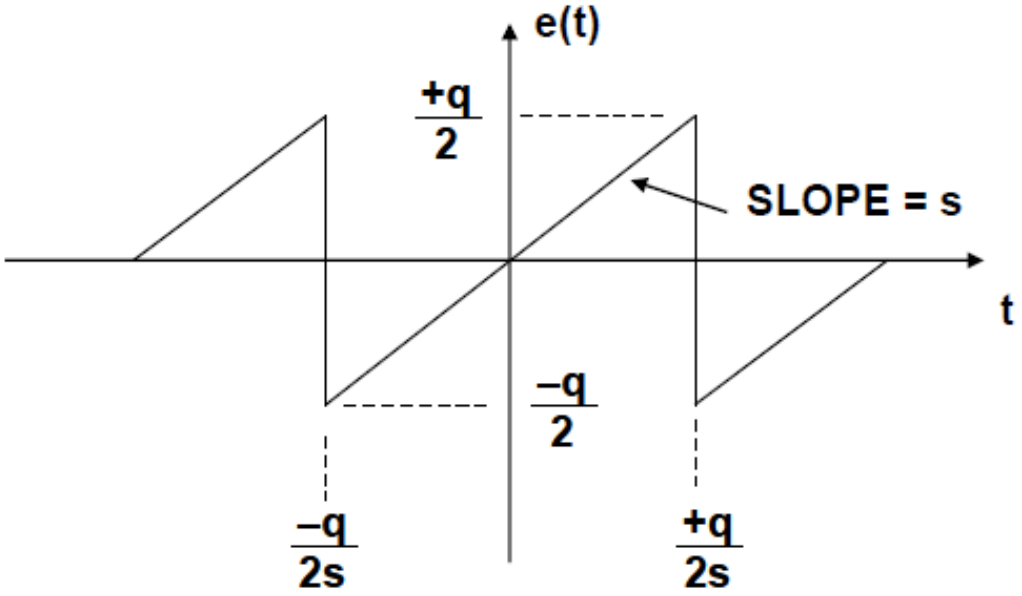

Figure 37: The quantization error as a function of time plotted with respect to peak-to-peak amplitude of the least-significant bit of an ADC (q) [64].

The input referred noise is the noise generated by the internal circuits of the ADC mainly due to Johnson-Nyquist noise, the noise generated by the PCB and the noise generated by any poor grounding techniques or improper power supply decoupling. The resulting effect of the input-referred noise is observed as the shift in the transition regions of an ADC. In other words, matching an analog input signal within some certain range to a certain digital code, the outcome is the spread of digital codes for the same analog input signal.

The noise analysis can be applied to a radiometric data acquisition system in two different ways. The DC analysis is performed to estimate the amount of input referred noise exists on the radiometric acquisition which is an indicator of the quality of the PCB design and grounding techniques in addition to performance of

the ADC under operating conditions. On the other hand, the noise detected from the AC analysis is the combination of the quantization noise, input-referred noise and distortion.

For the TWICE radiometer acquisition system design, our primary concern is to achieve a low-noise system for radiometric acquisition. In other words, the noise coupled by the PCB design, any noise due to improper grounding of the system or the noise generated by the ADC during the radiometric acquisition should be minimized in the system so that the NEΔT performance of the front-end receivers and the antenna is not degraded.

A battery has been used in the test setup for determining the input-referred noise to minimize the noise coupled into the system due to grounding. During the test, numerous numbers of samples have been acquired from the battery by all 3 different ADC on the prototype C&DH board. The statistical analysis of the battery acquisition is done to evaluate the noise performance of the acquisition as shown in Figure 38 for the ADS1178 Σ-Δ ADC.

The measured standard deviation is calculated for all 3 different ADCs on the C&DH board. The battery testing measurements have been repeated using the evaluation board of the ADS1178 and AD7606. The measured standard deviation for the input-referred noise on the C&DH and evaluation boards is in counts and μV in addition to the differential nonlinearity (DNL) of the ADC in ADC least significant bits (LSB) are given in Table 16. The measured standard deviation is the root-mean square (RMS) noise level of the ADC. The value is affected by the ADC

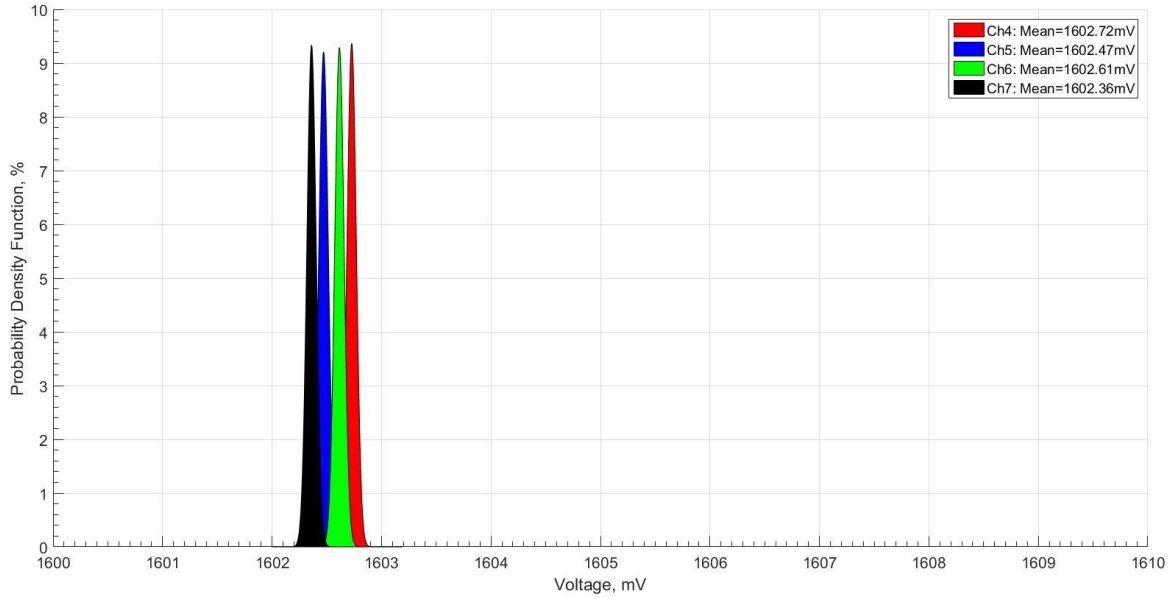

Figure 38: Measurement of battery voltage using the ADS1178 with 4 ADC channels.

DNL, the internal noise of the ADC, grounding of the test setup and the noise generated by any electromagnetic interference (EMI) issues on the PCB.

All of the ADCs except for the AD7609 have acceptable performance since their noise levels are generally lower than the NEΔT of the radiometers (expected radiometric resolution of 100-250 μV for TWICE radiometric channels). The comparison of the noise testing measurements using the C&DH board and the evaluation board of the manufacturer shows that the C&DH board does not add any significant noise even though the C&DH is a mixed analog-digital circuit board design contrary to analog evaluation boards.

Table 16: The ADC input-referred noise measurement results

ADC	Type	One LSB in µV	*DNL (LSB)	C&DH Measured Average STD		Eval. Board Measured Average STD	
				Counts	µV	Counts	µV
ADS1178	ΔΣ	76	±0.3 (max)	0.42	32	0.42	32
AD7606	SAR	152	±0.5 to ±1	0.78	119	0.79	120
AD7609	SAR	76	±0.8 to +2	2.56	194	N/A	N/A

*DNL: Differential non-linearity from the datasheet of the ADCs.

The comparison of all 3 different ADCs indicate that the Σ-Δ ADC ADS1178 has better noise performance as expected based on the previous discussion given on the ADC architectures. The analysis is further extended to calculate the effective resolution for each ADC. Even though the ADCs being tested are advertised as 16 or 18 bits per chip, the resolution is reduced due to ADC input-referred noise. The measured effective resolution for all 3 ADCs is given in Table 17. As it is expected, the best performance is obtained for ADS1178 since it performs oversampling at modulator and digital averaging in decimal filter. The performance of other ADCs can be further improved by oversampling the radiometric signals inside the ADC and digital averaging at the FPGA.

4.8.3.4 Thermal Acquisition

Negative temperature coefficient type thermistors are connected at the analog input channels of AD7609 for the acquisition. The thermistors are expected to be used for

Table 17: The measured effective resolution of the ADCs

ADC	Type	# of bits	Type of Inputs Applied	Effective Resolution (bits)	
				Datasheet	Measured
ADS1178	ΔΣ	16	Single ended	15.8*	15.6
AD7606	SAR	16	Single ended	N/A	15.2
AD7609	SAR	18	Differential	N/A	15.5

*This value is obtained when a differential input signal is applied.

monitoring the temperature for different subsystems for the system health in addition to assessing the temperature information of the ambient calibration target for the end-to-end calibration of the instrument.

The next consideration is the accuracy and stability of the thermal acquisition of analog thermistor signal by the AD7609. The thermistors are held at stable room temperature during the test. The thermocouple measurements are also performed using a multimeter while the thermistor data being acquired. The thermistor acquisition through AD7609 and multimeter reading are plotted in Figure 39. The reading through different channels of the ADC are close each other within 100 mK. Also, all 3 temperature acquisition through the ADC plotted in Figure 39 have the standard deviation of 10 mK indicating the stable ADC acquisition of the thermal signals on the prototype C&DH board. Furthermore, the multimeter reading differs only around 0.1 K from the thermistor readings. This shows that the measurements are reliable considering 0.1 K accuracy of the thermistor and 0.1 K resolution of the multimeter reading.

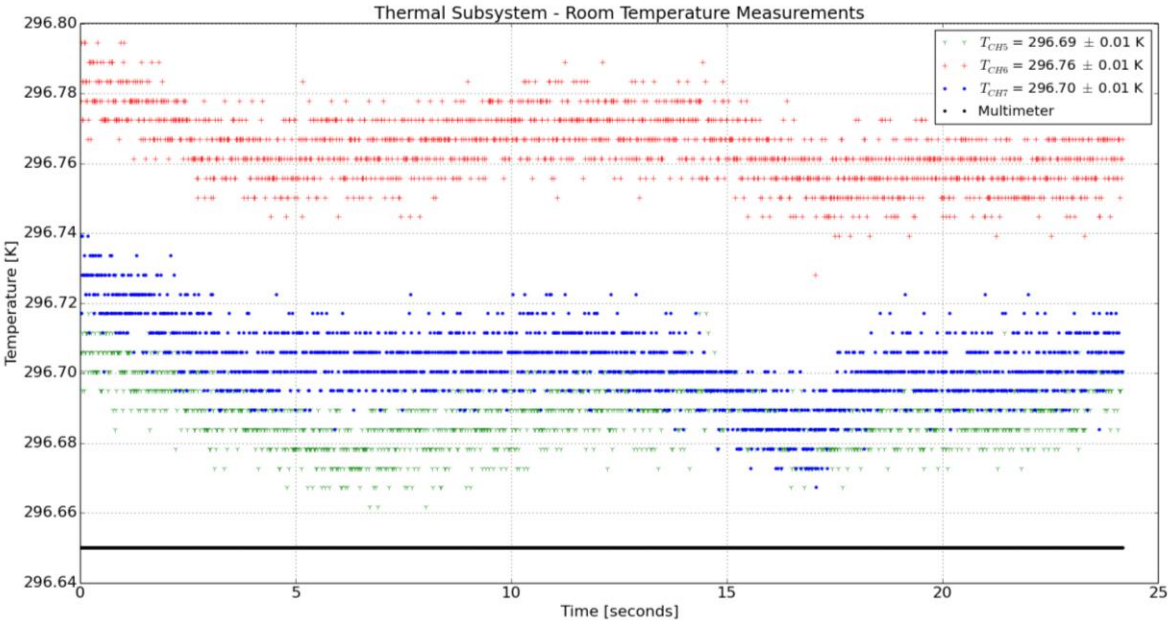

Figure 39: Thermistor data acquisition using the analog input channels of the 18-bit SAR ADC AD7609.

4.8.3.5 Testing the Connectors for Analog Radiometric Signals

There are Micro-D, MSSS and SSMB type connectors on the prototype C&DH board as given in Figure 26. The noise performance of the connectors can directly affect the noise performance of the radiometric acquisition as it has been defined at the ADC input-referred noise section. Therefore, an input-referred noise test discussed in the previous section for the radiometric acquisition testing has been applied to check the performance of the connectors. Hence, a battery is connected to the analog input pins of the same ADC but interfacing with different connectors for testing. Numerous numbers of samples are collected through each channel for the ADS1178 and AD7606 ADCs. The measured average standard deviation for each channel in

μV for ADS1178 and AD7606 is shown in Figure 40 for all 3 different types of connectors. The results show that the noise performance of the connectors is similar both for ADS1178 and AD7606. This indicates that the noise immunity of all the

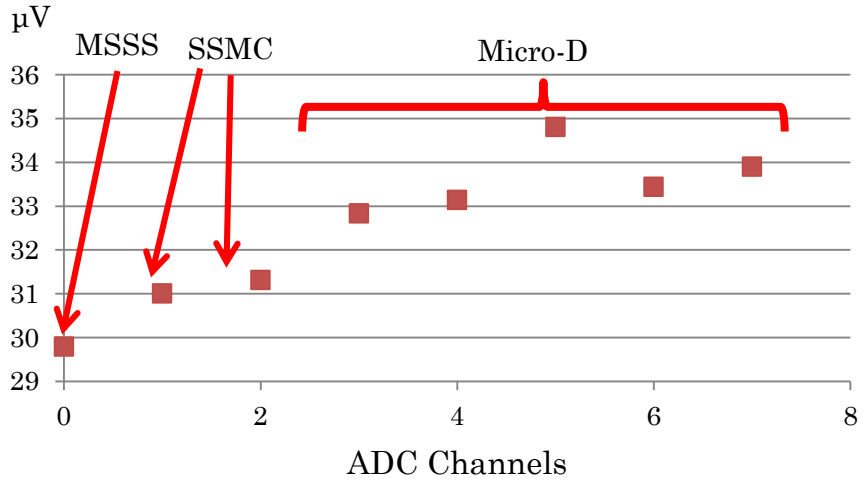

a)

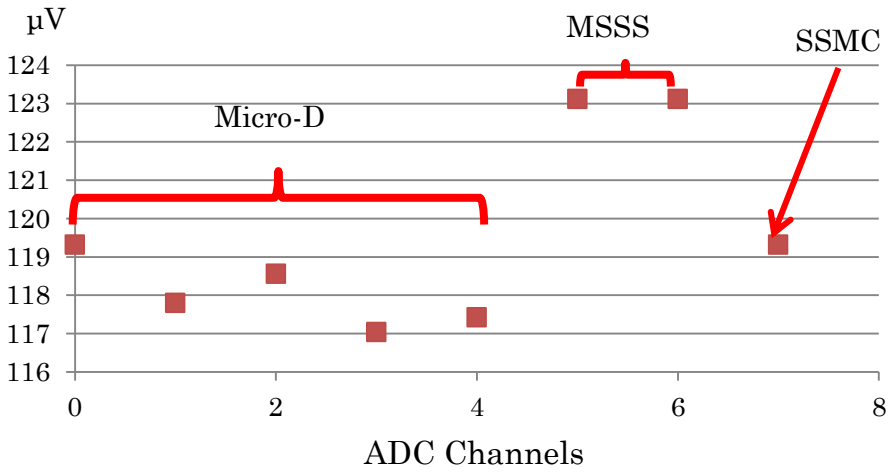

b)

Figure 40: ADC noise test: Effect of connector typr on the acquisition performance. a) ADS1178, b) AD7606.

connectors used in the design is similar when they are being tested with a battery as the source of the acquisition.

4.9. C&DH Final Boards Design and Testing

This section explains the design and testing of the final C&DH boards.

4.9.1 Final Board Design Considerations

The design considerations are determined based on the functionality, integration and environmental testing.

The functional testing and results are discussed in the previous section. All the ADCs tested meet the functional requirements of the TWICE C&DH system. The Micro-D connector is selected for the final design due to physical size requirements of the system since all the connectors have similar functional performance.

The radiation testing results are analyzed in Chapter 5. Based on the discussion given, ADS1178 is not suitable for TWICE design since destructive events are observed. The PROASIC3E/L FPGA, AD7606 and INA3221 have acceptable radiation performance for the TWICE instrument on-orbit operation.

4.9.2 Bit Analysis – Revisit

The calculations presented in the prototype design section can be further extended using the TWICE radiometer parameters since the full-range span assumption made for the system noise temperature cannot be held true. Also, an analysis is required based on the final ADC selection for the final board design to optimize the system performance by using the test results.

Our goal is to extend the bit analysis for the calculation of the ADC bit resolution in terms of temperature instead of voltage by using the expected receiver noise temperature and the output voltage specifications. Our consideration for this analysis is to compare the bit resolution in temperature with the expected NEΔT performance of the TWICE receivers.

In laboratory conditions, the ambient target measurements at room temperature (295 K) and liquid nitrogen source measurements as a cold target (77 K) can be used to estimate the dynamic range of the receiver output. Thus, one can express the dynamic range of the radiometer output voltage as:

$$\Delta V_{radiometer} = V_{amb} - V_{cold} \tag{IV.10}$$

where V_{amb} is the radiometer output voltage when looking at the ambient target at room temperature and V_{cold} is the measurements with liquid nitrogen source. Please note that the on-orbit operational dynamic range of the instrument is different than the dynamic range used in the laboratory measurements since the instrument scans the cold sky reflector for cosmic background radiometric measurements at 2.7 K. Thus, one should estimate the on-orbit dynamic range to guarantee that it is within the ADC analog input range. Using the hot and cold target measurements, the radiometric gain in Kelvin per Volts can be expressed as:

$$G = \frac{T_{amb} - T_{cold}}{V_{amb} - V_{cold}} \ [\mathrm{K/V}] \tag{IV.11}$$

One Kelvin temperature in terms of voltage can be expressed as:

$$1\ \mathrm{K} = 1/\mathrm{G} \tag{IV.12}$$

The ADC bit resolution for a 16-bit ADC is calculated using the definition given in Equation (IV.3) as:

$$V_{bit} = \frac{10}{2^{16}} = 152\ [\mu\mathrm{V}] \tag{IV.13}$$

The expected bit resolution in temperature [Kelvin] is calculated for each TWICE receiver based on the expected receiver noise temperature and the dynamic range at the voltage output. The results are summarized in Table 18 for each TWICE radiometer. The expected resolution is less than 0.1 Kelvin for all channels except 670 GHz receiver where it has 156 mK bit resolution. Thus, the radiometric

Table 18: Expected bit resolution in temperature for the TWICE radiometers for the 16-bit ΔΣ ADC (AD7606).

Radiometer	T_{rec} [K]	Expected Dynamic Range [ΔV]	Gain [K/Volt]	1 K in Volts	Bit Resolution for AD7606
118 GHz	500	1.08 V	199	5.03 mV	**30 mK**
183 GHz	1400	507 mV	424	2.36 mV	**64 mK**
240 GHz	500	1.08 V	199	5.03 mV	**30 mK**
310 GHz	700	864 mV	249	4.02 mV	**38 mK**
380 GHz	900	720 mV	299	3.35 mV	**45 mK**
670 GHz	3800	210 mV	1024	977 μV	**156 mK**

acquisition is performed at the level where it meets the design specifications for NEΔT performance.

The next section provides a brief discussion on the final design of the C&DH boards.

4.9.3 Final Board Design

The final C&DH board block diagram given in Figure 41 presents the main ICs used in the system design as well as how the system interfaces with the other subsystems of the TWICE instrument. The final C&DH board mainly consists of an FPGA, 2 16-bit SAR ADCs, the current sensing and voltage monitoring IC and connectors used for the interface.

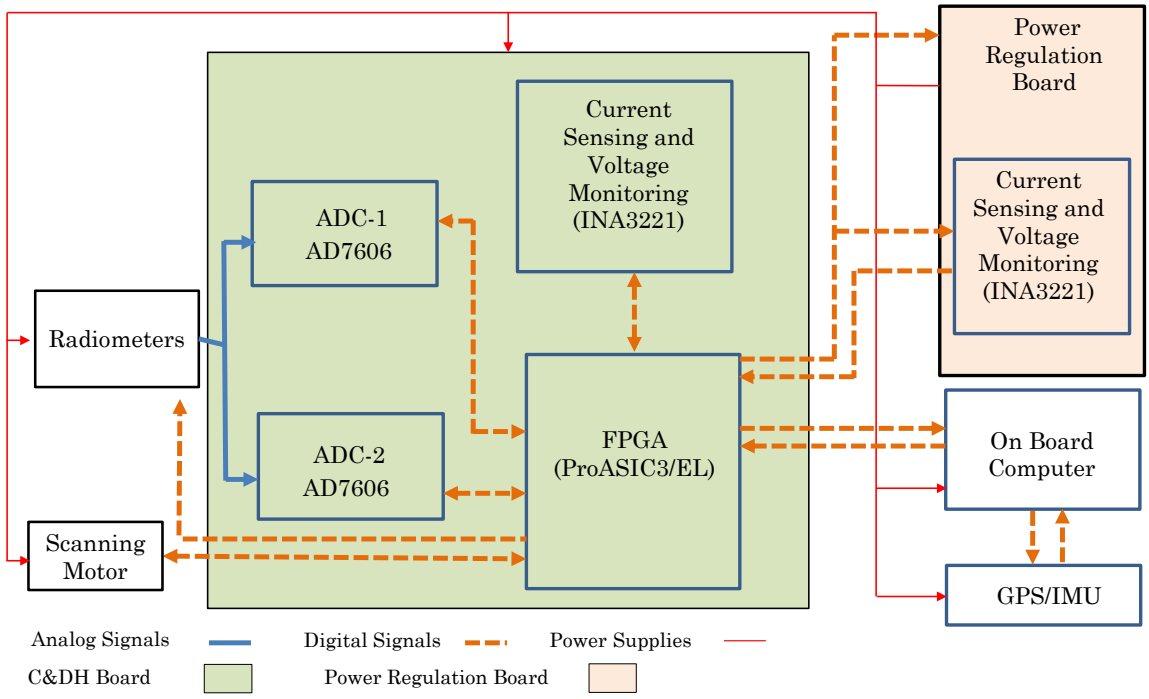

Figure 41: The final C&DH board overview showing the main ICs used in the design and how the system interfaces with the other subsystems of the TWICE instrument.

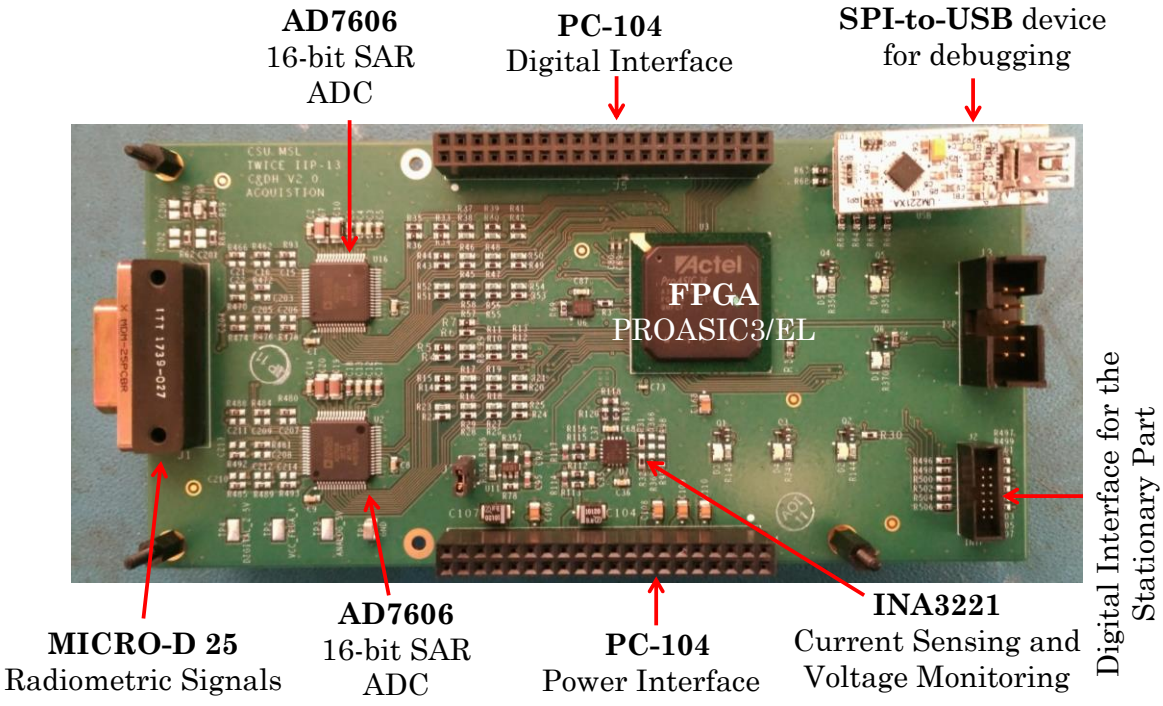

Figure 42: The top side view of the final C&DH board.

The top-layer view of the fabricated final C&DH board is given in Figure 42 . The PC/104 connectors are used for interfacing with the power regulation board. One side of the PC/104 connector is used for transmitting the regulated power to the C&DH board. The other PC/104 connector acts as a digital interface for transmitting the control signals as well as the current and voltage information of different sub-circuits acquired by INA3221s on the power regulation board.

4.9.4 The Integration of the Final C&DH with Prototype Power Regulation

The fabricated final C&DH boards have been integrated with the prototype power regulation board for the functionality and noise analysis of the final system. The test setup is illustrated in Figure 43. During the test, the final C&DH board is

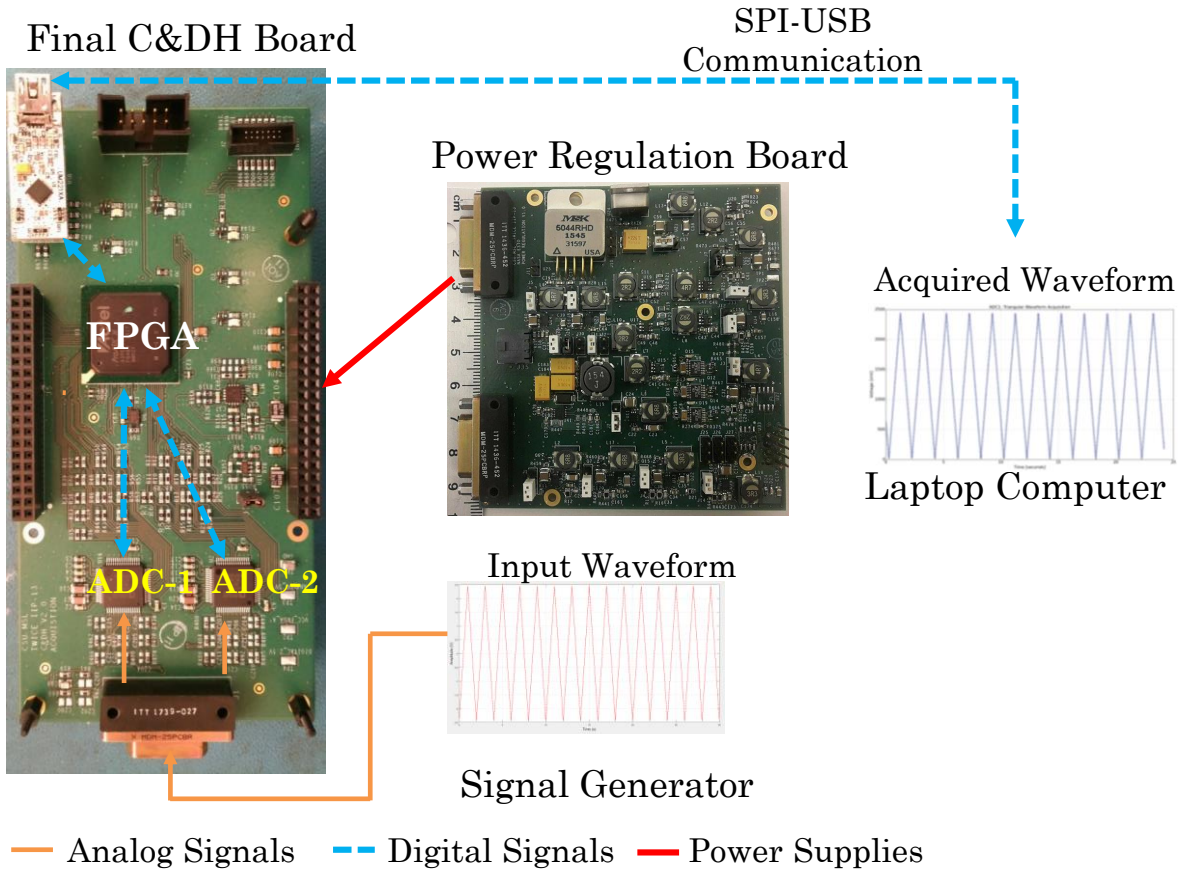

Figure 43: Testing the functionality of the final C&DH board integrated with the prototype power regulation boards.

powered with the prototype power regulation board. A saw-tooth signal waveform generated from the function generator is fed into all analog inputs of the ADCs for synchronous acquisition controlled by the FPGA. The digitized data is received on the external laptop computer from the FPGA through an SPI-to-USB communication module. The test results indicate that the VHDL programming of the FPGA and the acquisition software coded in Python running on the external laptop computer is performing well to meet the system design requirements.

The battery voltage is acquired to determine the input-referred noise level of the final C&DH system in addition to performing other functional tests on the board. For this test, a battery is connected to all analog input channels of the ADCs for simultaneous acquisition of the analog signals. The ADCs are controlled by the FPGA during the testing. The digitized data are recorded in an external laptop computer after being sent by the FPGA through SPI-USB communication. Figure 44 shows the acquired data from the battery in counts for all eight analog channels of an ADC on the final C&DH board. The results indicate that for all the channels, the standard deviation of the acquired data is around 0.5 counts. This indicates that the input-referred noise level of the final C&DH boards is negligible. This, in turn,

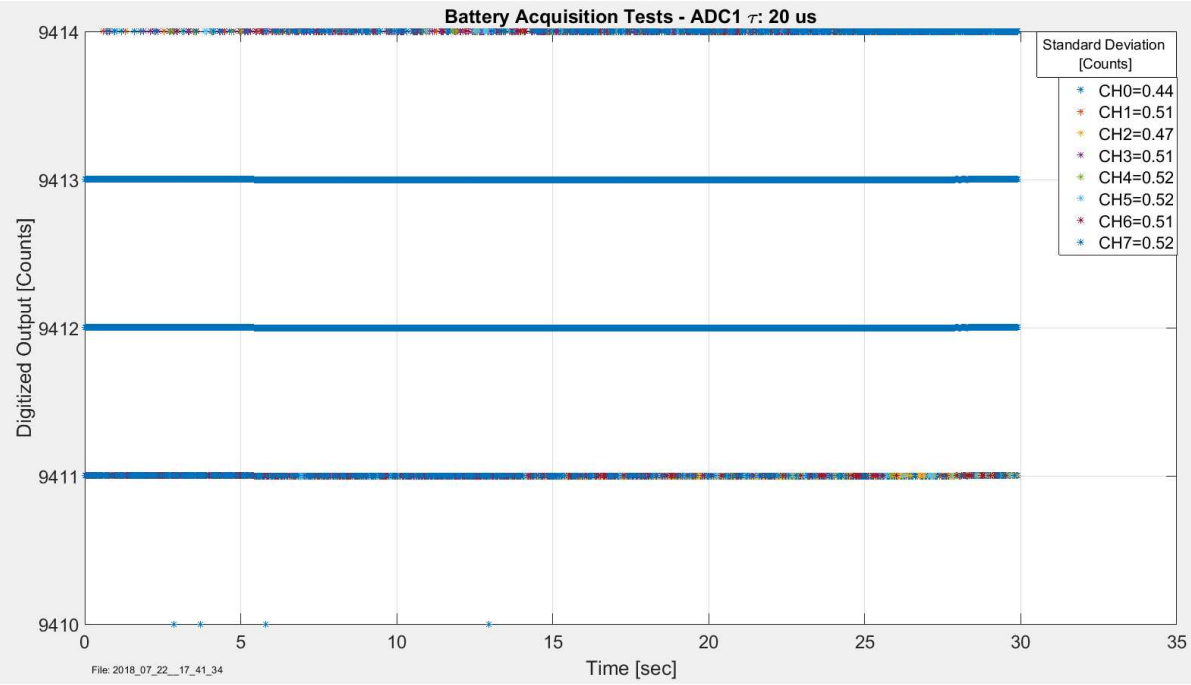

Figure 44: The battery acquisition test results are shown with the measured standard deviation for each channel for one of the ADCs on the final C&DH board.

shows that the design does not add any significant noise to the radiometric measurements.

The power consumption of the final C&DH board is also analyzed in addition to functional and noise performance. The power consumption of the C&DH board is measured as around 250 mW when the board is fully functional. During this test, two indicator LEDs were on, ADCs were continuously performing radiometric acquisition and FPGA was operational.

4.10. Power Regulation Boards Final Design and Testing

The design specifications given in Table 9 are also used for the final power regulation board design. However, the voltage regulator ICs failed or resulted in high output voltage transients during the radiation testing are not considered for the final design. A more detailed discussion on the radiation testing of the voltage regulator ICs are provided in Chapter V.

The final power regulation board design uses only commercial-off-the shelf (COTS) parts. However, the ICs used on the final power regulation board are resistant to single-event latch-up and any other destructive events at TWICE orbital altitude. Furthermore, each front-end block can be separately turned on or off using the analog switches controlled by the FPGA on the C&DH board without affecting the operational capability of the other subsystems.

The top-layer view of the fabricated final power regulation board is given in Figure 45. The PC/104 connectors are used for interfacing with the C&DH board as described in the previous section. The C&DH power interface given in Figure 45 is

used to transmit the regulated power to the C&DH board while the C&DH digital interface transmits the control signals as well as the current and voltage information of different sub-circuits acquired by INA3221s on the power regulation board. The regulated power is sent to the front-end receivers through a Micro-D connector. The CubeSat bus power is the input power of the power regulation system.

The final power regulation board is stacked with the final C&DH board through mounting holes and PC/104 type connectors. Therefore, the bottom layer of the power regulation board is designed to shield noisy signals from the C&DH board. As shown in Figure 46, none of the ICs and other discrete components used in the design is mounted on the bottom layer of the board except some discrete

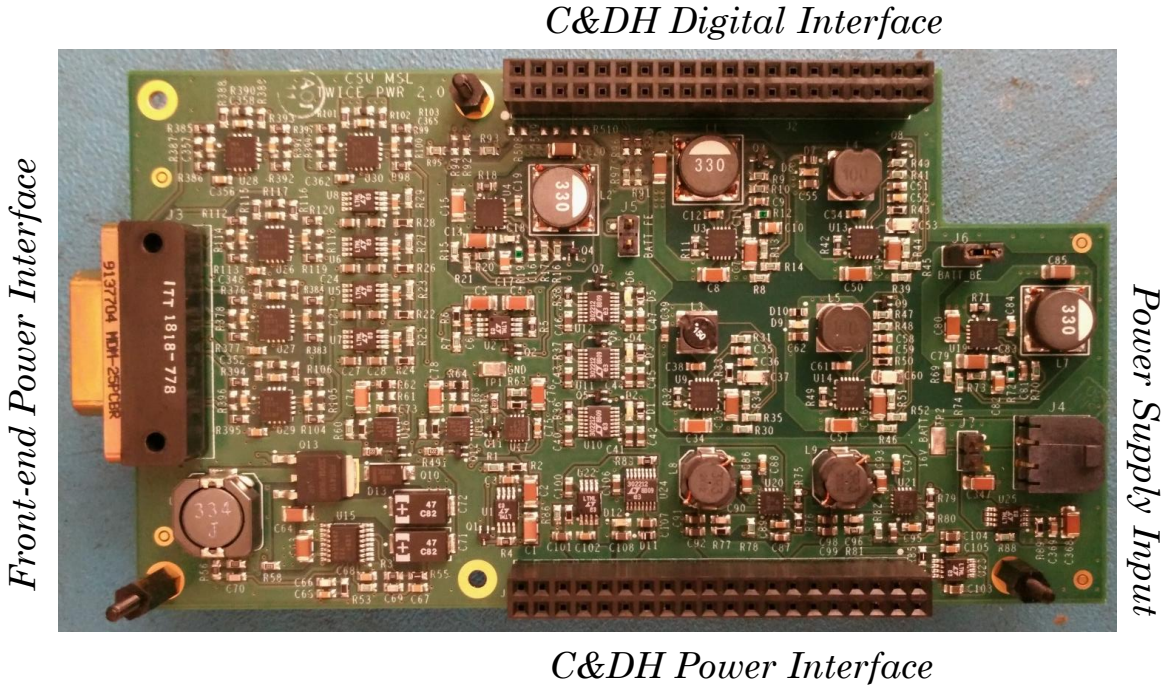

Figure 45: Top side view of the final power regulation board.

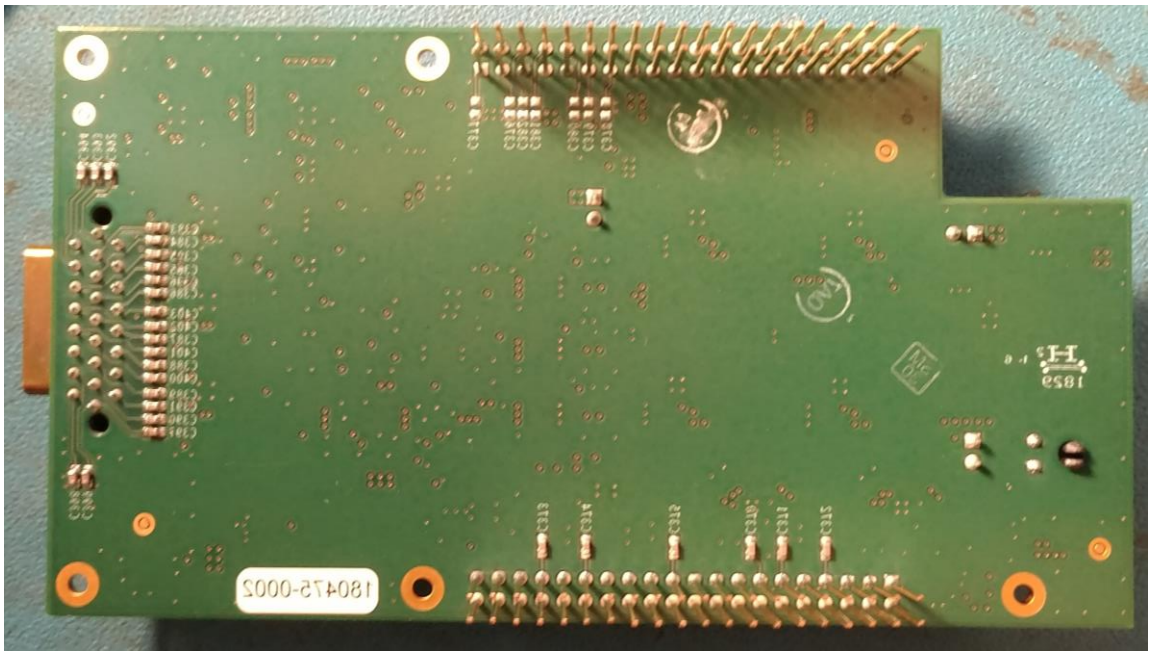

Figure 46: Bottom side view of the final power regulation board.

components for noise filtering. In addition, the noisy high-frequency switching signals on the power regulation boards are routed at the top layer to maximize the isolation of the noise generated on the power regulation board from the sensitive parts of the C&DH board performing radiometric acquisition.

The functionality of the power regulation board is checked separately before it is integrated with the final C&DH board. The regulated power for each specific device of the TWICE instrument is verified at the output of the power regulation board. A demonstration board with dummy resistors mimicking the voltage and current characteristics of the TWICE subsystems is connected at the output of the power regulation board. A low-ripple and stable output waveform is verified at the output when the system is fully operational.

4.11. Integrated Final C&DH and Power System Testing

The manufactured final C&DH and power regulation boards are stacked through PC/104 type connects and five mounting holes as shown in Figure 47. The horizontal dimensions of the power regulation board are determined in a way that the stacking of two boards will allow the connectors for external interfaces to be mounted easily on the board. These external connectors including the SPI-to-USB interface, FPGA programmer cable of FLASHPRO4 and the connector for transmitting the signals for the stationary part interface are shown on the right side of Figure 47. In addition, the 3-D dimensions of the final integrated system are also small enough to enable this system to fit into C&DH housing of the TWICE instrument as shown in the CAD model given in Figure 13.

The functionality and the noise performance of the integrated final C&DH and power regulation boards are analyzed before integration of the system with TWICE

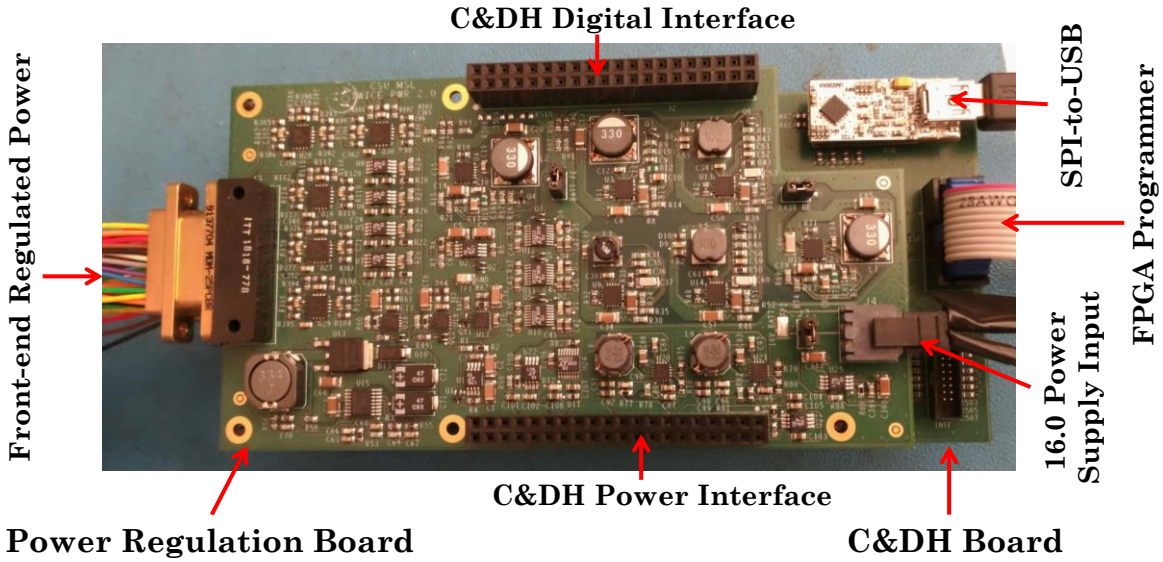

Figure 47: Top view of the integrated final C&DH and power regulation boards.

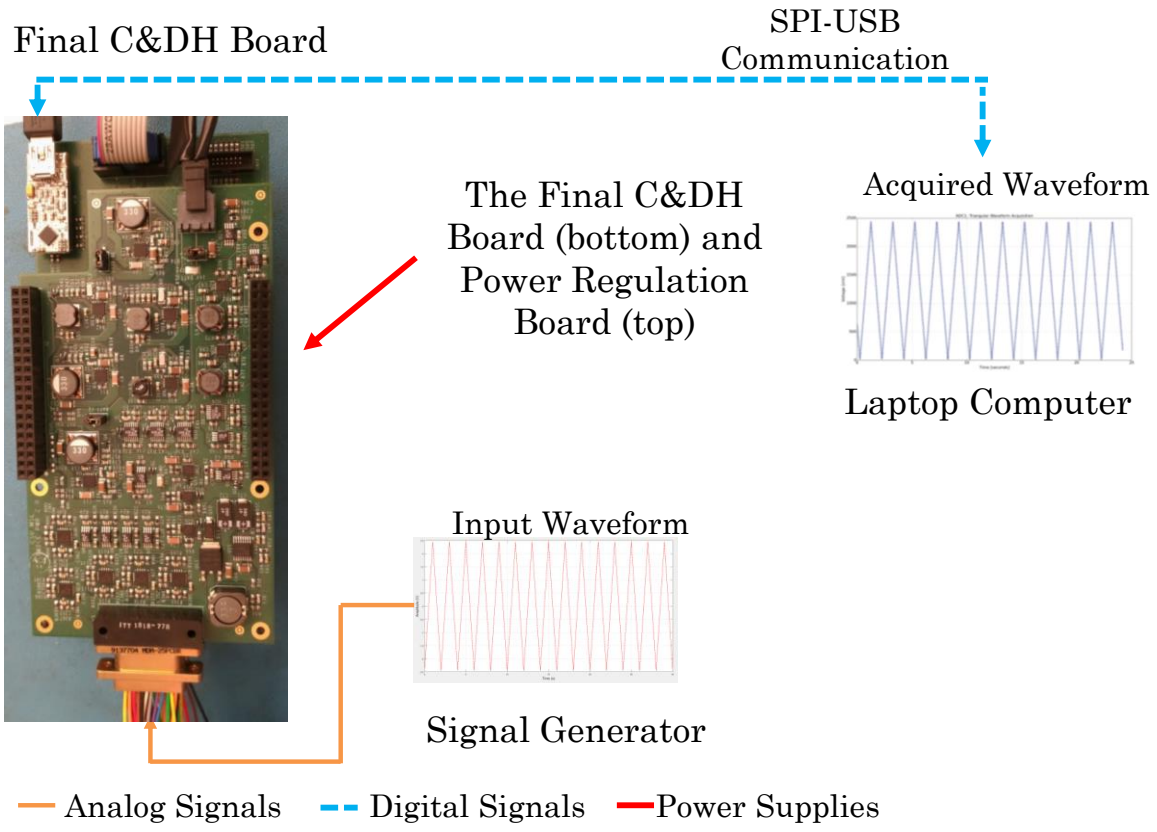

Figure 48: Testing the functionality of the integrated final C&DH and power regulation boards.

receivers. The test setup for the functionality testing of the integrated system is given in Figure 48. During the functionality test, the final C&DH board is powered from the final power regulation board which is stacked at the top of the C&DH. For this test, a saw-tooth waveform is generated from the function generated for the synchronized simultaneous digital acquisition through all 16 analog channels of the C&DH board. The goal of this test not only to check the hardware design of two boards, but also verify that the final VHDL programming of the VHDL and the acquisition software in Python are compatible to each other and they both meet the

design requirements. The acquired digital signals by the ADCs which are controlled by the FPGA are transferred to an external laptop computer through SPI-to-USB communication. The received data is successfully verified on the external laptop computer.

The next consideration is to check the noise performance of the integrated system. The stacking scheme can couple noise on the radiometric acquisition. As explained in the final power regulation board design section, the isolation of the noisy signals from the sensitive parts of the C&DH is performed at the design stage. The goal is to perform a noise testing and compare them with the results of the integration of the final C&DH board with the prototype power regulation board.

For the noise test, a similar test setup is used with the on given in Figure 48 except a battery is used as a source for the analog input channels instead of a function generator. The acquired samples are given in Figure 49 with the standard deviations are noted for each channels. The results show that all the analog channels of the ADC have RMS noise levels around 0.4 counts. A comparison of the results presented in Figure 49 with those given in Figure 44 shows that the final integrated system has better noise performance. This, in turn, demonstrates that there is a high level of noise isolation between two boards.

The final test conducted on the final integrated system is to verify the switching signal of the 670 GHz receiver generated by the FPGA on the C&DH board. The goal is not only check the suitability of the signal waveform to operate 670 GHz 1st LNA block, but also verify the timing of the signal with the acquisition from the

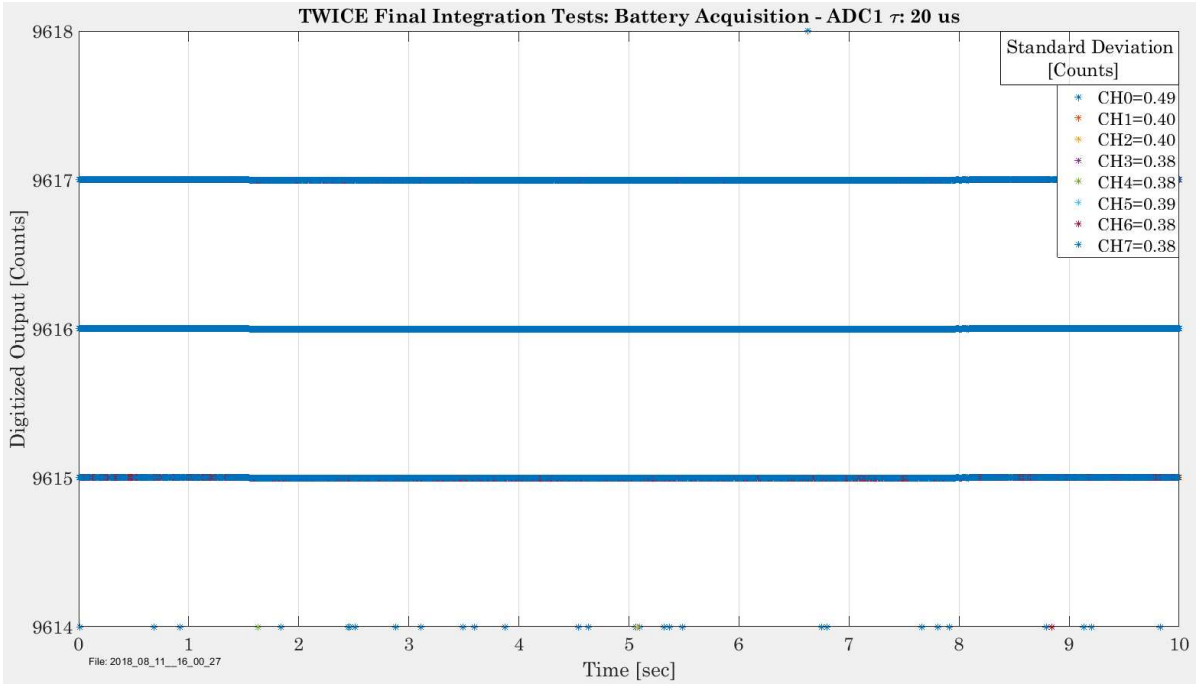

Figure 49: Testing the noise performance on the radiometric acquisitions of the integrated final C&DH and power regulation boards.

ADCs. The scope output of the switching signal is provided in Figure 50. An RC filter is mounted on the C&DH board close to the output pin of the switching signal to provide a clean square waveform as given in Figure 50. The filter removes the overshoots and undershoots in the signal. However, the filter slows down the rise and fall time of the signal waveform from 15 ns to 450 ns. When considered with 15 µs measured response time of the 670 GHz receiver to the switching signal, a 400 ns delay in the signal rise and fall times is negligible for our case.

The switching signal is input to the analog channels of the radiometric acquisition circuit on the C&DH board for verification of the timing of the signals. During the test, synchronized simultaneous acquisition of the switching signal by the ADCs

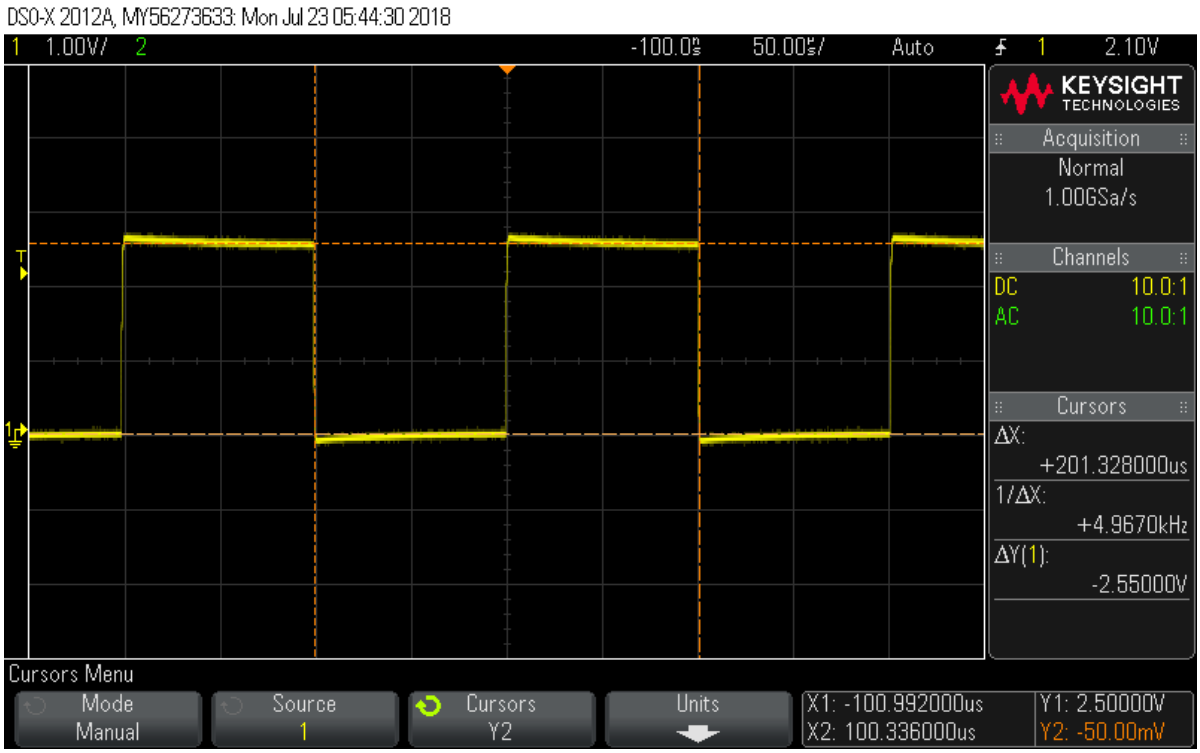

Figure 50: Oscilloscope measurement output of the 670 GHz LNA switching signal generated from the FPGA.

controlled by the FPGA is performed. The acquired signals are filtered inside the FPGA before they transmitted to the external laptop computer. A 1 ms window of the received signal waveform is plotted in Figure 51. The testing of timing has shown that the signal generation and the radiometric acquisition are successfully synchronized by the FPGA.

The integration testing of the final boards shows that the boards are ready for the receiver integration and end-to-end receiver operation. The receiver characterization is explained in Chapter VI.

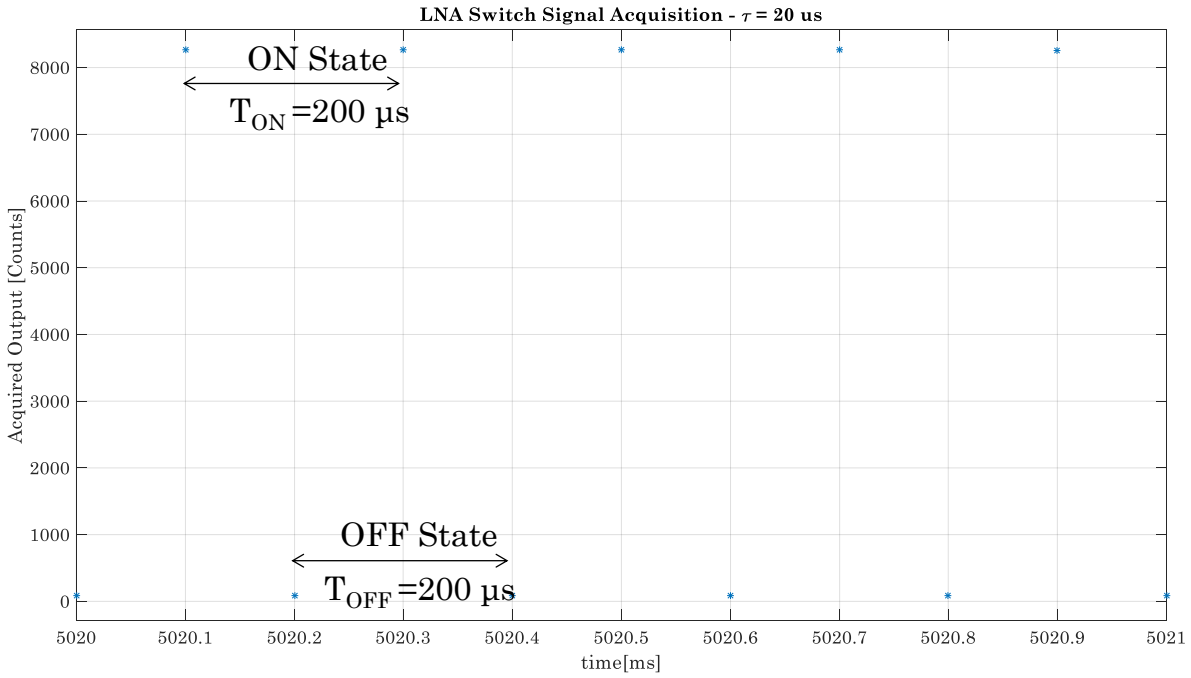

Figure 51: The 670 GHz switching signal acquisition by the ADCs to verify the timing of the radiometric acquisition.

4.12. Conclusions

A low-noise, low-power consumption Command and Data Handling (C&DH) system of TWICE has been designed. The primary functions of the C&DH system are the synchronous simultaneous acquisition of the radiometric signals and system health data, controlling the on/off switching of the first transistor stage of the first 670 GHz low-noise amplifier (LNA) block synchronized with radiometric acquisition, and interfacing with the other subsystems of the TWICE instrument. To accommodate the 6U CubeSat form factor, the C&DH subsystem needs to meet stringent CubeSat requirements of mass, volume and power consumption, in addition to meeting functional requirements. A detailed system analysis is

performed to determine the design parameters for the optimum design architecture. On the other hand, the power regulation boards are designed to reliably provide the required current and voltages to other subsystems of TWICE instrument at low output voltage swing and high efficiency.

The functional tests and analysis have been successfully conducted on each separate design element as well as the integrated system. The noise performance of radiometric acquisition system is analyzed. The tests have shown that the final integrated C&DH and power regulation boards meet the size, weight and mass requirements of the TWICE instrument in addition to functional and environmental requirements.

Chapter V On-Orbit Instrument Reliability

The instrument reliability based on the radiation testing is explained in this chapter. The designed TWICE radiometer 6U-class satellite instrument should have reliable on-orbit operation in addition to fulfilling the functional requirements.

Radiation related reliability issues have been analyzed. A heavy-ion radiation testing has been performed to characterize the radiation performance of the critical commercial-off-the shelf (COTS) parts under LEO-like radiation environment. The radiation test results have been analyzed to estimate on-orbit failure rate. System level radiation related failure mitigation techniques have been proposed to improve the system reliability.

5.1. Introduction

The electronics systems for a space application should be designed based on severe temperature and radiation environment conditions in space. The thermal fluctuations within the system can be prevented up to some degree with employing a thermal controlled environment for the space electronic. Also, the parts can be easily selected from those having suitable operating temperature range for the space conditions as defined in the datasheet of the parts. The on-orbit thermal conditions of space electronics can be emulated at a thermal and vacuum chamber in the prelaunch phase.

The system reliability due to radiation effects in space requires special attention. A similar approach with the thermal reliability cannot be applied to the radiation

reliability since the space qualified parts sold in the market have limited availability at high cost with long lead times. The most of the state of the art part sold in the market do not have space qualified version. In addition, a system level design consideration might be required even though a design is made with space qualified parts for critical missions. Thus, a methodology called radiation hardness assurance is required to ensure the reliability of the electronics of any space system under harsh space radiation environment [65].

The radiation hardness assurance includes analyzes of the space environment conditions for a specific mission, the system and device level radiation analysis of the electronic systems, part selection and studying electronic device failures and failure mitigation techniques [66], [67].

5.2. Radiation Effects on Electronics

The radiation effects on electronics can be studied in three main categories as single event effect, total ionizing dose effect and displacement damage effect according to the type of the effect they result in on electronic devices.

5.2.1 Total Ionizing Dose Effects

A cumulative long-term degradation of the device due to ionizing radiation exposure is given by the total ionizing dose (TID). The amount of accumulation on the device is expressed in units of rad per silicon. The degradation effect on the device functionality of TID depends on the amount of dose accumulated. Therefore, TID characteristics of a mission should be analyzed based on the expected lifetime of the

instrument. TID effects can be minimized by applying proper shielding on the electronic systems by blocking the particles to reach to the device silicon [68], [69].

TID testing of the devices are performed on the accelerated particle testing facilities where the on-orbit dose accumulation of a space mission is mimicked in much shorter period of time to see the device response under some certain dose of TID accumulation [65].

5.2.2 Single Event Effects

When an ion impacts on a semiconductor, it can generate electron-hole pairs through direct ionization. In that case, the energy lost by the ion through the path length is known as a linear energy transfer (LET). If the charge deposited on the semiconductor exceeds the critical charge limit, it can disrupt the functionality of the electronic circuit. These unwanted effects of radiation on electronic devices are called single-event effects (SEEs). They are called as “single event” since they occur as a result of single particle reactions [70]. Proton particles may also cause SEEs. The proton may generate SEE due to proton ionization but it is so rare since protons can produce a very small amount of ionization on the particle. However, proton induced SEEs occur as a result of nuclear reactions that they cause on the device. SEEs may occur because of ionization particles generated on the nuclear reactions. The SEE generation mechanisms for a heavy ion and a proton are illustrated graphically in Figure 52 for a comparison.

SEEs are completely random events, which can occur at any time starting from the launch of the instrument to the end of the mission lifetime. As a result, the SEEs

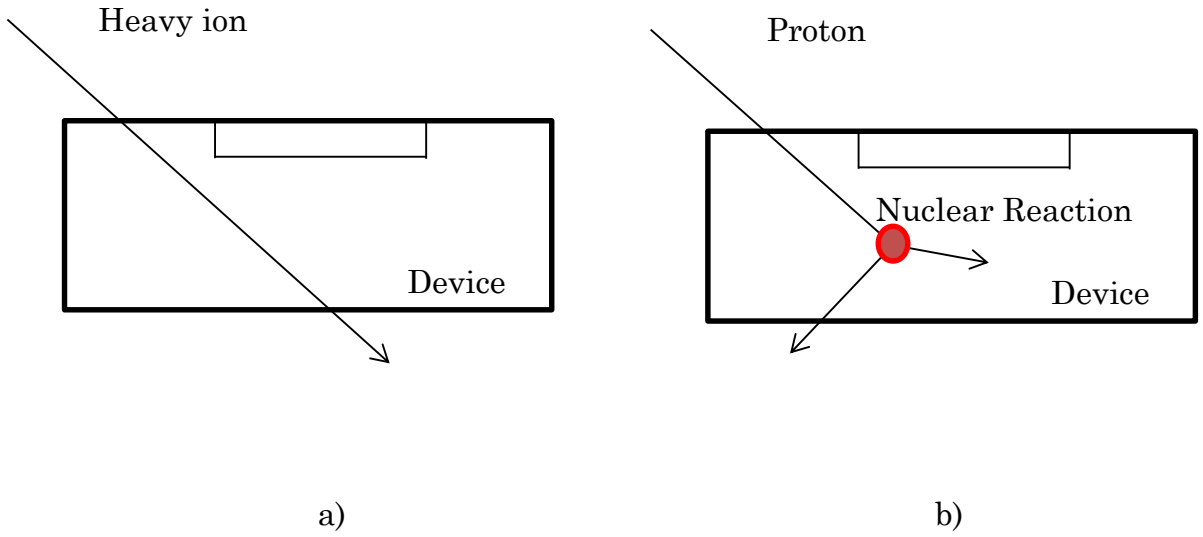

Figure 52: SEE mechanisms. a) SEEs due to passage of a heavy ion through the electronic device, b) SEE due to ionization of the produced ions as a result of a nuclear reaction of proton hitting on the device.

are expressed in terms of probability not in dose units used in TID effects. SEEs cannot be prevented with shielding where it is effectively used to prevent TID related errors. Furthermore, SEEs occur for a short-period of time but their effects might be permanent [65].

SEEs can be destructive or non-destructive depending on the device structure and the level of ionization. Definitions related to SEEs will be provided first before going into the types of the SEEs on the devices [71], [72], [73].

5.2.2.1 Definitions

- **Flux:** It is the number of particles passing though unit area perpendicular to the incoming beam per unit time. It is expressed in units of [ions $cm^{-2}s^{-1}$].

- **Fluence:** The integral of flux with respect to time yields fluence. In other words, it is the number of particles passing through unit area perpendicular to the incoming beam for a given time. It is expressed in units of [ions cm^{-2}].
- **Linear Energy Transfer (LET)**: It is the amount of energy lost by the particle per unit length as it travels through a material. It is expressed in units of [MeV cm^2 mg^{-1}]. It is assumed that the amount of energy deposited on the material per unit path length equals to the energy lost by the particle [74]. LET is formulized as:

$$LET = -\frac{1}{\rho}\frac{dE}{dx} \text{ [MeV cm}^2\text{ mg}^{-1}\text{]} \tag{V.1}$$

where ρ is the density of the material in [mg/ cm^3] and x is the path length.

LET is an important parameter for the analysis of SEE events since it defines the amount of energy deposited on the material. However, the charge deposited needs to exceed a critical limit to cause an SEE as it is explained in the previous section. This minimum LET level is called as the threshold LET. The charge deposited also depends on the angle of the beam since the path length increases by the secant of the angle. In this case, it is called as the effective LET. It does not refer to a change in the LET level of the particle but change of the effect of the particle on the material due to change in the path length. However, there are some exceptions for the effective LET to be held true [75]:

a. The case where the path length that charge collection occurs is a comparable fraction of the total range of the particle travels resulting in LET variations along the path.
b. The case where the charge collection occurs mostly by diffusion due to the spherical volume resulting in no variation of LET with angle.
c. The case where the device aspect ratio of the volume is small resulting in a complex angular dependency.
d. The case where the device package blocks the ions when the device is rotated.
e. The case where the ions have insufficient range in the particle traveling through devices having charge collection at some depth. Especially for p-substrates, this could be an issue where the charge collection may occur at 60 µm depth or more.

- **SEE Cross-section:** The SEE cross-section is an important tool to make predictions for the number of SEE events may occur for a specific mission under specified environmental conditions. In other words, SEE cross-section might be named as the radiation characteristics of the specific device for the laboratory conditions being tested.

  SEE cross-section is expressed as the ratio of the number of events to the effective fluence for the given LET level:

$$\sigma = \frac{number\ of\ events}{fluence\ x\ cos\theta}\ [\frac{\text{cm}^2}{\text{device}}] \qquad \text{(V.2)}$$

where θ is the angle of the beam with respect to normal direction of the device under test. The SEE cross-section is plotted against the LET level of the particle that the device being tested with.

The cross-section depends on operation conditions of the device under test such as temperature and electric bias. The number of observed events may be increased at elevated temperatures resulting in a larger cross-section.

- **Sensitive Volume:** It is referred as the device volume where the charge is being collected. The sensitive volume is much larger in lateral directions than in vertical dimension for electronic devices.

  The device under test can have more than one sensitive volume. Treating the sensitive volume as a single large volume instead of smaller multiple volumes will generate higher events in the devices due to low-LET particles traveling along long paths in larger volumes. As a result, estimating it as a single sensitive volume might generate worst-case scenario for the device cross-section estimate. Larger sensitive volume thickness may result in an increase of the latchup LET threshold since the critical deposited energy needed for latchup will be increased [76].

5.2.2.2 Errors Due to Single Event Effects

The SEEs may lead to destructive and non-destructive events. The destructive events are named as hard errors while non-destructive events are called as soft errors. The hard errors result in permanent failure in the device functionality. The hard errors might cause physical damage to the device. The soft errors are

temporarily failures which happen a short period of device operation time. Power-reset might be required to bring back the device into operational mode from soft error depending on the error type.

a. **Single-Event Bit-Upset (SEBU):** It is the change of a bit in a register. When an ion strikes on the device, the charge deposited on the device register may cause it to change the state. If it happens at more than one bit as a result of a single ion hit, it can be named as multiple-bit upset. The event results in a soft error in the device.

b. **Single-Event Burnout (SEB):** A single-event ion may induce a localized high current state resulting in destruction of the device. Field-effect transistors (FETs) are more prone to SEBs. The resulting event is considered as a destructive SEE.

c. **Single-Event Gate Rupture (SEGR):** It is similar to SEBs. It is a breakdown and conduction path through the gate oxide of a metal oxide semiconductor FET (MOSFET) device due to strike of an ion on the device. The event is in general destructive resulting in permanent loss in the device functionality. However, the device might be recoverable in some cases after SEGR but the performance of the device is degraded in that case.

d. **Single-Event Transient (SET):** In digital circuitry, it is observed as the change in pulse-width and amplitude of the signal. For power devices such as regulators, the observed effect is a short-term increases or decreases in the voltage at the output of a regulator. They are not destructive to the device

being observed. However, they may result in destructive events on the devices that they interact [77].

e. **Single-Event Latchup (SEL):** An ion impact on a complementary metal oxide semiconductor (CMOS) device can activate a parasitic silicon-controlled rectifier (SCR) in the proximity of pn junctions in NMOS and PMOS transistors. This low-impedance SCR path formed in a CMOS device impairs the device functionality and is known as a single-event latch-up (SEL). The low-impedance path remains even when ions causing the SEL are no longer present. For non-destructive SELs, a power-on reset is required to eliminate this path and return the IC to normal operation, but the SEL may give latent damage to the IC resulting in the degradation of the device performance. However, in other cases, i.e. destructive SELs, the device is unable to operate after power cycling due to permanent loss of functionality [78].

   The CMOS devices are more susceptible to SELs due to their structure with PMOS and NMOS transistors. When an ion hits to the device, the P+/N- well junction of the device becomes forward biased. This, in turn, may cause a voltage drop across the substrate resistance if the impulse is high enough for sustaining for a long time. As a result, a parasitic p-n-p transistor is activated between the P+, N-Well and P substrate of the device. The current flowing on the activated p-n-p transistor turns on the parasitic n-p-n transistor formed between N-Well, P- and N+ of the CMOS structure. The collector of the activated n-p-n transistor drives the base of the activated p-n-

p transistor forming a self-sustaining thyristor structure. The resulting p-n-p-n thryistor in a CMOS device is shown in Figure 53 [65].

The latchup sensitivity of a device depends on the LET level of ions, the range of particle in the device and several operating conditions including temperature and electrical bias. An increase in temperature of the device reduces the effective distance between the N+, P+ and N-Well diffusion regions easing the trigger of excited carriers. As a result, the latch-up sensitivity of the device will increase with increasing the temperature. The

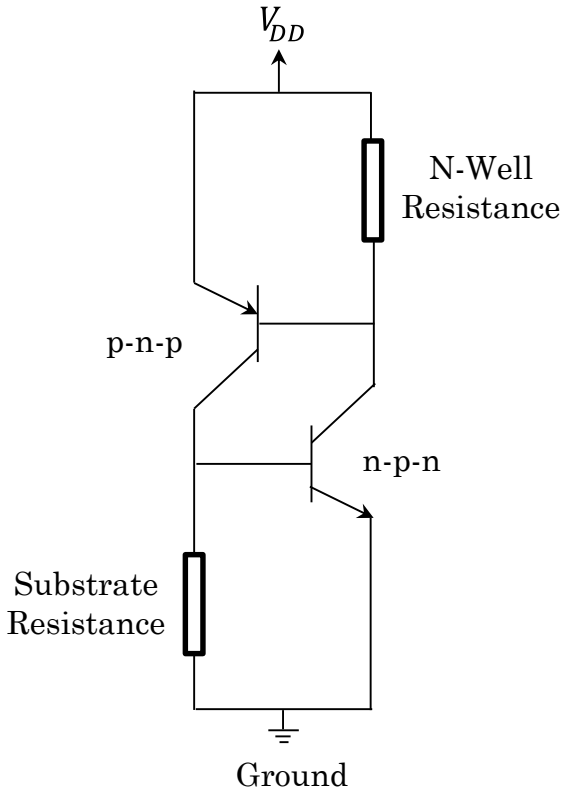

Figure 53: A p-n-p-n thyristor is activated inside a CMOS structure due to an ion strike.

threshold LET can be significantly reduced with an increase in temperature [79], [80].

Bulk CMOS structures are more prone to SELs compared to epitaxial CMOS structure since there is no separation in the junctions for diffusion into the substrate resulting in a very long charge collection path for charge generation by ions within the substrate. However in epitaxial CMOS structures, a thin epitaxial layer is placed limiting the charge collection region. On the other hand, scaling the devices with the advancement of the technology increases the SEL risk even for epitaxial structures. An isolated substrate can be inserted to isolate different regions of the CMOS structure instead of junction isolation in an epitaxial CMOS [81].

f. **Single-Event Functional Interrupt (SEFI):** It is a temporary loss of device functionality in its intended manner. An ion strike on the configuration register may result in a bit upset causing functional anomalies in the device operation. As an example, the device may get into a test mode or processor reboot. The device reconfiguration might be required, or a digital reset signal might be sent or a power-reset can be applied to exit the device from SEFI mode [66].

5.3. Space Radiation Environment

The space radiation environment can be analyzed with respect to the main sources of the radiation.

5.3.1 Geomagnetically Trapped Particles

These particles include the trapped electrons and protons in the radiation belts and heavy ions trapped in the magnetosphere. Long-term solar activity affects the level of trapped particles. One solar cycle is 11 years consisting of 7 years of solar maximum and 4 years of solar minimum. Amount of trapped particles reaches to maximum level during solar minimum [74].

The satellite missions sent into the space to investigate the trapped particles have shown that the trapped heavy ions and electrons do not have enough energy levels to cause single event effects [82]. However, they have shown that trapped protons mostly existing at inner Van Allen belt may cause SEEs [81], [83].

5.3.2 Solar Particles

Solar particles are directly emitted from the Sun reaching the orbital altitude from any direction. Solar heavy ions may cause SEEs due to ionization on the device [74]. The solar proton particles may cause SEEs but can occur at high inclination for low altitude orbits. Their concentration is directly related to solar activity since they originate at Sun. At solar minimum, they are at lower flux levels compared to their flux at solar maximum.

5.3.3 Galactic Cosmic Ray (GCR) Particles

Protons and heavy ions originating from outside of the solar system are called as GCR particles. The level of GCR particles are conversely related to solar activity since they need to fight against the solar wind to reach the interplanetary space. As

a result, the highest GCR particles occur during solar minimum. In addition, the ionization state of the particle affects their concentration. For those passing through interstellar matter become ionized. They cannot penetrate through the Earth's magnetosphere as much as ions that do not go through ionizing material.

The GCR particles are high energetic particles of heavy elements resulting in intense ionization when they pass through material. Even though GCR particles have low flux levels, they are a significant threat to space electronics.

5.3.4 TWICE Expected Radiation Environment

The TWICE 6U-class small satellite instrument is expected to be at LEO orbit with ~400 km altitude at 51.6° inclination for a 1-2 year mission lifetime as explained in Section III. At TWICE altitude level, the flux level of the trapped particles in the Van Allen belt shows largest variations increasing from 200 km to 600 km. The exposure to GCR and solar particles is gradually increasing with increased altitude. Trapped particles in the Van Allen belts gradually increase with increasing inclination around TWICE inclination. The exposure to GCR and solar particles is greatest at polar orbits since the protection of the geomagnetic fields is no longer effective. Towards the inclination angle of TWICE from polar orbits, particle concentration gets lower as a result of closer geomagnetic lines [65].

The CREME96 software is used to estimate the TWICE orbital environmental levels under various conditions [84]. The simulated flux levels at TWICE orbital altitude with respect to kinetic energy of particles for various ion species are given

in Figure 54. The environmental conditions are used with device cross-section information to estimate the event rate for on-orbit operation.

5.4. TWICE Electronics Reliability Consideration against Radiation

COTS parts have been widely used in space projects with reduced budgets, including SmallSats and CubeSats, since COTS parts normally have advantages over radiation hardened (RadHard) parts in terms of price and availability. Also, many state-of-the-art electronic components are available only as commercial grade

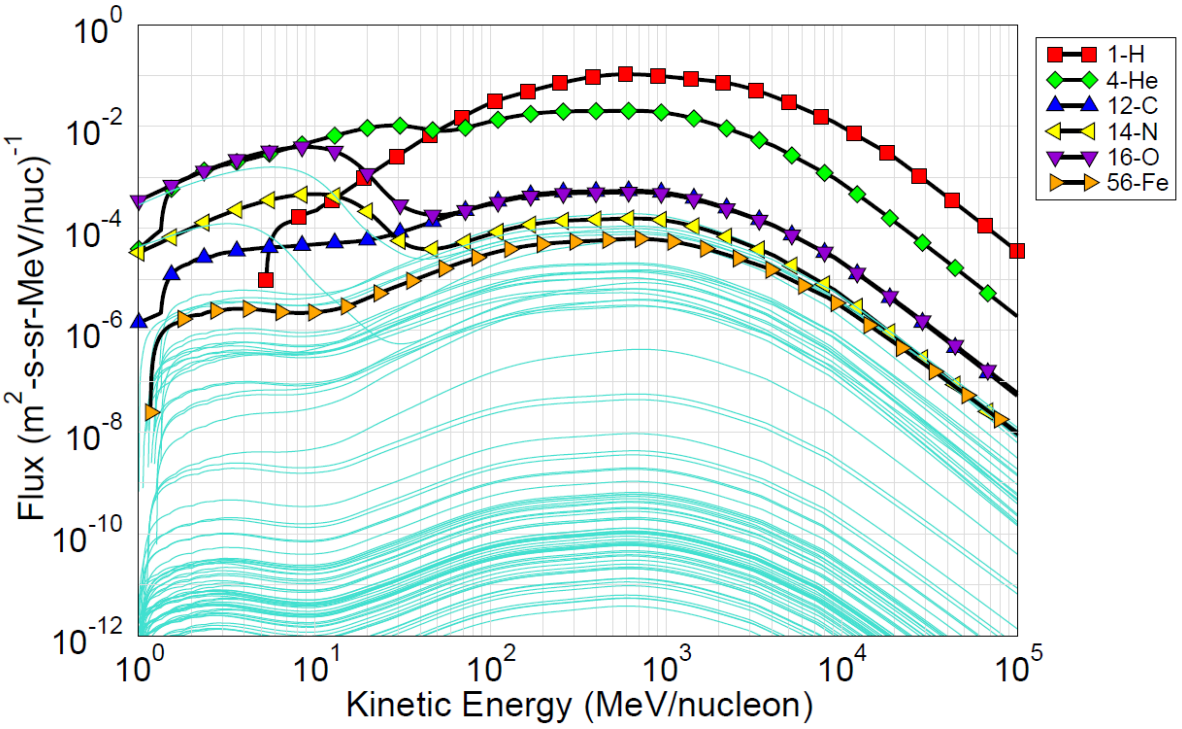

Figure 54: Estimated flux values with respec to particle kinetic energy for various ions at solar minimum for TWICE orbital parameters using CRÈME96 simulation tool.

parts. This in turn limits the number of choices and availability of advanced technology with RadHard parts. In addition, RadHard parts often have much longer lead times than COTS parts, creating another limiting factor for SmallSat projects, which typically have short development times [85].

Radiation reliability analysis is required for the TWICE electronics since it employs COTS parts in the design. The main considerations for the reliability are long term radiation dose accumulation in silicon and single particle effects.

5.4.1 Total Ionization Dose Analysis for the TWICE Electronics

The expected radiation dose accumulation on TWICE electronics with 3 mm of aluminum shielding is calculated using the SHIELDDOSE2 tool of Space Environment Information System (SPENVIS) program at 400 km circular orbit with 51.6° inclination angle [86]. The accumulation of radiation in silicon with respect to aluminum thickness used in shielding for TWICE electronics is given in Figure 55 after 1 year of orbital operation.

For TWICE C&DH housing, 3 mm aluminum thickness is considering for shielding the electronic instruments from dose accumulation. This is given as the red line on the plot given in Figure 55. Since the mission lifetime is expected to be 1-2 years, a cumulative radiation dose of much less than 5 krad (Si) is expected for TWICE electronics with the aluminum shielding [67], [87]. It is expected that the risk associated with the total ionizing dose effects is minimized with proper shielding [65], [85], [88], [89]. Therefore, only single event effects (SEE) on the components of the C&DH and power subsystems need to be considered.

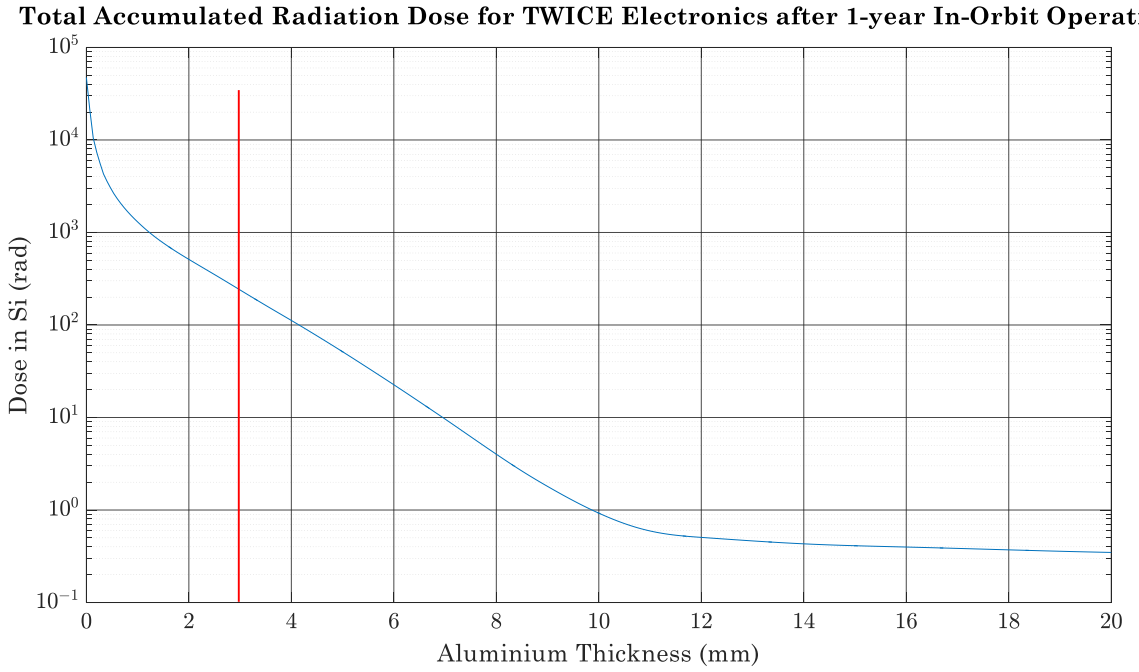

Figure 55: Estimated total accumulated radiation dose for TWICE electronics after 1 year in-orbit operation using SPENVIS program.

5.4.2 Single Event Effect Analysis for TWICE Electronics

The study for the single event effects on TWICE electronics require an extensive analysis of the electronic parts under expected radiation conditions at the TWICE orbital altitude. Heavy-ion testing is used to perform ground radiation analysis of the electronic components for the reliability analysis. The objective of heavy ion radiation testing is to determine the performance of these ICs in a LEO-like radiation environment against SEEs.

5.4.2.1 Heavy-Ion Radiation Testing Preparation

A system-level analysis has been performed for the TWICE C&DH and power subsystems to identify COTS parts that are critical for mission success as

candidates for radiation testing. Analog-to-digital converters (ADCs) in the C&DH subsystem continuously digitize analog radiometric signals with 20 μs integration time, resulting in approximately 50,000 samples per second per channel. The minimum resolution of analog-to-digital conversion of 16 bits per channel is required to provide discretization errors that are smaller than the expected radiometric resolution of TWICE [26], [39], [41]. Both Delta-Sigma (ΔΣ) and Successive Approximation Register (SAR) ADCs meet the high resolution and low sampling speed requirements for the TWICE instrument. A 16-bit ΔΣ ADC ADS1178 (TI) and a 16-bit SAR ADC AD7606 (Analog Devices) have been tested to characterize SEEs and improve the reliability of radiometric acquisition. In addition, voltage regulators provide supply voltages with the required currents to each subsystem of TWICE. Therefore, voltage regulators have been tested to characterize SEEs and improve the reliability of power regulation for TWICE subsystems. These ICs include step-down regulators, LTC3406 and LTC3621, very low-dropout (VLDO) regulator LT3022, low-noise LDO micro-power positive regulators LT1763 and LT1962, and a negative regulator LT1964 by Linear Technology. In addition, current sensing and voltage monitoring devices (INA3221s) continuously check for current and voltage anomalies in the TWICE subsystems to improve system reliability. The selected parts and their properties are summarized in Table 19.

The ground testing with heavy-ions require other considerations since the ground testing facilities do not have exactly the same radiation environment as it is in

space. Therefore, the lid of each IC was removed to allow low-energy ions to penetrate into the SEE sensitive part of the device during ground radiation testing [73]. Figure 56 shows a photo of the AD7606 ADC IC after lid removal.

The SEEs are previously explained in detail in single event effects section under radiation effects on electronics. Each type of SEE may require a different test

Table 19: Critical COTS parts in TWICE C&DH subsystem for heavy ion testing at the Texas A&M Cyclotron Institute Radiation Effects Facility.

Part Number	Function	Vendor	Properties
ADS1178	ΔΣ ADC	Texas Instruments	16-bit, 8-channel simultaneous sampling, differential
AD7606	SAR ADC	Analog Devices	16-bit, 8-channel simultaneous sampling, single-ended
INA3221	Current Sensing And Voltage Monitoring	Texas Instruments	3-channel shunt and bus voltage monitor
LT1763	Linear Regulator	Linear Technology	Low-noise, low-dropout, micro-power
LT1962	Linear Regulator	Linear Technology	Low-noise, low-dropout micro-power
LT1964	Linear Regulator	Linear Technology	Low-noise, low-dropout negative micro-power
LT3022	Linear Regulator	Linear Technology	Very low-dropout
LTC3406	Switching Regulator	Linear Technology	Synchronous step-down
LTC3621	Switching Regulator	Linear Technology	Synchronous step-down

methodology to detect and investigate the failure. Also, for each specific IC, not all SEEs are concern based on the design architecture of the IC and the functionality of the IC within the TWICE instrument. Therefore, for each IC heavy-ion testing, different SEE considerations will be employed.

SEBUs observed on the acquired data from analog to digital converters is not a concern for the TWICE project since the acquired data is not used in any critical hardware part. As an example, the case where high expected SEBU event rate for the on-orbit operation corresponding to one event per day will be compensated by

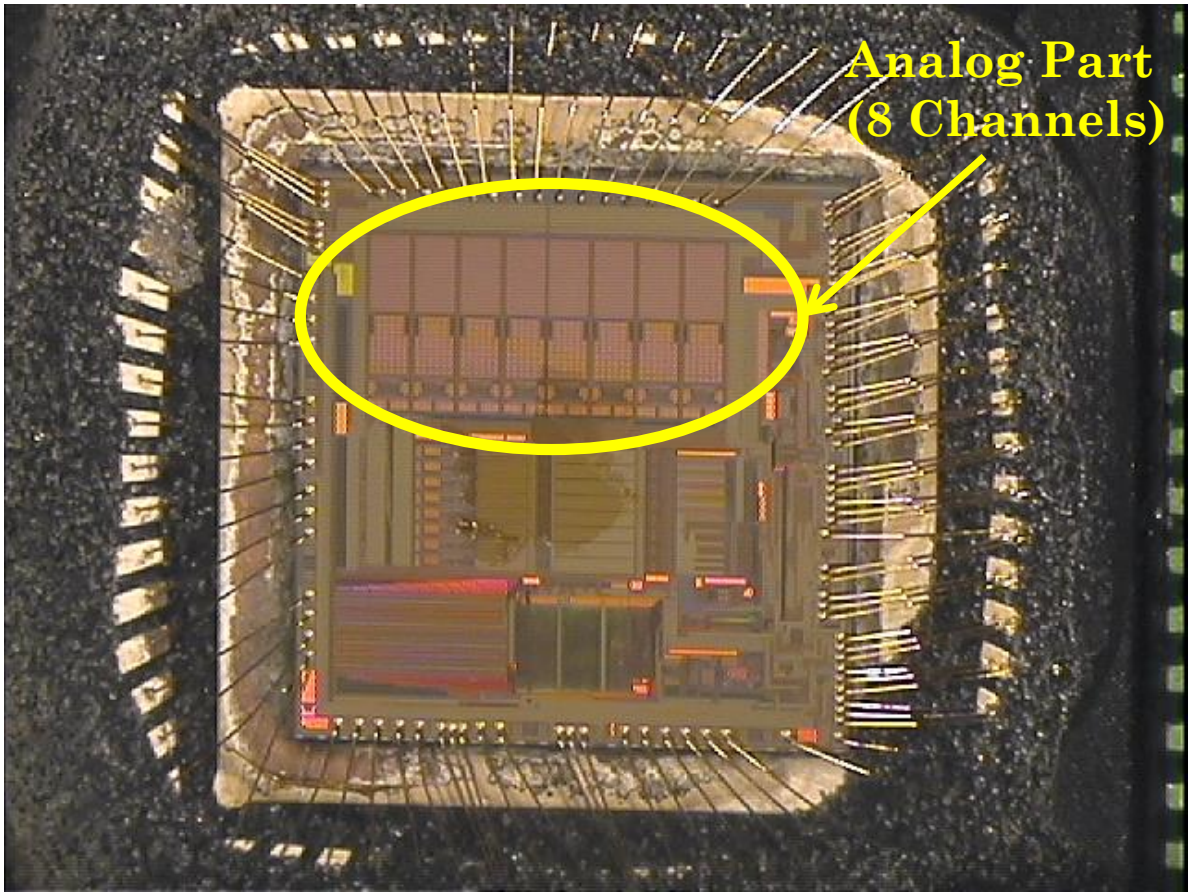

Figure 56: Photo of AD7606 IC after package lid removal by decapsulation.

just ignoring the distorted acquired radiometric sample out of millions of samples acquired per day. However, the SELs are critical for ADC operational capability considering their CMOS structure since SELs might be destructive for the device. For voltage regulators, our main consideration is the transients at the regulated output voltage in addition to destructive events could be observed on these devices. The transients at the output of a voltage regulator may damage the device being supplied from the regulator. Therefore, a reliable system should not have large transients at the output to protect other systems. For current sensing and voltage monitoring devices, the main consideration is the upsets can be observed on the communication and configuration registers in addition to destructive events resulting in permanent failure of the ICs. The SEFIs may occur as a result of bit upsets in the configuration registers. In addition, the bit upsets in the acquired samples are not critical for our operation since we are mostly concerned about the acquired voltage and current samples throughout some period of time instead of individual samples for improving the overall system reliability.

Heavy-ion SEE testing has been performed at the TAMU Cyclotron Institute Radiation Effects Facility in College Station, TX [90], for the ADS1178 ADC on June 2, 2016 (CSU and JPL personnel) and for the other ICs on March 13-14, 2017 (CSU personnel). International SEE testing standards (EIA/JESD57 [72] and ASTMF1192 [71]) have been followed by applying both standard ESA procedures [73] and NASA guidelines [65]. For radiation testing, the device under test has been

bombarded with 15 MeV silver (Ag) or argon (Ar) ions at normal incidence to obtain a cross-section curve to analyze the radiation characteristics of the IC.

The heavy-ion radiation testing setup requires careful consideration of the test conditions since any flaw in the test setup may result in misinterpretation of the results. The operating conditions of the ICs under test need to be determined for the worst-case operating conditions for the specific SmallSat or CubeSat mission. The radiation susceptibility characteristics of an IC determined by radiation testing are valid for the given conditions and may not be applied to another mission unless the test is performed for a broad range of operating conditions of the IC. Furthermore, the test setup needs to provide full remote access and control of the ICs under test to monitor and change the test conditions since the radiation cave is isolated from the control room.

The test setup for radiation testing of INA3221 current sensing and voltage monitoring devices is shown in Figure 57. For this test, INA3221 testing boards were connected to the TWICE C&DH board during radiation testing. The FPGA on the C&DH board was programmed in VHDL to allow acquisition from the INA3221 while it was exposed to heavy ions. The radiation test setup for the ADCs was similar to that for the INA3221, except that a sawtooth-wave analog signal provided by the function generator was supplied to the analog input channels of each ADC for acquisition, and the C&DH boards were removed from the test setup. For voltage regulator testing, a data acquisition and recording device with high sampling rate was used to detect transients at the outputs of the regulators.

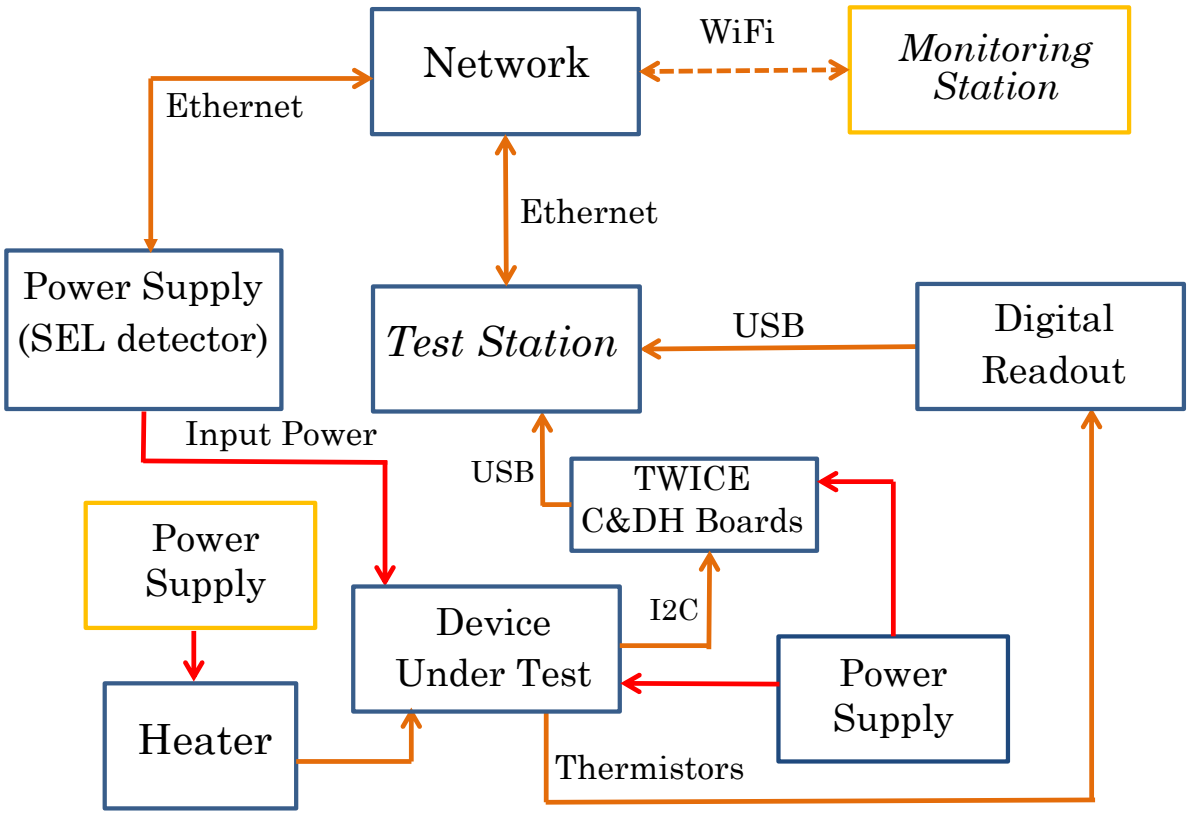

Figure 57: Block diagram of the radiation testing configuration for INA3221, the current sensing and voltage monitoring IC.

During radiation testing, the beam source is aligned at normal incidence with the decapsulated portion of the IC under test prior to heavy ion testing. Figure 58 shows the alignment of the decapsulated AD7606 with the beam source for heavy-ion testing. Beam angles that are positioned off normal incidence can be also used in heavy ion radiation testing to obtain different effective LET values than those available at the testing facility, but the validity of the test setup should be verified for each device technology and package [75]. The enlarged imagery of the decapsulated IC under microscope before the test setup provides easiness to

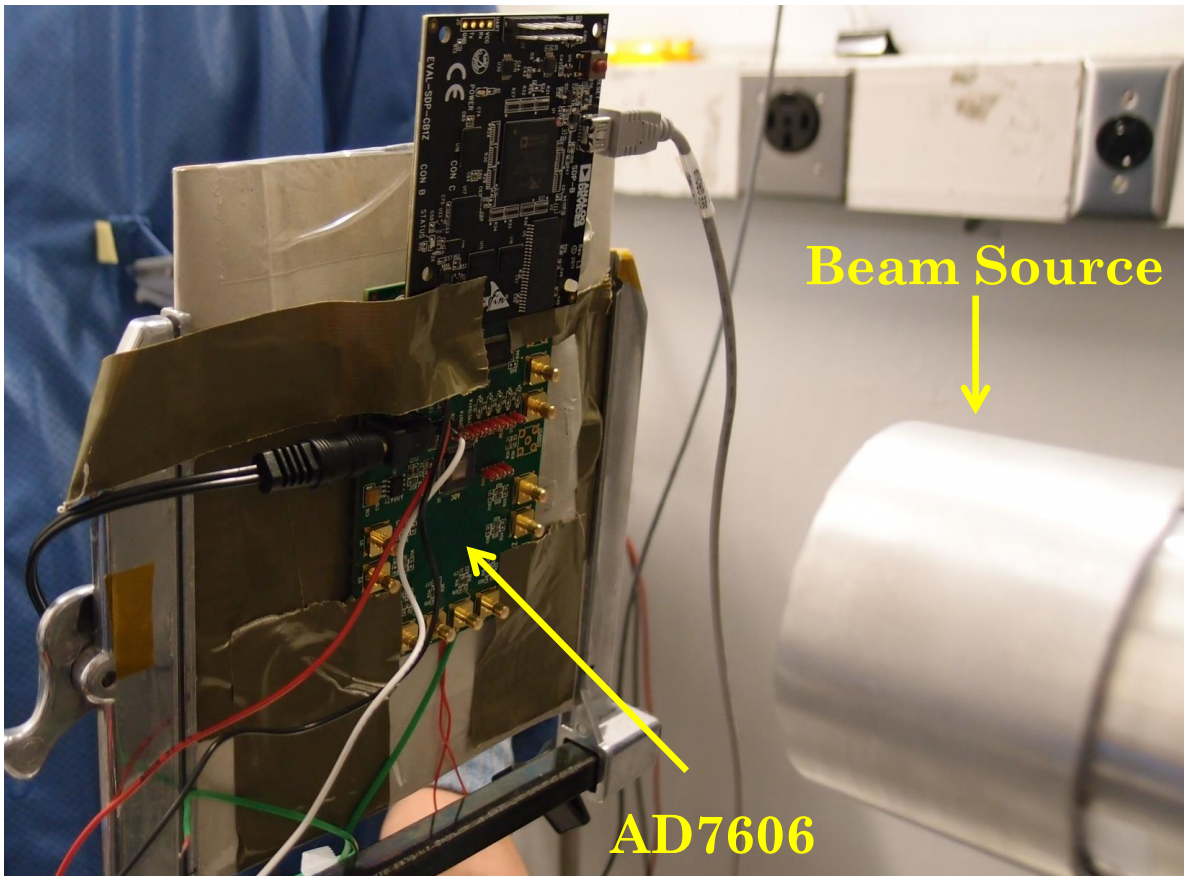

Figure 58: Decapsulated AD7606 aligned with the beam source for heavy-ion testing.

perform fine beam alignment with the IC for the heavy ion testing. The microscope imagery of the fine beam alignment with INA3221 device is shown in Figure 59.

5.4.2.2 Heavy Ion Radiation Testing Results

SELs are our main consideration for heavy ion ADC testing [91]. SEL tests of ADS1178 ADCs have been conducted at 42.2 MeV-cm^2/mg effective LET (LET_{Eff}) level at two flux rates of 10^2 and 10^3 ions/cm^2/s at a room temperature of 17°C with Ag ions. Destructive SELs have been observed on the internal digital circuitry (core

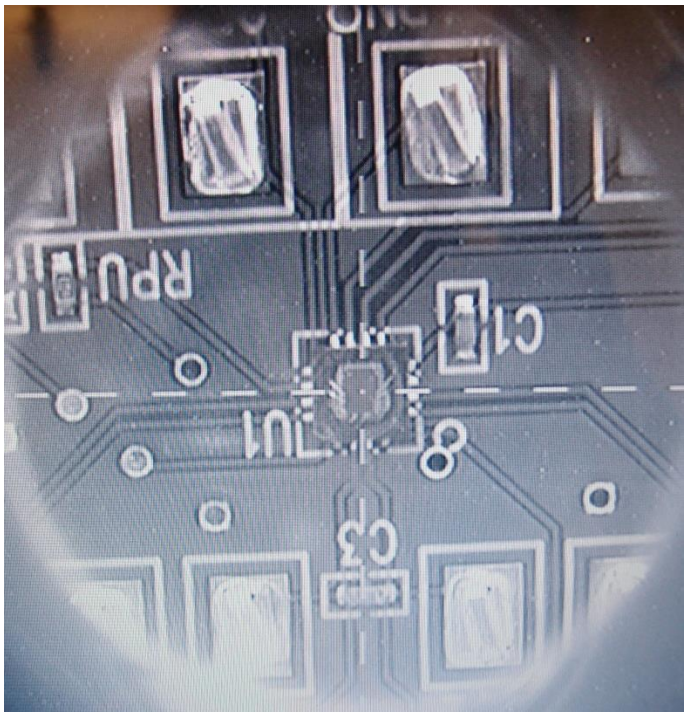

Figure 59: The microscope image of the fine alignement of INA3221 device with the heavy-ion beam source.

of the ADC) at both flux rates, and the devices under test permanently lost their functionality at fluence level of less than 10^5 ions/cm^2. Further analysis can be performed to determine the latch-up regions in the device, as defined in [92].

SEL testing of AD7606 ADCs has been performed at flux rates varying from 10^4 to 10^5 ions/cm^2/s with Ag and Ar ions. During tests, the device has been powered with 5.0 V analog and 2.5 V digital supplies. Non-destructive SELs have been detected at room temperature in the analog and digital portions of the IC during Ag ion testing and only in the analog portion of the IC during Ar ion testing. The Ag and Ar ion tests were repeated at elevated temperature (85°C) to observe the effects of temperature on SEL cross-section since the SEL susceptibility of the IC is expected

to increase with temperature [93]. No significant increase in the number of counted non-destructive SELs has been observed at the elevated temperature.

The latch-up cross sections at the testing points are calculated using Equation (V.2) where σ is the SEL cross-section per device in our case and θ is the angle between the device sensitive area and the beam. The number of events observed during the heavy ion radiation testing and the resulting cross-section of the AD7606 at room temperature are provided in Table 20. Heavy ion SEL testing of AD7606 indicates that the device is susceptible to SEL when operated with 5.0 V analog and 2.5 V digital supplies.

A 4-parameter Weibull fit [94], [95] is used to estimate the cross-section curves for the AD7606 based on the calculated cross-section from heavy ion radiation data. It is recommended to perform radiation testing at as many beam LET levels as possible to obtain full SEL characterization of the device [96]. However, it may not be feasible to fully characterize the device considering the stringent requirements of SmallSats with low budgets, short development cycles and lifetimes [16]. Therefore, our motivation for this radiation testing is to obtain a basic understanding of device

Table 20: SEL test results for AD7606 at room temperature

Beam Ions	LET_{eff} [MeV-cm^2/mg]	Events [counts]	Effect. Fluence [ions/cm^2]	σ_{SEL} [cm^2/device]
Ar	8.4	6	1.0×10^{7}	5.98×10^{-7}
Ag	42.2	175	0.9×10^{7}	1.96×10^{-5}

behavior for a worst case device event rate estimation in the LEO radiation environment for TWICE, as well as to develop error mitigation techniques. Considering the test results in Table 20, the threshold LET value for the AD7606 is assumed to be close to 8 MeV-cm^2/mg. This value is used to estimate the worst case failure rate considering a steep slope of the cross-section curve at the lower end and the number of events observed with Ar ion testing [97]. A four-parameter Weibull fit of possible AD7606 SEL cross-section curves with 95% confidence level and 10% fluence uncertainty [73] for different widths and shapes based on radiation test data under the given assumptions is shown in Figure 60. The device sensitive volume has been calculated using the integral rectangular parallelepiped method (IRPP) [98]. The calculated device in-orbit soft error rate (SER) is found to vary from 3.5x10^{-6} for the cross-section curve with the smallest area to 5.1x10^{-6} events/device/day for the curve with the largest area, with 100 mil Al shielding

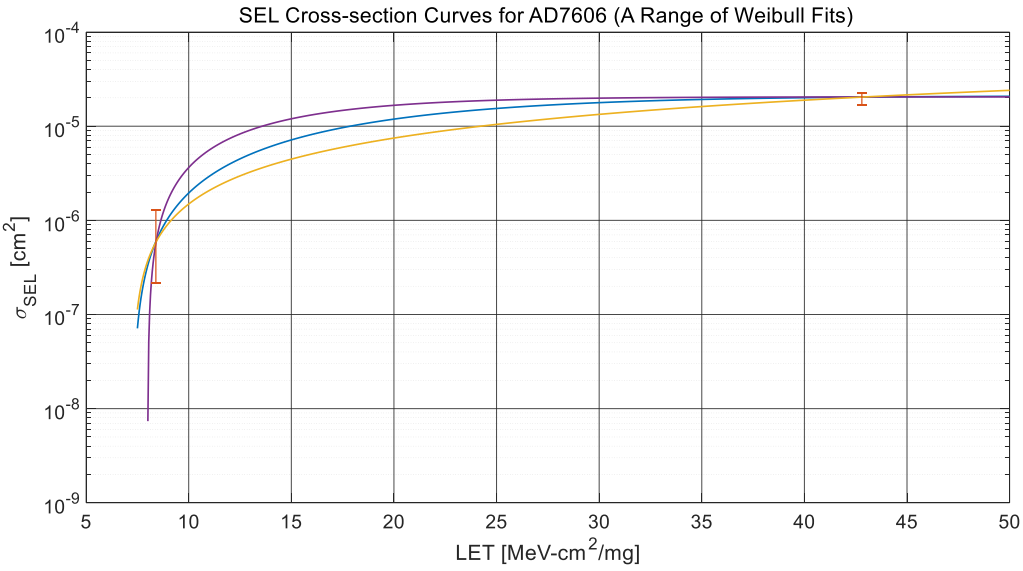

Figure 60: AD7606 SEL cross section curve at room temperature with 95% confidence level and 10% fluence uncertainty [73].

using the CREME96 module [99]. This corresponds to an average of 170 on-orbit failures-in-time (FIT) per device with an uncertainty of 40 FIT. The level of uncertainty of FIT value is negligible for the AD7606 error rate calculations for the CubeSat instrument since it will result in an uncertainty of less than $1x10^{-3}$ events for a short-term mission with this low FIT uncertainty value.

The radiation test results for the voltage regulators are summarized in Table 21. For these tests, ions with a flux rate ranging from 10^2 to 10^5 ions/cm^2/s have been used, with ion species varying with the device type, as shown in Table II. The stopping effective fluence level has been chosen as 10^7 ions/cm^2.

Destructive SEEs have been observed during testing of monolithic switching regulators of LTC3406 and LTC3621. After power cycling of the ICs, the devices

Table 21: Summary results of radiation testing of regulators.

IC	Beam Ions	LET_{eff} [MeV-cm^2/mg]	Observation
LTC3406	Ag	42.2	Destructive SEE
LT1763	Ag	42.2	Neg. SET (60% of V_{out})
LT1763	Ar	8.4	Neg. SET (30% of V_{out})
LT1962	Ag	42.2	None (Noisy output)
LT1964	Ag	42.2	Pos. SET
LT3022	Ag	42.2	Pos. and Neg. SET
LTC3621	Ag	42.2	Destructive SEE

were no longer operational. Non-destructive SETs have been observed during radiation testing of LT1763, LT1964 and LT3022. The observed SET response of these regulators depends on input/output voltage, load capacitance and operating temperature [77]. During radiation testing of LT1763, the internal protection circuitry has resulted in negative transients observed at the output of LT3022 are shown in Figure 61. The amplitude of the transient is about 50% of the regulated output voltage. Recovery time of the output waveform is measured as a few tens of μs and depends on the load current and output capacitance.

Finally, the INA3221 ICs have been bombarded with Ag ions with flux rates ranging from 10^4 to 10^5 ions/cm^2/s up to 10^7 ions/cm^2 of effective fluence, with the device under test at both 17°C and 85°C. Multiple bit upsets have been observed on

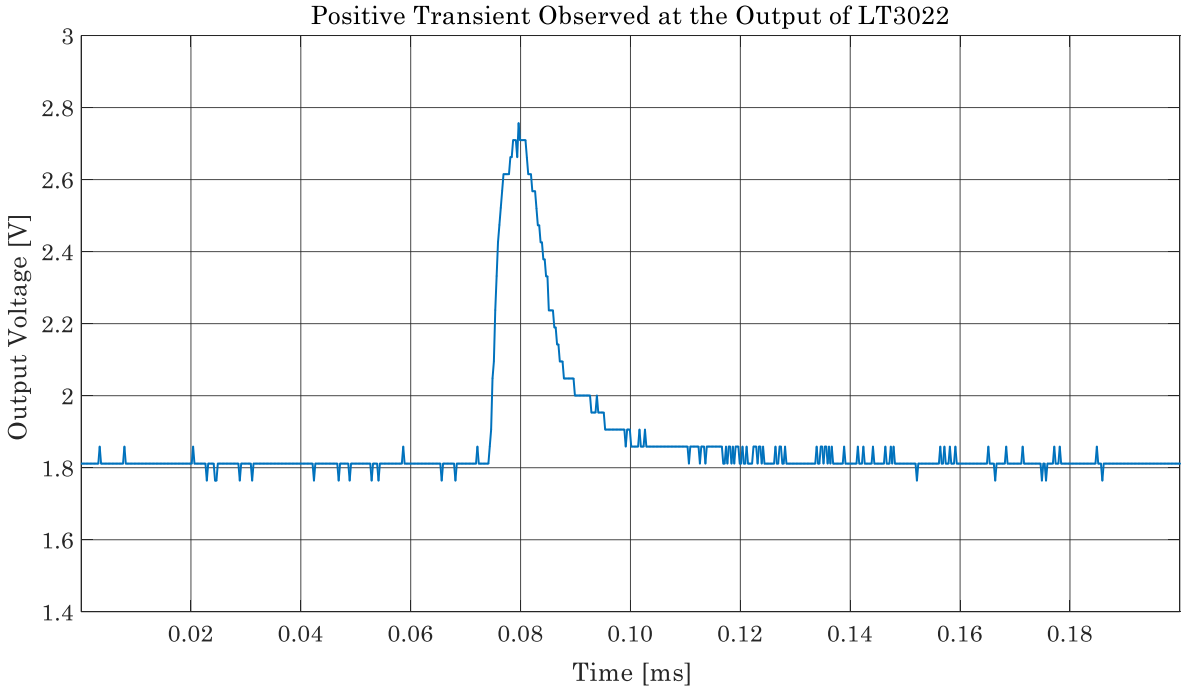

Figure 61: Positive transients observed at the output of LT3022

the acquisition of shunt and bus voltage values. No bit upsets have been detected on the communication bits sent to the FPGA on the C&DH board. Bit upsets on the acquired data are not critical for system functionality since any acquired sample with the upset can be easily identified and discarded using the information from multiple channels of the radiometer as well as filtering techniques such as a median filter [100]. However, a bit upset on the configuration registers can disrupt the device functionality. As a result, no further analysis on the bit upsets is considered to be necessary for mission success since the upset was only observed on the acquired data samples.

5.5. TWICE Radiation Risk Analysis and Mitigation

Destructive events in components result in permanent failure of the device functionality. Therefore, any component experiencing a destructive event during radiation testing should not be considered for the flight design. However, any device having a non-destructive SEE response may be used in a SmallSat or CubeSat mission after careful radiation analysis and mitigation at the system level if there is no RadHard device available that meets the design and mission requirements [101].

5.5.1 Central Processing Unit

The central processing unit (CPU) sending command signals and interfacing with other systems is one of the most critical parts of the instrument. High reliability of the instrument CPU needs to be ensured for mission success. TWICE uses a RadHard Microsemi ProASIC3 type FPGA. The operational characteristics of this

FPGA under LEO radiation conditions are ensured through the data provided by Microsemi [102]. Several heavy-ion radiation tests of this FPGA have been conducted by the Radiation Effects and Analysis Group of NASA's Goddard Space Flight Center (GSFC). The test results are publicly accessible from the NASA GSFC radiation database [103].

5.5.2 Current Sensing and Voltage Monitoring ICs

The INA3221 acquires the shunt and bus voltage with an internal analog-to-digital data converter. This device may be considered for the instrument design since no destructive events, single-event functional interrupts or bit upsets in the configuration and communication bits have been observed during radiation testing. To mitigate bit upsets in the acquisition data, the averaging property of this IC should be set to a sufficiently long integration time constant to eliminate the effect of bit errors. In addition, the digitized output should be used after the long-term averages have been calculated. Parts that are critical for mission success could also be monitored with two redundant INA3221s to obtain reliable measurements.

5.5.3 Analog to Digital Data Converters

The reliability of the ADCs is essential to the success of a radiometer instrument since they perform the digital acquisition of the radiometer's analog output. For ground-based instruments, ΔΣ ADCs may be preferred since their internal oversampling and noise shaping circuitries provide low noise and up to 32 bits of resolution for radiometric signal acquisition, at the cost of lower sampling speed

and higher latency than other ADC architectures [50]. Destructive events have been observed during radiation testing of a ΔΣ ADC (ADS1178). This indicates that this IC is not suitable for a LEO SmallSat or CubeSat mission. Although recent developments in CMOS technology have allowed some RadHard ΔΣ ADCs to be made commercially available, the functional performance of these devices is significantly degraded in comparison to that of non-RadHard ΔΣ ADCs [104]. As a result, they do not meet both the stringent SWaP requirements of SmallSats [16] and the need for synchronous, simultaneous low-noise, high-resolution sampling of the 16 radiometric channels of TWICE [43]. In addition, we have not been able to find any commercially available radiation tolerant ΔΣ ADC that meets our project requirements [91], [105]. As a result, the TWICE mission will not consider RadHard ΔΣ ADCs due to their functional limitations for the mission requirements.

The radiation test results have shown that only non-destructive events have been observed on the SAR ADC (AD7606). This indicates that this ADC may be used after necessary SEE mitigation and protection techniques are implemented to improve the reliability of the system. The current consumption of the SAR ADC in a non-destructive latch-up state is significantly increased from its nominal value, i.e., approximately a 0.5 A increase per device is expected. This in turn can result in a device breakdown and can cause power loss of a CubeSat due to high current consumption from the satellite electric power system if the device remains in a non-destructive state on orbit. A latch-up prevention and protection circuit design is required to improve mission reliability. For instance, non-destructive SELs

observed on the data converter of the Compact Reconnaissance Imaging Spectrometer for Mars (CRISM) have shown that the effects of non-destructive events can be mitigated through latch-up protection in space [106].

TWICE continuously performs on-orbit current sensing and voltage monitoring of the ADCs by using INA3221 devices. This will enable detection of increased ADC current consumption due to an SEL. In this case, the power to the ADC is cycled by a reset signal sent from a RadHard FPGA to the power regulator of the ADC. In addition, the RadHard FPGA continuously receives digitized radiometric data from the ADCs at a sampling rate up to 20 μs. An ADC in a latch-up state will be unable to perform acquisition and send an SPI communication to the FPGA. The latch-up detection time will be less than 1 ms through the response of the ADC to the SPI communication. Additional measures to protect the system from the effect of latch-ups may be implemented, depending on the type of instrument, including resistive protection or switching circuits.

5.5.4 Voltage Regulators

Reliability of voltage regulators is critical for mission success since the operational capabilities of other devices rely on the power supplied by these devices. The limited power available to SmallSats and CubeSats motivates circuit designers to choose efficient methods for power regulation, while at the same time ensuring reliable and low-noise output voltages.

In SmallSat and CubeSat missions, switching power supplies are desirable for their high power efficiency (up to 90% or more), as compared to linear regulators. High

efficiency is achieved through the on-off switching power mechanism of these regulators. Monolithic switching regulators are prone to destructive events such as single-event burnout and single-event gate rupture due to the vulnerability of MOSFET devices to heavy ions [107]. The monolithic switching regulators tested for the TWICE instrument are not considered for the final design due to destructive events. A substitute switching regulator will be chosen to achieve high reliability and efficiency. In addition to radiation effects, a designer also needs to consider the noise generated by switching regulators. The effects of switching noise need to be minimized through effective filtering in addition to proper grounding and PCB layout design techniques. Furthermore, digital control of switching regulators can improve system reliability by minimizing the transients generated by switching power converters. In this case, the designer needs to optimize the radiation reliability of the digital control circuits, such as FPGAs, by using RadHard and reliable components [108].

Linear regulators have design advantages over switching regulators for use in battery-powered circuits since they provide reliable and low-noise output voltages with rapid transient-step response to load changes in addition to current and thermal protection [107]. Transients in the regulated voltage due to ionization effects can damage or degrade the performance of sensitive electronic components by producing noise-like effects. Positive transients with large overshoot can cause destructive events in CMOS devices. Negative transients with large undershoot can result in functional interrupts in processors and memories [109]. In addition,

voltage regulation for SmallSat or CubeSat instruments is considered to be local regulation on circuit boards due to the stringent size restrictions for those instruments. Therefore, small transients on a voltage regulator output may interrupt the operation of sensitive electronic parts [77].

The amplitudes of these transients can be reduced to acceptable levels by applying necessary SET mitigation techniques. At the PCB layout design level, implementing ground connection as a star bus topology or a ground plane and placing capacitors close to the voltage and ground pads of the regulators will help reduce transients by minimizing parasitic effects [109]. At the circuit design level, an output filter with large capacitance value having low equivalent series resistance (ESR) and low equivalent series inductance (ESL) will reduce the effect of the transient on the output voltage with the penalty of increased recovery time. However, low output impedance of the regulator may overcome the effect of increasing the value of the bypass capacitor after a certain level of improvement. This in turn makes clamping circuits necessary for the protection of sensitive electronics in a SmallSat or CubeSat. Fast-switching diodes can be used at the output of the regulator to clear the voltage transients due to SEEs. A sophisticated approach could be designing a RadHard Darlington transient protection circuit, which is widely used in the semiconductor industry for circuit protection [110]. The designed mitigation technique needs to be tested for variations of input/output voltage, load capacitance, load current, and operating temperature for the SmallSat or CubeSat mission to improve the reliability of the system [77].

5.6. Conclusions

A system-level analysis has been performed for the TWICE C&DH and power subsystems to identify COTS ICs that are critical for mission success as candidates for radiation testing. Then, critical COTS parts for the C&DH and power subsystems of the TWICE millimeter- and sub-millimeter-wave radiometer instrument for a 6U-Class satellite have been tested at the Texas A&M University (TAMU) Cyclotron Institute Radiation Effects Facility [90]. The objective of radiation testing is to determine the performance of these ICs in a LEO-like radiation environment against SEEs. Heavy-ion radiation testing at the Texas A&M Cyclotron Institute Radiation Effects Facility has been performed on June 2, 2016 (by CSU and JPL) and March 13-14, 2017 (by CSU). During the radiation testing, the critical COTS parts have been tested for SEEs, including single-event latch-ups (SELs), single-event transients (SETs) and single-event bit-upsets (SEBUs).

Device and system level SEE analysis has been performed on critical COTS ICs in the C&DH subsystem of the TWICE millimeter-wave radiometer instrument for CubeSat deployment. The radiation test results have indicated that the ADS1178 ADC is not suitable for operation in LEO-like radiation conditions due to observed destructive SEEs. However, the AD7606 ADC is used in the final design of the TWICE instrument due to low-event rate with proper mitigation techniques. The level of 170 FIT per device for the AD7606 can be tolerated, even though it is higher than that of a typical RadHard device (i.e., a few FIT per device). INA3221 devices

for current sensing and voltage monitoring have experienced non-destructive SEEs. There is no bit upset detected in the configuration bits of INA3221 ICs. Therefore, they are used in the final TWICE C&DH board design.

Nondestructive events are not detected during the radiation testing of linear regulators. However, LT1763 is not considered for the final power regulation board design due to large amount of voltage transient detected at the regulator output voltage supply line. On the other hand, switching regulators carry a high risk of permanent damage in the LEO radiation environment. The switching regulators LTC3406 and LTC3621 are not considered for the final design. Instead, TPS54821 and TPS54226 are used in the final design since they are considered to be reliable for the TWICE instrument based on the radiation testing data available for this ICs.

The SEE characteristics of ADCs, voltage regulators and current sensing and voltage monitoring ICs are analyzed. All of these COTS IC components are critical parts of the C&DH and power subsystems of the TWICE millimeter-wave radiometer instrument. The SEE analysis was extended to include the examination of system-level radiation susceptibility and the evaluation of mitigation techniques based on radiation testing results. This study provides useful information for understanding and analysis of SEE effects on C&DH and power subsystems of SmallSat and CubeSat missions.

Chapter VI Radiometer Characterization and Testing

This chapter presents front-end receiver performance evaluation integrated with the TWICE C&DH system. The TWICE prototype 670 GHz, final 670 GHz, final 240/380 GHz receivers are characterized to determine their performance. The stability, noise and NEΔT performance of the receiver is evaluated while the radiometer is performing end-to-end radiometer operation with calibration targets. The techniques to improve the radiometer performance are discussed. The analysis presented in this chapter is valuable for both radiometer front-end and control and data handling systems design.

6.1. Introduction

The prototype 670 GHz TWICE receiver shown in Figure 62, the final 670 GHz and 240/380 GHz receivers are integrated with TWICE C&DH system to perform end-to-end radiometer testing and characterization. First, the prototype receiver testing is conducted. Then, the analysis for the final receivers is presented. The main

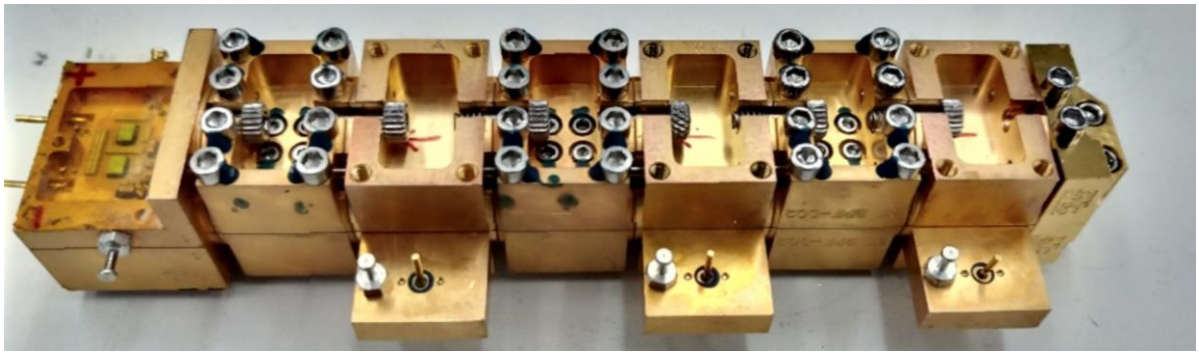

Figure 62: The NGC 670 GHz prototype front-end receiver.

considerations for analyzing the system performance are explained in the following sections.

6.2. Y-Factor Analysis

Y-factor tests are performed on a radiometer system to determine the measured receiver noise temperature and the temperature to voltage response function of the receiver. These tests are important to check the reliability of the radiometer.

To perform Y-factor measurements, the radiometer under test measures two targets at different but known temperatures (e.g. ambient and cold targets). The ratio of the power measured from the ambient target (P_{amb}) to that from the cold target (P_{cold}) is expressed as the Y-factor value of the radiometer [111]:

$$Y = \frac{P_{amb}}{P_{cold}} = \frac{T_{amb} + T_{rec}}{T_{cold} + T_{rec}} \tag{VI.1}$$

where T_{amb} and T_{cold} are ambient and cold target temperatures, respectively. T_{rec} is the receiver noise temperature that Y-factor test is intended to determine using the measured Y-factor.

The received power by the receiver is converted into voltage by the power detector diode before it is transmitted to the back-end acquisition system as explained in Chapter II. The acquisition systems digitize the analog radiometric voltage in the form of quantized level called counts. Thus, (VI.1) can be expressed in radiometric counts acquired by the digitizer back-end since the voltage digitized by the analog-to-digital converter (ADC) chips in the back-end system is proportional to power detected by the detector diode in the front-end receiver:

$$Y = \frac{C_{amb}}{C_{cold}} \tag{VI.2}$$

The expression given above states that the Y factor of a radiometer is simply found by taking the ratio of the ADC counts when the radiometer is measuring the brightness temperature of an ambient and a cold target.

Reorganizing the terms in (VI.1) yields a useful formulation to calculate the receiver noise temperature as:

$$T_{rec} = \frac{T_{amb} - YT_{cold}}{Y - 1} \text{ [K]} \tag{VI.3}$$

The measured Y-factor found from Equation (VI.2) and the known temperatures of the ambient and cold targets are used in the above equation to determine the receiver noise temperature of a radiometer.

The radiometric gain for a radiometer relates the measured output voltage to the antenna temperature measurements of the radiometer mapping the linear transfer function. The radiometric gain is calculated using the ambient and cold target measurements as the following:

$$G = \frac{T_{amb} - T_{cold}}{C_{amb} - C_{cold}} \text{ [K/V]} \tag{VI.4}$$

To avoid degrading the radiometric resolution, the full dynamic range (i.e. the range between the possible minimum and maximum brightness temperatures sensed by a radiometer) of the temperature-to-voltage gain should span a large fraction of the dynamic range of the ADC. Otherwise, ADC's sensitivity might be unable to resolve

the minimum detectable change at the input of the radiometer. This, in turn, would degrade the noise equivalent temperature (NEΔT) performance of the receiver front-end and the antenna. In other words, a smaller radiometric gain will result in a better NEΔT performance of a radiometer [34].

6.2.1 TWICE Prototype System: Y-Factor Measurements and Results

The Y-factor measurements of the TWICE 670 GHz prototype receiver using the C&DH system is performed using an ambient target at 295 K room temperature and a calibration target immersed in liquid nitrogen at 77 K degree as shown in Figure 63.

The receiver output voltage measurements are taken while the receiver observing the ambient source and cold source. The ADCs on the signal conditioning circuit of

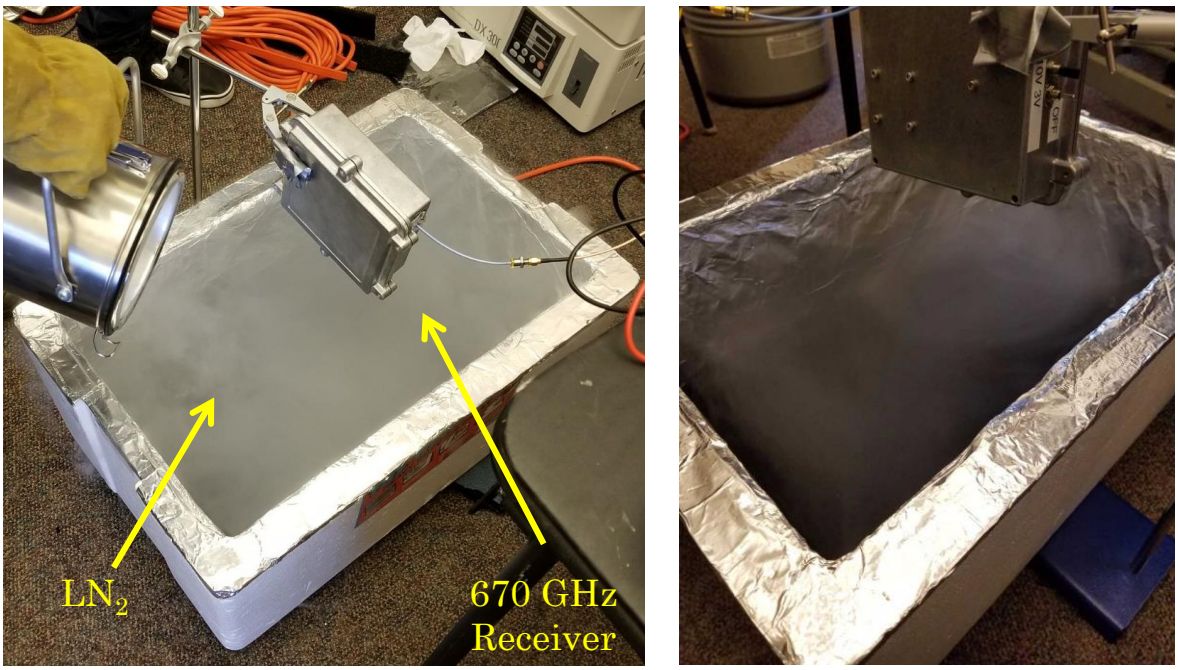

Figure 63: The Y-factor measurements of 670 GHz protptype receiver using LN_2 as the source for cold temperature target.

the C&DH board have continuously performed acquisition of the analog radiometric signals. The acquired data is plotted in counts and Volts on Figure 64. The Y-factor is calculated using Equation (VI.2) from the measured ambient and cold counts as:

$$Y = \frac{C_{amb}}{C_{cold}} = \frac{5226}{5009} = 1.043 \tag{VI.5}$$

Using the calculated Y-factor value, the 670 GHz prototype receiver noise temperature is calculated from Equation (VI.3) as:

$$T_{rec} = \frac{T_{amb} - YT_{cold}}{Y - 1} = \frac{295 - 1.043 * 80}{1.043 - 1} = 4893 \text{ [K]} \tag{VI.6}$$

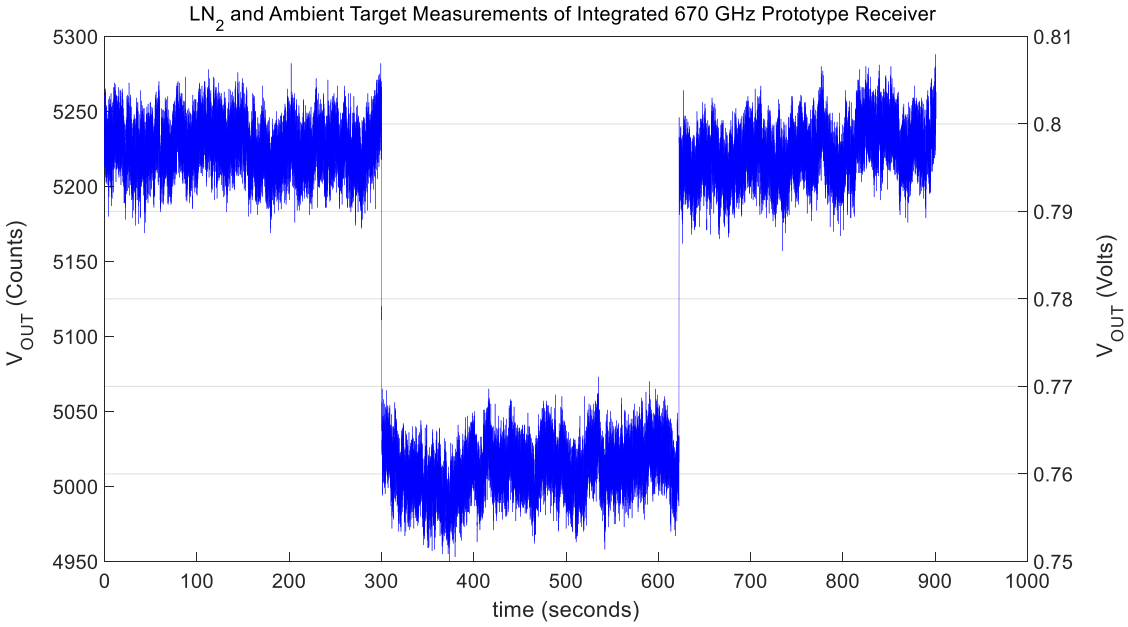

Figure 64: Acquired radiometric data from C&DH prototype boards during ambient-cold target Y-factor measurements of 670 GHz prototype radiometer.

The radiometric gain of the TWICE 670 GHz prototype receiver is found from Equation (VI.4) using the acquired data in counts and the temperature information of the warm and cold targets as the folowing:

$$G = \frac{T_{amb} - T_{cold}}{C_{amb} - C_{cold}} = 0.9927 \text{ [K/counts]} \quad \text{(VI.7)}$$

6.2.2 Radiometric Noise Equivalent Delta-Temperature

The measurement uncertainty is defined by the Joint Committee for Guides in Metrology as the parameter that characterizing the dispersion of the measured values from the actual measurand [112]. For a radiometer, it can be attributed as the sensitivity of the radiometric system to sense the input brightness temperature under existence noise in the system and can be expressed as the noise equivalent delta temperature (NEΔT). The radiometer NEΔT performance can be measured by looking at an ambient calibration target at constant room temperature. The receiver output will show some variations due to receiver noise uncertainty and random gain fluctuations due to 1/f noise. The standard deviation of the digitized radiometer output voltage can be calculated in counts for one calibration cycle time. The measured standard deviation in counts then multiplied with the radiometric gain which is found by using Equation (VI.4) to calculate the measured NEΔT of a radiometer. This is formulized as:

$$NE\Delta T_{measured} = Counts\ x\ G \text{ [K]} \quad \text{(VI.8)}$$

The analysis can be extended to calculate the effective bandwidth of the radiometer. Using the definition of NEΔT given for an ideal radiometer in Section II by ignoring the gain fluctuations, and the measured receiver noise temperature found in Equation (VI.3), the effective bandwidth can be calculated for the integration time used.

6.3. Stability Analysis

The stability of a radiometer depends on stochastic and deterministic properties of the instrument. The stochastic properties of a radiometer are driven by the noise present in the radiometric measurements. The stochastic properties of a radiometer can be considered as stationary and ergodic between each calibration cycle of the radiometer. Long term gain drift and temperature dependency of the radiometers are considered as deterministic properties [113], [114]. Deterministic factors can be corrected with proper calibration methods including two-point end-to-end calibration of the instrument with external calibration targets. Thus, the deterministic factors will not considered in the stability analysis for the TWICE instrument.

Frequency domain and time domain response of the TWICE 670 GHz prototype radiometer are analyzed to determine the stochastic factors affecting the instrument stability for radiometric measurements. For both analyses, radiometric measurements are taken when the antenna is looking at an ambient calibration target at constant room temperature. The analog signal conditioning circuit controlled by the FPGA on the C&DH board has performed continuous acquisition

of the radiometric signals. The frequency domain and time domain analysis use the same dataset for the analysis of the instrument stability.

6.3.1 Frequency Domain Analysis

The frequency domain analysis focuses on the flicker noise and white noise present in the instrument with respect to frequency. The fast Fourier transform (FFT) is applied to the measured digitized antenna temperatures in time domain for the conversion into frequency domain.

The initial analysis of the 670 GHz prototype receiver has revealed that the receiver has flicker noise at the level might degrade the performance of the radiometer for antenna temperature measurements. Further analysis that we performed has shown that the flicker noise is mainly generated from the detector diode.

To mitigate the effect of 1/f noise, conventional calibration techniques employ a Dicke-switching mechanism on the path to the antenna from the receiver front-end to a switch connecting the receiver input to a reference load [34]. However, the stringent size, weight and power requirements of CubeSats [16] have made a Dicke-switched load radiometer architecture not feasible for our design.

As a result, the proposed algorithm relies on controlling the gain of the overall receiver block to eliminate the effect of 1/f noise since it is detected as random fluctuations of the radiometer output voltage due to gain instability. Therefore, as graphically illustrated in Figure 65, a switching mechanism has been proposed on the receiver to switch the first transistor stage of the first LNA block periodically on and off with a digital switching signal from the FPGA on the C&DH board.

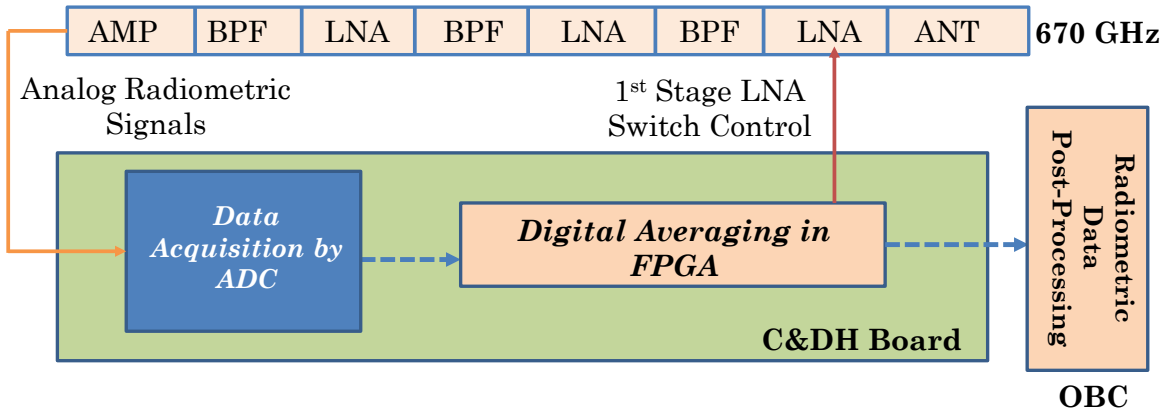

Figure 65: The proposed 1/f noise mitigation technique for the 670 GHz receiver.

Independent of the target that antenna is viewing, the 1/f noise is expected to affect the measured radiometric data when both the switch is on and off with the same gain factor for each acquired sample. For this technique, the switching frequency needs to be higher than the highest 1/f noise frequency so that we can track the same 1/f noise on the acquired samples at two different positions of the switch. In addition, the response time of the receiver is important at high switching mode since if the response time is longer than one half-cycle of the LNA switching frequency, the receiver cannot be operated.

To determine the response time of the 670 GHz prototype receiver, a digital clock signal is generated from the FPGA on the C&DH board for controlling the first LNA block of the receiver as shown in Figure 65. The receiver output is connected to an oscilloscope for continuous monitoring of the analog output voltage. As shown in Figure 66, the response time is measured as around 15 µs. This result is interpreted as at least first 15 µs of the radiometric measurements needs to be ignored due to transition in the receiver response from the switch OFF state to switch ON state or

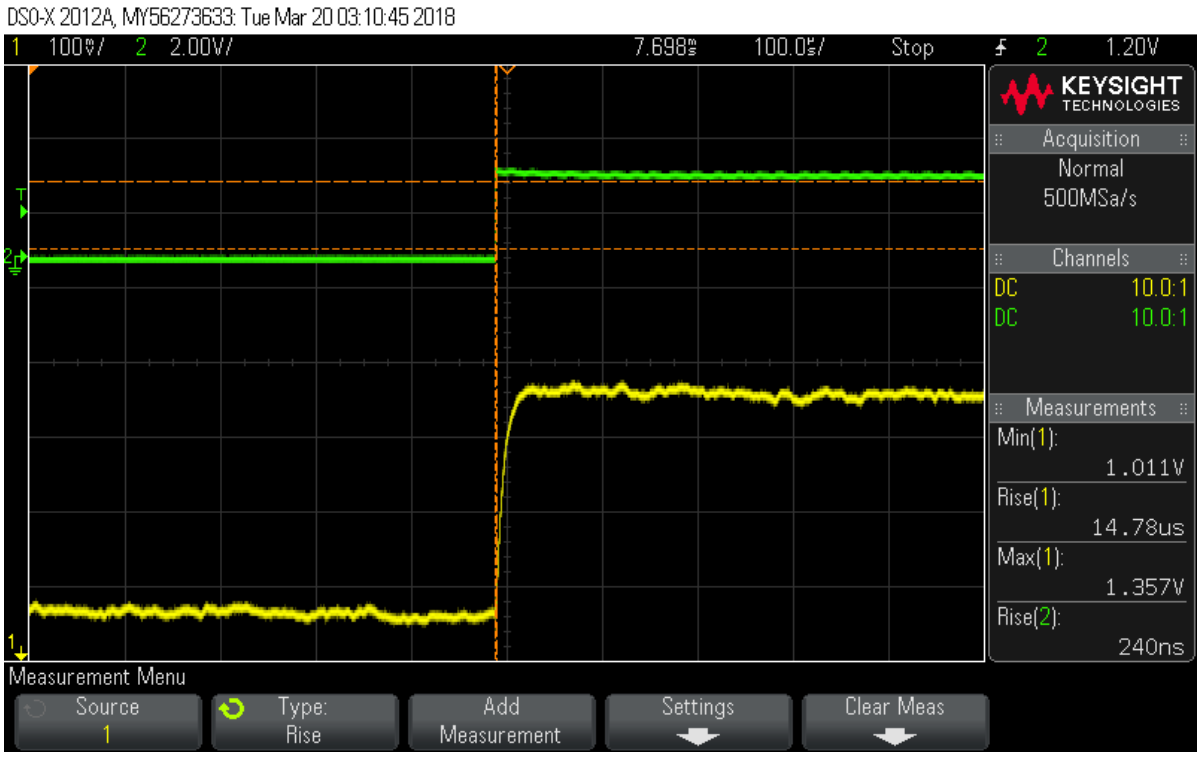

Figure 66: The oscilloscope measurements of the LNA switch response time of the 670 GHz prototype receiver.

vice versa. Thus, 5 kHz LNA switching frequency would be a good compromise based on the receiver 1/f noise characteristics and the receiver response time.

The ADC sampling time is chosen as 20 µs corresponding to 50 kSPS sampling speed of the ADC. The sampling speed chosen is a good compromise considering 23 kHz cut-off frequency of the internal second order low-pass filter of the AD7606 chip [ref]. In addition, 20 µs sampling time implies that there will be 5 samples acquired by the ADC at each state of the switch. Considering the transition time, ignoring first samples at each switch state will ensure reliable measurements by providing necessary time for the receiver to response the switch state change.

The detailed LNA switching control diagram is provided in Figure 67. The success of the switched LNA 1/f noise correction technique also depends on the synchronization of the switch control with the radiometric acquisition. Hence, a VHDL program has been written to synchronize the switch's operating position synchronously with the radiometric acquisition and to generate a digital filter inside the FPGA to perform oversampling and averaging of the radiometric signal. As depicted in the diagram, the first sample at each switch cycle is ignored from the radiometric measurements.

The samples labeled Q_R and Q_A in the diagram given in Figure 67 refer to the samples acquired during OFF state as reference and during ON state as antenna in accordance with a Dicke switching referencing. However, the antenna

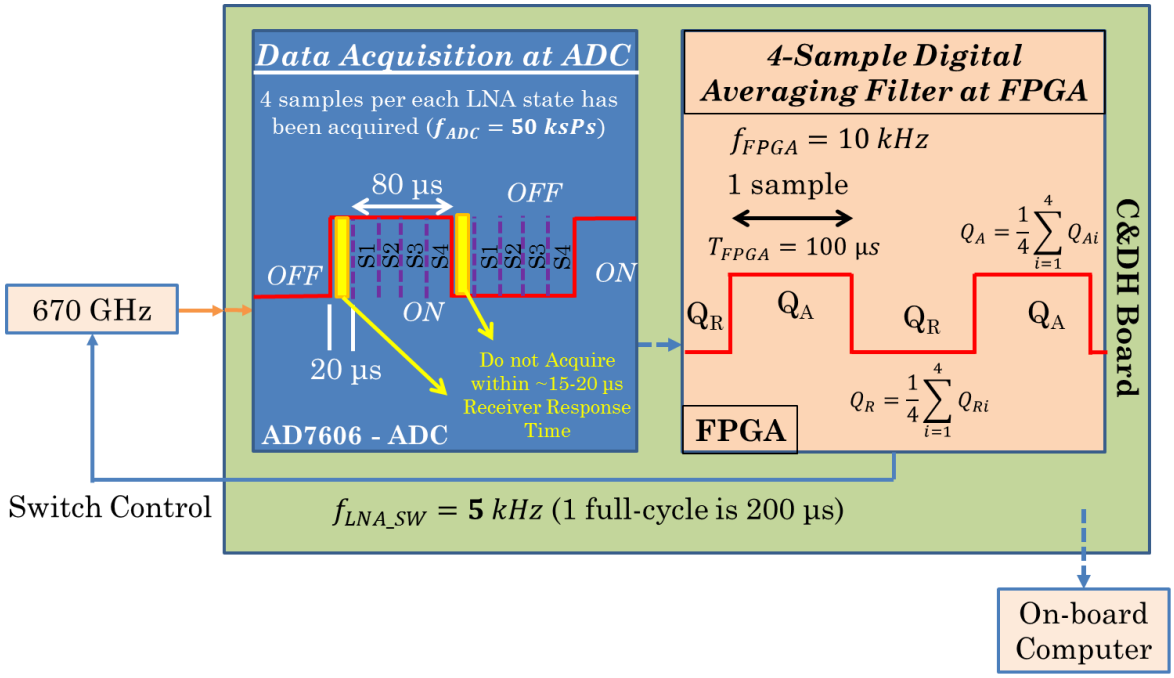

Figure 67: The detailed implementation of 1/f noise mitigation technique for the 670 GHz recevier.

measurements are always acquired by the radiometer independent from the switch position in oppose to a Dicke switching technique where the receiver measures the reference load and the antenna depending on the switch position.

The post-processing of the digitized and filtered radiometric data is executed on the OBC. The first step of the post processing is implemented to average the digitized and filtered data for one radiometer footprint time (4 ms). The measured data are averaged for each switch state separately as graphically illustrated in Figure 68. The radiometer output voltage is obtained from the OBC has 2 samples per the sampling period corresponding to ON and OFF states.

The final data processing is performed at the ground station to obtain the measured output voltage of the radiometer corresponding to a footprint on the surface. This

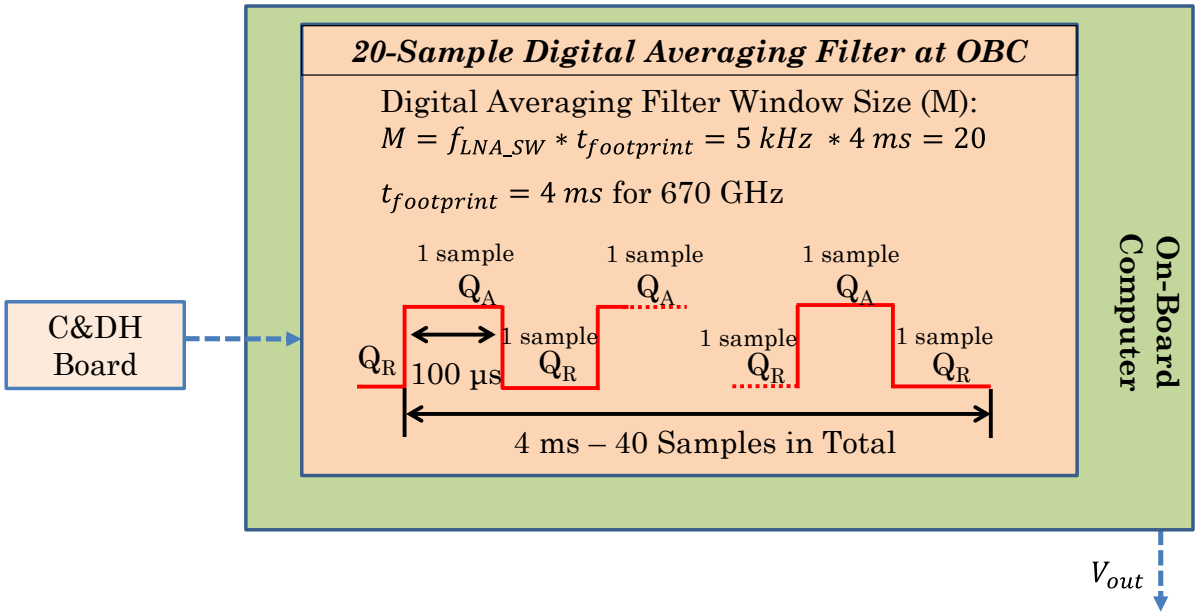

Figure 68: The post-processing of the acquired and filter data on the OBC for the 1/f noise mitigation technique for the 670 GHz recevier.

stage is a requirement since both the ON and OFF states should be sent to the ground station for verification of the receiver gain for reliable system operation. As discussed previously on this section, the final receiver is calculated as the radio of two states for the elimination of the 1/f noise effect. This can be formulized as:

$$V_{out,final} = \frac{\sum_1^M Q_A}{\sum_1^M Q_R} \text{ [V/V]} \tag{VI.9}$$

The acquired radiometer output by the C&DH and processed by the OBC is given in Figure 69. The top plot shows a 1 second window for the LNA switch ON position radiometer measurements when the antenna is looking at an ambient target at constant room temperature. The plot at the bottom shows the receiver output voltage measurement after the proposed post-processing technique in the ground

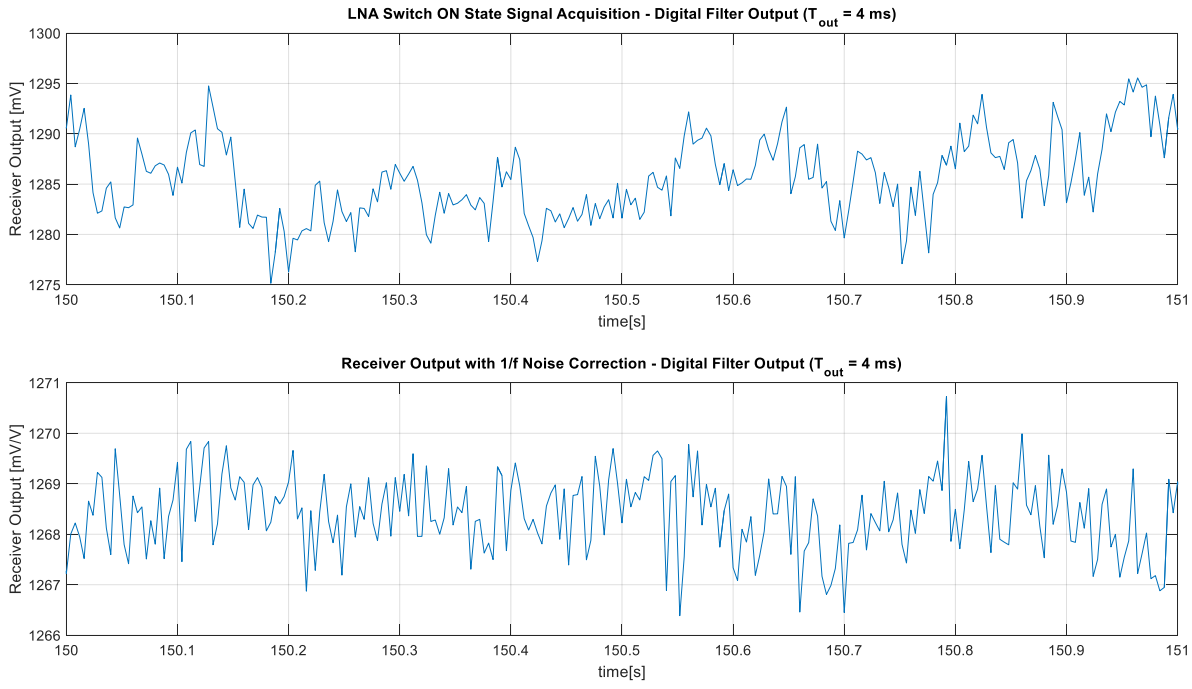

Figure 69: The 670 GHz prototype receiver output voltage measurement with 1/f noise mitigation technique implemented.

station. It is important to note that the spread in the measurement is apparently lower in the post-processed data compared the ON state measurements provided at the top plot.

The frequency domain analysis is performed to validate the proposed 1/f noise mitigation technique. The output spectrum obtained after the FFT calculations of the measurements is given in Figure 70 for both 1/f noise corrected measurements and the measurements without 1/f noise correction. The results show that the 1/f noise correction significantly improves the receiver 1/f noise performance relative to the case without 1/f noise correction. At the given frequency, the shift in the spectrum is more than 100 times in the vertical axis. Furthermore, the white noise level can be seen at around 10^{-9} normalized Volts^2/Hertz on the orange plot where 1/f noise correction is applied. This corresponds to around 4 GHz of the effective

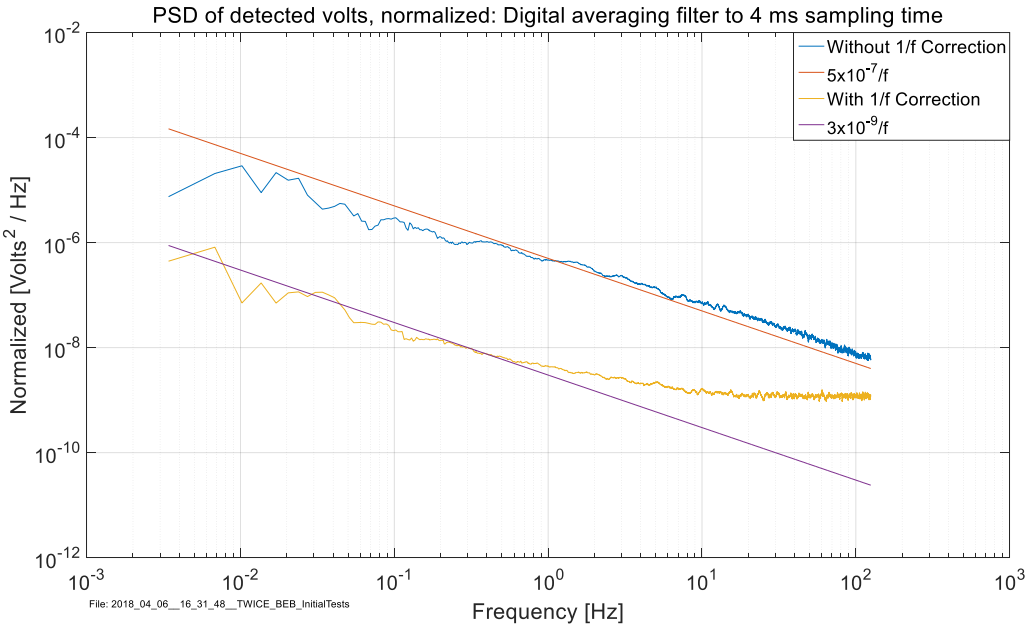

Figure 70: The FFT analysis of radiometric acquisition for 1/f noise correction of the 670 GHz prototype receiver.

bandwidth of the receiver revealing another successful outcome of the implemented result. Furthermore, from the slope given on the 1/f noise curve, the corner frequency for the 1/f noise is approximated around 2-3 Hz corresponding that the 1/f noise is not expected to degrade the performance of the receiver when it is calibrated at around every 1 second through end-to-end calibration targets.

6.3.2 Time Domain Analysis

The time domain stability of a radiometer based on the stochastic properties depends on the frequency stability of different noise sources as a function of time. Thus, a time series analysis of radiometric antenna temperature measurements is required to analyze the phase and frequency fluctuations from a time series of measurements.

The radiometric antenna temperature measurements can be expressed in discrete time domain as [114]:

$$T_{A,i} = \frac{1}{N} \sum_{k}^{k+N-1} T_{A,j} \tag{VI.10}$$

where $T_{A,j}$ is the digitized sample of the ADC at every τ sampling time in ADC counts and $T_{A,i}$ is the averaged digital samples obtained for one averaging period of the radiometer output.

The standard variance of the radiometric measurements is calculated as [113]:

$$\sigma^2 = \frac{1}{N-1} \sum_{1}^{N} T_{A,i} - T_A \tag{VI.11}$$

where σ is the standard deviation of the measurements and T_A is the averaged antenna temperature measurements for N samples.

The standard variance analysis can be applied to the time series data for analyzing the stability for different noise sources [113]. However, this analysis is not convergent for the noise sources in a radiometer having random fluctuations since the variations do not occur around a mean value. Therefore, a statistical variance analysis is required to analyze random noise sources in a radiometer.

The Allan variance is applied to time domain measurements of a radiometer as a measure of radiometric stability. The Allan variance can distinguish between the dominating noise sources in a radiometer which are white noise and flicker noise. Further analysis could be applied using other statistical variance analysis methods including the Hadamart variance and Theo variance to distinguish higher order noise terms but it is not required for a radiometric analysis.

The goal of Allan variance analysis is to express the variance as a function of the ADC sampling time τ to distinguish the power spectra of different noise sources. This is accomplished by building a basis for the power spectra of the noise sources with respect to variance of the measurements.

For a signal source having a power spectrum defined for positive finite frequency spectrum:

$$S(f) = \frac{K_i}{f^k} \tag{VI.12}$$

where K_i is a constant, the Allan variance relates the variance of the signal to the integration time as [114]:

$$\sigma^2(\tau) = K_i \tau^k \tag{VI.13}$$

The noise sources considered for Allan variance analysis of a radiometer are quantization noise, white noise, flicker noise, random walk and random run noise. These noise sources can be expressed in the form given in Equation (VI.13) with the value of k and respective slope on the Allan deviation plot is given in Table 22. The averaging of the signals is expected to help reducing the quantization noise and white noise until the effects of flicker noise becomes dominant on the measurements. This point is expressed as bias instability or sometimes stability where averaging no longer helps to reduce the noise. Further averaging beyond the bias point will eventually increase the noise level due to random walk noise as a result of the integration.

Table 22: Noise types and their characteristics on the Allan variation analysis for the radiometric stability.

Noise Type	k	Allan Deviation Slope [dB/dec]
Quantization	-2	-1
White Noise	-1	-1/2
Flicker Noise	0	0
Random Walk	1	+1/2
Random Run	2	+1

An Allan variance analysis has been performed for the TWICE 670 GHz prototype receiver to determine the stability of the instrument. The calculated Allan deviation is plotted with respect to the averaging time in Figure 71. It is clearly seen from the plot that the Allan deviation of the 670 GHz receiver almost perfectly matches with the theoretical noise levels existing in the radiometer instrument. It is important to note that the quantization noise is already minimized from the measurements as a result of the averaging filter inside the FPGA. It is also important to note that 1 second of calibration cycle will be enough for the TWICE instrument for maintaining the stability of the radiometer. Furthermore, when the averaging is increased, the dataset is exactly follows random walk noise and random run slope as expected.

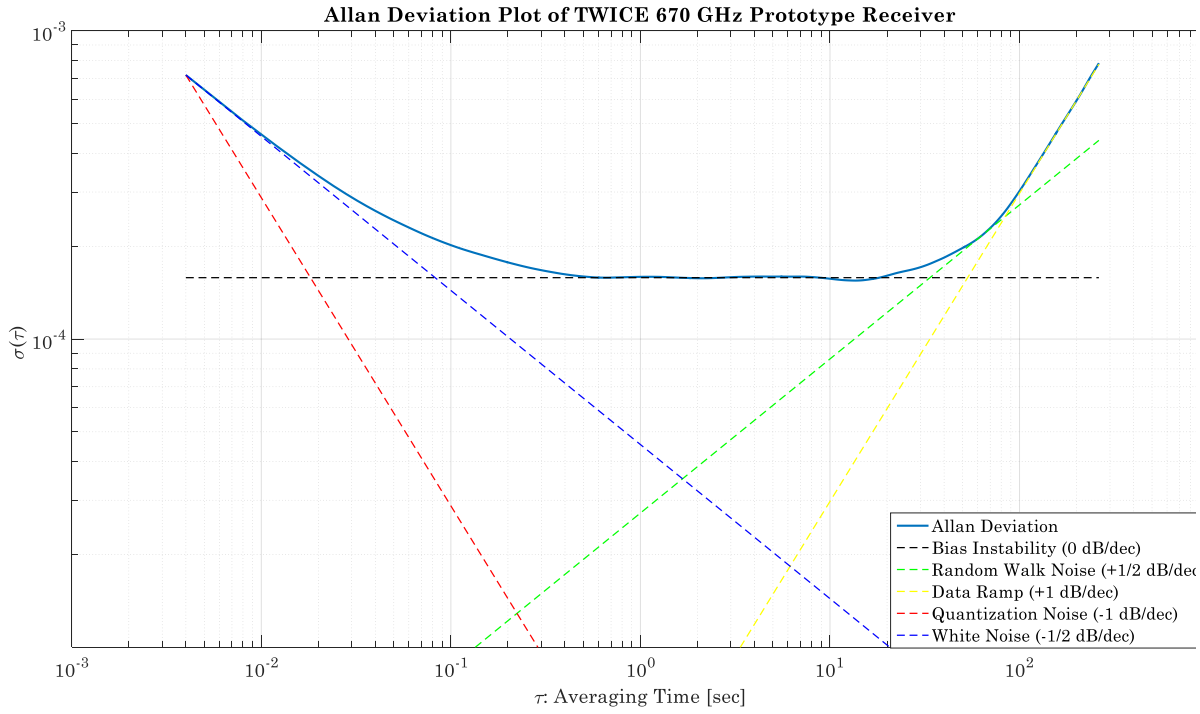

Figure 71: The Allan deviation analysis of radiometric acquisition with the TWICE 670 GHz prototype receiver.

6.4. TWICE Final Integrated Radiometer Characterization

The integration of the final TWICE C&DH and power regulation boards presented in Chapter IV are integrated with the final TWICE front-end receivers to perform end-to-end system testing. The integration and testing of the final system is performed at NASA/JPL, Pasadena, CA on August 20, 2018 and August 21, 2018. The integrated system testing consists of functionality and compatibility testing followed by the performance analysis.

6.4.1 Integration and Compatibility of the TWICE Instrument

The compatibility of the final C&DH and power regulation boards with the final TWICE receivers designed by NGC and JPL is analyzed before performing end-to-end system testing. For the final C&DH board, the acquisition noise, and the precision and stability of the switching signal are the main concerns in addition to other verified performance specifications which are discussed in Chapter IV.

The acquisition noise performance of the ADCs at the pre-integration testing is measured as around 0.5 counts. This, in turn, indicates that the boards are performing low-noise acquisitions as expected from the testing results presented in the Radiometric Data Acquisition System section of this thesis.

The switching signal output is verified with oscilloscope measurements. The signal waveform is measured at 5 kHz without any ripple, undershoot or overshoot on the signal trace. The scope output is plotted in Figure 72 verifies that the 670 GHz LNA switching signal generated from the FPGA is suitable for the device operation.

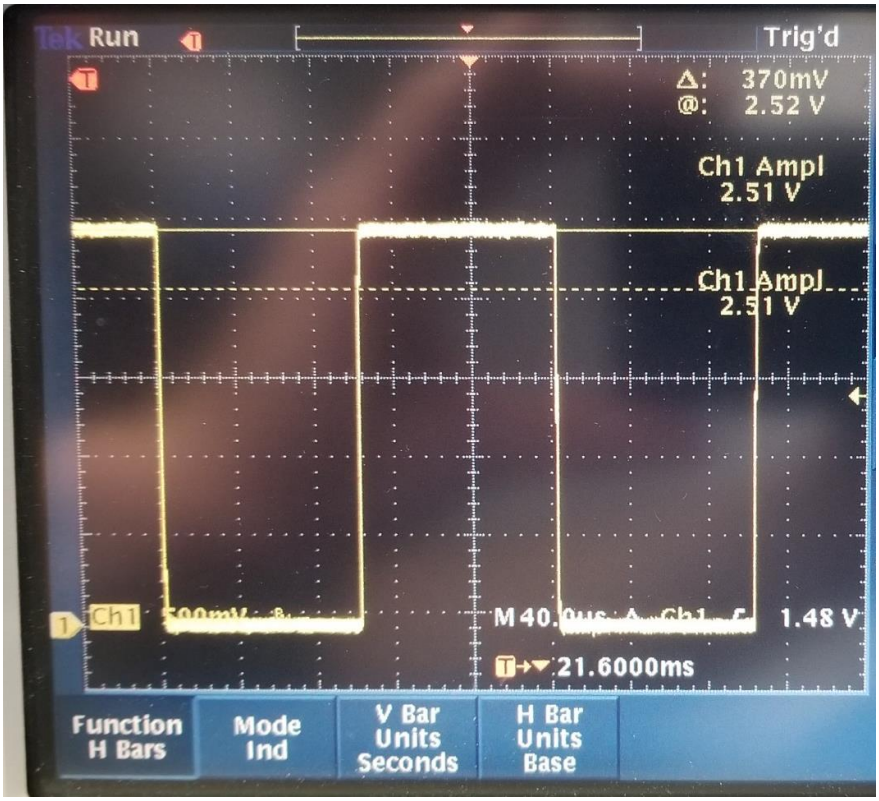

Figure 72: The oscilloscope measurements at NASA/JPL of the switching signal generated from the FPGA for the final 670 GHz receiver integration.

The next consideration is the compatibility of the final power regulation board for the operation of the final TWICE receivers. Large output voltage ripple or transients at the start-up can be dangerous for the receivers if they are beyond the design specifications. In addition, the video amplifier supply of the receivers requires the synchronization of the differential power rail at the start-up.

The start-up transients and voltage output ripple are measured with an oscilloscope for the devices which are sensitive to power supply stability. For these tests, dummy resistive loads are used mimicking the behavior of the specific device to be tested. In addition, the timing and the start-up voltage waveforms are measured for

the +10.0 V and -10.0 V sources for the video amplifiers in the TWICE receivers. The oscilloscope measurements are given in Figure 73 for the differential voltage pairs at the start-up condition. A 3 ms of time delay between two power lines is measured even though the negative voltage supply is obtained after an extra voltage regulation for the inverting the voltage from the positive power supply when compared to positive voltage supply. The measured delay is negligible for the device specifications and in comparison to a 30 ms delay of the tracking-power supply used at JPL for powering the devices. Furthermore, the power supply output is smooth and does not generate any overshoot in addition to its fast and synchronized response.

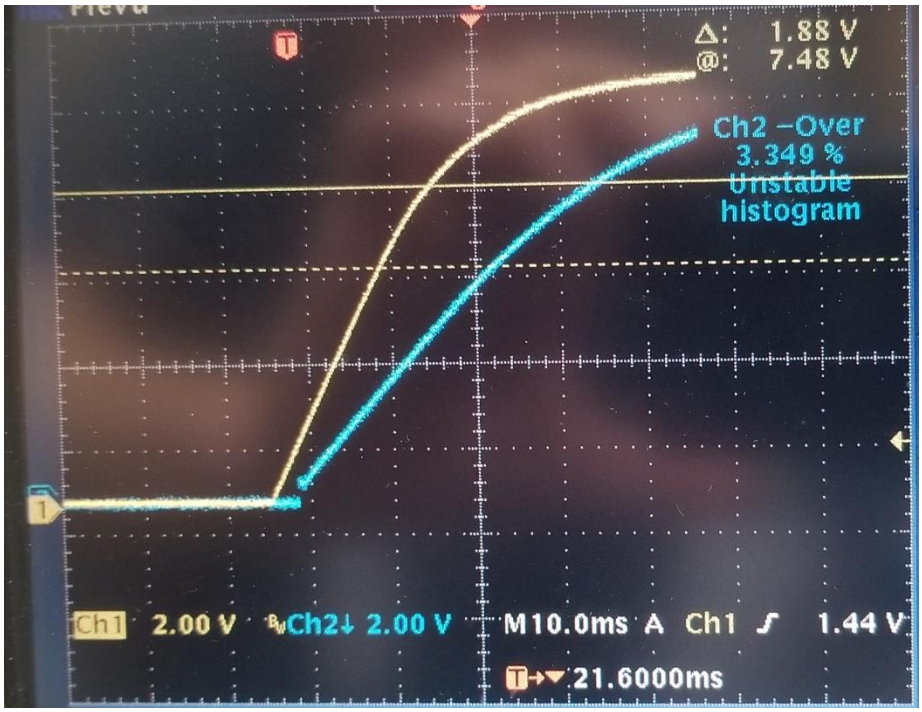

Figure 73: The oscilloscope measurements at NASA/JPL of +10.0 V and -10.0 V for video amplifier power supply. A small time delay (3 ms) between the power supplies for differential power rails of video amplifiers is detected.

The functionality of the receivers is verified separately before integrating them with the final C&DH and power regulation boards. The drain and gate of the receivers are driven by a clean laboratory power source at JPL. Figure 74 shows the final 670 GHz receiver pre-integration testing.

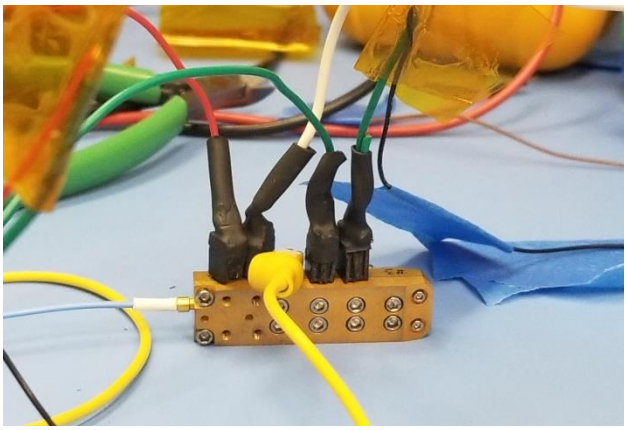

Figure 74: The TWICE final 670 GHz receiver under test at NASA/JPL.

6.4.2 End-to-End TWICE Integrated System Testing

TWICE 670 GHz receiver, 240/380 GHz receiver, the final C&DH and power regulation boards are integrated to perform end-to-end radiometric measurements. All the receivers and the C&DH board are powered from the power regulation board during the integrated system testing. The analog radiometric channels of the ADCs are performed radiometric acquisition of the analog receiver output voltage. The synchronized simultaneous acquisition is controlled by the FPGA. In addition, the 670 GHz radiometric acquisition is synchronized with the LNA switching signal generated from the FPGA.

The radiometric measurements from an ambient target at room temperature and from LN_2 cold temperature source are performed for Y-factor, radiometric sensitivity and frequency stability analysis of the final TWICE receivers. The test setup where 240/380 GHz and 670 GHz receivers are mounted on a lifted platform is shown in Figure 75. The receiver outputs are connected to analog input channels of the signal conditioning circuit on the final C&DH board. An external laptop computer is used to receive and store the measured data transmitted from the FPGA on the final C&DH board.

During the test, the receivers observed an ambient target for the first 5 minutes. Then, the LN_2 source is observed for the next 5 minutes. Finally, the test is ended with 5 minutes of ambient target measurements. The output waveforms obtained through 240 GHz, 310 GHz and 670 GHz radiometric channel measurements are

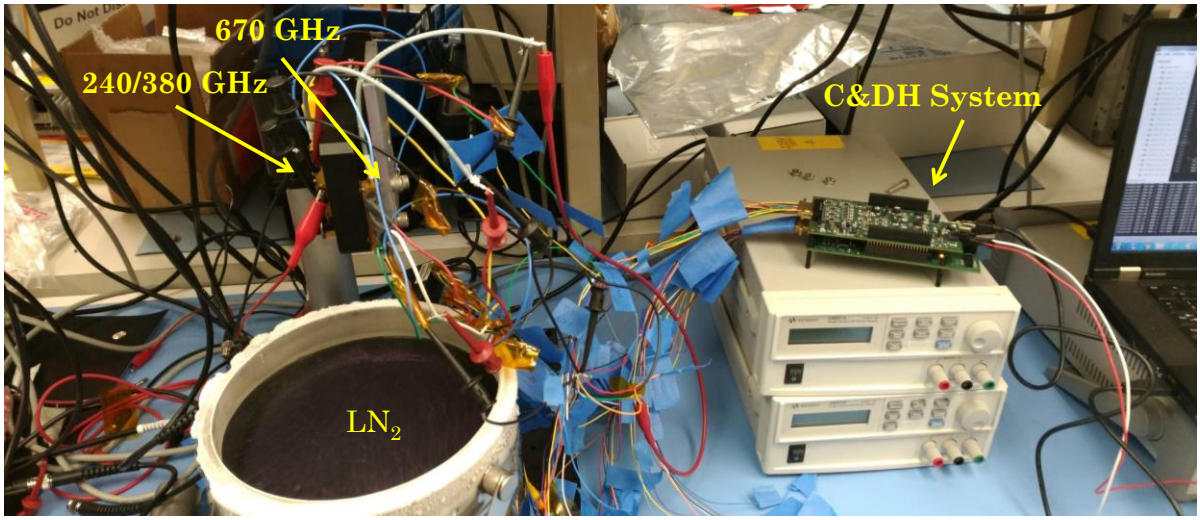

Figure 75: TWICE final integrated system is performing radiometric measurements from LN_2 for Y-factor and stability analysis

plotted in ADC counts in Figure 76. For the 670 GHz receiver, the plot is only shown for the LNA ON state output of the receiver. The plot shows that the temperature output difference observed by the radiometers is detected at the output voltage response by the radiometric acquisition. This measurement results are used in the next subsection for the receiver analysis.

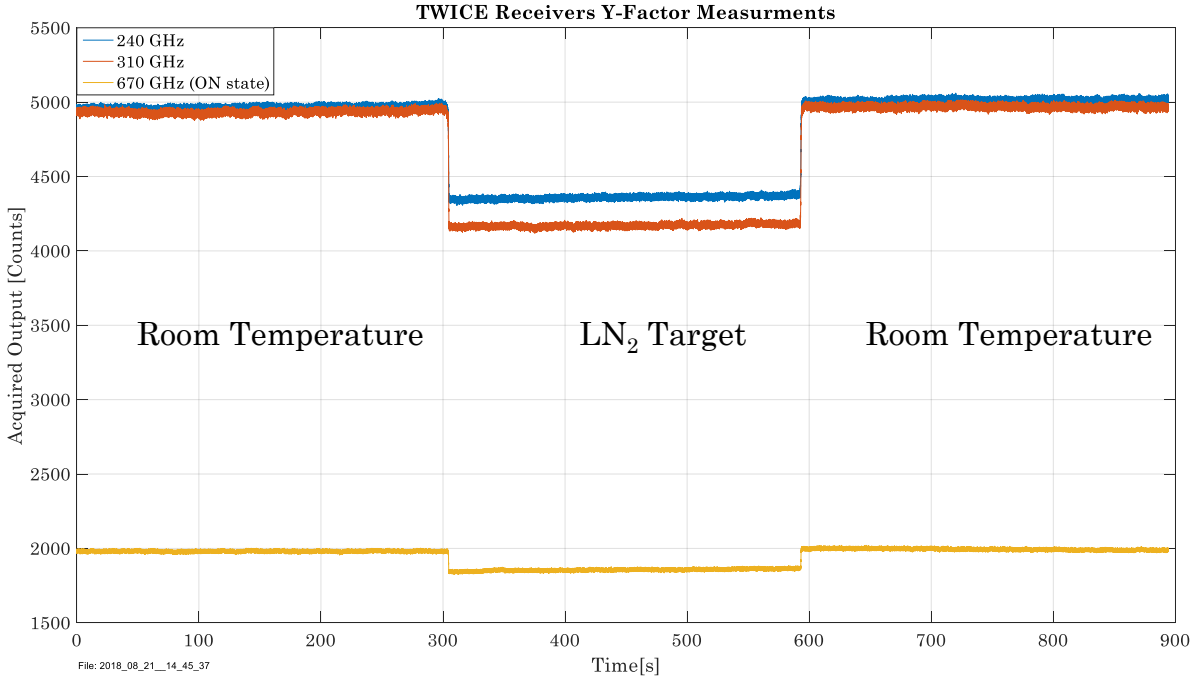

Figure 76: The final C&DH system acquired the radiometer output voltage for 240 GHz, 310 GHz and 670 GHz final TWICE receivers durin Y-factor testing/

6.4.2.1 TWICE Final 670 GHz Receiver: Y-Factor Analysis

From the measurements given in Figure 76 and using the Equation (VI.2), the Y-factor for the final 670 GHz receiver is calculated as:

$$Y = \frac{C_{amb}}{C_{cold}} = \frac{1980}{1860} = 1.0645 \qquad \text{(VI.14)}$$

Using the formula for the receiver noise temperature given in Equation (VI.3) with the assumptions of 293 K room temperature and 80 K cold target temperature, the 670 GHz receiver noise temperature is calculated as:

$$T_{rec} = \frac{T_{amb} - YT_{cold}}{Y - 1} = \frac{293 - 1.0645 * 80}{1.0645 - 1} = 3222 \text{ [K]} \quad \text{(VI.15)}$$

The noise figure of the 670 GHz receiver in dB is calculated as:

$$NF = 10 \log\left(\frac{T_{rec}}{290} + 1\right) = 10.8 \text{ dB} \quad \text{(VI.16)}$$

The noise figure calculated for the final 670 GHz receiver is very close to 10.6 dB noise figure given in the NGC specifications sheet for the receiver. This indicates that the end-to-end system tests are performed successfully.

6.4.2.2 TWICE Final 310 GHz Receiver: Y-Factor Analysis

Similar calculations with the 670 GHz analysis are made to find the Y-factor for the 310 GHz receiver:

$$Y = \frac{C_{amb}}{C_{cold}} = \frac{4930}{4170} = 1.18 \quad \text{(VI.17)}$$

Using the Y-factor result, the receiver noise temperature is found as:

$$T_{rec} = \frac{T_{amb} - YT_{cold}}{Y - 1} = \frac{293 - 1.18 * 80}{1.18 - 1} = 1089 \text{ [K]} \quad \text{(VI.18)}$$

The noise figure in dB is expressed as:

$$NF = 10\log\left(\frac{T_{rec}}{290} + 1\right) = 6.8 \text{ dB} \quad \text{(VI.19)}$$

The noise figure found for 310 GHz receiver almost perfectly matches with the expected value by the NGC indicating that the C&DH system is functioning well with the integrated system.

6.4.2.3 TWICE Final 240 GHz Receiver: Y-Factor Analysis

Analysis made for 670 GHz and 310 GHz receivers is followed for 240 GHz receiver:

$$Y = \frac{C_{amb}}{C_{cold}} = \frac{4970}{4360} = 1.14 \quad \text{(VI.20)}$$

The receiver noise temperature is found as:

$$T_{rec} = \frac{T_{amb} - YT_{cold}}{Y - 1} = \frac{293 - 1.14 * 80}{1.14 - 1} = 1442 \text{ [K]} \quad \text{(VI.21)}$$

The noise figure in dB is calculated as:

$$NF = 10\log\left(\frac{T_{rec}}{290} + 1\right) = 7.8 \text{ dB} \quad \text{(VI.22)}$$

The Y-factor results are analyzed in the next section.

6.4.2.4 Evaluation of Y-Factor Testing Results

The Y-factor testing results for 670 GHz, 310 GHz and 240 GHz receivers have shown that the acquired receiver output data are in agreement with the expected values determined by the NGC for the receiver noise temperature calculations.

These results show that the final C&DH board and power regulation board meet the design requirements for the Y-factor analysis of the system.

6.4.2.5 670 GHz LNA Switching Filter

The LNA switching technique is implemented on the final 670 GHz receiver for the 1/f noise mitigation as described for the prototype receiver design in the previous sections. The acquired data from the final 670 GHz receivers during the Y-factor measurements presented above are filtered by applying the 1/f noise filtering technique on the prototype receiver. The un-filtered Y-factor measurement data for the ON-state of the 670 GHz receiver and the filter output waveform are plotted in Figure 77. Even though the filter is designed for 1/f noise corrections from the spectrum domain data, the improvement of the measured data with the filter is apparent on the time series plot.

A frequency spectrum response is evaluated to quantify the effect of the LNA switching filter on the 1/f noise performance of the final receiver. A FFT is performed on both of datasets given in Figure 77 for the comparison. The FFT plots are given in blue for the filtered response and in orange for the un-filtered response in Figure 78. A 20 dB difference between two curves is observed indicating that the 1/f noise filter is effective on the dataset. Further analysis on the dataset shows that the white noise level of the filtered output is centered on around 10^{-9} Volts^2/Hz. This results in around 4 GHz of effective bandwidth for the receiver. A comparison of 4 GHz effective bandwidth with 20 GHz expected useful bandwidth for 670 GHz receiver given in Table 2 shows that the integrated system meets the design

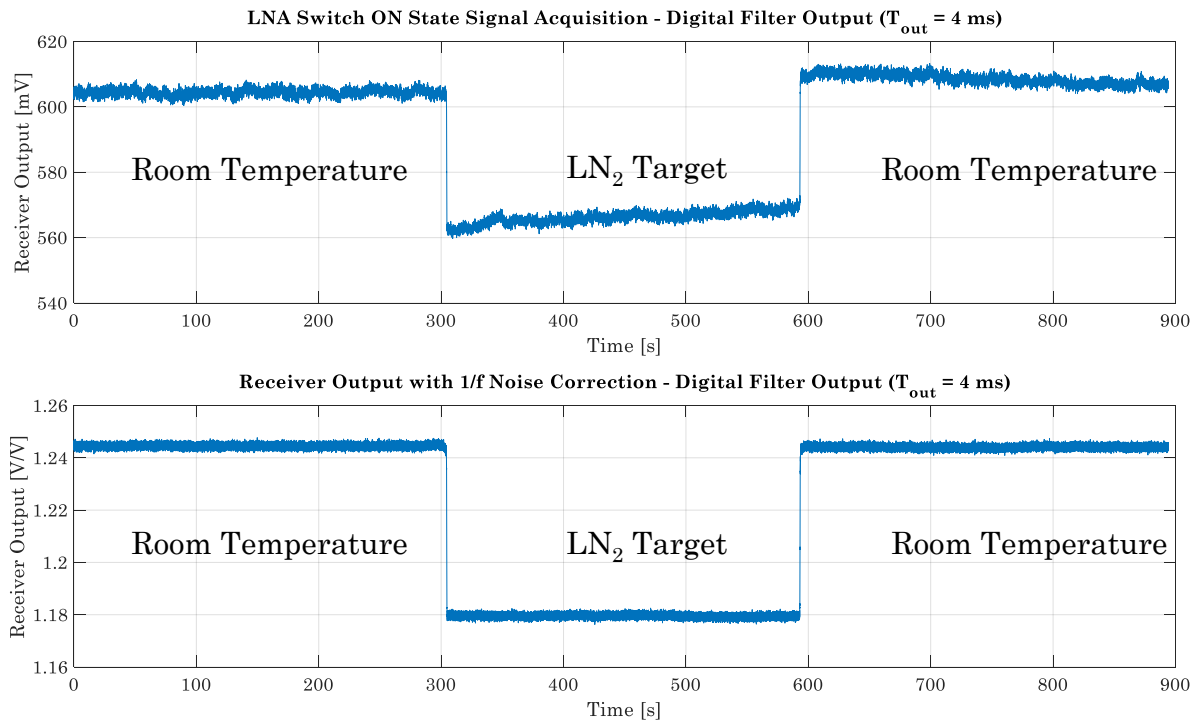

Figure 77: The final 670 GHz receiver unfiltered (top) and filtered (bottom) output results are presented.

specifications since effective bandwidth is calculated for an ideal square band. Furthermore, the slope of the frequency spectrum for the filtered waveform shows that the LNA switching technique results in 1/f noise knee frequency close to 1 Hz indicating that the mitigation technique is effective on the radiometric acquisition.

6.4.2.6 240/310 GHz Digital Filtering and FFT Analysis

The ADC sampling rate for 240 GHz and 310 GHz frequency channels are set to 20 µs while the footprint sampling time requirement is only 4 ms as given in Table 4. The digital averaging filter is applied to radiometric acquisitions performed from 240 GHz and 310 GHz channels. The output waveforms obtained after digital processing are given in counts and Volts in Figure 79. As receiver noise temperature

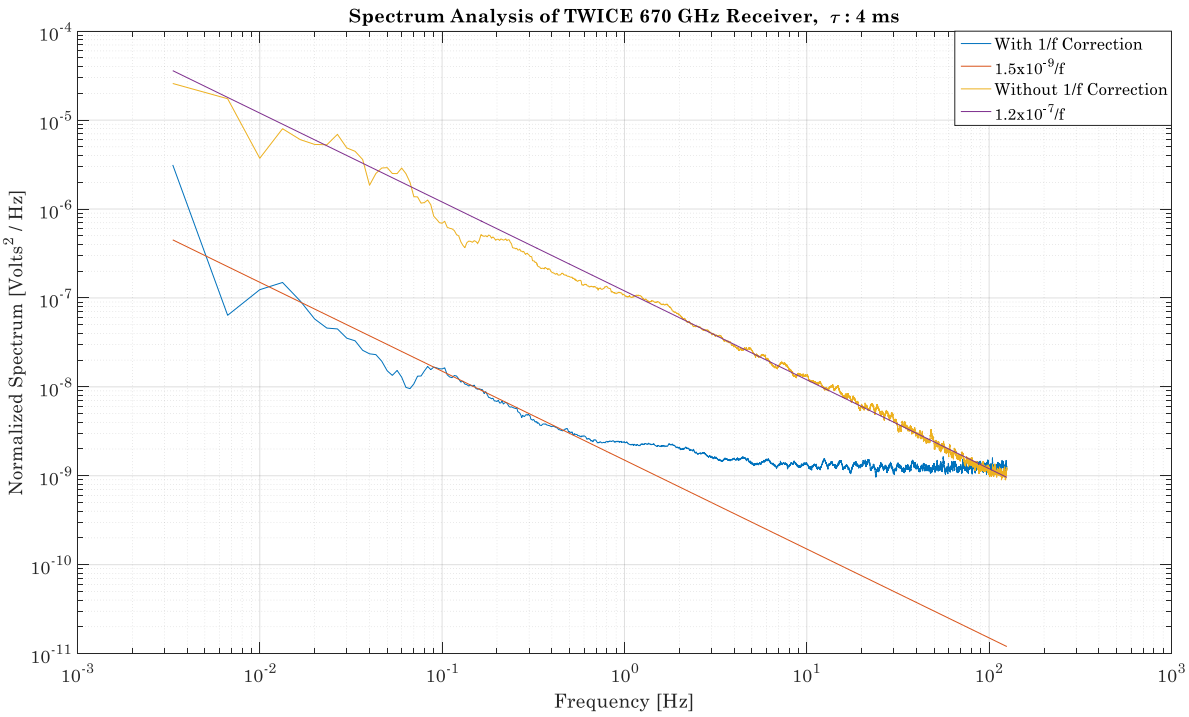

Figure 78: The frequency analysis is performed on the final 670 GHz receiver for the study of the 1/f noise filtering effect on the measurements.

calculations show 240 GHz receiver has lower dynamic range in comparison to 310 GHz receiver.

A frequency spectrum analysis is performed on the time series plot given in Figure 79 obtained from the radiometric acquisitions through the final 240 GHz and 310 GHz receivers. The FFT analysis of the final 240 GHz receiver is given in Figure 80. The plot shows that white noise floor gets flattened somewhere between 10^{-9} Volts^2/Hz and 10^{-10} Volts^2/Hz. This indicates that the receiver around 2 GHz effective bandwidth. A comparison with the bandwidths given in the design specification in in Table 2 verifies that the system is performing well. Furthermore, the spectral performance of the 240 GHz is close to those obtained for the filtered

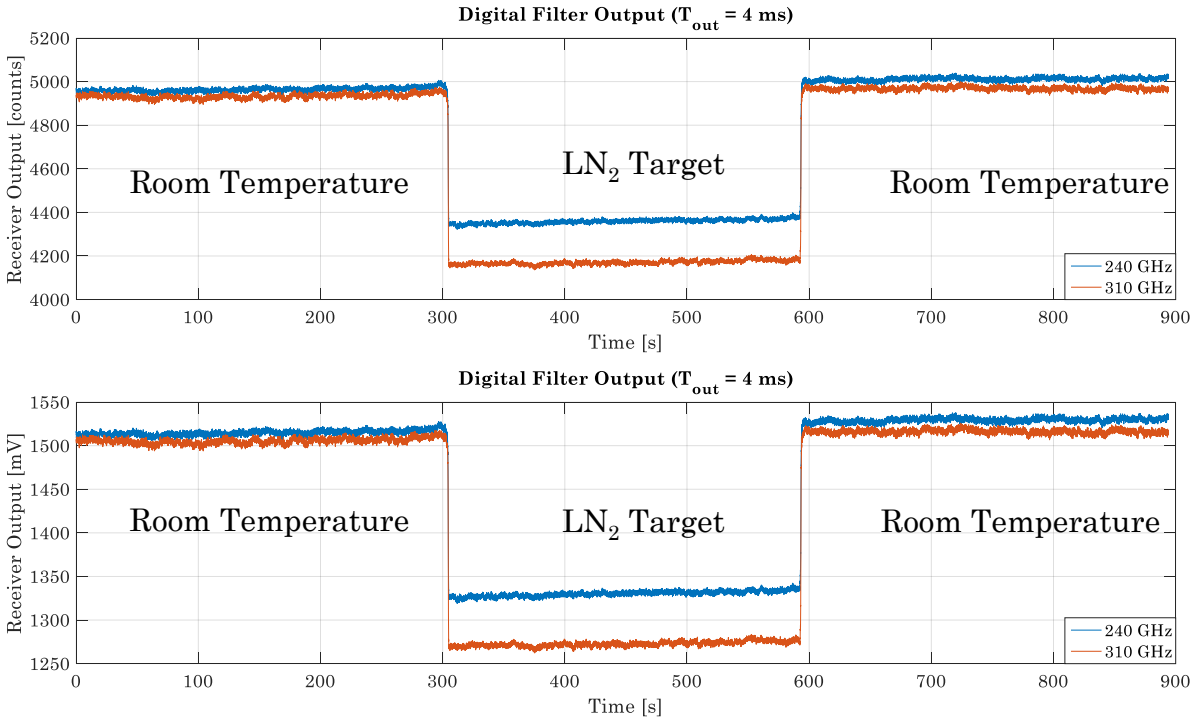

Figure 79: Digital filtering is applied on the radiometric measuremetns form the final 240 GHz and 310 GHz receivers given in counts (top) and Volts (bottom).

670 GHz receiver even though there is no LNA switching or other means of 1/f noise calibration technique being employed in the final 240 GHz receiver.

A similar FFT analysis can be also repeated for the final 310 GHz receiver. The FFT plot shown in Figure 81 indicates a similar white noise floor for the 310 GHz receiver with the 240 GHz receiver resulting in 2 GHz of effective bandwidth.

6.4.2.7 TWICE Final Integrated System: NEΔT Analysis

The radiometric gain defined in Equation (VI.7) is calculated from the Y-factor measurement results for the final TWICE 670 GHz, 310 GHz and 240 GHz radiometric channels. The measured radiometric resolution for the TWICE channels

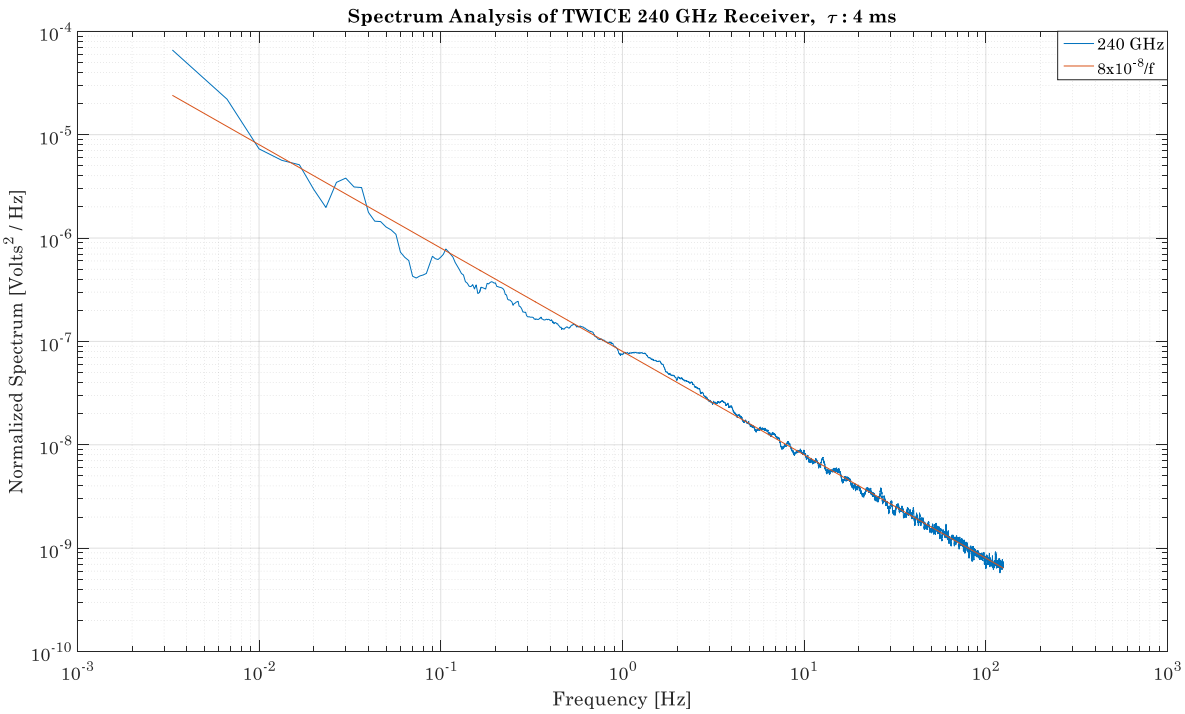

Figure 80: FFT analysis of the final 240 GHz receiver.

at these frequencies are found by using the definition in Equation (VI.8). The standard deviation is obtained from the Y-factor measurements to be used in the calculation of the NEΔT.

The results for the NEΔT analysis is summarized in Table 23 for three radiometric channels tested. All three radiometric channels have acceptable performance in terms of the radiometric sensitivity considering that those results are obtained for 4 ms of integration time. It is also important to note that the NEΔT performance of the 670 GHz receiver is substantially improved in parallel to expectation based on the analysis made in the previous sub-section. The results presented in this analysis indicate that the noise coupled into the radiometric measurements by the final C&DH board is negligible.

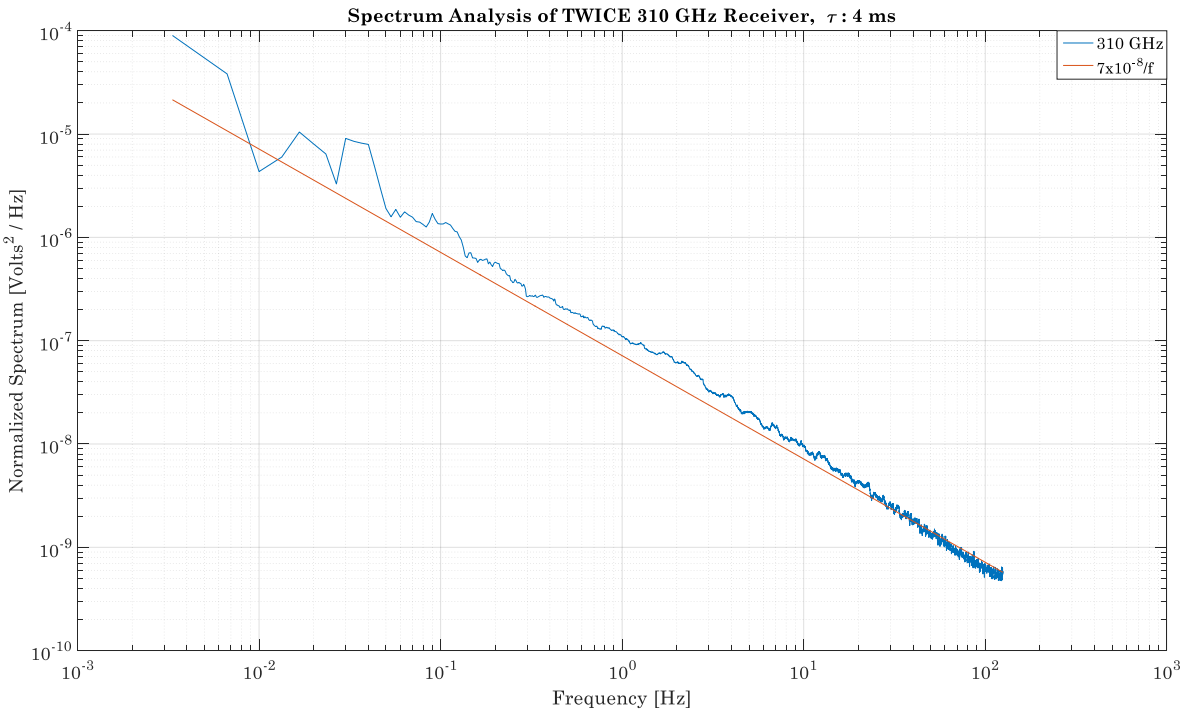

Figure 81: FFT analysis of the final 310 GHz receiver.

6.5. Conclusions

The integration of the C&DH system with the TWICE receivers is performed. The stability, accuracy and sensitivity of the radiometric system are the main parameters determining the quality of the radiometric measurements. Y-factor and radiometric noise-equivalent delta-temperature characterization is investigated. The stability of the radiometric systems is studied both in the time and frequency domain. The effects of noise sources on the radiometric signals are analyzed. The mitigation technique for 1/f noise from the 670 GHz receiver measurements is designed and successfully tested.

Table 23: The NEΔT analysis of the final TWICE receivers.

Frequency	Gain [K/counts]	Measured NEΔT [K]	Integration Time [ms]
240 GHz	0.3492	1.6	4
310 GHz	0.2803	1.3	4
670 GHz (Switch: ON)	1.775	3.6	4
670 GHz (Filtered)	3282 [K/ratio*]	2.3	4

*ratio: (ON State/OFF State) = [V/V]

End-to-end system analysis and radiometric measurements are performed. The integrated system characterization is studied. The results are compared with the design requirements for the TWICE radiometer instrument.

The final C&DH and power regulation boards are compatible with the final TWICE receivers. The integrated system performs low-noise synchronized and simultaneous radiometric acquisitions. The 670 GHz 1st LNA block is successfully controlled by the FPGA on the C&DH board. The switching is synchronized with the radiometric acquisition. The digital averaging filter is applied to all the radiometric channels.

Chapter VII Radiometer Wave Model

Radiometer wave model is a useful technique for radiometer noise characterization since it allows analyzing each part of the radiometer utilizing the scattering matrices to calculate the end-to-end flow of the noise as a signal. Scattering matrices provide easiness to calculate the interaction of each part with other parts within the radiometer instrument. Signal flow-graph theory is a practical way to calculate the waves travelling within the system hardware.

This chapter performs a complete noise characterization of a radiometer instrument as well as individual noise performance of each part and the coupling effects on each part from the other parts of the instrument. The goal is to obtain a radiometer noise wave model to analyze the noise characteristics of radiometers and build an artificial radiometer with controlled parameters effecting noise performance of the system for the neural network calibration model that will be presented in the next chapter.

7.1. Radiometer Noise Wave Representation

A Dicke-switch direct detection radiometer has been used to provide a generalized idea that can be applied to any architecture. The radiometer block diagram is given in Figure 82. The incident energy upon the antenna is denoted by the apparent antenna temperature distribution (T_{AP}) perceived as antenna temperature (T_{ant}) by the antenna that is measured as the voltage (V_{out}) at the output of the receiver.

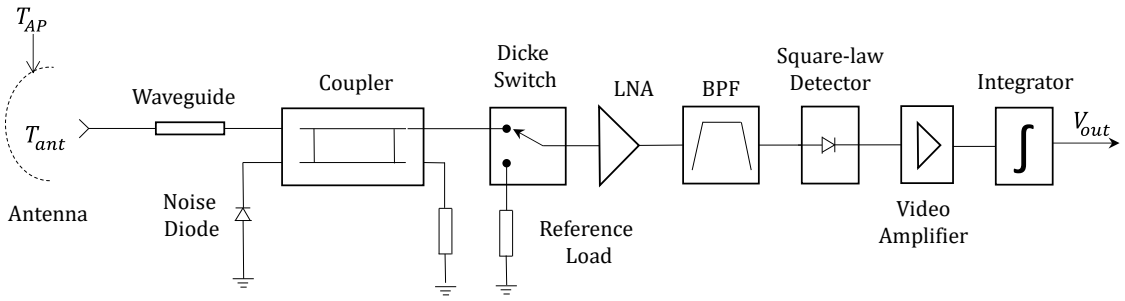

Figure 82: A Dicke-switching direct detection radiometer.

The block diagram of a Dicke-switch direct detection radiometer is useful to analyze the radiometer architecture for radiometric operational characteristics but does not provide easiness to perform a noise analysis. Therefore, the radiometer instrument given in Figure 82 is illustrated in Figure 83 for the noise wave diagram. The connections of each block on this diagram are made to ease the understanding of the noise waves propagating in the system. It is not intended to show the physical connections of the system.

In the noise-wave representation, $\bar{a}$ (5x1) and $\bar{b}$ (5x1) are the incident and outgoing waves respectively defined over a 1 Hz bandwidth. Scattering matrix is given as $\bar{\bar{S}}$ (5x5) and the internally generated noise waves are represented by $\bar{n}$ (5x1). The outgoing waves are defined as the scattered incident waves with internally generated noise added into [115]:

$$\bar{b} = \bar{\bar{S}}\bar{a} + \bar{n} \tag{VII.1}$$

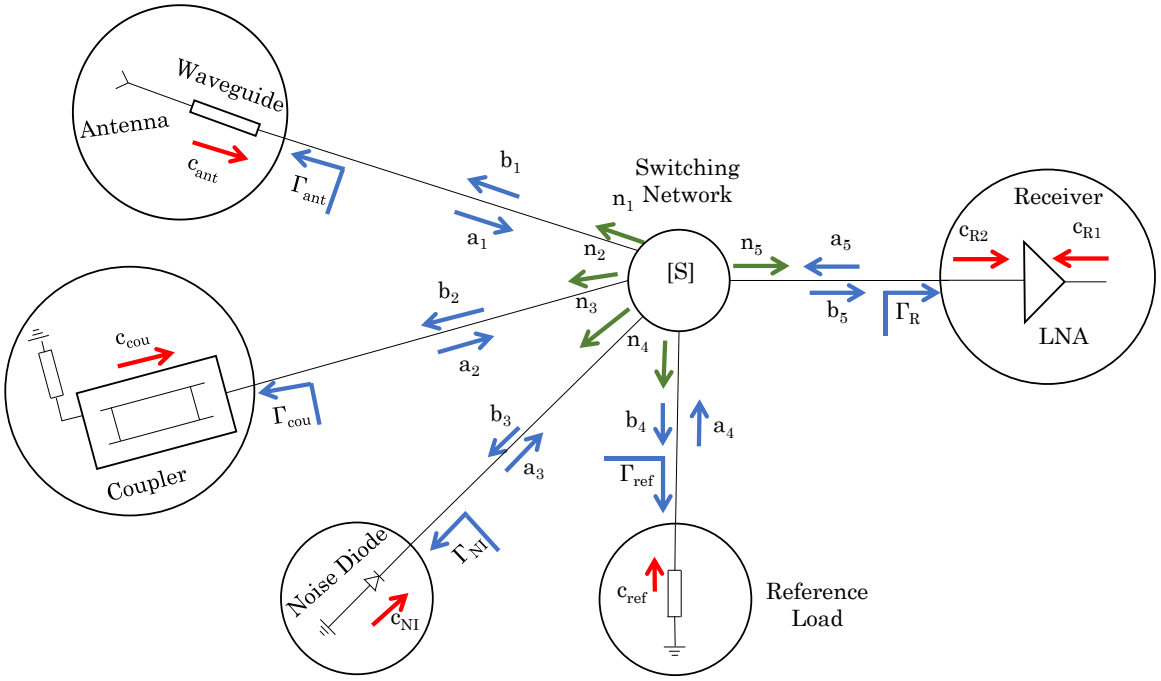

Figure 83: Noise-wave representation of the Dicke-switching direct-detection radiometer shown in Figure 82.

Similarly, the incident waves ($\bar{a}$) are represented in terms of reflected incoming waves and the source waves ($\bar{a}_s$) [116]:

$$\bar{a} = \bar{\bar{\Gamma}}\bar{b} + \bar{a}_s \tag{VII.2}$$

where $\bar{\bar{\Gamma}}$ is a diagonal matrix such that each entry of the matrix represents the reflection coefficient looking into the port:

$$\bar{\bar{\Gamma}} = diag([\Gamma_{ant}\ \Gamma_{cou}\ \Gamma_{NI}\ \Gamma_{ref}\ \Gamma_R]) \tag{VII.3}$$

The source waves ($\bar{a}_s$) in Equation (VII.2) are:

$$\bar{a}_s = [c_{ant}\ c_{cou}\ c_{NI}\ c_{ref}\ c_{R1}]^T \tag{VII.4}$$

where c_{ant} is the noise collected by the antenna from the scene, c_{cou} is the noise generated by the internal matched load of the coupler, c_{NI} is the noise generated by the noise diode and injected by the coupler, c_{ref} is the noise generated by the reference load and c_{R1} is the noise generated by the receiver towards its input.

The final goal of the noise wave calculations of the radiometer is to derive a relationship relating the input temperature and noise temperatures of different parts of the radiometer to the output voltage that is needed for radiometer calibration analysis. The outgoing waves are represented in terms of source waves by using Equation (VII.2) in Equation (VII.1) as:

$$\bar{b} = \bar{\bar{S}}\bar{a} + \bar{n} = \bar{\bar{S}}\left(\bar{\bar{\Gamma}}\bar{b} + \bar{a}_s\right) + \bar{n} = \bar{\bar{S}}\bar{\bar{\Gamma}}\bar{b} + \bar{\bar{S}}\bar{a}_s + \bar{n} \tag{VII.5}$$

$$\bar{b} - \bar{\bar{S}}\bar{\bar{\Gamma}}\bar{b} = \bar{\bar{S}}\bar{a}_s + \bar{n} \tag{VII.6}$$

$$\left(\bar{\bar{I}} - \bar{\bar{S}}\bar{\bar{\Gamma}}\right)\bar{b} = \bar{\bar{S}}\bar{a}_s + \bar{n} \tag{VII.7}$$

where $\bar{\bar{I}}$ is 5x5 identity matrix. Then, it is defined as:

$$\bar{b} = \left(\bar{\bar{I}} - \bar{\bar{S}}\bar{\bar{\Gamma}}\right)^{-1}\left(\bar{\bar{S}}\bar{a}_s + \bar{n}\right) \tag{VII.8}$$

Now a new variable is defined to ease the representations of the equations:

$$\bar{\bar{\Lambda}} \stackrel{\text{def}}{=} \left(\bar{\bar{I}} - \bar{\bar{S}}\bar{\bar{\Gamma}}\right)^{-1} \tag{VII.9}$$

$$\bar{b} = \left(\bar{\bar{I}} - \bar{\bar{S}}\bar{\bar{\Gamma}}\right)^{-1}\left(\bar{\bar{S}}\bar{a}_s + \bar{n}\right) = \bar{\bar{\Lambda}}\left(\bar{\bar{S}}\bar{a}_s + \bar{n}\right) \tag{VII.10}$$

$$\bar{b} = \bar{\bar{\Lambda}}\bar{\bar{S}}\bar{a}_s + \bar{\bar{\Lambda}}\bar{n} \tag{VII.11}$$

With the addition of the noise waves at the input of the amplifier, the input waves are represented as [117]:

$$\overline{b'} = \bar{b} + \bar{c} \tag{VII.12}$$

b' in Equation (VII.12) is the equivalent total input wave and $\bar{c}$ stands for the noise waves at the input of the LNA and defined as:

$$\bar{c} = [0\ 0\ 0\ 0\ c_{R2}] \tag{VII.13}$$

where c_{R2} is the noise generated by the receiver at the input of LNA.

The waves at the output of the LNA before the filter and the can be written as:

$$\overline{b''} = S_{21}\overline{b'} \tag{VII.14}$$

where the gain of the amplifier is represented in terms of the S parameters of the amplifier as [27]:

$$G = |S_{21}|^2 \tag{VII.15}$$

The power detected by the detector diode is the auto-correlation of the input waves at the input of the detector given by Equation (VII.14). The detector power can be written as when the effect of the filter on the waves except the limiting the bandwidth is ignored [118], [117]:

$$\langle b''(b'')^H \rangle = G\langle b'(b')^H \rangle \tag{VII.16}$$

$$\langle b''(b'')^H \rangle = G\overline{\overline{N}} \tag{VII.17}$$

where $\overline{\overline{N}}$ is defined as the correlation matrix of the input waves. Then the voltage detected by the square-law detector is given as [27], [118]:

$$V_{det} = C_d G\overline{\overline{N}}_{(5,5)} \tag{VII.18}$$

where C_d is the constant of the power detector. The voltage at the output of the video amplifier is:

$$V_{video} = G_{VA}C_d G\overline{\overline{N}}_{(5,5)} \tag{VII.19}$$

where G_{VA} is the gain of video amplifier (V/V). The voltage at the output of the low-pass filter that is to be digitized by the back-end board can be written as:

$$V_{LPF} = g_{LPF}G_{VA}C_d G\overline{\overline{N}}_{(5,5)} \tag{VII.20}$$

where g_{LPF} is the attenuation of the low-pass filter. Finally, the noise matrix $\overline{\overline{N}}$ needs to be represented in terms of temperature to reach our goal in noise wave analysis for calibration analysis. In this study, the Raleigh-Jeans limit of the Planck

function is used [27]. The noise waves over 1 Hz bandwidth are expressed as a product of Boltzmann constant (k_B) and the physical temperature (T) [119]. The equivalent input total wave defined in Equation (VII.12) and its Hermitian is given as:

$$\bar{b'} = \bar{\bar{\Lambda}}\bar{\bar{S}}\bar{a}_s + \bar{\bar{\Lambda}}\bar{n} + \bar{c} \tag{VII.21}$$

$$\begin{aligned}\left(\bar{b'}\right)^H &= \left(\bar{\bar{\Lambda}}\bar{\bar{S}}\bar{a}_s + \bar{\bar{\Lambda}}\bar{n} + \bar{c}\right)^H \\ &= \bar{a}_s{}^H\bar{\bar{S}}^H\bar{\bar{\Lambda}}^H + \bar{n}^H\bar{\bar{\Lambda}}^H + \bar{c}^H\end{aligned} \tag{VII.22}$$

Then the noise matrix given in Equation (VII.17) is calculated as:

$$\bar{\bar{N}} = \langle b'(b')^H \rangle \tag{VII.23}$$

$$\bar{\bar{N}} = \langle (\bar{\bar{\Lambda}}\bar{\bar{S}}\bar{a}_s + \bar{\bar{\Lambda}}\bar{n} + \bar{c}).(\bar{a}_s{}^H\bar{\bar{S}}^H\bar{\bar{\Lambda}}^H + \bar{n}^H\bar{\bar{\Lambda}}^H + \bar{c}^H) \rangle \tag{VII.24}$$

$$\begin{aligned}\bar{\bar{N}} = {} & \bar{\bar{\Lambda}}\bar{\bar{S}}\langle \bar{a}_s\bar{a}_s{}^H \rangle \bar{\bar{S}}^H\bar{\bar{\Lambda}}^H + \bar{\bar{\Lambda}}\langle \bar{n}\bar{a}_s{}^H \rangle \bar{\bar{S}}^H\bar{\bar{\Lambda}}^H + \langle \bar{c}\bar{a}_s{}^H \rangle \bar{\bar{S}}^H\bar{\bar{\Lambda}}^H + \bar{\bar{\Lambda}}\bar{\bar{S}}\langle \bar{a}_s\bar{n}^H \rangle \bar{\bar{\Lambda}}^H \\ & + \bar{\bar{\Lambda}}\langle \bar{n}\bar{n}^H \rangle \bar{\bar{\Lambda}}^H + \langle \bar{c}\bar{n}^H \rangle \bar{\bar{\Lambda}}^H + \bar{\bar{\Lambda}}\bar{\bar{S}}\langle \bar{a}_s\bar{c}^H \rangle + \bar{\bar{\Lambda}}\langle \bar{n}\bar{c}^H \rangle + \langle \bar{c}\bar{c}^H \rangle\end{aligned} \tag{VII.25}$$

Each term in the above equation can be calculated as:

1. The correlation of the source waves:

$$\langle \bar{a}_s\bar{a}_s{}^H \rangle = k_B\bar{\bar{T}}_s \tag{VII.26}$$

where k_B is the Boltzmann constant and $\bar{\bar{T}}_s$ is the temperature matrix defined as:

$$\bar{\bar{T}}_s = diag[T_A\ T_{cou}\ T_{NI}\ T_{ref}\ T_R] \quad \text{(VII.27)}$$

where T_A is the antenna physical temperature, T_{cou} is the noise temperature of the matched load of the coupler, T_{NI} is the equivalent noise temperature injected thorough the noise diode, T_{ref} is the physical temperature of the reference load and T_R is the physical temperature of the isolator at the input of the LNA [116], [118]

2. The correlation of the noise and source waves: The noise waves ($\bar{n}$) are uncorrelated with the source waves ($\bar{a}_s$) [116]:

$$\langle \bar{n}\bar{a}_s{}^H \rangle = 0 \quad \text{(VII.28)}$$

3. The correlation of the noise waves at the input of the receiver (LNA) and the source waves: It is assumed that the isolator at the input of the LNA isolates the noise to (c_{R2}) and from (c_{R1}) the receiver:

$$\langle \bar{c}\bar{a}_s{}^H \rangle = [0\ 0\ 0\ 0\ c_{R2}]^T [c_{ant}\ c_{cou}\ c_{NI}\ c_{ref}\ c_{R1}]^* \quad \text{(VII.29)}$$

4. Similar to the second term calculated in Equation (VII.28):

$$\langle \bar{a}_s \bar{n}^H \rangle = 0 \quad \text{(VII.30)}$$

5. The correlation of the noise waves:

a. Bosma's Theorem: The noise waves contributed by the network are simply those necessary to cancel the effects of the correlation present in the scattered waves ($\bar{\bar{S}}\bar{a}$, given in Equation (VII.1)) to maintain the

lack of the correlation in the output waves and to achieve balance in power flow [120]. Thus, the correlation of the noise waves is formulized as;

$$\langle \bar{n}\bar{n}^H \rangle = k_B T_{SN}\left(\bar{\bar{I}} - \bar{\bar{S}}\bar{\bar{S}}^H\right) \tag{VII.31}$$

where T_{SN} is the physical temperature of the switching network.

6. The correlation of the noise waves and the noise generated at the input of the LNA are uncorrelated [116]:

$$\langle \bar{c}\bar{n}^H \rangle = 0 \tag{VII.32}$$

7. Similar to the third term calculated in Equation (VII.29):

$$\langle \bar{a}_s \bar{c}^H \rangle = 0 \tag{VII.33}$$

8. Similar to the sixth term calculated in Equation (VII.32):

$$\langle \bar{n}\bar{c}^H \rangle = 0 \tag{VII.34}$$

9. The correlation of the noise added at the receiver:

$$\langle \bar{c}\bar{c}^H \rangle = [0\ 0\ 0\ 0\ c_{R2}]^T [0\ 0\ 0\ 0\ c_{R2}]^* = diag[0\ 0\ 0\ 0\ k_B T_{LNA}] \tag{VII.35}$$

$$\langle \bar{c}\bar{c}^H \rangle = k_B \bar{\bar{C}} \tag{VII.36}$$

$$\bar{\bar{C}} = diag[0\ 0\ 0\ 0\ T_{LNA}] \tag{VII.37}$$

where T_{LNA} is the equivalent LNA (receiver) noise temperature [116], [117].

The noise matrix is further simplified by employing the resulting calculation of each term given above:

$$\bar{\bar{N}} = \bar{\bar{\Lambda}}\bar{\bar{S}}k_B\bar{\bar{T}}_s\bar{\bar{S}}^H\bar{\bar{\Lambda}}^H + \bar{\bar{\Lambda}}k_BT_{SN}\left(\bar{\bar{I}} - \bar{\bar{S}}\bar{\bar{S}}^H\right)\bar{\bar{\Lambda}}^H + k_B\bar{\bar{C}} \tag{VII.38}$$

$$\bar{\bar{N}} = k_B\left[\bar{\bar{\Lambda}}\bar{\bar{S}}\bar{\bar{T}}_s\bar{\bar{S}}^H\bar{\bar{\Lambda}}^H + \bar{\bar{\Lambda}}T_{SN}\left(\bar{\bar{I}} - \bar{\bar{S}}\bar{\bar{S}}^H\right)\bar{\bar{\Lambda}}^H + \bar{\bar{C}}\right] \tag{VII.39}$$

$$\bar{\bar{T}}_{RAD} \stackrel{\text{def}}{=} \left[\bar{\bar{\Lambda}}\bar{\bar{S}}\bar{\bar{T}}_s\bar{\bar{S}}^H\bar{\bar{\Lambda}}^H + \bar{\bar{\Lambda}}T_{SN}\left(\bar{\bar{I}} - \bar{\bar{S}}\bar{\bar{S}}^H\right)\bar{\bar{\Lambda}}^H + \bar{\bar{C}}\right] \tag{VII.40}$$

$$\bar{\bar{N}} = k_B\bar{\bar{T}}_{RAD} \tag{VII.41}$$

where T_{SN} is the physical temperature of the Dicke switch, $\bar{\bar{C}}$ is the diagonal correlation noise matrix of the LNA depends on the its physical temperature (T_{LNA}) and ($\bar{\bar{T}}_s$) is the temperature matrix defined in Equation (VII.27).

Finally, using Equation (VII.20), the analog voltage digitized by the back-end is expressed as:

$$V_{LPF} = k_Bg_{LPF}G_{VA}C_dGB\bar{\bar{T}}_{RAD\,(5,5)} \tag{VII.42}$$

where G is the gain of the LNA (V/V), C_d is detector diode constant (V/W), G_{VA} is the gain of video amplifier (V/V) and B is the bandwidth (Hertz).

7.2. Radiometer System Consideration

Equation (VII.42) is the final equation that will be used to generate radiometer output voltage. Therefore, the next step is to define the radiometer parameters for simulation of the developed artificial radiometer.

7.2.1 Antenna Parameters

Antenna parameters are analyzed as a separate section different than the other parts of the radiometer since it requires further calculations to analyze the loss generated within the antenna block.

The antenna block includes the antenna itself and the waveguide connecting antenna to the radiometer. The antenna model is modelled by including all the losses in the antenna and waveguide as well as the noise generated by these components. The definitions and assumptions used in this model are listed as:

- Assume that the antenna measures a scene having the equivalent brightness temperature of antenna which is represented as T_{BA}. Please note that it is not the brightness temperature of the scene, it is the brightness temperature of the scene realized by the antenna. In other words, the apparent temperature of the scene (T_{AP}) is assumed to be equal to the temperature realized by the antenna. This term is used to distinguish the effect of the scene temperature from the effect on antenna physical temperature on the collected noise power by the antenna. One should introduce the radiation pattern calculation into the calculations to estimate the brightness temperature of the scene as the following:

$$T_{BA} = \frac{\iint T_{AP}(\theta,\varphi)F_n(\theta,\varphi)d\Omega}{F_n(\theta,\varphi)d\Omega} \quad \text{(VII.43)}$$

where F_n is the normalized antenna radiation pattern over 4π steradian and θ and φ are elevation and azimuth angles of the antenna respectively [27].

- Assume that antenna has uniform physical temperature of T_{Ant_PHY}. In the real case, more than one thermistor could be used to monitor the physical temperature of the antenna where antenna has big aperture resulting in large temperature gradients across the surface.
- The antenna loss is defined by L_{ANT}.
- The waveguide loss is expressed with L_{WG}.
- The transmission-line physical temperature is represented with T_{WG_PHY}.
- The equivalent noise temperature of the antenna and the waveguide is called as T_{Ant-WG}.
- The noise temperature of the waveguide defined at the output of the waveguide is T_{WG}.
- The noise temperature of the antenna defined at its output is T_{Ant}.

The antenna temperature at the input port of the receiver T_A, as defined in the temperature matrix in Equation (VII.27) is expressed as:

$$T_A = T_{Meas} + T_{Ant-WG} \quad \text{(VII.44)}$$

where T_{Meas} is the antenna measurements of the scene attenuated by the losses in the waveguide and the antenna expressed as:

$$T_{Meas} = \frac{T_{B-Ant}}{L_{ANT} L_{WG}} \tag{VII.45}$$

The equivalent noise temperature of the antenna and waveguide in Equation (VII.44) is defined in terms of antenna (T_{Ant}) and waveguide noise temperatures (T_{WG}) and waveguide loss (L_{WG}):

$$T_{Ant-WG} = \frac{T_{Ant}}{L_{WG}} + T_{WG} \tag{VII.46}$$

The antenna and waveguide noise temperatures are expressed in terms of their physical temperatures as the following:

$$T_{Ant} = \left(1 - \frac{1}{L_{ANT}}\right) * T_{Ant\_PHY} \tag{VII.47}$$

$$T_{WG} = \left(1 - \frac{1}{L_{WG}}\right) * T_{WG\_PHY} \tag{VII.48}$$

7.2.2 Radiometer System Parameters

The specifications used to define the hardware parts are summarized in Table 24. Please note that the parameters chosen on this table are determined to generate wide-range of various operating scenarios for testing worst-case estimates for a radiometer operation.

7.3. Radiometer Noise Wave Model Demonstration

Several test cases have been generated to demonstrate the system operation and capability as well as checking the effect of model parameters on the radiometer output voltage measurements.

Table 24: Parameters of a typical Dicke-switch direct detection microwave radiometer given in Figure 82 [27], [34], [117], [118]. Note input parameters have much wider range than a conventional radiometer.

Parameter	Value
Antenna Reflection Coefficient	0.03
Antenna Loss	0.05 dB
Waveguide Loss	0.05 dB
Coupling Factor	15 dB
Excess Noise Ratio (ENR) of Noise Diode	25 dB ± 0.01 dB/K
Directivity of Coupler	20 dB
Return Loss from the Dicke Load	30 dB
Isolation of the Dicke Switch	25 dB
Insertion Loss of the Dicke Switch	0.15 dB
Return Loss of the Dicke Switch	23 dB
LNA Reflection Coefficient	0.03
Power Detector Constant	2300 [V/W]

Among those tests, the basic operational capability of the internal calibration sources including noise diode and matched reference load have been checked for their operational characteristics. Figure 84 shows a case where the radiometer output is plotted for various antenna temperature observations when the Dicke-switch is on the reference load, the Dicke-switch on the antenna path with noise injected and without noise injected from the noise diode. As clearly seen from the

plot, the operational behavior for the radiometer given is an expected scenario among different sources.

Further tests have been conducted to analyze the noise waves within the receiver. From the tests, it has been observed that the coupling between the various design elements of the radiometer degrade the performance of the radiometer as expected. The tests conducted are not only useful for modeling a functional radiometer for deep learning calibration that will be explained in the next chapter, but also important to fully assess the radiometer operational characteristics and factors affecting its performance.

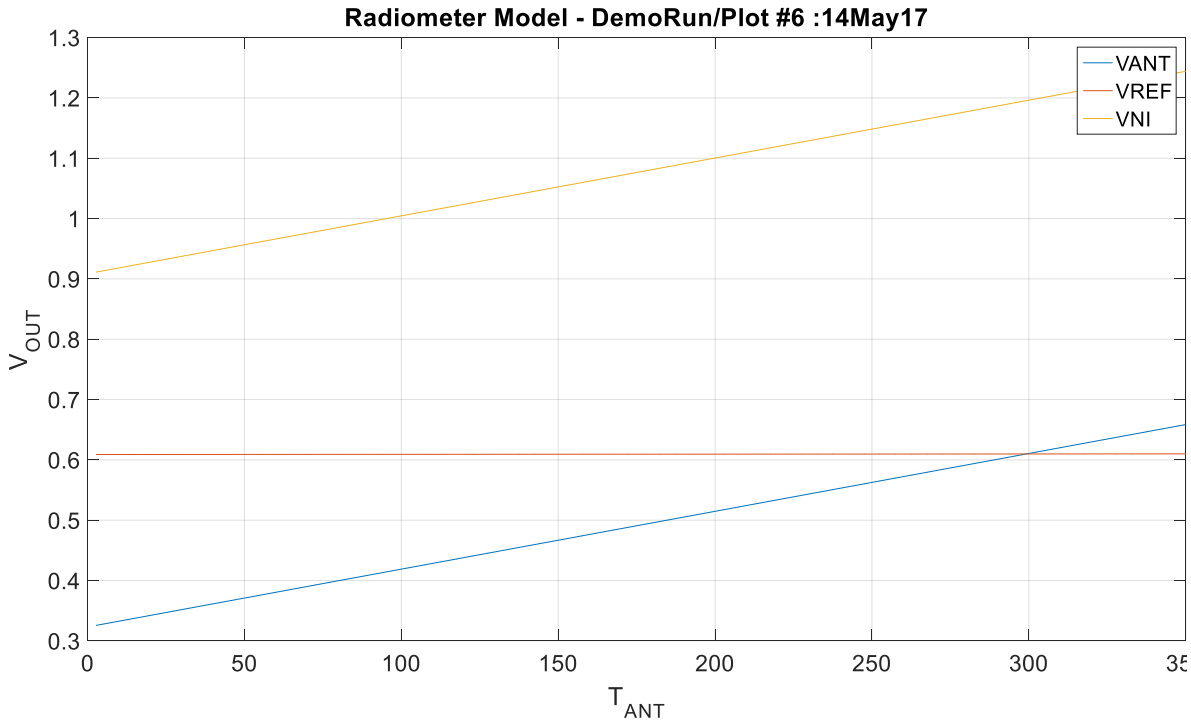

Figure 84: The output voltage reading of the Dicke-switching radiometer given in Figure 82 with respect the antenna temperature measurements over a wide dynamic range.

7.4. Conclusions

The radiometer noise-wave model is developed to perform radiometer noise characterization and calculations. A Dicke-switching direct-detection radiometer is artificially generated for performing noise analysis. The effect of each subsystem in the designed radiometer architecture on the noise performance of the system is investigated for several different cases. The effect of conventional calibrators and how they interface with the rest of the radiometer instrument is analyzed. The designed noise-wave model is used not only for the demonstration of the deep learning calibrator designed in the next chapter but also for improving the knowledge on the radiometer operation.

Chapter VIII Radiometer Calibration

This chapter presents a deep learning based new technique for the calibration of microwave and millimeter wave radiometers. The conventional calibration techniques are explained to provide a comparable basis for the proposed new technique. The new technique is studied in detail. The advantages and pending issues are discussed. The demonstration of the new method is first performed on an artificially generated radiometer using the wave model on the previous chapter. Then, the calibration technique is applied to radiometric measurements of High Frequency Microwave and Millimeter-wave Radiometer (HAMMR) instrument obtained during the West Coast Flight Campaign in 2014.

8.1. Introduction

Microwave and millimeter-wave radiometers have been widely used to improve understanding of the distribution of atmospheric water vapor and its dynamics for decades to provide information for studies in hydrology, agriculture, meteorology, climatology and oceanography [27], [121]. Accuracy, sensitivity, stability and measurement uncertainty are used as figures of merit of a radiometer. The accuracy of a radiometer determines the reliability of the retrieved parameters from the measurements. On the other hand, radiometric resolution (sometimes called sensitivity) provides the minimum detectable change of a radiometer due to its internal noise. Therefore, improved accuracy and radiometric resolution improve the quality of the geophysical products retrieved from radiometric measurements,

including water vapor, cloud water and ice contents, soil moisture, sea-surface wind speed and superficial sea salinity [35].

Calibration plays a major role in determining the radiometric accuracy and stability. There has been various calibration techniques employed in the radiometers that are discussed in the next section. The deep learning calibrator is explained in detail after conventional methods are presented.

8.2. Conventional Calibration Techniques

Conventional calibration techniques include employing external calibration targets at different physical temperature, internal calibrators including matched Dicke-load and noise diodes, and vicarious sources which are external to the radiometer instrument such as observing ocean surface [35]. These techniques are summarized in Figure 85 with respect to their grouping based on the way they are being implemented.

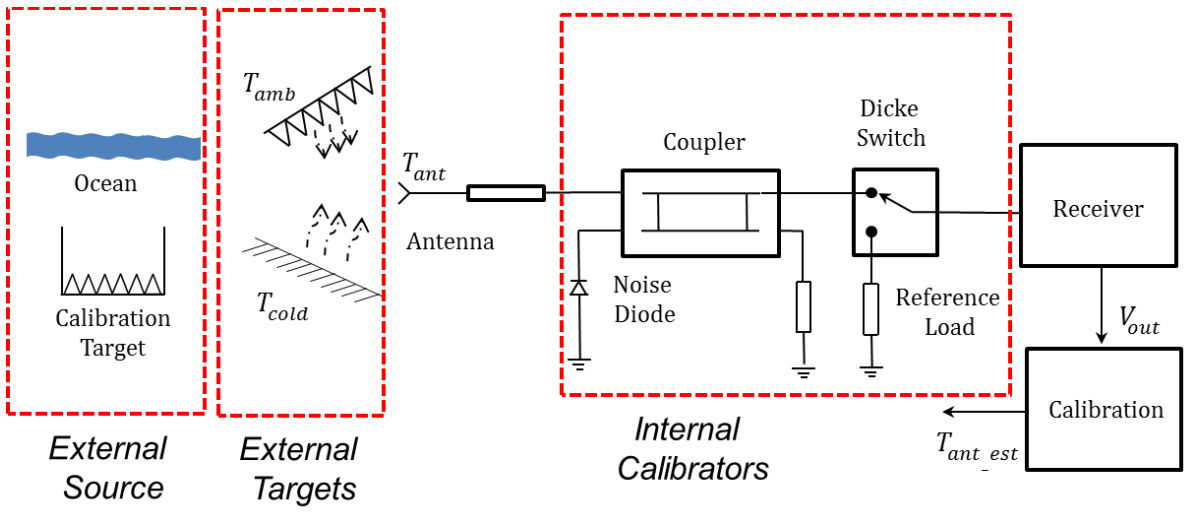

Figure 85: Current calibration techniques employed in microwave and millimeter-wave radiometers.

Microwave and millimeter-wave radiometers are usually calibrated using a two-point calibration scheme by measuring two external calibration targets at widely separated, known temperatures as shown in Figure 85 [122]. Assuming a linear response of the radiometer without gain fluctuations, the radiometric calibration of output voltage to antenna temperature can be performed using end-to-end calibration. As shown in Figure 86.a, the ambient and cold targets with known temperatures are measured by the radiometer to determine the antenna temperature-to-voltage response of the system defined as:

$$T_{ant} = G * V_{out} - T_{rec} \tag{VIII.1}$$

where T_{ant} is the antenna temperature in Kelvin estimated from the output voltage

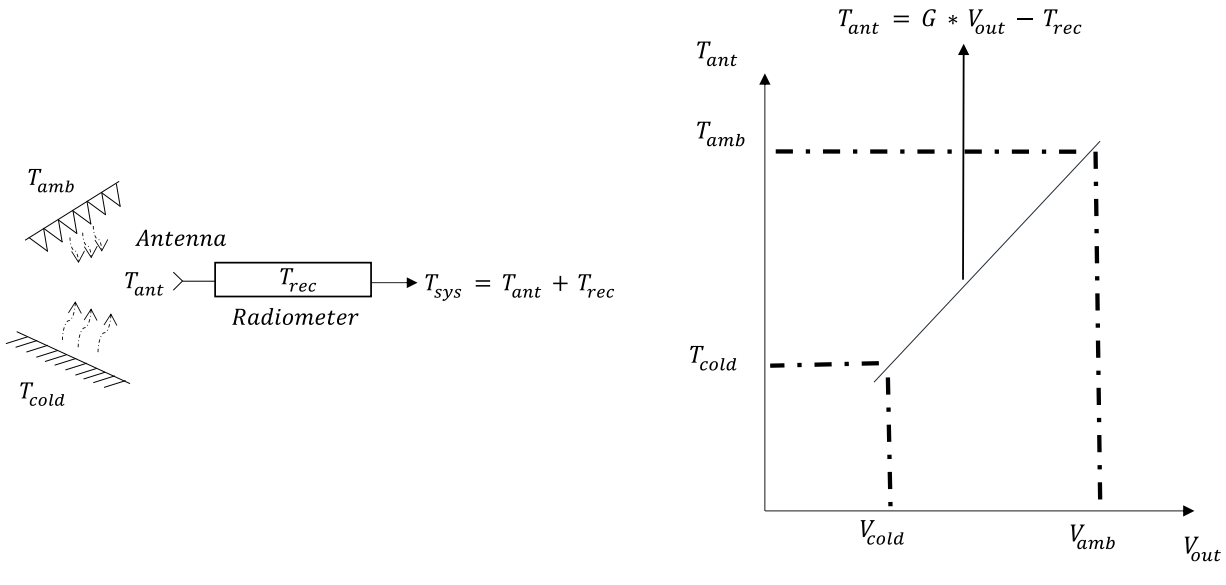

(a) (b)

Figure 86: Radiometer calibration: a) Radiometer noise diagram; b) Two-point radiometer calibration

measurement of V_{out} in Volts with slope G in Kelvin/Volt, and the receiver noise temperature T_{rec} in Kelvin. The most unstable parameter in Equation (VIII.1) is the calibration gain, which is governed by 1/f (Flicker) noise laws creating gain fluctuation [123]. This is especially significant when using wide band low noise amplifiers (LNA). The calibration gain is the slope of the line given in Figure 86.b defined as:

$$G = \frac{T_{amb} - T_{cold}}{V_{amb} - V_{cold}} \ [^{K}/_{V}] \tag{VIII.2}$$

The need to improve the accuracy and reliability of the radiometers has led to the use of several methods to overcome gain fluctuation by employing internal gain calibration techniques [34] including noise diodes and reference loads as shown in Figure 85, at the expense of radiometric resolution [124]. For instance, noise injection radiometers add a preset noise into the measurement path and Dicke radiometers switch the input signal between antenna and a reference source, which reduces the amount of time available for observation [35].

Internal gain calibration techniques used together with external calibration targets for two-point radiometric calibration improve accuracy and stability of a radiometer. However, it is a challenge to employ external calibration techniques in small satellites for end-to-end calibration due to their stringent design requirements on mass and volume [125]. However, complete end-to-end radiometric calibration cannot be accomplished by using only internal reference sources since the calibration source is inside the system after the antenna and will not account for its efficiency. In addition, internal calibration techniques add complexity to small

satellites in terms of power and mass to control and maintain the thermal stability of those calibration sources.

Finally, vicarious sources can be used to calibrate the radiometers as depicted in Figure 85. These sources exist in the laboratory environment or in nature such as ocean surface or cold sky. The calibration frequency for using the vicarious sources is not fast enough to maintain the stability of the instrument since these sources are not available all the time for viewing. Therefore, they cannot be used as a sole source of calibration. However, they are useful for radiometer gain correction or determining the unknown losses in the antenna and the waveguide where there is only internal calibration sources are employed [126].

8.3. Deep Learning Calibration

The discussion on conventional calibration techniques has revealed that all the techniques presented tries to generate a known source to estimate the unknown radiometric antenna temperature measurements by comparing with the reference used as depicted in Figure 85. Each method brings its own challenge and uncertainty for the radiometric measurements in addition to their advantage for the calibration. In addition, the emerging field CubeSats as discussed in the first chapter of this thesis has introduced new challenges for microwave and millimeter-wave radiometry in terms of mass, volume, power consumption and data telemetry rate. Another challenge for CubeSat radiometers is end-to-end calibration. External calibration targets are typically large in size and mass relative to radiometer antennas and optics. In addition, external calibration targets can limit the Earth

viewing portion of the scan or may reduce the number of available calibration measurements. In addition, it may be difficult to maintain homogeneous temperature distribution over the portion of the calibration target viewed by the radiometer antenna, as required for reliable calibration.

Recent advances in computational speed and deep learning neural network algorithms have significantly reduced the processing times and improved the accuracy of these algorithms [127]. A new approach for microwave and millimeter-wave radiometer calibration is developed by employing the advanced techniques of deep learning. The approach is applied without making any assumptions regarding the system linearity, radiometer architecture or presence of external calibration.

The basic definitions for the techniques employed for building the deep learning calibrator is explained in the next subsection before the method is analyzed in detail.

8.3.1 Theoretical Background

Artificial intelligence, machine learning and deep learning are the terms mostly encountered in recent years almost in every field due to recent advancements in technology. These closely related terms are depicted in Figure 87 from the most generalized definition to more specific one. The systems act or/and think like humans in a rational way can be defined as artificial intelligence (AI) systems. A system is considered as a machine learning system if it learns by itself from the tasks. The learning of a system is determined by the performance measure where the performance of a system should improve with an experience for performing

some given class of tasks. If the learning is performed based on a target goal, it is called as supervised learning. As an example, radar measurements can be recorded with respect to precipitation rate. These measurements can form a dataset to be used for training a network for the prediction of precipitation based on radar measurements. If there is no target dataset in the learning, it is called as unsupervised learning. A model can be built to estimate the similarities within the

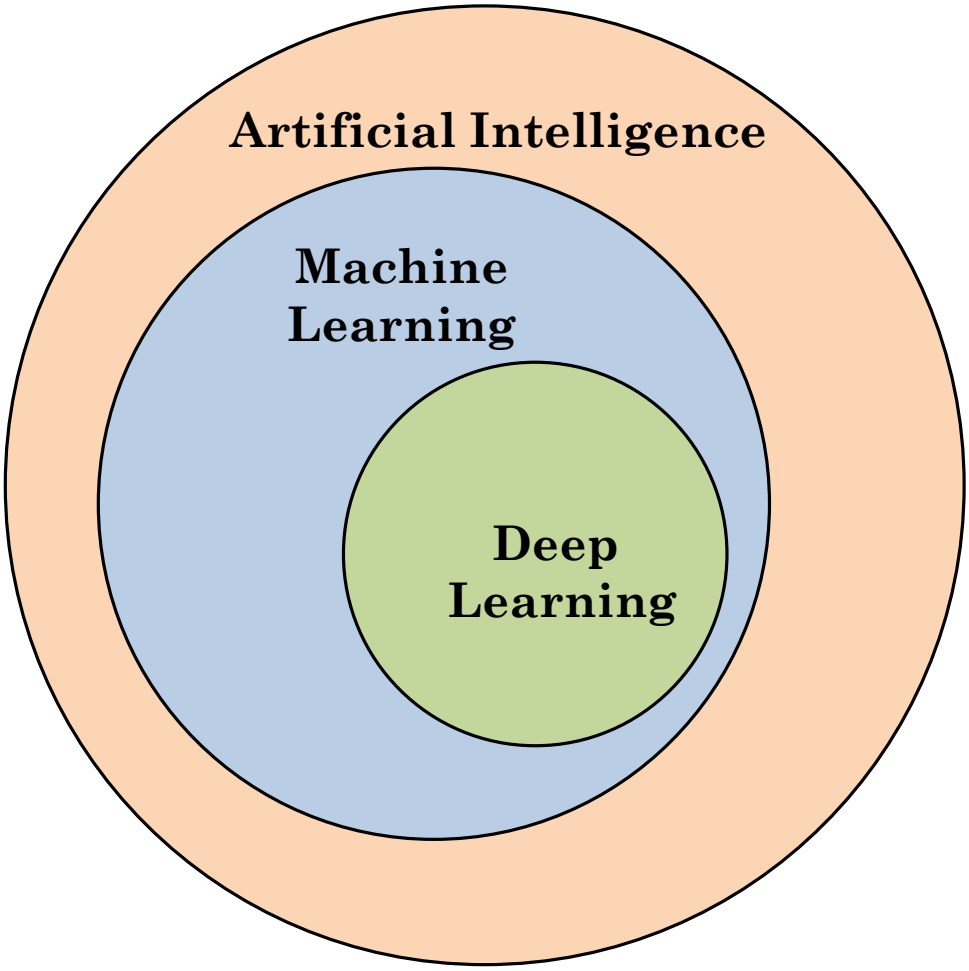

Figure 87: The diagram showing the relationship of the terms artificial intelligence, machine learning and deep learning from the most generalized definition to the more specific one.

dataset without having any dataset. For example, different car specifications can be compared to provide an estimate on the cars similar to each other based on specifications. Finally, reinforcement learning is the case where the award and penalty are given based on the system response. For example, an owner may teach to his dog to perform some specific movements when he calls some certain words result in a bone for the dog. All the machine learning systems are also an artificial intelligence system. However, an artificial intelligence system which is not capable of learning from the tasks it performs is not a machine learning system [128], [129].

A neural network can be defined as a combination of smaller computation units to form a set of algorithms to perform a specific task such as classifying or clustering. If the network consists of only one hidden layer, it is called as shallow network. Deep learning is term used to specify the depth of a network where there is more than one hidden layers in the system. Higher-layer network structure of deep learning algorithms enables to resolve complex computational problems at high accuracy. The recent advances in the computational technology have made deep learning algorithms applicable for solving complex problems. As outlined in Figure 87, all deep learning algorithms are also a machine learning and artificial intelligence algorithm [128], [129], [130].

The proposed model for radiometric calibration is based on a multilayer perceptron (MLP) feed-forward artificial neural network (ANN) utilizing a supervised deep learning algorithm to retrieve antenna temperatures from the voltage measurements at the output of the radiometer. The multiple layer structure of the

deep MLP model and the non-linear activation between layers make this option suitable for extraction of features to learn representations of complex radiometer data structure with multiple levels of abstraction [127], [129], [131].

The internal adjustable parameters of the MLP structure are the weights that define the input-output relationship of the network. A learning algorithm adjusts the weights of the network by minimizing the error of the cost function between the output and the desired values. The stochastic gradient descent (SGD) algorithm computes the average gradient by calculating the outputs and the errors for a few examples of large datasets to adjust the weights, resulting in frequent updates of those parameters with high variance. As a result, the loss function fluctuates due to high variance that helps the detection of different local minima for the SGD gradient calculation. In this way, the SGD significantly reduces computational time and memory usage while providing fast convergence for the training [132].

A neuron is the smallest computational unit in the neural network architecture. The data at the input of a neuron is transmitted to its output through activation functions, which define the system response of a single neuron to specific information at its input. The rectified linear unit (ReLU) non-linear activation function is a half-wave rectifier defined as:

$$f(x) = max(0, x) \tag{VIII.3}$$

where x is the input to a neuron in the network and $f(x)$ is the output of the neuron. The simple structure of the ReLU activation function compared to complex activation functions, including sigmoid and hyperbolic tangent, provides fast

learning in multiple layer networks allowing deep supervised learning without unsupervised pre-training [133], [134].

8.3.2 Deep Learning Calibrator

A deep learning neural network structure based calibration algorithm is designed. The number of layers and neurons at each layer in the MLP network depends on the complexity and non-linearity of the calibration problem. The optimum number of layers and neurons at each layer of the neural network model depends on each specific case based on the complexity of the problem. Those values are found after an optimization process and they are specific to the subjacent hardware being calibrated and the amount of available information such as inputs and dataset. Increasing number of layers provides high non-linearity to the system. The network can learn the complex data structure with multiple levels of abstraction with increased number of layers and neurons. However, having higher level of complexity than needed in the neural network model may result in slow convergence or not being able to converge to the desired performance.

The designed MLP neural network structure for the calibration problem contains three hidden layers as depicted in Figure 88. The measured radiometer antenna temperature is the final product of the ANN to be retrieved from the radiometer antenna and reference voltage measurements in addition to thermal measurements of the instrument.

The noise wave model of a radiometer is used to generate data for the MLP network since the noise wave representation of radiometers provides flexibility to introduce

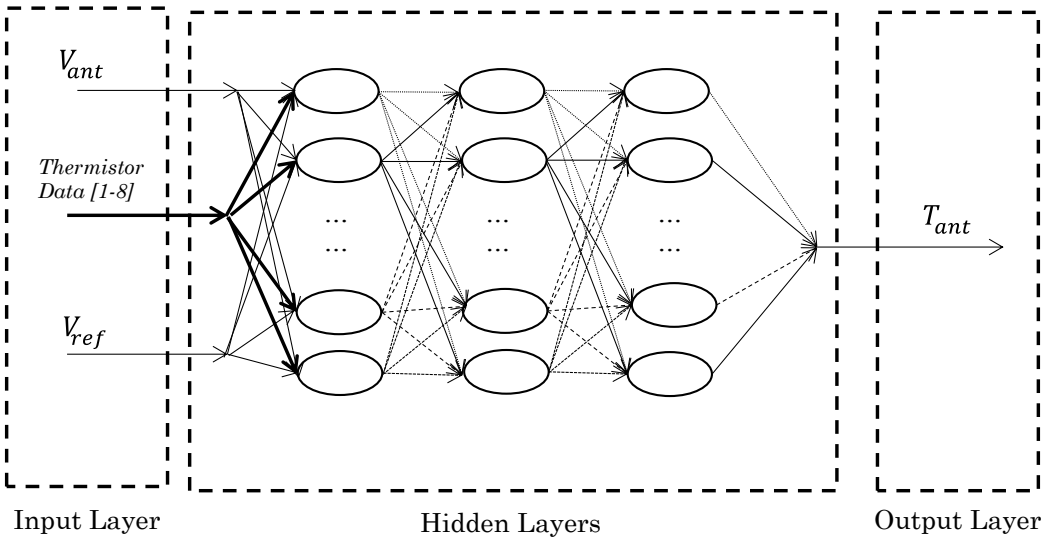

Figure 88: The ANN architecture for radiometer calibration used for the presented model.

uncertainty and noise into the system for testing the performance of the calibration process under various conditions. In addition, the noise wave model breaks down the radiometer architecture into a number of smaller parts, making it easier to calculate the noise waves originating from each separate part of the instrument [118].

The ANN uses the antenna temperature data for target values in the supervised learning of the system for training. As shown in Figure 88, the ANN model has three types of inputs:

- V_{ant} is the radiometer voltage output when the antenna leg is selected by the Dicke switch,
- V_{ref} is the radiometer voltage output when the Dicke switch is set to the reference load leg, and

- thermistor data, which consists of the acquired physical temperature of the antenna, waveguide, noise diode, coupler, switch, reference load, isolator and receiver electronics measured by the thermistors mounted on those subsystems. The input information from the thermistors is useful to understand the radiometer noise change with respect to physical temperature due to orbital variations, e.g., in the sunlight as compared to Earth eclipse.

The ANN model builds a relationship between the input and the output layers by assigning suitable coefficients to each neuron in each hidden layer. In this way, the model performs end-to-end calibration of the radiometer.

Common calibration strategies use a Dicke load or noise diodes to improve system stability for radiometric measurements. Then, two-point calibration is performed using measurements of hot and cold calibration targets to convert measured counts to volts [35]. However, the proposed model calibrates the instrument in a single step by directly providing the calibrated antenna temperature from the measurements, as opposed to conventional two-point calibration techniques in which the antenna temperature is estimated in two steps.

8.3.3 Deep Learning Calibrator Demonstration Results

The proof of concept of the deep learning MLP model that has been developed for calibration will be carried out by using the radiometer noise wave model derived in this paper. The radiometer chosen for this study is a basic Dicke radiometer. The radiometer is assumed to be operating in low-Earth orbit (LEO) conditions. It is also assumed that the temperature control of the system to keep the radiometer

instrument at a constant temperature still depends upon the external temperature since the CubeSat has stringent limitations for power and mass. Therefore, the temperature of each part of the radiometer system varies at a different rate due to orbital temperature fluctuations.

The orbital and radiometer operation parameters are provided in Table 25. Several datasets have been calculated from the noise-wave model under the orbital conditions provided in Table 25. Then, as a rule of thumb defined by the holdout method for an MLP neural network dataset selection, 70% of the samples of the dataset have been randomly selected for the training of the neural network [135]. The remaining samples are allocated for the testing and validation of the ANN.

The first test is the noise-free case where there is no uncertainty in the measurements of the antenna voltage from the radiometer for both the training and testing datasets. In addition, the thermistors perform precise measurements of the thermal state of the subsystems (i.e., assuming that they do not have any

Table 25: Orbital and radiometer operation parameters for the artificial radiometer that the deep learning calibrator is being applied

Parameter	Value
Antenna temperature range	From 2.7 K to 350 K
Orbital temperature range	From 233 K to 353 K
LNA gain variation	± 2.5 dB

uncertainty or bias). The goal of the noise-free test is to examine the performance of the calibration ANN under ideal conditions.

The ANN is trained using random selected training samples. Then, the antenna temperature of the radiometer has been predicted by the ANN using 20,000 randomly-selected samples from the testing dataset. Figure 89 shows a 5-Kelvin bin plot of the ANN predicted antenna temperatures versus the target antenna temperatures calculated from the noise-wave model of the radiometer. The root-mean square error (RMSE) and the standard deviation in the predictions are calculated as 48 mK.

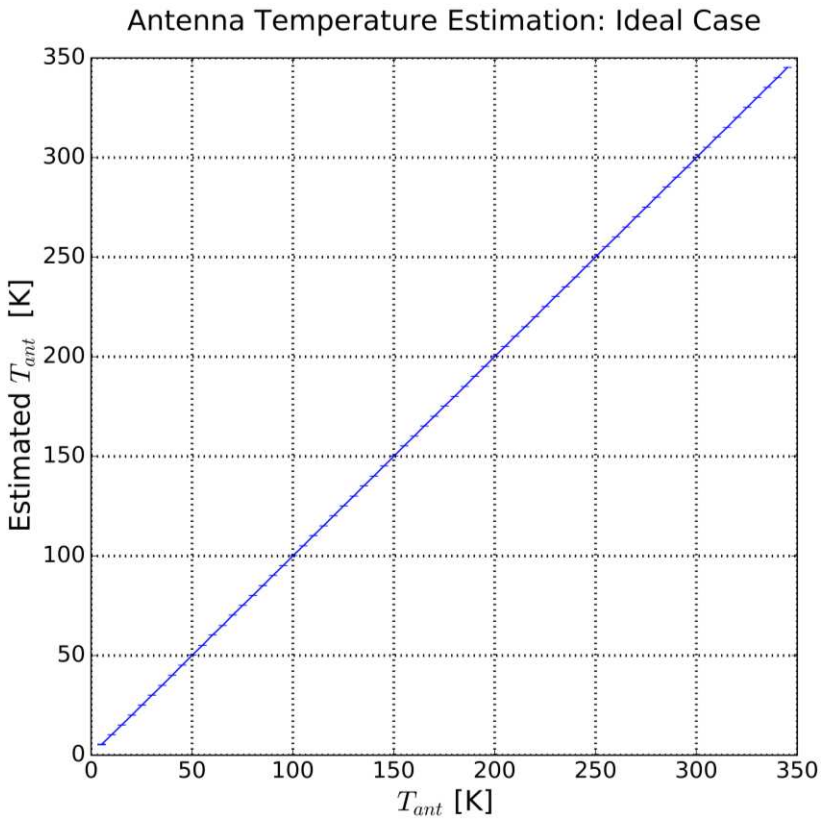

Figure 89: Comparison of antenna temperature estimated using the ANN model with the true temperatures for an ideal case.

However, the output voltage of an actual radiometer has uncertainty due to noise in the system as well as limited bandwidth and integration time [35]. The radiometric resolution of a total power radiometer is:

$$\Delta T = \frac{T_{sys}}{\sqrt{BW * \tau_{int}}} \tag{VIII.4}$$

where T_{sys} is the system noise temperature (K), BW is the equivalent noise bandwidth (Hz) of the radiometer and τ_{int} is the integration time (s) [34].

The goal of noise-added testing is to study the performance of the designed ANN for calibration under the presence of noise in the system. The noise wave model is used to generate 348,000 testing samples when the antenna is measuring targets with temperatures from 2.7 K to 350 K with 1 K resolution. Before applying these testing samples to the ANN for calibration, 0.1% zero-mean additive white Gaussian random noise is introduced into the radiometer output voltage measurements. The output voltage uncertainty of 0.1% accounts for gain fluctuations and corresponds to 0.3 K of uncertainty at an antenna temperature of 300 K. The same test is repeated for the uncertainty level of 0.3% at the radiometer voltage output (i.e. $\Delta T = 0.9$ K at $T_{ant} = 300$ K).

The resulting sensitivity of radiometric temperatures to antenna voltage measurements is defined by:

$$\Delta T/\Delta V = \frac{T_{max} - T_{min}}{V_{max} - V_{min}} \tag{VIII.5}$$

where V_{max} and V_{min} are the output voltage readings at the maximum (T_{max}) and minimum (T_{min}) temperature measurement during the test. Then, the output voltage uncertainty is expressed in terms of antenna temperature uncertainty as:

$$\Delta T_{noise} = (\Delta T/\Delta V) * \Delta V_{noise} \quad \text{(VIII.6)}$$

The expected uncertainty in the temperature in Equation (VIII.6) is ΔT_{noise}, and ΔV_{noise} is the amount of uncertainty present at the measured output voltage of the radiometer represented in Volts.

The expected and measured uncertainties in Kelvin when using the ANN for antenna temperature calibration for 0.1% uncertainty at the received radiometer output voltage are plotted with a bin size of 5 Kelvin, as presented in Figure 90a. As

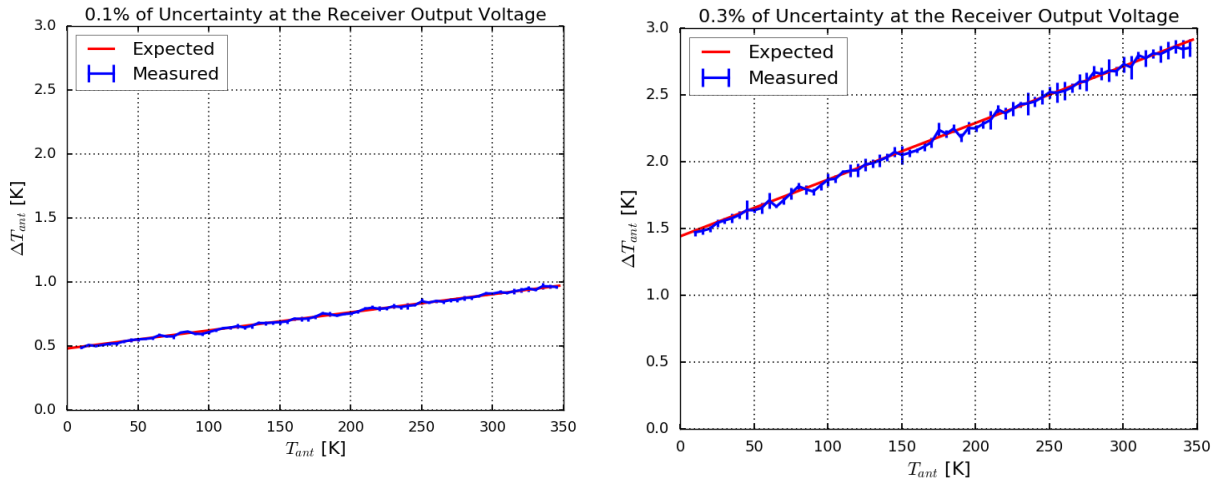

(a) (b)

Figure 90: Antenna temperature estimated using the ANN model when a) 0.1% uncertainty is present in the output voltage and b) 0.3% uncertainty is present in the output voltage.

shown in the plot, the measured noise is in agreement with the expected noise. We conclude that the ANN model does not add any significant noise to the retrievals.

In Figure 90b, the radiometer output voltage uncertainty is increased to 0.3%. Similarly to the results for 0.1% of the uncertainty level, the measured noise level agrees with the expected value. The test results for the ideal situation and the case with uncertainty in the radiometer output voltage indicate that the designed ANN model does not add any significant noise to radiometer calibration.

A radiometer operating in orbit has also inaccuracies in the acquired physical temperature information as a result of digitization and measurement errors. Therefore, in addition to 0.1% output voltage uncertainty, 0.1 K uncertainty in the thermal data is introduced to 20,000 randomly-selected samples of testing data. The current level of thermistor technology allows a physical temperature measurement precision of better than 0.1 K [136]. The estimated antenna temperatures of the ANN have been plotted with respect to expected antenna temperatures on Figure 91. The RMSE has been calculated as 0.75 K for the antenna temperature estimates for this case.

Several randomly-selected training sample datasets with various resolutions are generated using the noise wave model to analyze the effect of the training dataset resolution on the ANN estimates. Each training dataset with sample size from 1.2 million to 149 million is input to an ANN having the same structure as presented in Figure 88 to train for radiometer calibration. Each trained network for 5 epochs has been tested with the same three randomly-selected datasets having 20,000 noise-

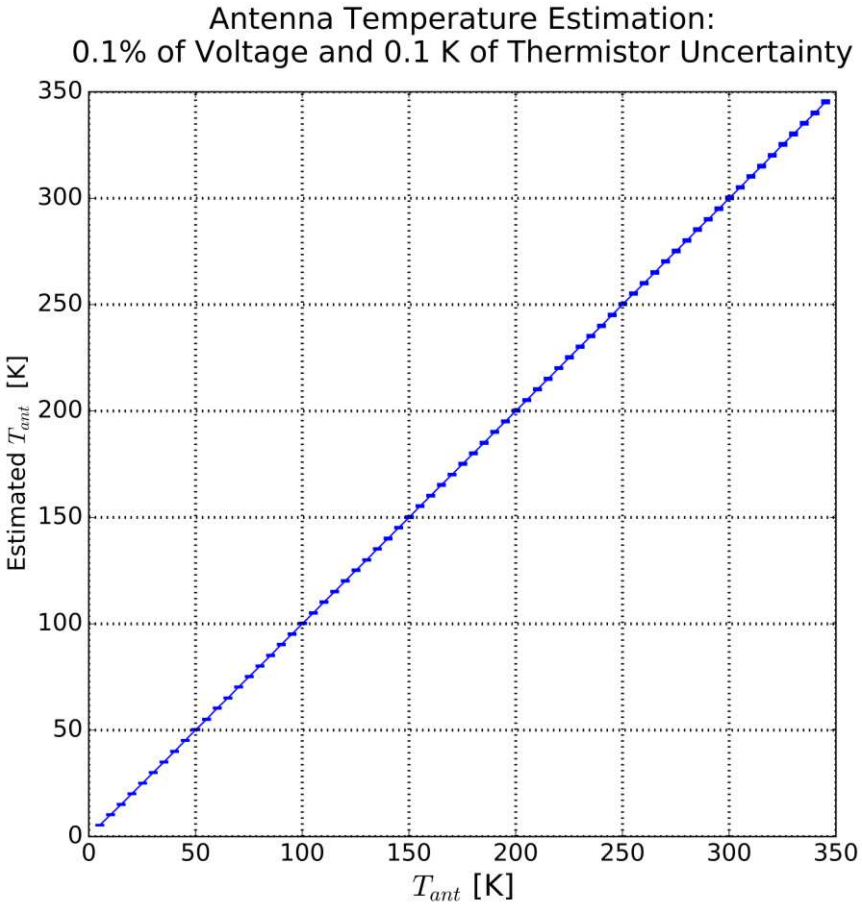

Figure 91: Antenna temperature estimates using the ANN model for a radiometer with 0.1% output voltage and 0.1 K thermistor reading uncertainties compared with the true temperatures.

free samples, with 0.1% and 0.3% radiometer output voltage uncertainty. The results are summarized in Table 26 with the expected RMSE values for noise free, 0.1% and 0.3% uncertainty test cases in addition to expected standard deviation (STD) values calculated at 300 K for 0.1% and 0.3% uncertainty test cases.

The RMSE and STD results provide a complete picture of the ANN performance since the RMSE is used to analyze how close the estimates are to the expected values while the STD provides information about how much uncertainty exists

around the mean estimate value. The measured RMSE values are close to the expected ones for the networks trained with larger numbers of the samples. This indicates that increasing the number of training samples improves the performance of the network to estimate the antenna temperatures for the networks having the same training epoch numbers. The measured and expected STD values are close to the expected results, confirming that the ANN does not add any significant noise when it is tested with networks having a different number of training samples.

The performance of the ANN for the accuracy of the estimates also depends on how well the network has learned during the training process [127]. The epoch number of the network for training defines how many times the training process is repeated using the complete training data samples. Therefore, the number of epochs used to

Table 26: The measured RMSE and STD performance for the antenna temperature retrievals of the ANNs trained for 5 epochs with different number of samples.

Training Samples (Millions)	RMSE [2.7-350] K			STD @ 300 K	
	Expected RMSE: 0 K	Expected RMSE: 0.73 K	Expected RMSE: 2.18 K	Expected STD: 0.9 K	Expected STD: 2.71 K
149	0.09	0.74	2.23	0.90	2.72
15	0.11	0.76	2.22	0.90	2.76
6.2	0.11	0.75	2.22	0.93	2.75
3.1	0.60	0.97	2.32	0.92	2.84
1.2	1.46	1.64	2.68	0.91	2.79

train the neural network is expected to affect the performance of the retrievals. To demonstrate the effect of training epochs on the accuracy of the estimates, the trained ANN with the lowest number of training samples among those ANNs listed in Table 26 is chosen. The developed noise-wave model for the Dicke radiometer is used to generate 1.2 million randomly-selected training samples to train several ANNs, each having different training epochs but the same training dataset. Then, each network has been tested with the same randomly-selected 20,000 testing samples. The results are summarized in Table 27. The accuracy of the retrievals significantly improves when the number of training epochs is increased. However, it is evident from the results that any further increase of the training epochs beyond 20 does not have significant improvement in the performance of the ANN for the tested calibration model.

The data used for training an ANN will have measurement uncertainty since it will

Table 27: The measured RMSE performance for the antenna temperature retrievals of the ANNs trained for different number of training epochs.

Training Epochs	RMSE [2.7-350] K		
	Expected RMSE: 0 K	Expected RMSE: 0.73 K	Expected RMSE: 2.18 K
5	1.46	1.64	2.68
10	0.80	1.10	2.40
20	0.16	0.76	2.25
40	0.05	0.75	2.23

be obtained from a real radiometer even if the radiometer is operating in a controlled environment in laboratory conditions. Therefore, uncertainty has been introduced into the voltage measurements obtained from the noise-wave model for training the ANN calibration model. The radiometer noise–wave model has been used to generate three randomly selected training data sets with noise-free, 0.1% and 0.3% of uncertainty, respectively. The ANN calibration model is trained for 40 training epochs using each of those three training datasets separately with 1.2 million training samples. The results are summarized in Table 28. The trained ANNs have similar performance when they are tested with samples having 0.1% and 0.3% of uncertainty. Finally, this test has shown that introducing uncertainty into the samples for training the ANN does not have a significant effect on the estimates, when compared to noise-free cases shown in Table 27.

In microwave and millimeter wave radiometry, it is desirable to have a linear

Table 28: The measured RMSE performance for the antenna temperature retrievals of the ANNs when different amount of uncertainty is introduced to the training samples

Noise Level of Training Dataset	RMSE [2.7-350] K		
	Expected RMSE: 0 K	Expected RMSE: 0.73 K	Expected RMSE: 2.18 K
0 (Noise Free)	0.048	0.75	2.23
0.1 % of Uncertainty	0.068	0.75	2.23
0.3 % of Uncertainty	0.195	0.77	2.23

calibration curve, as shown in Figure 86b, to perform reliable measurements in orbit with high accuracy. However, radiometers have non-linear temperature to voltage response, as shown in Figure 92a, due to imperfections in square-law detector diodes, amplifiers and analog-to-digital converters. The detector diodes have a square-law transfer function for the most of the radiometer's operating range, except for low signal detection. In addition, the third order intercept of the RF amplifiers and fourth order RF coefficient of the video amplifier contribute to the non-linear behavior of radiometers [36]. There are several ground-based calibration methods to check the linearity of a radiometer, including 3-point calibration and slope methods explained in [34]. However, those methods are not suitable to be used in on-orbit radiometers.

The noise wave model is used to generate data for a radiometer having a non-linear calibration curve to check the performance of the ANN model regarding linearity. The voltage-to-temperature calibration curve for such a radiometer is given in Figure 92a. The ANN model is trained by randomly-selected 2 million of training samples having 2 Kelvin of nonlinearity at 250 K antenna temperature and 0.1% radiometer output voltage uncertainty. The trained network is tested using 50,000 randomly-selected samples. The estimated antenna temperatures are plotted with 5 Kelvin bin size with respect to ground-truth antenna temperatures in Figure 92b. The RMSE of the ANN calibration is calculated as 0.3 Kelvin. These results indicate that a radiometer having non-linear calibration response can be calibrated on orbit by applying the ANN model.

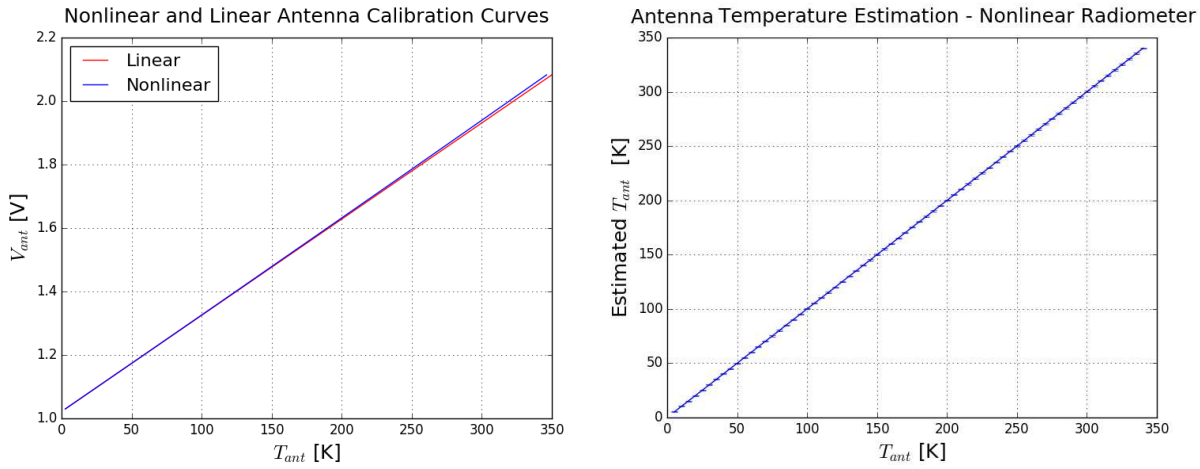

(a) (b)

Figure 92: ANN calibration performance. a) Nonlinear and linear antenna calibration curves and b) antenna temperature estimates using the ANN model for a nonlinear radiometer.

The ANN tests have been applied for an ideal radiometer, a radiometer having various uncertainties in the output voltage and the thermistor measurements as well as a radiometer with a non-linear radiometer response. The results have shown that the ANN model reliably performs low-noise radiometer calibration under various conditions.

8.3.4 Deep Learning Calibrator: Performance Evaluation

The proposed method of calibration for microwave and millimeter-wave radiometers is based on the deep learning ANN computation technique. This technique has been demonstrated using the radiometer noise wave model. It has been shown through calculations that the ANN model produces calibrated antenna temperatures at high accuracy (low RMSE value) directly, i.e., without any extra data provided by an

external target. The noise analysis of the model has shown that the ANN does not introduce any significant noise into the radiometric measurements, for a well-trained model. Therefore, the presented calibration model can be applied to calibrate microwave and millimeter-wave radiometers regardless of the architecture design, operating frequencies, bandwidths, etc.

The training dataset for the ANN model can be obtained from thermal vacuum chamber (TVAC) radiometric measurements during the pre-launch phase of the instrument development. During TVAC tests, the antenna performs radiometric measurements when viewing a calibration target with a known and varying temperature in a controlled environment. While radiometric measurements are being performed, the temperature of different parts of the instrument is continuously recorded with thermistors placed on the instrument. During TVAC testing, one may place as many thermistors as possible on various parts of the instrument for synchronized temperature monitoring with the radiometric acquisitions since the tests take place in a laboratory environment. Then, it can be determined which parts are critical for deep learning calibration based on the radiometric measurements and thermistor readings during TVAC testing. Pre-launch tests may also provide an opportunity to analyze the system before launch in addition to providing data for the training.

A proposed general approach has been demonstrated for different numbers of training samples and training epochs. The number of samples for training should be estimated for any specific radiometer mission based on the mission requirements

and orbital parameters. Then, the ANN architecture should be designed based on the complexity of the training dataset. Finally, the ANN model should be trained for a sufficient number of training epochs with the training samples obtained during the pre-launch tests to achieve the desired performance for radiometer calibration.

The ANN model that has been trained for a specific mission can be also tuned while the radiometer is on-orbit with the provided data from internal calibration sources or from cold-sky measurements to consider any changes in the radiometer system parameters including the aging of the instrument. Also, external calibration sources that do not exist in the instrument can be used to tune the neural network in-orbit operation. For this purpose, the radiometer can perform measurements over the ocean surface or cold sky to improve the on-orbit performance of the deep learning calibration [126]. Furthermore, cross-calibration of the antenna temperature measurements with another on-orbit radiometer performing nearly collocated measurements. This might be also used to retrain the ANN model to adjust the weights to improve on-orbit calibration [137], [138]. The proposed method can be also applied along with end-to-end calibration techniques. In this case, calibration using the ANN model may be used to correct estimates of calibration gain and receiver noise temperature. In addition, the technique presented in this study may be extended to perform analysis for time-varying statistical fluctuations and biases in calibration reference temperatures.

The proposed study can be applied to the radiometers operated from other platforms such as airborne or ground-based systems. In the next section, the demonstration of

the deep learning calibrator is performed on a microwave and millimeter-wave radiometer instrument designed for airborne applications.

8.4. HAMMR Deep Learning Calibration

A deep learning calibration technique has been introduced in the previous section as a new category for microwave and millimeter wave radiometry calibration. As discussed, the deep learning calibrator employs advanced techniques of neural networks to create an artificial radiometer mimicking the on-orbit response of the radiometer. The proposed technique has been successfully demonstrated on an artificially created noise-added Dicke-switching radiometer. The tests of the deep learning calibrator under various operating conditions of the artificial radiometer have shown that the calibrator is able to estimate the antenna temperature at high accuracy for all cases. However, the application of this new calibration technique to a physically-built radiometer has not been carried out yet.

This section focuses on the application of the new deep learning calibration technique for the calibration of a microwave and millimeter-wave radiometer instrument. For this study, the high-frequency airborne microwave and millimeter-radiometer (HAMMR) instrument is used for the demonstration of the deep learning calibrator on a physically built radiometer. The calibration methodology presented in this section can be considered as a pioneer for future calibration techniques for microwave and millimeter-wave radiometers using artificial intelligence. The techniques and results provided in this study are critical to

validate the performance of the deep learning calibrator on a physically built instrument.

8.4.1 High-Frequency Airborne Microwave and Millimeter-Wave Radiometer Overview

The High-Frequency Airborne Microwave and Millimeter-wave Radiometer (HAMMR) is a cross-track scanning airborne instrument with 25 radiometric channels from 18.7 to 183.3 GHz. The HAMMR instrument was built as a collaborative effort between Colorado State University (CSU) as the lead institution, NASA/Caltech Jet Propulsion Laboratory, National Center of Atmospheric Research (NCAR) and University of California at Los Angeles (UCLA) under NASA Earth Science Office Instrument Incubator Program. The block diagram of the HAMMR instrument given in Figure 93 shows the subystems of the instrument with respect to the responsible institution for each subsystem [139].

The HAMMR instrument has low-frequency dual-polarized microwave channels at 18.7, 23.8 and 34 GHz near water vapor absorption band, high-frequency millimeter-wave window channels at 90, 130 and 168 GHz, and sounding channels near 118.75 and near 183.31 GHz for temperature and water vapor profiling.

8.4.2 Conventional Calibration Techniques Employed in HAMMR Instrument

The microwave and millimeter radiometers of the HAMMR instrument are a noise-added Dicke-switching type radiometer. The existing calibration strategy of the HAMMR instrument relies on pre-flight calibration, in-flight calibration and

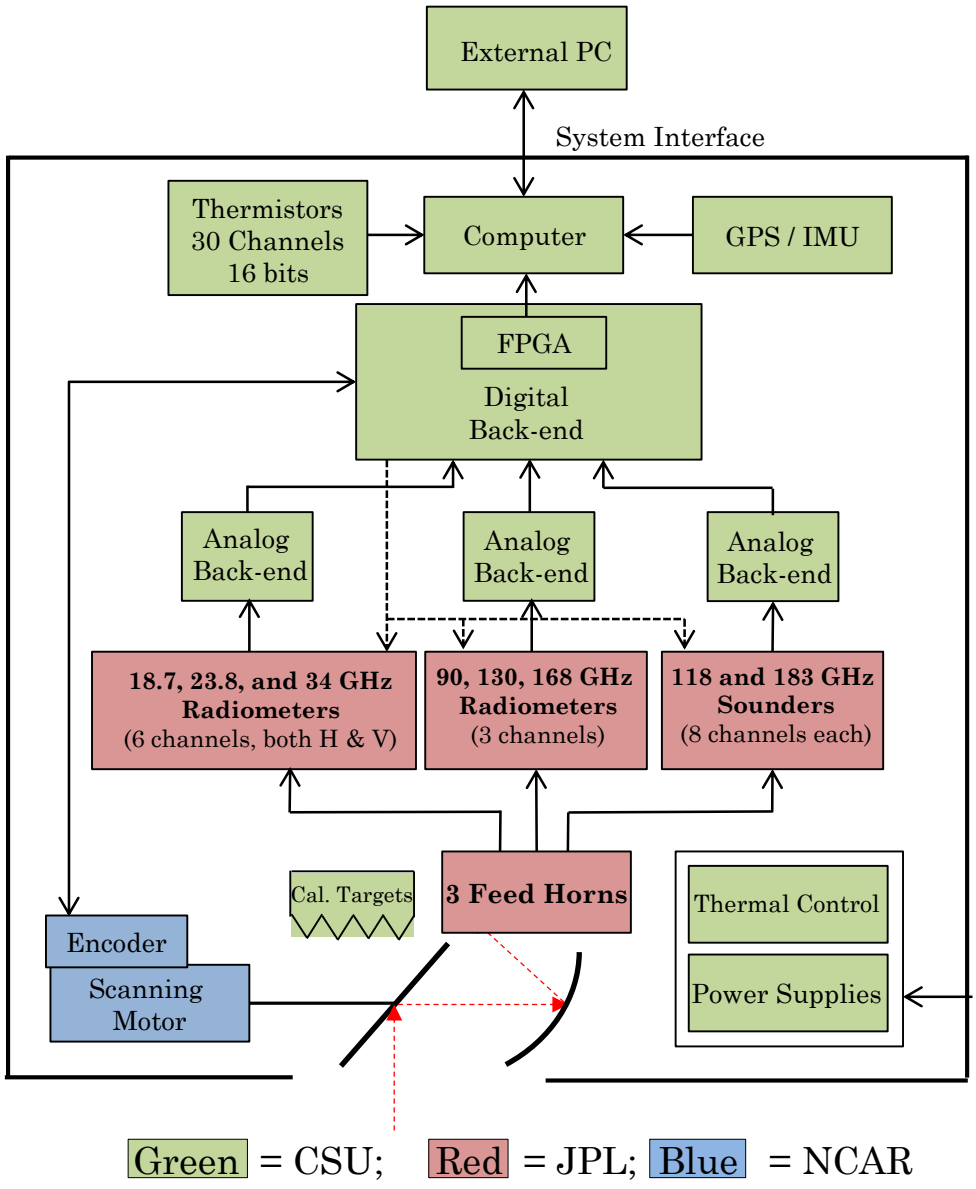

Figure 93: The instrument block diagram of the HAMMR instrument where color coding shows the responsible institution. CSU is shown in green, JPL is red and NCAR is in blue.

internal calibration targets. Before each flight, on-ground calibration of the instrument is performed by using liquid-nitrogen (LN_2) at 77 K as shown in Figure 94. During flight, a built-in ambient calibration target is measured at each cross-

track scan cycle of the HAMMR instrument to provide two point measurements for the estimation of voltage-to-temperature response curve of the instrument.

Three noise-injection diodes and Dicke-switching reference load are used as internal calibrators in the HAMMR radiometer in addition to external calibrators. During one scan cycle of the instrument, the operational modes of the instrument are the

(a)

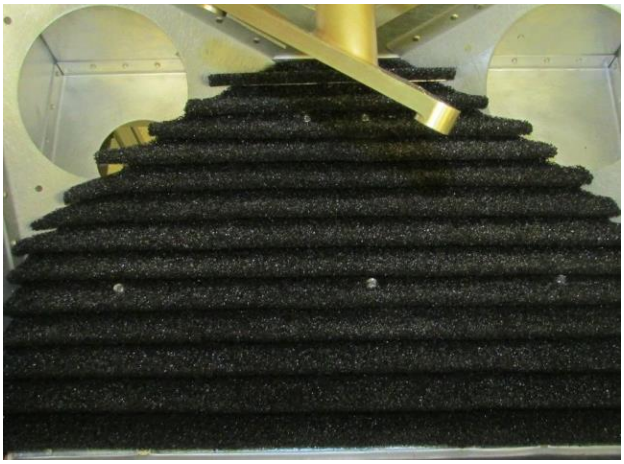

(b)

Figure 94: The calibration strategy of the HAMMR instrument: a) Pre-flight, on-ground calibration of the radiometer instruments, b) A built-in ambient calibration target for in-flight radiometric calibration

antenna, the first noise source added antenna, the second noise source added antenna, the third noise source added antenna and Dicke-switched to reference load. This scanning strategy for the calibration of the instrument is given in Figure 95.

8.4.3 HAMMR West Coast Flight Campaign

The HAMMR instrument was deployed on a Twin Otter aircraft for the West Coast Flight Campaign (WCFC) between Nov. 4 and Nov. 17, 2014, for a total of 53.5 hours. During the WCFC, the HAMMR instrument has performed radiometric measurements over land and ocean on a humid and dry day to monitor various atmospheric conditions over different surface conditions.

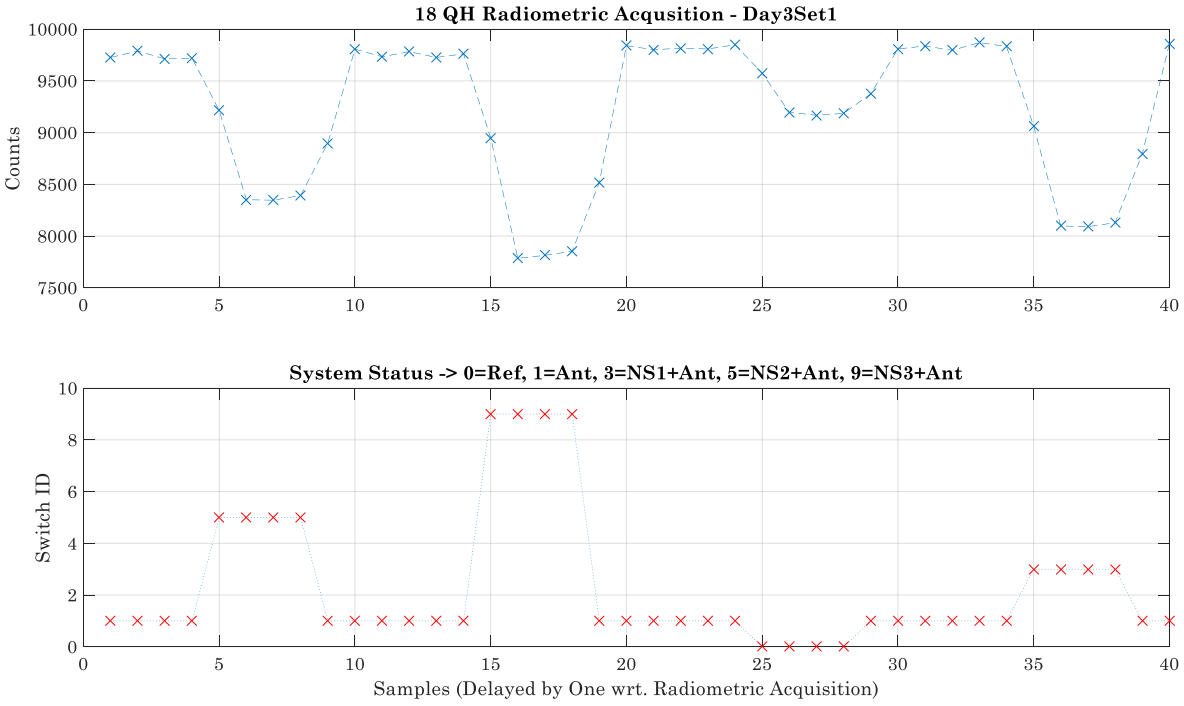

Figure 95: The calibration scanning strategy of the HAMMR instrument employs conventional calibration techniques.

The radiometric data collected during this campaign has been calibrated by employing the conventional calibration techniques [139]. The WCFC measurements of the HAMMR instrument will be used for the retrievals of cloud liquid water, atmospheric water vapor, and wind speed.

8.4.4 Deep Learning Calibrator Employed in HAMMR

The WCFC measurements of the HAMMR instrument are used to validate the performance of the deep learning calibrator. The main architecture used to train the deep learning calibrator for the HAMMR instrument in given in Figure 96. The demonstration of the deep learning calibrator on the HAMMR instrument is analyzed for quasi-horizontal (QH) 18 GHz microwave channel in this paper. The implementation of the deep learning calibration to other microwave and millimeter-

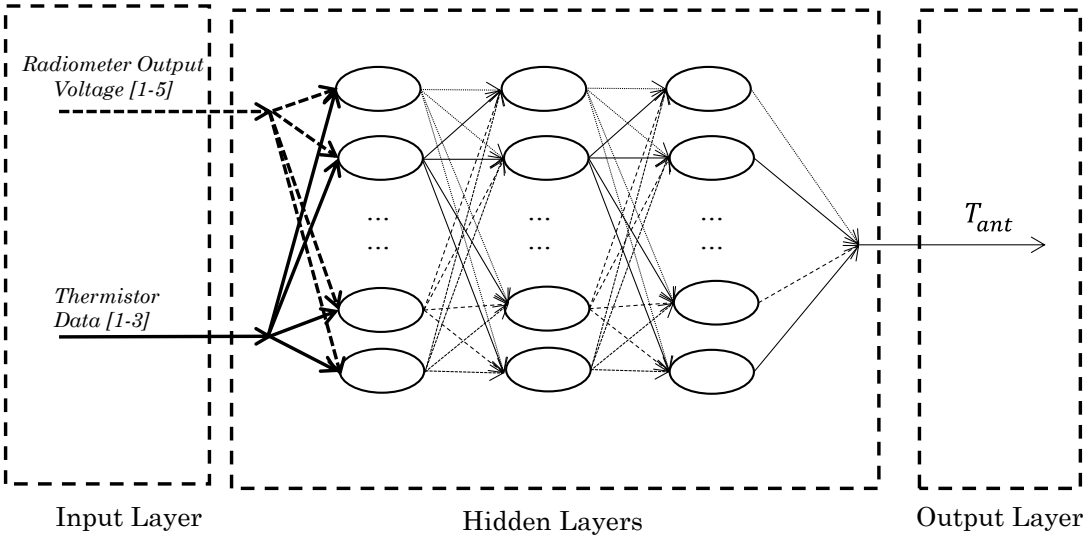

Figure 96: The ANN architecture used in the calibration of the HAMMR instrument.

wave channels follow the similar procedure with the one presented for the 18 GHz QH channel.

The inputs of the deep learning calibrator given in the input layer of the neural network for the 18 GHz QH channel are:

- Radiometer output voltage measurements:
    - Antenna voltage measurements
    - Antenna added noise source #1 voltage measurements
    - Antenna added noise source #2 voltage measurements
    - Antenna added noise source #3 voltage measurements
    - Reference load voltage measurements
- Thermistor readings:
    - Horn
    - MW receiver
    - Noise sources (A single thermistor)

The deep learning neural network model is trained with randomly selected 70% of the WCFC radiometric measurements of the HAMMR instrument at 18 GHz QH microwave channel. The trained network is tested by using 18 GHz QH channel radiometric measurements over San Joaquin River on the Day-3 of the WCFC.

The antenna temperature estimates using deep learning calibration algorithm are given with the conventional calibration technique result in Figure 97 for a one full-scan cycle radiometric measurements of the 18 GHz QH channel. The radiometer output voltage measurements when the radiometer is looking at the land surface,

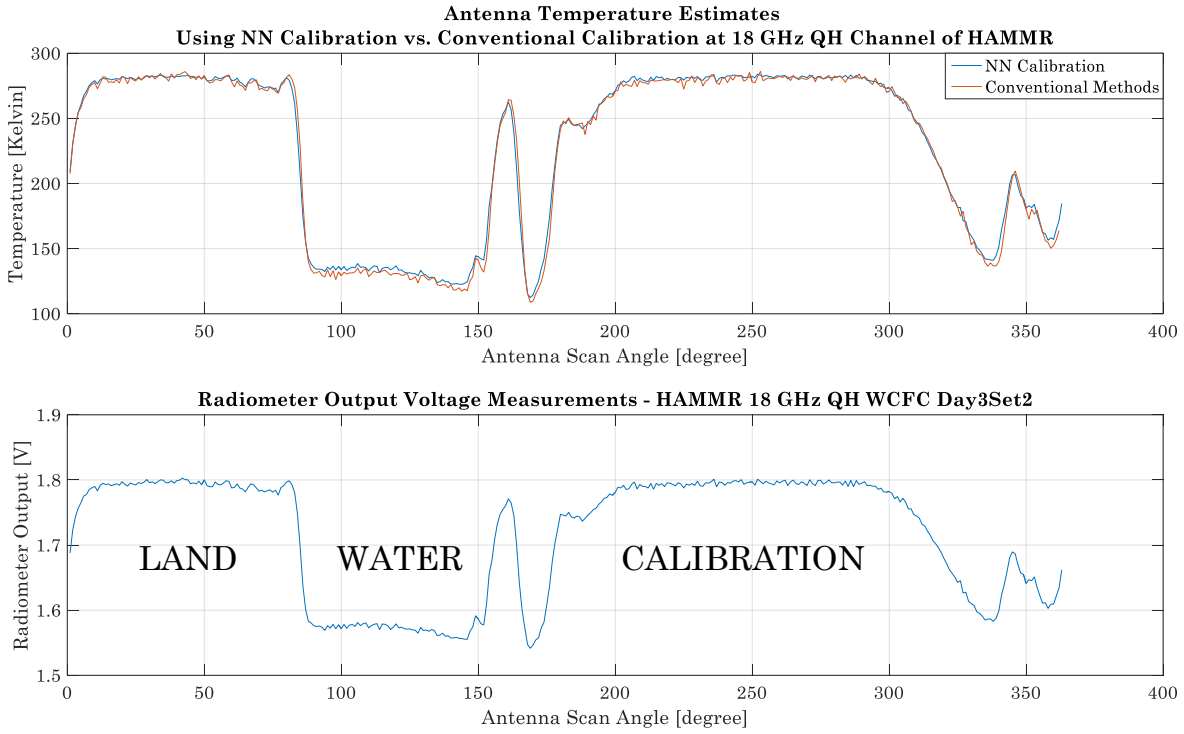

Figure 97: Deep learning calibrator results for one antenna scan cycle of the HAMMR WCFC measurements over San Joaquin River

ocean surface and the built-in ambient calibration is also plotted separately at the same figure with the retrievals.

The results presented in Figure 97 show that the deep learning calibration results agree well with the antenna temperature estimates using the conventional calibration techniques. The agreement in the results can be clearly seen in Figure 98 where the antenna temperature estimates obtained from deep learning calibrator are plotted against those for conventional techniques for the same scan cycle of the HAMMR instrument. The estimates for the overall antenna temperature measurement range are provided in Figure 98a showing that the deep

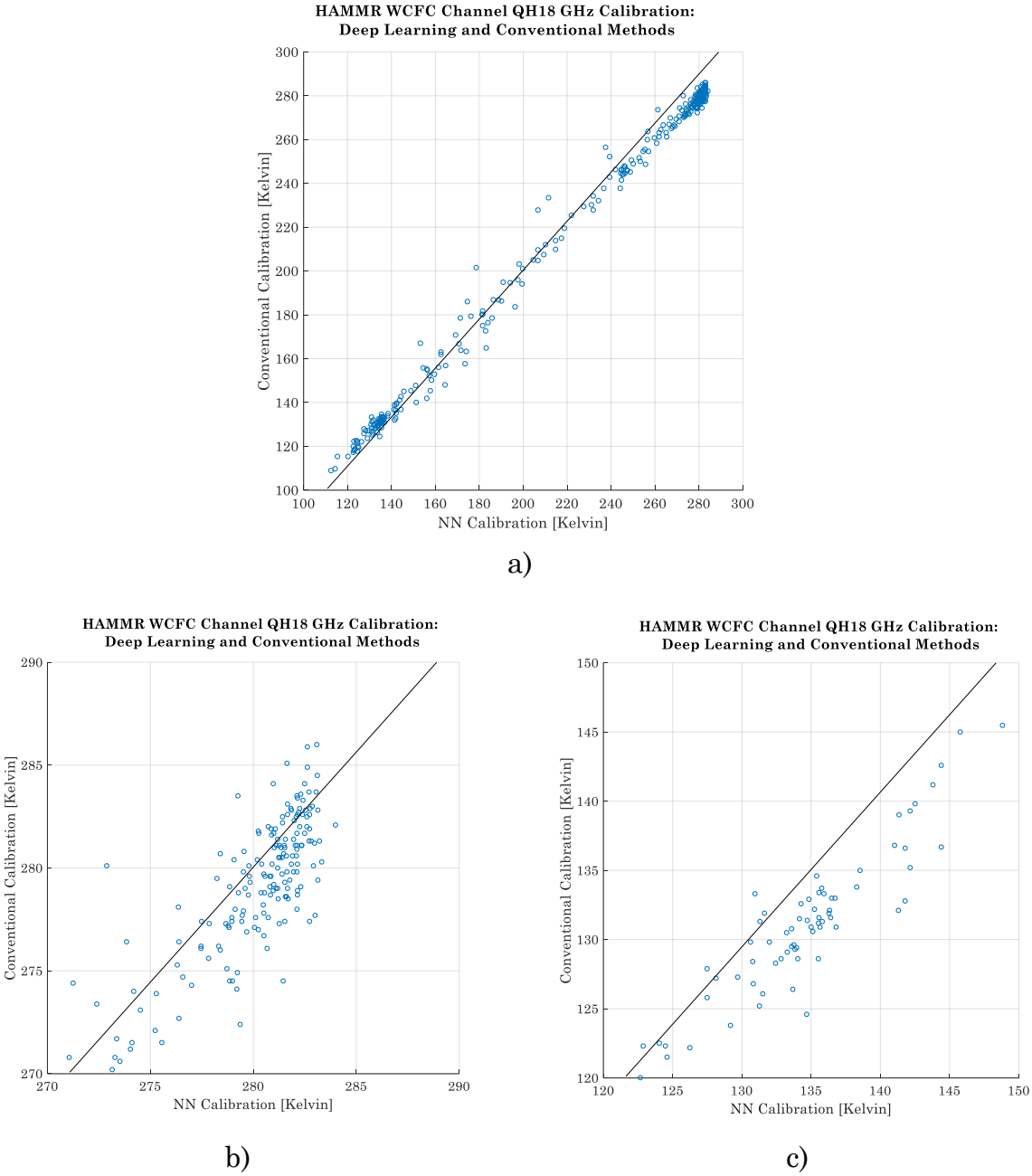

Figure 98: Scatter plot of deep learning calibrator results and conventional calibrator results for the HAMMR WCFC measurements over San Joaquin River. Antenna temperature estimate comparison for a) Full-range (RMSE: 4.5 K, STD: 4.3 K), b) Land measurements (RMSE: 1.4 K, STD: 1.4 K) and c) Water measurements (RMSE: 3.4 K, STD: 1.7 K).

learning calibrator is in agreement with the conventional calibration techniques. Figure 98b and Figure 98c show the deep learning calibrator antenna temperature estimates comparison with the conventional techniques for higher antenna temperatures and lower antenna temperatures respectively.

8.5. Conclusions

Artificial intelligence and machine learning are useful tools for implementing smart networks. A deep learning based calibration technique has been developed. The deep learning calibrator has been successfully applied to the artificially generated Dicke-switching radiometer which is presented in the previous chapter. The deep learning calibrator provides high accuracy antenna temperature estimates for several different radiometer hardware and operating conditions. The noise free testing cases has shown that the deep learning calibrator does not add any significant noise to the antenna temperature estimates. The new calibration technique performs well for a radiometer having high non-linearity and gain variations.

The deep learning calibrator is used to calibrate the HAMMR WCFC radiometric measurements. The antenna temperature estimates of the deep learning calibrator agree well with the estimates obtained from conventional calibration techniques for the HAMMR instrument. The results are expected to be improved if the HAMMR would have been designed for deep learning calibration.

The deep learning calibrator can be applied to microwave, millimeter-wave or sub-millimeter wave radiometer instruments operating from any platform including

spaceborne instruments. The training dataset of any radiometer can be collected during pre-launch testing at controlled laboratory environment. The deep learning algorithm can continue to learn during on-orbit operation. Vicarious sources can be used to tune in the algorithm.

Chapter IX Multi-angle and Multi-frequency Millimeter-wave Wet-Path Delay Retrievals

A new technique for wet-path delay (WPD) retrievals from millimeter-wave radiometric measurements is presented in this chapter. The technique relies on the sensitivity of radiometers to the WPD calculations at different observation angles for the same footprint spot on the ground through different frequency channels. The proposed method performs WPD using millimeter-wave window channels without relying on microwave or sounding channels. The microwave channel measurements are only used for the comparison of the retrieved WPD values with the millimeter-wave channel retrievals.

9.1. Background

Signals are distorted when they propagate through the atmosphere due to the permanent dipole of water-vapor molecules and the induced dipole moment of neutral atmospheric molecules. Distorted signal changes its path in the atmosphere to follow the shortest electrical path instead of traveling through the shortest geometric distance. This difference between electrical path length and geometric path length is referred as tropospheric radio-path delay. Path delay due to induced dipole of atmospheric gases mainly nitrogen and oxygen are called as dry path delay. Path delay as a result of permanent dipole of water vapor is called as wet-path delay. In a neutral atmosphere, the path delay is expressed as the sum of dry and wet components [32].

In this study, the main consideration is the wet component of the path delay since the ultimate goal is to predict amount of water vapor presence in the atmosphere. The detection of amount of water vapor through microwave and millimeter-wave radiometry relies on the frequency depended atmospheric attenuation of water vapor [140], [141], [142]. The permanent dipole of water vapor molecule defines the absorption bands of the radiometric measurements. The selection of microwave and millimeter-wave frequency channels for radiometric measurements to retrieve WPD has been explored in several studies and will not be further explained in this work [143].

9.2. Radiative Transfer Model for Millimeter-Wave WPD Retrieval

Assuming a radiometer antenna has an ideal pencil beam pattern, then the measured antenna temperature (T_{Ai}) by a radiometer at frequency i (up to 200 GHz) can be expressed as the sum of the individual contributions of upwelling (T_{up}), downwelling (T_{down}) and surface (T_{surf}) radiation using the Radiative Transfer Theory as [32]:

$$T_{Ai} = T_{up} + T_{surf} + T_{down} \tag{IX.1}$$

Upwelling brightness temperature is expressed as:

$$T_{up} = T_{atm\_up}(1 - \Upsilon_{ui}) \tag{IX.2}$$

where T_{atm_up} is the atmospheric temperature used for the calculation of the upwelling radiances and Υ_{ui} is the upwelling transmissivity calculated as:

$$\Upsilon_{ui} = e^{-\frac{\tau_i}{cos\theta}} \tag{IX.3}$$

where τ_i is the zenith optical depth of the atmosphere at given frequency i and θ is the incidence angle. The zenith optical depth is found by integrating the extinction coefficient ($\sigma_{ext,i}$) at frequency i over the atmospheric path from s' to s'':

$$\tau_i = \int_{s'}^{s''} \sigma_{ext,i}(s)\, ds \tag{IX.4}$$

The extinction coefficient given in the equation above is defined as the sum of scattering and absorption coefficients:

$$\sigma_{ext,i} = \sigma_{scat,i} + \sigma_{abs,i} \tag{IX.5}$$

where the absorption coefficient has dry and wet components as:

$$\sigma_{abs,i} = \sigma_{dry,i} + \sigma_{wet,i} \tag{IX.6}$$

For the frequencies up to 200 GHz, the clear-sky atmosphere can be considered as a non-scattering medium for radiance calculations. Therefore, only absorption coefficient will be considered. Thus, the optical depth is re-written as:

$$\tau_i = \int_{s'}^{s''} \sigma_{abs,i}(s)\, ds \tag{IX.7}$$

The surface brightness temperature contribution (T_{surf}) to antenna temperature measurements given in Equation (IX.1) is defined as:

$$T_{surf} = \Upsilon_{ui} e_i T_s \tag{IX.8}$$

where e_i is the emissivity calculated at given frequency i and T_s is the physical temperature of the surface. Finally, the downwelling radiation is the radiation received at the surface (T_{di}) and reflected back towards the radiometer:

$$T_{down} = T_{di}(1 - e_i)\Upsilon_{ui}) \tag{IX.9}$$

$$T_{di} = T_{atm\_down}(1 - \Upsilon_{di}) + T_{cb}\Upsilon_{di}) \tag{IX.10}$$

where Υ_{ui} in Equation (IX.9) is the downwelling transmissivity and is definition is similar to upwelling definition given in Equation (IX.3) but defined for radiation going down.

The antenna temperature measurement given in Equation (IX.1) is re-written using Equations (IX.2), (IX.8) and (IX.9):

$$T_{Ai} = T_{atm\_up}(1 - \Upsilon_{ui}) + \Upsilon_{ui}e_iT_s + T_{di}(1 - e_i)\Upsilon_{ui} \tag{IX.11}$$

The equation above can be simplified since the variation of surface emissivity among millimeter wave radiometric frequencies (e.g. between 90 GHz and 130 GHz) is negligible:

$$T_{Ai} = T_{atm\_up}(1 - \Upsilon_{ui}) + \Upsilon_{ui}eT_s + T_{di}(1 - e)\Upsilon_{ui} \tag{IX.12}$$

The main consideration of this study is to obtain a simplified form of radiative transfer theory to ease the derivation of the WPD retrieval model in the next section. Thus, Equation (IX.10) can be used in Equation (IX.12) to have the complete expression:

$$T_{Ai} = T_{atm_{up}}(1 - \Upsilon_{ui}) + \Upsilon_{ui} e T_s + (T_{atm_{down}}(1 - \Upsilon_{di}) + T_{cb}\Upsilon_{di})(1 - e)\Upsilon_{ui} \quad \text{(IX.13)}$$

The contribution of cosmic background radiation ($T_{cb}\Upsilon_{ui}\Upsilon_{di}(1 - e)$) to the antenna temperature measurements is negligible. Therefore, Equation (IX.13) is simplified into:

$$T_{Ai} = T_{atm\_up}(1 - \Upsilon_{ui}) + \Upsilon_{ui} e T_s + T_{atm\_down}(1 - \Upsilon_{di})(1 - e)\Upsilon_{ui} \quad \text{(IX.14)}$$

Furthermore, the downwelling and upwelling contributions travel through the same atmosphere. Therefore, the atmospheric temperature for upwelling and downwelling contributions are the same.

$$T_{atm\_up} = T_{atm\_down} = T_{atm} \quad \text{(IX.15)}$$

$$T_{Ai} = T_{atm}(1 - \Upsilon_{ui}) + \Upsilon_{ui} e T_s + T_{atm}(1 - \Upsilon_{di})(1 - e)\Upsilon_{ui} \quad \text{(IX.16)}$$

The downwelling and upwelling transmissivities can be considered to be same for the millimeter-wave radiometric channels with the assumption of a near-specular surface especially for the case where ocean surface wind speed is low resulting in negligible surface roughness.

$$\Upsilon_{ui} = \Upsilon_{di} = \Upsilon_i \quad \text{(IX.17)}$$

$$T_{Ai} = T_{atm}(1 - \Upsilon_i) + \Upsilon_i e T_s + T_{atm}(1 - \Upsilon_i)(1 - e)\Upsilon_i \quad \text{(IX.18)}$$

$$T_{Ai} = T_{atm} - T_{atm}\Upsilon_i + \Upsilon_i e T_s + T_{atm}\Upsilon_i - T_{atm}\Upsilon_i e - T_{atm}(\Upsilon_i)^2 + T_{atm}(\Upsilon_i)^2 e \quad \text{(IX.19)}$$

In the above equation, 2nd and 4th terms cancel each other:

$$T_{Ai} = T_{atm} + \Upsilon_i e T_s - T_{atm}\Upsilon_i e - T_{atm}(\Upsilon_i)^2 + T_{atm}(\Upsilon_i)^2 e \quad \text{(IX.20)}$$

Organizing terms in the above equation yields:

$$T_{Ai} = T_{atm} + \Upsilon_i e T_s - T_{atm}\Upsilon_i e + T_{atm}(\Upsilon_i)^2 (e - 1) \quad \text{(IX.21)}$$

A simplified formulation can be obtained to express the antenna temperature measurements as:

$$T_{Ai} = T_{atm}\left\{1 + \Upsilon_i e\left(\frac{T_s}{T_{atm}} - 1\right) + (\Upsilon_i)^2 (e - 1)\right\} \quad \text{(IX.22)}$$

Equation (IX.22) represents the final form of the radiative transfer definition relating antenna temperature measurements at millimeter-wave radiometric channels to upwelling, downwelling and surface radiation contributions. The second term in the above equation can be ignored for the cases where the surface temperature is close to the atmospheric temperature. In addition, the last term can be neglected if there is a strong absorption resulting in low transmissivity or very high emission from the surface.

9.3. Millimeter-Wave WPD Retrieval Model

The WPD retrieval model at millimeter-wave frequency channels derived is explained in this section. The proposed radiometric measurement technique is explained before the retrieval model is discussed.

9.3.1 Radiometric Information Content for Radiometric Measurements

Dry and wet absorption of the atmosphere are frequency dependent variables resulting in different atmospheric opacity at different frequencies for the same atmosphere. Using the absorption models for frequencies below 200 GHz, dry absorption and wet absorption for 1 cm, 10 cm and 30 cm wet path delay values with respect to observation frequency are plotted in Figure 99. As shown in this figure, water vapor has absorption lines at 22 GHz and 183 GHz. Other absorption lines are located at 60 GHz and 118 GHz used for temperature profiling of the atmosphere since they are defined for dry absorption. The frequency channels in between two absorption lines are called as window channels [124].

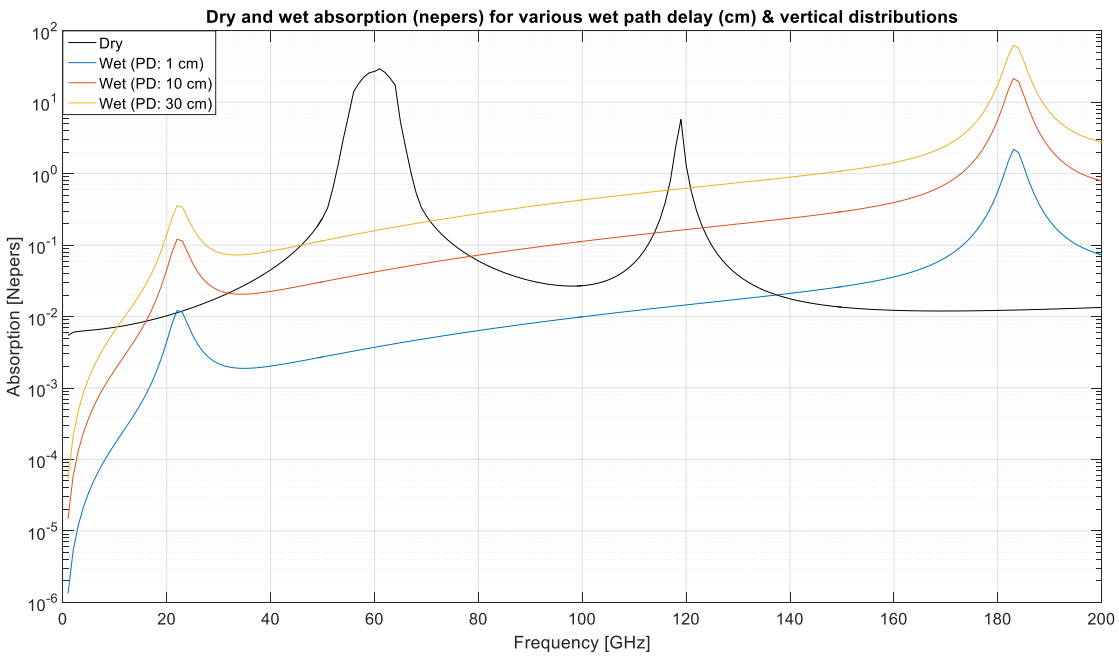

Figure 99: The water-vapor and oxygen absorption profiles for the frequencies below 200 GHz given at different atmospheric conditions.

The retrieval of the WPD from the antenna temperature measurements is not straightforward if one tries to directly employ the expression given in Equation (IX.22) obtained from single-frequency radiometric measurements since there are more than one unknown parameters need to be solved. Employing the antenna temperature measurements at frequency sets of 90 GHz and 130 GHz window channels for the retrievals of WPD have different sensitivity to wet absorptions and can help eliminating the dependency on the dry absorption coefficient since both frequency channels have similar dependency on the dry absorption as shown in Figure 99. Furthermore, observation angle of a radiometer at a given frequency is sensitive to water vapor since the path taken by the signal is different at every angle and affected by water content of the atmosphere on the line of sight. Therefore, a retrieval algorithm may utilize the information content of various angular observation of the same frequency channel to retrieve WPD.

For this study, 32° and 45° observation angles are chosen in addition to nadir view to obtain radiometric measurements sensitive to water vapor content in the atmosphere since the optical depth of the atmosphere given in Equation (IX.3) depends on the cosine of the observation angle.

The proposed retrieval algorithm relies on the observation of the same footprint at the same time through 90 GHz and 130 GHz frequency channels each having nadir, 32° and 45° observation angles. The selection of 32° and 45° observation angles in addition to nadir view of the radiometer is to obtain radiometric measurements sensitive to water vapor content in the atmosphere since the optical depth of the

atmosphere given in Equation (IX.3) depends on the cosine of the observation angle with respect to nadir view.

9.3.2 Retrieval Algorithm

There are two general approaches have been employed in WPD retrievals through microwave frequency channel radiometric measurements [33]. The inverse retrieval algorithms try to estimate the WPD content by iteratively solving the radiative transfer equation to a specified accuracy [7], [144]. The other method employed in microwave remote sensing for retrieving the WPD is based on a statistical approach [30], [145], [146]. The statistical method relates the brightness temperature measurements to atmospheric retrievals by employing retrieval coefficients.

The antenna temperature definition for millimeter-wave frequency channels can be further modified to minimize the sensitivity of the radiometric measurements to atmospheric variables except the transmissivity of the atmosphere. Thus, one can define the ratio of the antenna temperature measurement performed at two different radiometric channels i and j as:

$$r_{ij} = \frac{T_{Ai}}{T_{Aj}} \tag{IX.23}$$

$$r_{ij} = \frac{T_{atm}\left\{1 + \Upsilon_i e\left(\frac{T_s}{T_{atm}} - 1\right) + (\Upsilon_i)^2(e-1)\right\}}{T_{atm}\left\{1 + \Upsilon_j e\left(\frac{T_s}{T_{atm}} - 1\right) + \left(\Upsilon_j\right)^2(e-1)\right\}} \tag{IX.24}$$

$$r_{ij} = \frac{1 + \Upsilon_i e\left(\frac{T_s}{T_{atm}} - 1\right) + (\Upsilon_i)^2(e-1)}{1 + \Upsilon_j e\left(\frac{T_s}{T_{atm}} - 1\right) + \left(\Upsilon_j\right)^2(e-1)} \tag{IX.25}$$

The channel indices given above as i and j refer to any of the six channels at two different frequencies and three different observation angles. The ratio defined in the above equation can be simply expressed by defining a new variable for the terms related to surface temperature, atmospheric temperature and emissivity variables as:

$$m \triangleq e\left[\frac{T_s}{T_{atm}} - 1\right] \tag{IX.26}$$

$$n \triangleq e - 1 \tag{IX.27}$$

$$x_i \triangleq \Upsilon_i \tag{IX.28}$$

Then, the Equation (IX.25) is written as:

$$r_{ij} = \frac{1 + mx_i + nx_i^2}{1 + mx_j + nx_j^2} \tag{IX.29}$$

The goal for retrieving the WPD is to find an expression by using the above expression which relates the WPD to the measured antenna temperature ratios as the following:

$$WPD = f\left(r_{ij}\right) = f[g(x)] \tag{IX.30}$$

where f and g represent the functions mapping the ratios to the WPD and the transmissivity respectively. Regression techniques have been employed in the past to retrieve WPD from the microwave frequency radiometric measurements [30]. The regularization techniques and inverse solution methods such as Backus-Gilbert

have been used to solve the ill-posed regression problem for the retrieval of atmospheric parameters at microwave frequency channels [147], [148], [149].

The goal for employing the regularization in this study is to determine a non-linear expression relating the ratio of the measured antenna temperatures at millimeter-wave frequency channels to the WPD as defined in Equation (IX.30). The regularization ratio is the main driven factor to determine the success of a regularization method. The regularization term can be found by minimizing the squared error on the validation dataset for atmospheric retrievals such as the conjugate gradient method [150] or the techniques employing techniques based on Bayes' theorem [151].

The solution to the Equation (IX.30) relating the WPD to the ratio of the millimeter-wave antenna temperature measurements is suitable for the application of the Bayesian regularization since each individual ratio of the measurements is not independent from its neighboring cell when we consider the antenna footprints as a grid of many cells across the instrument swath-width [149].

The Bayesian regularization employs Bayes' rule of probability to determine the regularization term where each weight is a random variable for the solution of the probability function given as:

$$P(w|D,\alpha,\beta,M) = \frac{P(D|w,\beta,M)P(w|\alpha,M)}{P(D|\alpha,\beta,M)} \tag{IX.31}$$

where w is the set of weights and biases for the regularization of the non-linear regression approach for the solution of Equation (IX.29) to determine the relating

function in Equation (IX.30). In addition, D represents the dataset used in the regression analysis, α and β are the regularization terms and M is used to define the structure of the algorithm (i.e. the dimension and number of weights).

In the above equation, $P(D|w,\beta,M)$ is the likelihood function defining how likely a dataset will occur given a specific vector w. Our consideration is to find a set of parameters for w to maximize the likelihood function in the regularization. $P(w|\alpha,M)$ is the initialization of the weights prior to regression. $P(D|\alpha,\beta,M)$ is only used as a normalization factor to guarantee that the total probability is 1 and does not have direct effect to determine the parameters for w maximizing the likelihood function.

The calculation of the optimum regularization terms α and β, and the vector w can be performed by employing Levenberg-Marquardt (LM) optimization algorithm. The LM optimization eases the calculation of the Hessian matrices which are used to estimate the minimum points of the second order derivative solution to regularization terms [152].

The WPD retrieval algorithm at millimeter-wave window frequency channels is based on the estimation of the coefficients relating three different ratios of the antenna temperature measurements at two different frequencies and 3 different observation angles by employing the LM based Bayesian regularization technique. The three coefficients are:

$$r_{00} = \frac{T_{A130,0}}{T_{A90,0}} \tag{IX.32}$$

$$r_{11} = \frac{T_{A130,32}}{T_{A90,32}} \tag{IX.33}$$

$$r_{22} = \frac{T_{A130,45}}{T_{A90,45}} \tag{IX.34}$$

where $T_{A130,0}$, $T_{A130,32}$ and $T_{A130,45}$ are the antenna temperature measurements at 130 GHz frequency for nadir view, and 32° and 45° observation angles respectively. Similarly, $T_{A90,0}$, $T_{A90,32}$ and $T_{A90,45}$ stand for 90 GHz antenna temperature measurement at nadir view and 32° and 45° observation angles respectively.

Using these ratios defined, the definition given in Equation (IX.30) is rewritten as:

$$\mathrm{WPD} = \mathrm{f}(\mathrm{r}_{00}, \mathrm{r}_{11}, \mathrm{r}_{22}) \tag{IX.35}$$

Several different datasets are generated to estimate the regression coefficients of the above function by using the Bayesian regularization. For the simulated dataset, the parameters given in Table 29 are used with the assumption of no significant surface roughness [30]. The derived coefficients are provided at the end of this Chapter under WPD Retrieval Method Parameters.

9.4. Demonstration of the WPD Retrieval Method

The demonstration of the new method is performed using the millimeter-wave window channel measurements of the HAMMR instrument obtained during WCFC in 2014. The HAMMR instrument is described in Chapter VIII under HAMMR deep learning calibration section.

Table 29: Parameters of the dataset for Bayesian regularization

Parameter	Value
WPD	From 1 cm to 20 cm
Surface Emissivity	0.5 (±0.05)
Surface Temperature	288 K (±10 K)

The WPD retrievals of the HAMMR instrument has been performed by using the radiometric measurements at microwave channel frequency. However, high-frequency millimeter-wave channel measurements need to be used for WPD retrievals to obtain WPD retrievals with high-spatial resolution. The millimeter-wave radiometric retrievals obtained using the new method will be compared with the microwave channel retrievals of the HAMMR instrument.

The sensitivity of the ratios defined through Equations (IX.32) and (IX.34) obtained from HAMMR millimeter-wave window channel measurements during WCFC is analyzed for the HAMMR instrument in Figure 100. The antenna temperature measurements ratios for the radiometric measurements through 90 GHz and 130 GHz at nadir and 45° view over similar area at San Joaquin River on different days are given in Figure 100a and Figure 100b. The retrieved WPD through microwave channels are plotted in Figure 100c and Figure 100d for different day radiometric measurements. A simple data analysis for the ratios and their comparison with the retrieved WPD values at microwave channels as given in Figure 100 indicate that the ratios are sensitive to WPD as expected from the theoretical calculations made.

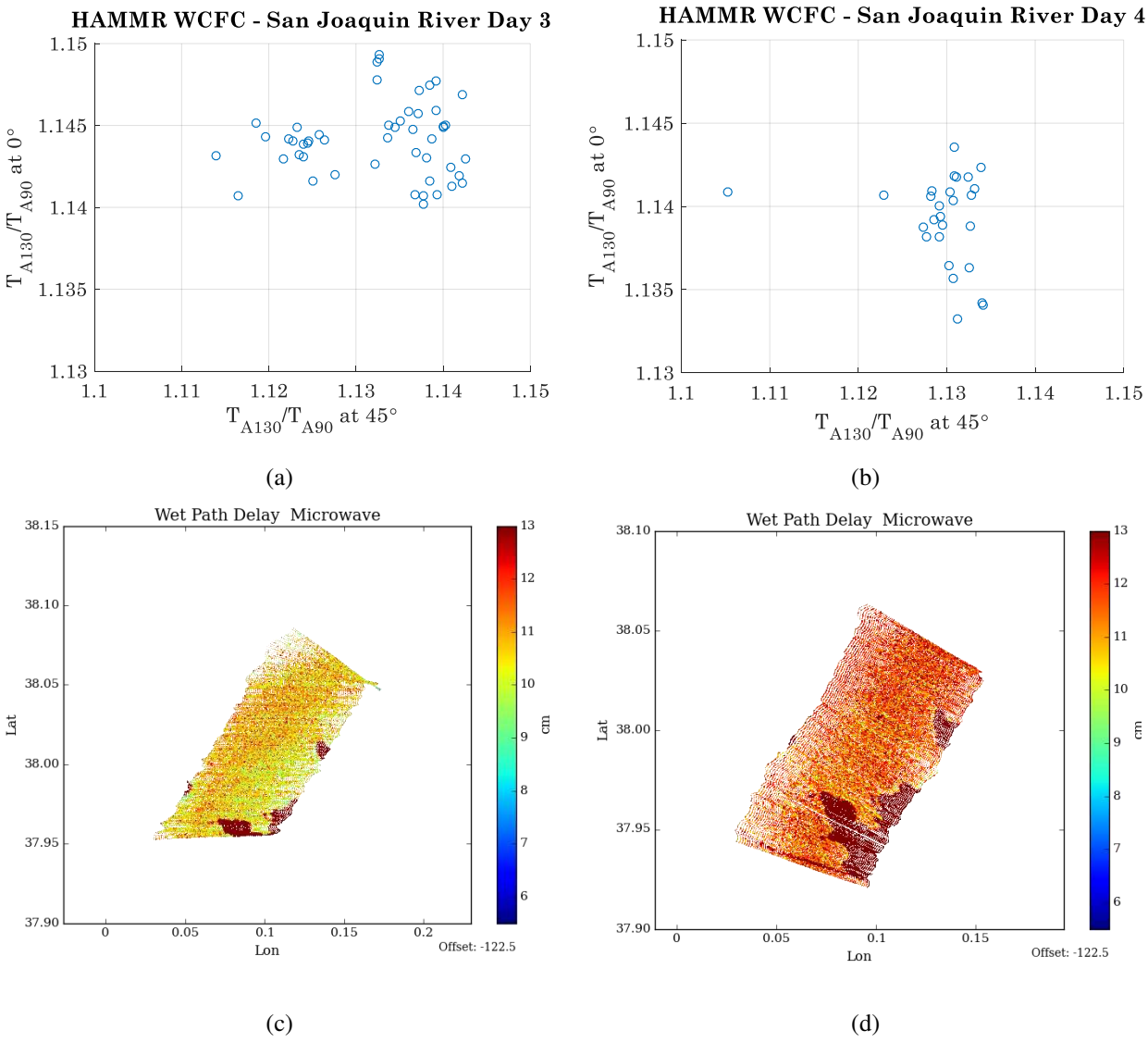

Figure 100: The sensitivity of the ratios obtained from HAMMR millimeter-wave window channel measurements over the San Joaquin River at different days for the WPD retrievals is analyzed: a) Ratios for the Day3, b) Ratios for the Day4, c) Microwave WPD retrievals for Day3 and d) Microwave WPD retrievals for Day4.

9.5. WPD Retrieval Results

The WPD retrieval algorithm derived using the ratios of the antenna temperature measurements at 90 and 130 GHz frequency channels at three different observation

angles by employing the Bayesian regularization is used to estimate the retrieved WPD values for the HAMMR WCFC radiometric measurements. The proposed method suggests viewing the same footprint with different frequency channels at various observation angles. However, the HAMMR cross-track scanning instrument is not designed for performing the radiometric measurements as the algorithm suggests. Therefore, the WPD retrievals will be performed through millimeter-wave channels of the HAMMR instrument when the instrument sees similar surface on the ground. The measurements where the instrument observes different surface properties through different observation angles will not be considered.

The WPD retrieval algorithm results are shown in Figure 101 when the proposed method is applied to the HAMMR WCFC measurements performed over San Joaquin River in 2014. The antenna temperature measurements obtained from 90 GHz and 130 GHz window channels at three different observation angles are provided at the top chart in Figure 101. Please note that big jumps in the antenna temperature measurements at only some specific observation angles but not observed on all due to the fact that those observations are performed on a land surface or water-land boundary. Therefore, the retrievals are valid for those retrieved from the regions which all the channels at all observation angles observe a similar surface which are given in red rectangular boxes on the figure. The retrieved WPD values through millimeter-wave channels are plotted at the chart at the bottom in Figure 101 with the microwave WPD retrievals as a comparison. The WPD retrieval results indicate that the estimated WPD values obtained from the

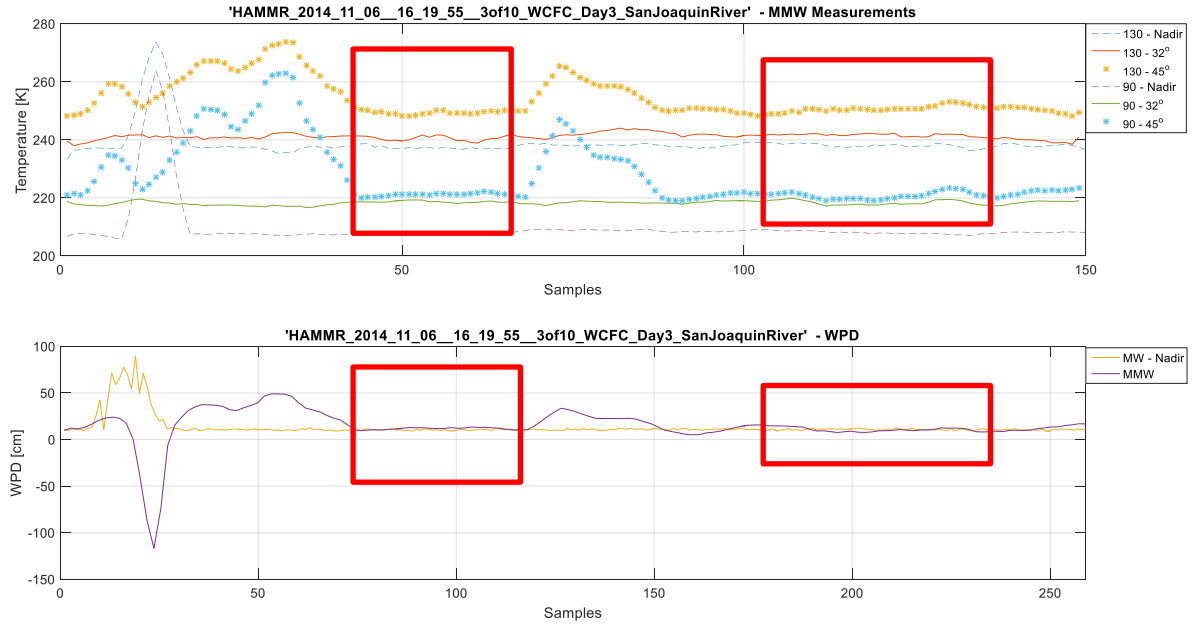

Figure 101: WPD retrievals using 90 GHz and 130 GHz millimeter-wave window channels of the HAMMR instrument for the WCFC measurements over San Joaquin River. Please note that retrieval zones are given in red.

proposed millimeter-wave retrieval technique are in agreement with the microwave channel retrievals.

The geo-located antenna temperature measurements of the HAMMR instrument that the WPD retrievals are performed from is given in Figure 102. The algorithm performs poor outside of the filtered zone since the instrument sees water-land boundary or land surface at off-nadir observation angles. This finding is in agreement with what the proposed algorithm suggests such that all the antenna temperature measurements used in the calculation of the ratios should observe the same footprint on the surface.

The WPD retrievals obtained from the HAMMR millimeter-wave window channel

Figure 102: Geo-located antenna temperature measurements of the HAMMR instrument for the WCFC measurements over San Joaquin River. Please note that retrieval valid zones are given in red.

measurements using the proposed algorithm are compared with the microwave retrievals obtained from the HAMMR microwave channel measurements in Figure 103. The scatter plot indicates that the retrievals obtained through the proposed technique are in close agreement with microwave channel retrievals.

9.6. Conclusions

The WPD retrievals at millimeter-wave channel radiometric measurements will provide better spatial resolution in comparison to microwave channel retrievals. A technique for retrieving WPD from employing only the millimeter-wave window channel measurements is presented in this study. The proposed algorithm relies on the measurements of 90 GHz and 130 GHz frequency channels at nadir, 32° and 45°

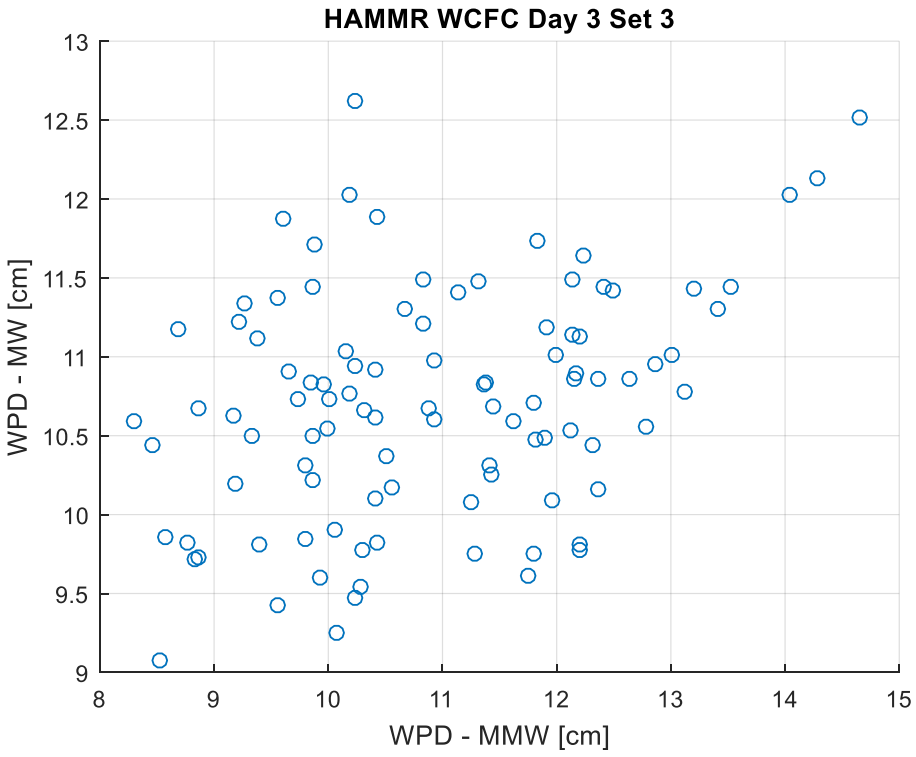

Figure 103: Comparison of WPD retrievals using 90 GHz and 130 GHz millimeter-wave window channels and microwave channels of the HAMMR instrument for the WCFC measurements over San Joaquin River.

observation angles. The algorithm is developed using the ratio of the measurements employing the Bayesian regularization.

The demonstration of the proposed algorithm with the HAMMR WCFC measurements performed in 2014 indicates that the WPD retrievals are in agreement with the microwave channel measurements. In the validation process with the HAMMR data, it has been assumed that the change of the WPD and other atmospheric and surface properties is negligible among different observation angles of this cross-track scanning radiometer within the retrieval zone. Thus, the accuracy of the measurements is expected to be improved if one applies the

proposed algorithm to the millimeter-wave measurements obtained from the exactly same footprint size.

The proposed algorithm could be further advanced by incorporating different millimeter-wave frequency channel measurements into the developed algorithm. Using the least number of frequency channels will have the benefit of generating an insensitive pair of frequencies to dry absorption while sensitive to wet absorption in addition to possible advantages in the instrument development. Furthermore, the algorithm can perform better when the dataset is enriched. However, the effect of the dataset used for the algorithm development on the WPD retrieval performance is expected to be limited since the ratios employed in this technique have low sensitivity to change in an atmospheric variable.

9.7. WPD Retrieval Method Parameters

Bayesian regularization LM solution parameters mapping the ratios to given in Equations (IX.32) to (IX.34) the WPD retrievals are given below:

- $\text{Input Offset} = [1.0250;\ 1.0285; 1.0327]$
- $\text{Input Gain} = [9.4709;\ 9.8163;\ 10.2739]$
- $\text{Input Bias} = \begin{bmatrix} -0.2715 \\ 0.6869 \\ -3.2776 \\ 0.6735 \\ 4.8737 \\ -2.2303 \\ -0.0289 \\ -1.1798 \\ -0.0110 \\ 0.9508 \end{bmatrix}$

- Input Weights $= \begin{bmatrix} 0.2661 & 0.4591 & 0.6042 \\ 0.5015 & 1.1541 & 0.9351 \\ -1.0258 & -0.5847 & -2.0360 \\ 0.3945 & 0.5419 & 1.3136 \\ 5.4870 & 2.8889 & -3.1782 \\ -3.1081 & -1.7838 & 2.7290 \\ -0.6609 & -1.0338 & 0.4080 \\ -1.3110 & -1.0188 & 1.9388 \\ -0.1709 & 0.1273 & 0.4799 \\ -0.9617 & -0.1265 & 0.7411 \end{bmatrix}$

- Output Bias $= [-2.3200]$

- Output Gain $= [0.1053]$

- Output Weights $= \begin{bmatrix} -0.6960 \\ 0.5065 \\ 5.2477 \\ -1.0963 \\ 4.4897 \\ -3.1140 \\ -1.1983 \\ -1.8275 \\ -1.3567 \\ -1.4548 \end{bmatrix}$

- Activation f(x) $= \frac{2}{1+e^{-2x}} - 1$

Chapter X Conclusions and Future Work

10.1. Conclusions

Atmospheric remote sensing from radiometer instruments on a CubeSat platform is studied from various different aspects including the instrument design, reliability of the instrument, receiver characterization, radiometer calibration and WPD retrievals.

The TWICE 6U Class satellite instrument has 16 radiometric channels from 118 GHz to 670 GHz frequencies. The TWICE instrument is being designed to provide radiometric measurements for the retrievals of lower-stratospheric, upper-tropospheric water vapor and cloud ice information in addition to temperature and water-vapor profiling through the sounding channels.

A low-power, low-noise and reliable C&DH board is designed for the TWICE instrument. The C&DH board performs low-noise, synchronous and simultaneous radiometric acquisition of 16 radiometric channels. In addition, the FPGA on the C&DH board controls the interfaces with the other subsystems and monitoring the instrument system health control through current sensing and voltage monitoring devices.

Noise coupled into the radiometric measurements at the digital acquisition may degrade the radiometer NEΔT performance achieved by the front-end receivers and the antenna. Therefore, the quality and reliability of radiometric measurements of TWICE cannot be achieved without a low-noise high precision radiometric

acquisition at the C&DH system. The design requirements for the C&DH system are described in detail. An extensive analysis is performed to determine the factors affecting the system performance for the optimum design architecture.

A reliable high-efficiency power regulation board is designed to power the front-end receivers and the C&DH board. The power regulation board design requirements are determined for a reliable on-orbit operation of the TWICE instrument at high-efficiency. The start-up transients, overshoots and undershoots are tested in addition to output voltage swing during normal operation for a reliable system operation.

For the reliability and the quality of radiometric measurement, the radiometer instrument should also meet the environmental operation requirements in addition to functional specifications. A device level and system level TWICE radiation hardness analysis is performed. The critical parts of the TWICE electronics are tested with heavy-ions at Texas A&M Cyclotron Facility. Mitigation and design strategies for the on-orbit radiation effects are proposed for the final C&DH and power regulation boards. The designed boards are expected to operate reliable under TWICE-like radiation environments.

The TWICE receivers are integrated with the C&DH and power regulation boards to perform end-to-end radiometer testing. A 1/f noise mitigation technique is implemented for the 670 GHz receivers by switching the 1st LNA block of the receiver. The synchronization of the switching signal generated from the FPGA with the radiometric acquisitions is successfully controlled by the FPGA. Y-factor and

stability tests are successfully performed on the prototype 670 GHz receiver at CSU. The final receiver testing integrated with the final C&DH system is performed at NASA/JPL. The test results have shown that the TWICE receivers, final C&DH board and power regulation board meet the design specification for the TWICE 6U class radiometer instrument in addition to size, weight and power requirements for 6U Class satellites.

Radiometer calibration plays a major role in the accuracy, reliability and stability of the radiometric measurements. It is discussed that conventional calibration techniques have challenges for the application on the microwave, millimeter and sub-millimeter-wave radiometers especially those designed for a CubeSat platform. A deep learning based calibration technique is developed for high accuracy and reliable radiometer calibration. The proposed deep learning calibration method is successfully demonstrated on an artificially generated Dicke-switching radiometer. Then, the deep learning calibrator is applied to the HAMMR instrument for the calibration of the radiometric channels. The HAMMR WCFC measurements are used for the demonstration of the new calibration technique on a physically designed instrument. The comparison of the deep learning calibrator results with the conventional calibration methods for the HAMMR instrument has shown that the deep learning calibration algorithm can provide high accuracy reliable antenna temperature estimates.

Finally, the WPD retrievals are critical for the understanding of the atmospheric dynamics as well as improving weather forecast and climate models. The high-

frequency millimeter-wave channel radiometric measurements provide high resolution radiometric data compared to microwave channel measurements. A WPD retrieval algorithm is developed for the millimeter-wave channel radiometric measurements. The designed algorithm is successfully applied to the HAMMR instrument WCFC radiometric measurements for the retrieval of WPD. The comparison of the millimeter-wave retrievals with the microwave retrievals of the HAMMR instrument for the same footprint size has shown that the algorithm performs WPD retrievals close to those for microwave channel retrieval algorithms.

10.2. Future Work

The developed deep learning calibrator algorithm may be applied for the on-orbit TWICE radiometer instrument calibration. TVAC measurements can be performed on ground after the instrument is integrated and tested. The data collected during TVAC testing can be used to train a deep learning calibration algorithm. Then, the algorithm can be tuned with the help of external ambient calibration target and cold sky reflector of the TWICE instrument for reliable on-orbit calibration.

Next, the developed WPD retrieval algorithm can be applied for the performing retrievals from other millimeter-wave channel radiometric measurements. The designed algorithm could be improved for performing high accuracy WPD retrievals from the radiometric measurements over land.

Furthermore, a compact retrieval algorithm can be developed for the WPD and cloud ice retrievals by using the millimeter and sub-millimeter-wave radiometric channels of the TWICE instrument. The information content obtained from each

radiometric channel of the TWICE instrument can be used to retrieve cloud ice size and particle information. The sounding channels for temperature and water vapor profiling along with the radiometric channels of the TWICE instrument will be valuable to assess a complete knowledge of the atmosphere.

Bibliography

[1] D. O. Starr and S. H. Melfi, "The role of water vapor in climate: A strategic research plan for the proposed GEWEX water vapor project (GVaP)," *NASA Conference Publications 3120,* 1991.

[2] T. Schneider, P. A. O'Gorman and X. J. Levine, "Water vapor and the dynamics of climate changes," *Reviews of Geophysics,* vol. 48, no. RG3001, 2010.

[3] E. R. Westwater, "The accuracy of water vapor and cloud liquid determination by dual-frequency, ground-based microwave radiometry," *Radio Science,* vol. 13, no. 4, pp. 677-685, 1978.

[4] J. R. Wang, P. E. Racette and J. R. Piepmeier, "A comparison of near-concurrent measurements from the SSMIS and CoSMIR for some selected channels over the frequency range of 50-183 GHz," *IEEE Transactions on Geoscience and Remote Sensing,* vol. 46, no. 4, pp. 923-933, April 2008.

[5] C. Kummerow, I. M. Hakkarinen, H. F. Pierce and J. A. Weinman, "Determination of precipitation profiles from airborne passive microwave radiometric measurements," *Journal of Atmospheric and Oceanic Technology,* vol. 8, pp. 148-158, 1991.

[6] S. T. Brown, B. Lambrigsten, R. F. Denning, T. Gaier, P. Kangaslahti, B. H. Lim, J. M. Tanabe and A. B. Tanner, "The High-Altitude MMIC Sounding

Radiometer for the Global Hawk unmanned aerial vehicle: Instrument description and performance," *IEEE Transactions on Geoscience and Remote Sensing,* vol. 49, no. 9, pp. 3291-3301, Sept. 2011.

[7] N. C. Grody, "Remote sensing of atmospheric water content from satellites using microwave radiometry," *IEEE Transactions on Antennas and Propagation,* Vols. AP-24, no. 2, pp. 155-162, Mar. 1976.

[8] L.-L. Fu, E. J. Christensen, C. A. Yamarone Jr., M. Lefebvre, Y. Menard, M. Dorrer and P. Escudier, "TOPEX/POSEIDON mission overview," *Journal of Geophysical Research,* vol. 99, no. C12, pp. 24,369-24,381, Dec. 1994.

[9] S. A. Buehler, C. Jimenez, K. F. Evans, P. Eriksson, B. Rydberg, A. J. Heymsfield, C. J. Stubenrauch, U. Lohmann, C. Emde, V. O. John, T. R. Sreerekha and C. P. Davis, "A concept for a satellite mission to measure cloud ice water path, ice particle size, and cloud altitude," *Quarterly Jounral of the Royal Meteorological Society,* vol. 133, no. S2, pp. 109-128, 2007.

[10] R. T. Austin, A. J. Heymsfield and G. L. Stephens, "Retrieval of ice cloud microphysical parameters using the CloudSat millimeter-wave radar and temperature," *Journal of Geophysical Research,* vol. 11, p. D00A23, 2009.

[11] S. Platnick, M. D. King, S. A. Ackerman, P. W. Menzel, B. A. Baum, J. C. Riedi and R. A. Frey, "The MODIS cloud product: Algorithms and examples from Terra," *IEEE Transactions on Geoscience and Remote Sensing,* vol. 41, no. 2, pp. 459-473, Feb. 2003.

[12] K. F. Evans, S. J. Walter, A. J. Heymsfield and M. N. Deeter, "Modeling of submillimeter passive remote sensing of cirrus clouds," *Journal of Applied Meteorology,* vol. 37, pp. 184-205, Feb. 1998.

[13] C. Jimenez, S. A. Buehler, B. Rydberg, P. Eriksson and K. F. Evans, "Performance simulations for a submillimeter-wave satellite instrument to measure cloud ice," *Quarterly Journal of the Royal Meteorological Society,* vol. 133, no. S2, pp. 129-149, 2007.

[14] J. H. Jiang, Q. Yue, H. Su, S. C. Reising, P. P. Kangaslahti, W. R. Deal , E. T. Schlecht, L. Wu and K. F. Evans, "A simulation of ice cloud particle size, humidity and temperature measurements from the TWICE CubeSat," *Earth and Space Science,* vol. 4, pp. 574-587, 2017.

[15] The CubeSat Program, "CubeSat Design Specification Rev.13," Cal Ploy, San Luis Obispo, CA, 2014. [Online]. Available: htttp://www.cubesat.org. [Accessed 20 Sept. 2018].

[16] The CubeSat Program, "6U CubeSat Design Specifications Rev. PROVISIONAL," Cal Poly, San Luis Obispo, CA. [Online]. Available: https://cubesat.org. [Accessed 20 Sept. 2018].

[17] NASA CubeSat Launch Initiative, "CubeSat 101: Basic Concepts and Processes for First-Time CubeSat Developers," Oct. 2017. [Online]. Available: https://www.nasa.gov/sites/default/files/atoms/files/nasa_csli_cubesat_101_50

8.pdf. [Accessed 20 Sept. 2018].

[18] J. Bouwmeester and J. Guo, "Survey of worldwide pico- and nanosatellite missions, distributions and subsystem technology," *Acta Astronautica,* vol. 67, no. 7-8, pp. 854-862, Oct. 2010.

[19] National Academy of Sciences, Engineering and Medicine, Achieving Science with CubeSats: Thinking Inside the Box, Washington, DC: The National Academies Press, 2016.

[20] Y. Rahmat-Samii, V. Manohar and J. M. Kovitz, "For Satellites, Think Small, Dream Big," *IEEE Antennas & Propagation Magazine,* pp. 22-30, Apr. 2017.

[21] S. C. Reising, T. C. Gaier, C. D. Kummerow, S. Padmanabhan, B. H. Lim, C. Heneghan, W. Berg, V. Chandrasekar, J. P. Olson, S. T. Brown, J. Carvo and M. Pallas, "Global Measurement of Temporal Signatures of Precipitation: Development of the Temporal Experiment for Storms and Tropical Systems Technology Demonstration Mission," *Proc. 2017 IEEE International Geoscience and Remote Sensing Symposium (IGARSS),* Fort Worth, TX, Jul. 2017, pp. 5931-5933.

[22] MIT Lincoln Laboratory, "Time-Resolved Observations of Precipitation structure and storm Intensity with a Constellation of Smallsats," Massachusetts Institute of Technology, [Online]. Available: https://tropics.ll.mit.edu/CMS/tropics/pdf/nasaTropicsFactSheet.pdf.

[Accessed 20 Sept. 2018].

[23] S. C. Reising, T. C. Gaier, C. D. Kummerow, V. Chandrasekar, S. T. Brown, S. Padmanabhan, B. H. Lim, S. C. Van Den Heever, T. S. L'Ecuyer, C. S. Ruf, Z. S. Haddad, J. Z. Luo, S. J. Munchak, G. Berg, T. C. Koch and S. A. Boukabara, "Overivew of Temporal Experiments of Storms and Tropical Systems (TEMPEST) CubeSat Constellation Mission," in *IEEE Microwave Theory and Techniques Society International Microwave Symposium Digest*, May 2015.

[24] W. Blackwell, G. Allen, C. Galbraith, T. Hancock, R. Leslie, I. Osaretin, L. Retherford, M. Scarito, C. Semisch, M. Shields, D. Toher, K. Wight, D. Miller, K. Cahoy and N. Erickson, "Nanosatellites for earth environmental monitoring: The MicroMAS project," *12th Specialist Meeting on Microwave Radiometry and Remote Sensing of the Environment (MicroRad),* pp. 1-4, Rome, 2012.

[25] J. T. Johnson, C. C. Chen, A. O'Brien, G. E. Smith, C. McKelvey, M. Andrews, C. Ball, S. Misra, S. Brown, J. Kocz, R. Jarnot, D. C. Bradley, P. N. Mohammed, J. F. Lucey and J. R. Piepmeier, "The CubeSat Radiometer Radio Frequency Interference Technology Validation (CUBERRT) Mission," *In Proceedings of the 2016 IEEE International Geoscience and Remote Sensing Symposium (IGARSS),* p. 299–301, Beijing, China, 10–15 Jul. 2016.

[26] M. Ogut, X. Bosch-Lluis, S. C. Reising, Y. V. Goncharenko, P. Kangaslahti,

E. Schlecht, R. Cofield, N. Chahat, S. Padmanabhan, J. Jiang, S. T. Brown, W. R. Deal, A. Zamora, K. Leong, S. Shih and G. Mei, "Command and Data Handling (C&DH) Subsystem for the Tropospheric Water and Cloud Ice (TWICE) 6U-Class Satellite Instrument," *Proc. 2017 IEEE International Geoscience and Remote Sensing Symposium (IGARSS),* Fort Worth, TX, Jul. 2017, pp. 2744-2747.

[27] F. Ulaby, R. Moore and A. Fung, Microwave Remote Sensing: Active and Passive, Vol. I - Microwave Remote Sensing Fundamentals and Radiometry, Reading, MA: Addison-Wesley, 1981.

[28] N. Bohr, "The Quantum Postulate and the Recent Development of Atomic Theory," *Nature,* vol. 121, pp. 580-590, Apr. 1928.

[29] N. C. Grody, "Remote Sensing of the atmosphere from satellites using microwave radiometry," in *Atmospheric Remote Sensing by Microwave Radiometry*, New York, Wiley-Interscience, 1993, pp. 259 - 314.

[30] T. T. Wilheit and A. T. C. Chang, "An algorithm for retrieval of ocean surface and atmopsheric paramters from the observations of the scanning multichannel microwave radiometer," *Radio Science,* vol. 15, no. 3, pp. 525-544, May-June, 1980.

[31] J. R. Piepmeier, D. R. Long and E. G. Njoku, "Stokes Antenna Temperatures," *IEEE Transactions on Geoscience and Remote Sensing,* vol. 46, no. 2, pp. 516-526, Feb. 2008.

[32] M. A. Janssen, in *Atmospheric Remote Sensing by Microwave Radiometry*, New York, Wiley-Interscience, 1993.

[33] S. J. Keihm, M. A. Janssen and C. S. Ruf, "TOPEX/Poseidon Microwave Radiometer (TMR): III. Wet Troposphere Range Correction Algorithm and Pre-Launch Error Budget," *IEEE Transactions on Geoscience and Remote Sensing,* vol. 33, no. 1, pp. 147-161, Jan. 1995.

[34] N. Skou and D. Le Vine, Microwave Radiometer Systems Design and Analysis, Second ed., Norwood, MA: Artech House Inc., 2006.

[35] P. Racette and R. H. Lang, "Radiometer Design Analysis Based Upon Measurement Uncertainty," *Radio Science,* vol. 40, p. RS5004, 2005.

[36] V. S. Reinhardt, Y. C. Shih, P. A. Toth, S. C. Reynolds and A. L. Berman, "Methods for Measuring the Power Linearity of Microwave Detectors for Radiometric Applications," *IEEE Transactions on Microwave Theroy and Techniques,* vol. 43, no. 4, pp. 715-720, Apr. 1995.

[37] A. B. Tanner and A. L. Riley, "Design and performance of a high-stability water vapor radiometer," *Radio Science,* vol. 38, no. 3, p. 8050, 2003.

[38] D. M. Pozar, Microwave Engineering, Second ed., Crawfordsville: John Wiley & Sons, Inc., 1998.

[39] S. C. Reising, P. Kangaslahti, E. Schlecht, J. Jiang, X. Bosch-Lluis, M. Ogut, Y. Goncharenko, S. Padmanabhan, R. Cofield, N. Chahat, S. T. Brown, W. Deal, A. Zamora, K. Leong, S. Shih and G. Mei, "Tropospheric Water and

Cloud ICE (TWICE) Millimeter and Submillimeter-wave Radiometer Instrument for 6U-Class Nanosatellites," in *41st International Conference on Infrared, Millimeter, and Terahertz waves (IRMMW-THz)*, Copenhagen, Denmark, Sept. 2016.

[40] W. R. Deal, A. Zamora, W. Yoshida, M. Lange, B. Gorospe, K. Nguyen and G. X. Mei, "A low-power 670-GHz InP HEMT receiver," *IEEE Transactions on Terahertz Science and Technology,* vol. 6, no. 6, pp. 862-864, Nov. 2016.

[41] P. Kangaslahti, E. Schlecht, J. Jiang, W. R. Deal, A. Zamora, K. Leong, S. C. Reising, X. Bosch and M. Ogut, "CubeSat scale receivers for measurement of ice in clouds," *Proc. 14th Specialist Meeting on Microwave Radiometery and Remote Sensing of the Environment (MicroRad 2016),* Helsinki, Finland, Apr. 2016, pp. 42-47.

[42] S. Q. Kidder and T. H. Vonder Haar, Satellite Meteorology: An Introduction, San Diego, California: Academic Press, 1995.

[43] M. Ogut, S. C. Reising, X. Bosch-Lluis, Y. V. Goncharenko, B. Kilmer, P. Kangaslahti, E. Schlecht, R. Cofield, A. Skalare, S. Padmanabhan, J. Jiang, S. T. Brown, W. R. Deal and A. Zamora, "Design, Testing and Reliability Analysis of Command and Data Handling (C&DH) Subsystem for the Tropospheric Water and Cloud Ice (TWICE) Instrument for a 6U-Class Small Satellite," *Proc. 2018 IEEE International Geoscience and Remote Sensing Symposium (IGARSS),* Valencia, Spain, Jul. 2018.

[44] B. Baker, "A Glossary of Analog-to-Digital Specifications and Performance Characteristics," *Texas Instrument Application Report,* SBAA147B, Aug. 2006, Revised Oct. 2011.

[45] W. Kester, "Which ADC Arhitecture is Right for Your Application," *Analog Dialogue,* Vols. 39-06, pp. 1-8, Jun. 2005.

[46] A. Kay and T. Green, Analog Engineer's Pocket Reference, Fourth ed., Texas Instruments, 2015.

[47] C. Pearson, "High-Speed, Analog-to-Digital Converter Basics," *Texas Instruments Application Report,* SLAA510, Jan. 2011.

[48] B. Baker, "How Delta-Sigma ADCs Work - Part 1," *Texas Instruments, Analog Applications Journal,* no. Q3, pp. 13-16, 2011.

[49] B. Baker , "How Delta-Sigma ADCs work, Part 2," *Texas Instruments, Analog Applications Journal,* no. Q4, pp. 5-7, 2011.

[50] J. M. De La Rosa, R. Schreier, K.-P. Pun and S. Pavan, "Next-Generation Delta-Sigma Converters: Trends and Perspectives," *IEEE Journal on Emerging and Selected Topics in Circuits and Systems,* vol. 5, no. 4, pp. 484-499, Dec. 2015.

[51] R. Curran, "Exploring Different SAR ADC Analog Input Architectures," [Online]. Available: http://www.analog.com/en/technical-articles/exploring-different-sar-adc-analog-input-architectures.html. [Accessed 20 Sept. 2018].

[52] Analog Devices, "AD7091," [Online]. Available:

http://www.analog.com/en/products/ad7091.html. [Accessed 20 Sept. 2018].

[53] Analog Devices, "AD7656," [Online]. Available: http://www.analog.com/en/products/ad7656.html. [Accessed 20 Sept. 2018].

[54] Analog Devices, "AD7606," [Online]. Available: http://www.analog.com/en/products/ad7606.html. [Accessed 20 Sept. 2018].

[55] Texas Instruments, "ADS1178," [Online]. Available: http://www.ti.com/product/ADS1178. [Accessed 20 Sept. 2018].

[56] Analog Devices, "AD7609," [Online]. Available: http://www.analog.com/en/products/ad7609.html. [Accessed 20 Sept. 2018].

[57] Microsemi, "ProASIC3," [Online]. Available: https://www.microsemi.com/product-directory/fpgas/1690-proasic3. [Accessed 20 Sept. 2018].

[58] GlenAir, "Micro-D Connectors and Cables," [Online]. Available: https://www.glenair.com/micro-d/index.htm. [Accessed 20 Sept. 2018].

[59] Micro-Mode, "Blindmate Connectors," [Online]. Available: https://micromode.com/product-category/blindmates-connectors/. [Accessed 20 Sept. 2018].

[60] ITT Cannon, "SSMB/SSMC," [Online]. Available: https://www.ittcannon.com/products/ssmb-ssmc/. [Accessed 20 Sept. 2018].

[61] Harwin, "PC/104 and PC/104 Plus Connectors," [Online]. Available: https://www.harwin.com/product-highlights/pc104-pc104-plus-connectors/.

[Accessed 20 Sept. 2018].

[62] Texas Instruments, "INA3221," [Online]. Available: http://www.ti.com/product/INA3221. [Accessed 20 Sept. 2018].

[63] Analog Devices, "LTC3621," [Online]. Available: http://www.analog.com/en/products/ltc3621.html. [Accessed 20 Sept. 2018].

[64] W. Kester, "Analog Devices, MT-001 Tutorial," [Online]. Available: http://www.analog.com/media/en/training-seminars/tutorials/MT-001.pdf. [Accessed 20 Sept. 2018].

[65] C. Poivey, "Radiation hardness assurance for space systems," in *Proc. IEEE NSREC Short Course Notebook, Radiat. Effects*, 2002.

[66] P. E. Dodd, M. R. Shaneyfelt, J. R. Schwank and J. A. Felix, "Current and Future Challenges in Radiation Effects on CMOS Electronics," *IEEE Transactions on Nuclear Science,* vol. 57, no. 4, pp. 1747-1763, Aug. 2010.

[67] S. Bourdarie and M. Xapsos, "The near-Earth space radiation environment," *IEEE Trans. Nucl. Sci.,* vol. 55, no. 4, pp. 1810-1832, Aug. 2008.

[68] D. M. Fleetwood, "Total ionizing dose effects in MOS and Low-Dose-Rate-Sensitive Linear-Bipolar Devices," *IEEE Transactions on Nuclear Science,* vol. 60, no. 3, pp. 1706-1730, Jun. 2013.

[69] T. R. Oldham and F. B. McLean, "Total ionizing dose effects in MOS oxides and devices," *IEEE Transactions on Nuclear Science,* vol. 50, no. 3, pp. 483-499, Jun. 2003.

[70] R. A. Reed, J. Kinnison, J. C. Pickel, S. Buchner, P. W. Marshall, S. Kniffin and K. A. LaBel, "Single-event effects ground testing and on-orbit rate prediction methods: The past present and future," *IEEE Trans. Nucl. Sci.,* vol. 50, no. 3, pp. 622-634, Jun. 2003.

[71] ASTM F1192-11, "Standard Guide for the Measurement of Single Event Phenomena (SEP) Induced by Heavy Ion Irradiation of Semiconductor Devices," ASTM Committee F01 on Electronics, 2011.

[72] JEDEC Standard JESD57, "Test Procedures for the Measurement of Single-Event Effects in Semiconductor Devices from Heavy Ion Irradiation," Dec. 1996.

[73] European Space Agency, "Single Event Effects Test Method and Guidelines," ESCC Basic Specification No.25100-2, Oct. 2014.

[74] E. Peterson, Single Event Effects in Aerospace, New Jersey: John Wiley & Sons Inc., 2011.

[75] R. Koga, "Single-event effect ground test issues," *IEEE Trans. Nucl. Sci.,* vol. 43, no. 2, pp. 661-670, Apr. 1996.

[76] J. F. Dicello, M. Wasiolek and M. Zaider, "Measured microdosimetric specrtra of energetic ion beams of Fe, Ar, Ne and C: Limitations of LET disctributions and quality factors in space research and radiation effects," *IEEE Transactions on Nuclear Science,* vol. 38, no. 6, pp. 1203-1209, Dec. 1991.

[77] A. H. Johnston, T. F. Miyahira, F. Irom and J. S. Laird, "Single-event transients in voltage regulators," *IEEE Trans. Nucl. Sci.,* vol. 53, no. 6, pp. 3455-3461, Dec. 2006.

[78] G. Bruguier and J.-M. Palau, "Single particle-induced latchup," *IEEE Trans. Nucl. Sci.,* vol. 43, no. 2, pp. 522-532, Apr. 1996.

[79] W. A. Kolasinski, R. Koga, E. Schnauss and J. Duffey, "The Effect of Elevated Temperature on Latchup and Bit Errors in CMOS Devices," *IEEE Transactions on Nuclear Science,* vol. 33, no. 6, pp. 1605-1609, Dec. 1996.

[80] A. H. Johnston, B. W. Hughlock, M. P. Baze and R. E. Plaag, "The Effect of Temperature on Single-Particle Latchup," *IEEE Transactions on Nuclear Science,* vol. 38, no. 6, pp. 1435-1441, Dec. 1991.

[81] J. Adolphsen, J. L. Barth, E. G. Stassinopoulos, T. Gruner, M. Wennersten, K. A. LaBel and C. M. Seidleck, "Single Event Upset Rates on 1 Mbit and 256 Kbit Memories: CRUX Experiment on APEX," *IEEE Transactions on Nuclear Science,* vol. 42, no. 6, pp. 1964-1974, Dec. 1995.

[82] J. R. Cummings, A. C. Cummings, R. A. Mewaldt, R. S. Selesnick, E. C. Stone, T. T. Von Rosenvinge and J. B. Blake, "SAMPEX Measurements of Heavy Ions Trapped in the Magnetosphere," *IEEE Transactions on Nuclear Science,* vol. 40, no. 6, pp. 1458-1462, Dec. 1993.

[83] A. Campbell, P. McDonald and K. Ray, "Single Event Upset Rates in Space," *IEEE Transactions on Nuclear Science,* vol. 39, no. 6, pp. 1829-1835, Dec.

1992.

[84] Vanderbilt University School of Engineering, "the CREME site," [Online]. Available: https://creme.isde.vanderbilt.edu/CREME-MC. [Accessed 20 Sept. 2018].

[85] D. Sinclair and J. Dyer, "Radiation Effects and COTS Parts in SmallSats," in *Proc. 27th Annual AIAA/USU Conference on Small Satellites*, Logan, Utah, Aug. 2013.

[86] European Space Agency, "Space Environement Information System," [Online]. Available: https://www.spenvis.oma.be/. [Accessed 20 Sept. 2018].

[87] R. W. Kingsbury, "Optical communications for small satellites," Dept. Aeronautics and Astronautics, M. I. T., Cambridge, 2015.

[88] R. Netzer, K. Avery, W. Kemp, A. Vera, B. Zufelt and D. Alexander, "Total Ionizing Dose Effects on Commercial Electronics for CubeSats in Low Earth Orbits," *Radiation Effects Data Workshop (REDW),* Jul. 2014, pp. 1-7.

[89] R. Kingsbury, F. Schmidt, K. Cahoy, D. Sklair, W. Blackwell, I. Osarenting and R. Legge, "TID Tolerance of Popular CubeSat Components," in *Radiation Effects Data Workshop (REDW), 2013 IEEE*, San Francisco, CA, USA, Jul. 2013.

[90] Texas A&M University Cyclotron Institute, "Radiation Effects Facility," [Online]. Available: https://cyclotron.tamu.edu/ref/. [Accessed 20 Sept. 2018].

[91] F. Irom and S. G. Agarwal, "Compendium of single-event latchup and total

ionizing dose test results of commercial analog to digital converters," *IEEE Radiation Effects Data Workshop,* pp. 1-14, 2012.

[92] A. H. Johnston and T. F. Miyahira, "Latchup Test Considerations for Analog-to-Digital Converters," in *the SEE Symposium*, Manhattan Beach, CA, Apr. 2000.

[93] F. W. Sexton, "Destructive single-event effects in semiconductor devices and ICs," *IEEE Trans. Nucl. Sci.,* vol. 50, no. 3, pp. 603-621, Jun. 2003.

[94] E. L. Petersen, J. C. Pickel, J. H. Adams, Jr. and E. C. Smith, "Rate Prediction for Single Event Effects - a Critique," *IEEE Transactions on Nuclear Science,* vol. 39, no. 6, pp. 1577-1599, Dec. 1992.

[95] J. C. Pickel, "Single-event effects rate prediction," *IEEE Trans. Nucl. Sci.,* vol. 43, no. 2, pp. 483-495, Apr. 1996.

[96] R. Ladbury, "Statistical properties of SEE rate calculation in the limits of large and small event counts," *IEEE Trans. Nucl. Sci.,* vol. 54, no. 6, pp. 2113-2119, Dec. 2007.

[97] R. Ladbury, "Strategies for SEE hardness assurance - from buy-it-and-fly-it to bullet proof," in *IEEE Nuclear and Space Radiation Effects Conference (NSREC 2017)*, New Orleans, LA, USA, Jul. 2017.

[98] L. D. Edmonds, "Recommendations Regarding the Use of CREME96 for Heavy-Ion SEU Rate Calculations," *JPL Unpublished,* Jul. 2005.

[99] A. Tylka, J. Adams, P. Boberg, B. Brownstein, W. Dietrich, E. Flueckiger, E.

Peterson, M. Shea, D. Smart and E. Smith, "CREME96: A revision of the cosmic ray effects on micro-electronics code," *IEEE Trans. Nucl. Sci.,* vol. 44, no. 6, pp. 2150-2160, Dec. 1997.

[100] H.-M. Lin and A. N. Wilson Jr., "Median filters with adaptive length," *IEEE Trans. Circuits Syst.,* vol. 35, no. 6, pp. 675-690, Jun. 1988.

[101] R. Ladbury, "Radiation Hardening at the System Level," IEEE NSREC, Short Course, Waikiki, Jul. 2007.

[102] Microsemi, "RT ProASIC3 FPGAs," [Online]. Available: https://www.microsemi.com/products/fpga-soc/radtolerant-fpgas/rt-proasic3. [Accessed 20 Sept. 2018].

[103] NASA Goddard Space Flight Center, "GSFC Radiation Data Base," [Online]. Available: https://radhome.gsfc.nasa.gov/radhome/RadDataBase/RadDataBase.html. [Accessed 20 Sept. 2018].

[104] Texas Instruments, "ADS1282-SP Radiation Tolerant High-Resolution Delta Sigma ADC," [Online]. Available: http://www.ti.com/lit/ds/symlink/ads1282-sp.pdf. [Accessed 20 Sept. 2018].

[105] L. Z. Scheick, G. R. Allen and L. D. Edmonds, "Single-Event Effect Qualification of 24 Bit Analog-to-Digital Converters," *IEEE Radiation Effects Data Workshop (REDW),* pp. 1-5, 2013.

[106] R. H. Maurer, M. E. Fraeman, M. N. Martin and D. R. Roth, "Harsh

Environments: Space Radiation Environment, Effects, and Mitigation," *Johns Hopkins APL Technical Digest,* vol. 28, no. 1, pp. 17-29, 2008.

[107] P. C. Adell and L. Z. Scheick, "Radiation effects in power systems: A review," *IEEE Trans. Nucl. Sci.,* vol. 60, no. 3, pp. 1929-1952, Jun. 2013.

[108] P. C. Adell, A. F. Witulski, R. D. Schrimpf, F. Baronti, W. T. Holman and K. F. Galloway, "Digital Control for Radiation-Hardened Switching Convereters in Space," *IEEE Transactions on Aerospace and Electronic Systems,* vol. 46, no. 2, pp. 761-770, 2010.

[109] ST Microelectronics, "Minimizing the SET-related effects on the output of a voltage regulator," Jun. 2010. [Online]. Available: www.st.com/resource/en/application_note/cd00234144.pd. [Accessed 20 Sept. 2018].

[110] K. O'Malley, "Linear Regulator Protection Circuitry," Apr. 2001. [Online]. Available: https://www.onsemi.com/pub/Collateral/SR005AN-D.PDF. [Accessed 20 Sept. 2018].

[111] A. R. Kerr, M. J. Feldman and S. K. Pan, "Receiver noise temperature, the quantum noise limit, and the role of the zero-point fluctuations," National Radio Astronomy Observatory, Charlottesville, VA, Sept. 1996.

[112] Joint Committee for Guides in Metrology, "Evaluation of measurement data - Guide to the expression of uncertainty in measurement," JCGM 100:2008, GUM 1995 with minor corrections, Sept. 2008.

[113] W. J. Riley, Handbook of Frequency Stability Analysis, Boulder, CO: NIST Special Publication 1065, Jul. 2008.

[114] W. D. Stanley, "Investigation of Allan Variance for Determining Noise Spectral Forms With Application to Microwave Radiometry," NASA Contractor Report 194985, Hampton, VA, Nov. 1994.

[115] S. W. Wedge and D. B. Rutledge, "Wave Techniques for Noise Modeling and Measurement," *IEEE Transactions on Microwave Theory and Techniques,* vol. 40, no. 11, pp. 2004-2012, Nov. 1992.

[116] J. Randa, "Noise Characterization of Multiport Amplifiers," *IEEE Transactions on Micowave Theory and Techniques,* vol. 49, no. 10, pp. 1757-1763, Oct. 2001.

[117] I. Corbella, F. Torres, A. Camps, N. Duffo, M. Vall-llossera, K. Rautiainen, M. Martín-Neira and A. Colliander, "Analysis of Correlation and Total Power Radiometer Front-Ends Using Noise Waves," *IEEE Transactions on Geoscience and Remote Sensing,* vol. 43, no. 11, pp. 2452-2459, Nov. 2005.

[118] A. Camps, "Noise wave analysis of Dicke and noise injection radiometers: Complete S parameter analysis and effect of temperature gradients," *Radio Science,* vol. 45, p. RS5004, 2010.

[119] S. W. Wedge and D. B. Rutledge, "Noise Waves and Passive Linear Multiports," *IEEE Microwave and Guided Wave Letters,* vol. 1, no. 5, pp. 117-119, May 1991.

[120] H. Bosma, "On the theory of linear noisy systems," *Philips Res. Repts. Suppl.,* no. 10, 1967.

[121] L. Yujiri, M. Shoucri and P. Moffa, "Passive Millimeter-Wave Imaging," *IEEE Microwave Magazine,* pp. 39-50, Sept. 2003.

[122] I. Corbella, A. J. Gasiewski, M. Klein, V. Leuski, A. J. Francavilla and J. R. Piepmeier, "On-board accurate calibration of dual-channel radiometers using internal and external references," *IEEE Transactions on Microwave Theory and Techniques,* vol. 50, no. 7, pp. 1816-1820, Jul. 2002.

[123] R. W. Saunders, T. J. Hewison, S. J. Stephen and N. C. Atkinson, "The Radiometric Characterization of AMSU-B," *IEEE Transactions on Microwave Theory and Techniques,* vol. 43, no. 4, pp. 760-771, Apr. 1995.

[124] F. T. Ulaby, R. K. Moore and A. K. Fung, Microwave Remote Sensing: Active and Passive, vol. 1, Reading, Massachusetts: Addison-Wesley, 1981.

[125] The CubeSat Program, "CubeSat Design Specification Rev.13," Cal Poly SLO, San Luis Obispo, CA, Feb. 2014.

[126] C. Ruf, "Detection of calibration drifts in spaceborne microwave radiometers using a vicarious cold reference," *IEEE Trans. Geosci. Remote Sens.,* vol. 38(1), pp. 44-52, 2000.

[127] Y. LeCun, Y. Bengio and G. Hinton, "Deep Learning," *Nature,* vol. 521, pp. 436-444, 28 May 2015.

[128] S. J. Russell and P. Norvig, Artificial Intelligence: A Modern Approach, New

Jersey: Prentice Hall, 1995.

[129] S. Haykin, Neural Networks and Learning Machines, 3rd ed., New Jersey: Pearson Education, Inc., 2009.

[130] J. Schmidhuber, "Deep Learning in Neural Networks: An Overview," *Neural Networks,* vol. 61, pp. 85-117, 2015.

[131] Y. Bengio, "Learning Deep Architectures for AI," *Foundations and Trends in Machine Learning,* vol. 2, no. 1, pp. 1-127, 2009.

[132] L. Bottou and O. Bousquet, "The Tradeoffs of Large Scale Learning," in *Advances in Neural Information Processing Systems*, 207.

[133] X. Glorot, A. Bordes and Y. Bengio, "Deep Sparse Rectifier Neural Networks," in *14th International Conference on Artificial Intelligence and Statistics*, 2011.

[134] V. Nair and G. E. Hinton, "Rectified Linear Units Improve Restricted Boltzmann Machines," in *Proceedings of the 27th International Conference on Machine Learning (ICML-10)*, 2010.

[135] R. Kohavi, "A study of cross-validation and bootstrap for accuracy estimation and model selection," *Proc. 14th Int. Joint Conf. Artificial Intelligence,* pp. 338-345, 1995.

[136] G. Lavenuta, "Negative Temperature Coefficient Thermistors," QTI Sensing Solutions, [Online]. Available: https://www.thermistor.com/sites/default/files/specsheets/Negative-

Temperature-Coefficient-Thermistors.pdf. [Accessed 20 Sept. 2018].

[137] C. Kummerow et al., "The status of the tropical rainfall measuring mission (TRMM) after two years in orbit," *J. Appl. Meteor.,* vol. 39, pp. 1965-1982, 2000.

[138] M. Ablain, S. Phillipps, N. Picot and E. Bronner, "Jason-2 global statistical assesment and cross-calibration with Jason-1," *Marine Geodesy,* vol. 33:sup1, pp. 162-185, 2010.

[139] S. C. Reising, P. Kangaslahti, A. B. Tanner, S. Padmanabhan, O. Montes, C. Parashare, X. Bosch-Lluis, T. Johnson, V. Hadel, K. Ng, T. C. Gaier and B. Razavi, "Demonstration of high-frequency airborne microwave and millimeter-wave radiometer (HAMMR) to improve spatial resolution of wet-tropospheric path delay measurements for coastal and inland water altimetry," in *NASA Earth Science Technology Forum*, NASA Conference Center, Leesburg, VA, USA, 2015.

[140] P. Rosenkranz, "Water vapor microwave continuum absorption: A comparison of measurements and models," *Radio Sci.,* vol. 33, no. 4, pp. 919-928, Jul.-Aug. 1998.

[141] P. W. Rosenkranz, "Absorption of microwaves by atmospheric gases," in *Atmospheric Remote Sensing by Microwave Radiometry*, New York, Wiley-Interscience Publication, 1993, pp. 37-79.

[142] H. J. Liebe, "A contribution to modeling atmospheric millimeter-wave

properties," *Frequenz,* vol. 41, pp. 31-36, 1987.

[143] S. Sahoo, X. Bosch-Lluis, S. C. Reising and J. Vivekanandan, "Radiometric information content for water vapor and temperature profiling in clear skies between 10-200 GHz," *IEEE J. Sel. Topics Appl. Earth Observ. Remote Sens.,* 2014.

[144] F. J. Wentz, "A model function for ocean microwave brightness temperatures," *Journal of Geophysical Research,* vol. 88, pp. 1892-1908, Feb. 1983.

[145] J. C. Alishouse, S. A. Snyder, J. Vongsathorn and R. R. Ferraro, "Determination of Oceanic Total Precipitable Water From the SSM/I," *IEEE Transactions on Geoscience and Remote Sensing ,* vol. 28, no. 5, pp. 811-816, Sept. 1990.

[146] J. W. Waters, K. F. Kunzi, R. L. Pettyjohn, R. K. Poon and D. H. Staelin, "Remote sensing of atmospheric temperature profiles with Nimbus-5 microwave spectrometer," *Journal of Atmospheric Science,* vol. 32, pp. 1953-1969, 1975.

[147] G. Backus and F. Gilbert, "Uniqueness in the inversion of inaccurate gross earth data," *Phil. Trans. R. Soc. London,* vol. A266, pp. 123-192, 1970.

[148] A. N. Tikhonov, "The solution of ill-posed problems and the regularization method," *Dokl. Acad. Nauk USSR,* vol. 151, no. 3, pp. 501-504, 1963.

[149] D. T. Davis, Z. Chen, J.-N. Hwang, L. Tsang and E. Njoku, "Solving inverse

problems by Bayesian iterative inversion of a forward model with applications to parameter mapping using SMMR remote sensing data," *IEEE Transactions on Geoscience and Remote Sensing,* vol. 33, no. 5, pp. 1182-1193, Sept. 1995.

[150] C. Goutte and J. Larsen, "Adaptive regularization of neural networks using conjuage gradient," *Proceedings of IEEE International Conference on Acoustics Speech and Signal Processing,* vol. 2, pp. 1201-1204, 1998.

[151] D. J. MacKay, "Bayesian interpolation," *Neural Computation,* vol. 4, pp. 415-447, 1992.

[152] D. Foresee and M. Hagan, "Gauss-Newton approximation to Bayesian learning," *Proceedings of the 1997 International Joint Conference on Neural Networks,* vol. 3, pp. 1930-1935, 1997.

List of Abbreviations

ADC	Analog-to-Digital Converter
ADCS	Attitude Determination and Control Systems
AI	Artificial Intelligence
ANN	Artificial Neural Network
BPF	Band Pass Filter
C&DH	Command and Data Handling
CMOS	Complementary Metal-Oxide Semiconductor
COTS	Commercial-off-the Shelf
CPU	Central Processing Unit
CSLI	CubeSat Launch Initiative
CubeRRT	CubeSat Radiometer Radiometer Radio Frequency Interference Technology Validation
CSU	Colorado State University
DNL	Differential Non-Linearity
EMI	Electromagnetic Interference
ESL	Equivalent Series Inductance
ESR	Equivalent Series Resistance
ESTO	Earth Science Technology Office
FET	Field-Effect Transistor
FFT	Fast Fourier Transform

FIT	Failures-In-Time
FPGA	Field Programmable Gate Array
GCR	Galactic Cosmic Ray
GPS	Global Positioning System
GSFC	Goddard Space Flight Center
HEMT	High Electron Mobility Transistor
I2C	Inter-Integrated Circuit
IC	Integrated Circuit
IF	Intermediate Frequency
IIP	Instrument Incubator Program
IIRP	Integral Rectangular Parallelepiped Method
InP	Indium Phosphide
ISS	International Space Station
JPL	Jet Propulsion Laboratory
PWM	Pulse-Width Modulation
JTAG	Joint Test Action Group
LED	Light Emitting Diode
LEO	Low-Earth Orbit
LET	Linear Energy Transfer
LM	Levenberg-Marquardt
LNA	Low Noise Amplifier
LSB	Least Significant Bit

MEMS	Micro-electromechanical Systems
MicroMAS	Micro-sized Microwave Atmospheric Satellite
MIT	Massachusetts Institute of Technology
MLP	Multilayer Perceptron
MOSFET	Metal Oxide Semiconductor FET
NASA	National Aeronautics and Space Administration
NCAR	National Center of Atmospheric Research
NEΔT	Noise Equivalent Delta Temperature
NGC	Northrop Grumman Corporation
NTC	Negative Temperature Coefficient
OBC	On-Board Computer
PCB	Printed Circuit Board
RadHard	Radiation Hardened
ReLU	Rectified Linear Unit
RF	Radio Frequency
RMS	Root-Mean Square
RPM	Revolution per Minute
SAR	Successive Approximation Register
SCR	Silicon Controlled Rectifier
SEB	Single-Event Burnout
SEBU	Single-Event Bit-Upset
SEE	Single-Event Effect

SEFI	Single-Event Functional Interrupt
SEGR	Single-Event Gate Rupture
SEL	Single-Event Latch-up
SER	Soft Error Rate
SET	Single-Event Transient
SGD	Stochastic Gradient Descent
SmallSat	Small Satellite
SPDT	Single-Pole Double-Throw
SPENVIS	Space Environment Information System
SPI	Serial Peripheral Interface
SPS	Samples-per-Second
SWaP	Size, Weight and Power
TAMU	Texas A&M University
TEMPEST-D	The Temporal Experiment for Storms and Tropical Storms Demonstrator
TI	Texas Instruments
TID	Total Ionizing Dose
TRL	Technology Readiness Level
TROPICS	The Time Resolved Observations of Precipitation structure and storm Intensity with a Constellation of SmallSats
TWICE	Tropospheric Water and Cloud Ice

UCLA	University of California at Los Angeles
USB	Universal Serial Bus
VHDL	Very High Speed Integrated Circuit (VHSIC) Hardware Description Language
VLDO	Very Low-Dropout
VLSI	Very-Large Scale Integration
WCFC	The West Coast Flight Campaign
WPD	Wet Path Delay